Advanced Modulations of Optical Interconnections for Mega-Datacenters

Lu, Xiaofeng

Publication date:
2018

Document Version
Publisher's PDF, also known as Version of record

Citation (APA):
Lu, X. (2018). *Advanced Modulations of Optical Interconnections for Mega-Datacenters*. DTU Fotonik.

Advanced Modulations of Optical Interconnections for Mega-Datacenters

Ph.D. Thesis

Xiaofeng Lu

1st May 2018

DTU Fotonik
Department of Photonics Engineering
Technical University of Denmark
Building 343
2800 Kgs. Lyngby
DENMARK

DTU Fotonik
Institut for Fotonik

Preface

This thesis presents a summary of my Ph.D. research in the period from May 1st, 2015 to April 30th, 2018. The project, i.e. HOT project (Ultra-high Optical Transport), was in association with Mellanox Technologies Denmark. The experiments in this work were mainly conducted at DTU Fotonik (Technical University of Denmark, Department of Photonics Engineering), and partly at Institute of Telecommunications, Warsaw University of Technology, Warsaw, Poland.

The Ph.D. project was partly financed by the Innovationsfonden, Denmark (Danish Innovative Foundation) and the DTU VIP Scholar Programme and supervised by

- Darko Zibar (main supervisor), Associate Professor, DTU Fotonik, Technical University of Denmark, Kgs. Lyngby, Denmark.
- Lars Dittmann (co-supervisor), Professor, DTU Fotonik, Technical University of Denmark, Kgs. Lyngby, Denmark.
- Idelfonso Tafur Monroy (co-supervisor), Professor, Department of Electrical Engineering, Technical University of Eindhoven, Eindhoven, the Netherlands.
- Steen Christensen (co-supervisor), Mellanox Technologies, Roskilde, Denmark.

Abstract

Recently, we are experiencing a soar of the traffic needs for the data networks with the paradigm shifting of industry and the upgrade of the information infrastructure. It places a bandwidth-hunger of the data interconnections in almost all scenarios, particularly for ones between and inside large-scale datacenters. Besides the needs for data-rate, the design and deployment of datacenter interconnects are limited by other equally important requirements, e.g. power consumptions, costs, latencies, footprint, lifetime and reliability. Thus, the current simple modulation scheme, i.e. non-return-to-zero (NRZ), lags behind expectations for the future development. For this reason, advanced modulation schemes and physical configurations have been proposed in the past few years.

This thesis summaries a three-year Ph.D. research on the advanced modulations for the large datacenter interconnections, using 850 nm vertical-cavity surface-emitting lasers (VCSELs). The majority covers the application of multi-dimensional coded modulations in the transmission systems with intensity-modulated direct-detection (IM/DD) schemes. It presents the benefits of both multi-level signals and multi-subcarrier systems.

The work starts with the design of four and eight-dimensional multi-level modulation formats, and further simplifications regarding the complexity of the modulation and demodulation, as well as the decision process. Then, an eight-dimensional eight-level format, i.e. BB8, with equivalent 2 bit/symbol, is theoretically proposed and experimentally demonstrated. It is further extended to a family of eight-dimensional modulation formats, named as E_8Flex-m. The family based on the optimal eight-dimensional lattices. It provides a smooth transition of the bit-rate with a finer granularity of 0.125 bit/symbol. Based on the similar designing philosophy, we demonstrated a 24-dimensional pulse amplitude modulation (PAM), by combining the temporally adjacent symbols, based on the densest lattice in 24-D space, i.e. Leech lattice. Formats with equivalent 2 bits are designed and demonstrated. It shows that the performance of the 24-D PAM outperforms its 8-D counterpart, as well as the conventional PAMs in a 100 Gbit/s system. Further, we extend such format into a bit-rate flexible version by using the cutting and scaling techniques on the hyperspace.

To enhance the performance, we combine the above mentioned rate-flexible hyperspace formats with the multi-subcarrier techniques, such as discrete multitone (DMT) and carrier-less amplitude phase modulations (CAP). We demonstrate a world record 120 Gbit/s DMT using 850 nm multi-mode VCSELs over 100 m MMFs and four-dimensional formats. Based on that, we demonstrate the transmission with a serial of four-dimensional formats loaded with general benefits in data-rates. A further application of the eight-dimensional formats on DMT transmissions is investigated, showing a series of benefits in the bit-rate increase, the reach extension, and the enhancement of the tolerance for the thermal and insertion loss. Meanwhile, the experiments of the 24-D rate-flexible formats loaded for the multi-band CAP transmission are demonstrated. It shows the further improvement of the performances, including the reach, thermal tolerance and the insensitivity of the insertion loss.

Some other advanced modulation schemes related with this three-year research are briefly introduced, such as the mode-selective launching and the optical compensation techniques for the mode-division multiplexing of optical angular momenta.

In summary, this thesis presents various alternative modulation schemes, opening new possibilities and feasibilities of multi-dimensional coded modulations in future products, improving the state of the art techniques, extending the understanding of the benefits gained for the next generation optical data links used inside and between mega-datacenters, and hopefully bringing them closer to the actual deployments.

Resumé

For nylig oplever vi en stigning i trafikbehovene for datanetværkene med paradigmeskiftet af industrien og opgraderingen af informationsinfrastrukturen. Det placerer en båndbredde-sult af dataforbindelserne i næsten alle scenarier, især for dem mellem og inde i store datacentre. Ud over behovet for datahastighed er design og implementering af datacenterforbindelser begrænset af andre lige vigtige krav, f.eks. strømforbrug, omkostninger, ventetider, størrelsesformer, levetid og pålidelighed. Således ligger det nuværende enkle modulationsformat, dvs. non-return-to-zero (NRZ), bag forventningerne til den fremtidige udvikling. Af denne grund er avancerede modulationsformater og fysiske konfigurationer blevet foreslået i de sidste par år.

Denne afhandling opsummerer en treårig Ph.D. -forskning af de avancerede modulationer for de store datacenter sammenkoblinger, med hjælp af 850 nm vertical-cavity surface-emitting lasers (VCSELs). Størstedelen dækker anvendelsen af multidimensionale kodede modulationer i transmissionssystemer der benytter intensity-modulated direct-detection (IM/DD). Det præsenterer fordelene for både multi-level signal og multi-subcarrier systemer. Arbejdet starter med udformningen af fire og otte dimensionale modulations formater med flere niveauer og yderligere simplificeres med hensyn til kompleksiteten af moduleringen og de-moduleringen samt beslutningsprocessen. Derefter foreslås det otte-dimensionelle otte-niveau format, dvs. BB8, med ækvivalent 2 bit/symbol, teoretisk og demonstreret eksperimentelt. Den udvides yderligere til en familie af otte-dimensionelle modulationsformater, kaldet E_8Flex-m. Familien er baseret på de optimale otte-dimensionale gitter. Det giver en jævn overgang af bitrate med en fin granulering på 0.125 bit/symbol. Baseret på den tilsvarende designfilosofi demonstrerede vi en 24-dimensional puls amplitude modulering (PAM) ved at kombinere de temporært tilstødende symboler baseret på det tætteste gitter i 24-D rum, dvs. Leech lattice.

Formater med ækvivalente 2 bits er designet og demonstreret. Det viser, at den bedre ydelse af 24-D PAM overpræsterer sin 8-D modpart, såvel som de almindelige PAM formater i et 100 Gbit/s system. Ydermere, udvidede vi dette format til en bitrate fleksibel version ved at bruge skære og dele teknikker på hyper-rummet.

For at forbedre ydeevnen kombinerer vi de ovennævnte rate-fleksible hyper-rums formater med multi-subcarrier teknikker, såsom diskret multitone (DMT) og cairrer-less amplitude fase modulering (CAP). Vi demonstrerer en verdensrekord på 120Gbit/s DMT ved hjælp af 850 nm multi-mode VCSELs over 100 MMFs bærende fire-dimensionelle formater. På baggrund af dette demonstrerede vi transmissioner af en række af fire-dimensionelle formater, som alle viste en generel fordel i data rater. En yderligere anvendelse af de otte-dimensionelle formater via DMT-transmissioner er blevet undersøgt, hvilket viser en række fordele i form af bithastigheds forøgelse, transmissions forlængelse og forbedringen af tolerancen for termisk og indsættelsestab. I mellemtiden demonstreres eksperimenterne af de 24-D rate-fleksible formater, der er lastet til multi-band CAP-transmission. Det demonstrerer den yderligere forbedring af ydelsen, herunder transmissionslængden, termisk tolerance og ufølsomhed af indsættelsestab.

Nogle andre avancerede modulerings muligheder, der relaterer sig til disse treårige undersøgelser, er kort introduceret, såsom mode-selektive launching og optiske kompensationsteknikker til mode-division multiplexing af optisk vinkel-momenta. Sammenfattende præsenterer denne afhandling forskellige alternative modulerings muligheder, der åbner op for nye multidimensionel kodet moduleringer i fremtidige produkter, forbedring af de nyeste teknikker, udvidelse af forståelsen af de fordele, der er opnået for den næste generation af optiske datalink, der anvendes inde i og imellem mega-datacentre, og forhåbentlig bringe dem tættere på de faktiske implementeringer.

Acknowledgements

Before acknowledging all who contributed this thesis and the research achievements, I would like to express my gratitude first to the destiny, for bringing me here, giving me the opportunities and placing all the uncertainties in the past three years, and most importantly, telling me what a real life looks like and what I should cherish in my whole life.

Specifically, I would like to thank my supervision team members, Professor Darko Zibar, Professor Lars Dittmann, Professor Idelfonso Tafur Monroy, and Mr. Steen Christensen, for their visionary, imaginary, inspiring and insightful suggestions on my research direction, the strong administrative and finical assistant on the experiments I desired and the tolerance for my unusual way of thinking. My thanks are also given to Professor Lars-Ulrik Aaen Andersen and Professor Morten Willatzen for their impartial administrative support.

I would like to thank all my colleagues and friends I met at DTU for all the assistance received and joys shared. Among them, I would especially express my acknowledgement to Dr. Anna Tatarczak. We had a joyful period at DTU. What we could share is far beyond the experimental achievements and failures, music, arts, history, and jokes. I would also like to thank Antonio Jurado-Navas, Jesper, Vladimir, Sebastian, Victor, and Jose Antonio... and also our visiting scholars, Lisa, Ruslan, Lutz...

I would like to thank all my colleagues at Mellanox Technologies, Dr. Yaohui Chen, Dr. Dazeng Feng, Mr. Henning Lysdal, and Dr. Johan Jacob Mohr, especially for Yaohui, who appeared at a very right time during my Ph.D., and showed a high standard to all technical questions and a rigorous research attitude. He selflessly shared his professional experience and opinions on the industrial development. I also appreciated the warm hospitality from his family, which ceased my strong nostalgia.

I shall not forget our partner team in Poland, Professor Jarosław P. Turkiewic, Łukasz Chorchos and Dr. Grzegorz Stepniak. Pierogi with discussions on VCSELs might be the best feast in my life.

I would like to thank Dr. Henning Bülow and his family for sharing and instructing. The acknowledgment is given to all my previous German supervisors and friends.

I would like to thank my landlord lady and her family. It is she who told me the Danish secrete of happiness.

I would like to thank the architecture designer of the new DTU Fotonik building. The soft bench accommodates me for countless sleepless nights.

Finally but most importantly, I would like to thank my families, they are the only reason that I could explore in the darkness without fearing and worrying about the retreat. It is forever my Ithaca and the only place I could rest in the spring of 2016.

Thank you! Tak! 谢谢! Danke! Dziekuje!

Holte, 30 April 2018 Xiaofeng Lu, 陆晓风

Summary of Original Work

This thesis is based on the following original publications:

PAPER 1 **X. Lu**, D. Zibar, and I. Tafur Monroy, "Net 100 Gbit/s Eight-Dimensional Formats Loaded Discrete Multi-tone Transmission Using 850 nm Multimode VCSELs," in *Proc. Optical Fiber Communication Conference and Exposition, (OFC 2018)*, San Diego, CA, March 2018, paper M1I.5.

PAPER 2 **X. Lu**, D. Zibar, and I. Tafur Monroy, "Leech-CAP: A 24-Dimensional Rate-Flexible Alterative 100 G Solution for Intra-datacenter Interconnection," submitted to *44th European Conference on Optical Communication, (ECOC 2018)*, Roma, Italy, September 2018.

PAPER 3 **X. Lu**, V. S. Lyubopytov, L. Chorchos, G. Stepniak, M. Agustin, J. R. Kropp, N. N. Ledentsov, V. A. Shchukin, N. Ledentsov Jr., J. P. Turkiewicz, and I. Tafur Monroy, "100 G IM-DD 850 nm VCSEL-based Transceiver with Flexible Bit Rate using Eight-Dimensional PAM," in *Proc. 43rd European Conference on Optical Communication, (ECOC 2017)*, Gothenburg, September 2017, paper M.1.D.1.

PAPER 4 **X. Lu**, V. S. Lyubopytov, and I. Tafur Monroy, "24-Dimensional Modulation Formats for 100 Gbit/s IM-DD Transmission Systems Using 850 nm Single-Mode VCSEL," in *Proc. 43rd European Conference on Optical Communication, (ECOC 2017)*, Gothenburg, September 2017, paper Tu.2A.4.

PAPER 5 **X. Lu**, V. S. Lyubopytov, and I. Tafur Monroy, "Net 100G Data Transmission with 850 nm MM-VCSEL over 100m MMF Using Discrete Multi-tone of Four Dimensional Formats," in *Proc. 2017 Opto-Electronics and Communications Conference (OECC 2017)*, Singapore, July 2017.

PAPER 6 **X. Lu**, A. Tatarczak, V. S. Lyubopytov, and I. Tafur Monroy, "Optimized Eight-Dimensional Lattice Modulation Format for IM-DD 56 Gbit/s Optical Interconnections Using 850 nm VCSELs," in *IEEE/OSA Journal of Lightwave Technology*, vol. 35, no. 5, pp. 1407–1414, 2017 (highly scored).

PAPER 7 **X. Lu**, A. Tatarczak, and I. Tafur Monroy, "Eight Dimensional Optimized Modulation for IM-DD 56 Gbit/s Optical Interconnections Using 850 nm VCSELs," in *42rd European Conference on Optical Communication, (ECOC 2016)*, Düsseldorf, Germany, 2016, paper Tu.1.C.2 (highly scored).

PAPER 8 **X. Lu**, and I. Tafur Monroy,"8-dimensional Lattice Optimized Formats in 25-GBaud/s VCSEL based IM/DD Optical Interconnections," in *Proc. Asia Communications and Photonics Conference (ACP 2015)*, Hong Kong, China, November 2015, paper AS4D.3.

PAPER 9 A. Tatarczak, **X. Lu**, S. Rommel, S. Rodriguez, J. J. Vegas Olmos, and I. Tafur Monroy, "Radio-over-Fiber Transmission Using Vortex Modes," in *Proc. Microwave Photonics (MWP 2015)*, Paphos, Cyprus, September 2015.

PAPER 10 V. S. Lyubopytov, A. Tatarczak, **X. Lu**, R. V. Kutluyarov, S. Rommel, A. Kh. Sultanov, and Idelfonso Tafur Monroy, "Optical-domain Compensation for Coupling between Optical Fiber Conjugate Vortex Modes," in *Proc. 11th Conference on Lasers and Electro-Optics Pacific Rim (CLEO-PR 2015)*, Busan, Korea, August 2015. (post-deadline)

Other scientific reports associated with the project:

[PAPER 12] J. Estarán, **X. Lu**, D. Zibar, and I. Tafur Monroy, "Stokes Space in Direct-Detection Transmission Systems," in *Asia Communications and Photonics Conference (ACP 2015)*, Hong Kong, China, November 2015. (invited paper)

[PAPER 13] A. Tatarczak, **X. Lu**, and Idelfonso Tafur Monroy, "Improving the Capacity of Short-Reach VCSEL-based MMF Optical Links," in *Proc. Latin America Optics and Photonics Conference (LAOP 2016)*, Medellin, Colombia, August 2016.

[PAPER 14] **X. Lu**, A. Tatarczak, S. Rommel, S. Rodriguez, J. J. Vegas Olmos, and I. Tafur Monroy, "Microwave photonics technologies supporting high capacity and flexible wireless communications systems," in *Proc. Asia Communications and Photonics Conference (ACP 2015)*, Hong Kong, China, November 2015, paper ASu1J.5. (invited paper)

[PAPER 15] A. Jurado-Navas, A. Tatarczak, **X. Lu**, J. J. Vegas-Olmos, J. M. Garrido-Balsells, and I. Tafur Monroy, "850-nm hybrid fiber/free-space optical communications using orbital angular momentum modes," *OSA Optics Express*, vol. 23, no. 26, pp. 33721–33732, 2015.

Other scientific reports:

[C1] V. S. Lyubopytov, A. Tatarczak, **X. Lu**, R. V. Kutluyarov, S. Rommel, A. Kh. Sultanov, and I. Tafur Monroy, "Analysis of optical fiber complex propagation matrix on the basis of vortex modes," in *Proc. 2016 International Conference Laser Optics (LO 2016)*, St. Petersburg, Russia, 2016.

[C2] V. S. Lyubopytov, A. Tatarczak, **X. Lu**, R. V. Kutluyarov, S. Rommel, A. Kh. Sultanov, and I. Tafur Monroy, "Experimental Reconstruction of the Optical Fiber Complex Propagation Matrix in the Basis of Vortex Modes," submitted to *Optics Express*, 2018.

Contents

List of Figures

List of Tables

Chapter 1

Introduction

In recent years, Internet plus, i.e. 'Internet+', is widely recognized as the fourth industrial revolution, which is expected to shift the paradigm of the industrial development, boost the further economic growth and reshape the social relations. It is acknowledged and accepted by governments over the world as national strategies, among which the most famous ones include 'Made in China 2025' in China, 'Industry 4.0' in Germany, 'National Strategic Plan for Advanced Manufacturing' in the United States and 'Strategy for Industry 2050' in U.K. Such tendency re-defines the role that data are playing essentially and promotes the fast upgrades of the current generation of information infrastructures: the standardization of the fifth generation (5G) techniques is approaching its last phase to the actual deployment; The clusters of the large-scale data and computation-centers are sprouting over the whole planet; The satellite swarm based space Internet access is on its way down to the earth. Besides, the current trend of decentralization, which alleviates the traffic load on the backhaul networks by adding the redundancy on the local level, e.g. the cloud computing, and enhances the efficiency and security of the record of commercial transactions by adopting the distributive topology of data systems, e.g. the block chains, leads to a soar of traffic needs on the metro, access, and especially datacenter networks. Among all the technical difficulties, the tremendous volume of data merged and exchanged in and between datacenters, therefore, increasingly becomes a critical obstacle in the way paving to the future. Companies who are strongly relying on data start to investing in the network and computation infrastructure intensively. For instance, the Internet giants, such as Google, Facebook, and Alibaba, are constructing their private datacenter networks. The actual deployment of the 400 G datacenter networks is ex-

Table 1.1: Definition of datacenter scale [2].

Size Metric	Rack Yield	SQM(m^2)	DL(m)
Mega	≥9,001	≥22,501	≥216
Massive	3,001-9,000	7,501-22,500	128-216
Large	801-3,000	2,001-7,500	64-128
Medium	201-800	501-2,000	32-64
Small	11-200	26-500	8-32
Mini	1-10	1-25	1-8

cepted in 2019, and the further upgrade beyond 1T networks is approaching in next five years, i.e. 2023.

1.1 Optical interconnects for mega-datacenters

1.1.1 Requirements

A datacenter can be seen basically as a cluster of parallel supercomputers. Along with the upgrade of the scale, the construction of a datacenter gets increasingly complex and becomes far beyond simply piling computation and storage units. The data exchange between datacenters appears a major obstacle of the scalability. The scale of a datacenter is defined as listed in Tab. 1.1. For smaller scale datacenter, where the CPUs or racks are deployed closely, copper interconnects are sufficient for the bandwidth needs; whereas for datacenters with larger scale and more complicated hierarchy, optical interconnects become the mainstream solutions deployed in the current generation datacenters with connecting distance longer than few meters, due to its higher bandwidth and longer reach. Fig 1.1 shows the network topology of a modern datacenter[1]. The number of interconnects and traffic on a different layer, especially the spine plane, increases exponentially with the scale of computation nodes. Thus, the datacenter interconnection (DCI) is bandwidth-cost sensitive.

For reducing the cost of the bandwidth needs, a hierarchal deployment strategy is adopted. It means using different technologies for interconnects on the corresponding layer. Concretely, the intra-rack interconnects, i.e. <1 m, usually adopt copper links and printed circuit board (PCB) [3]. Recently, the polymer waveguide based intra-rack/on-board optical interconnect is also investigated [4], which is promising as an alternative for

---

[1] The diagram refers to the presentation of Facebook datacenters [1]

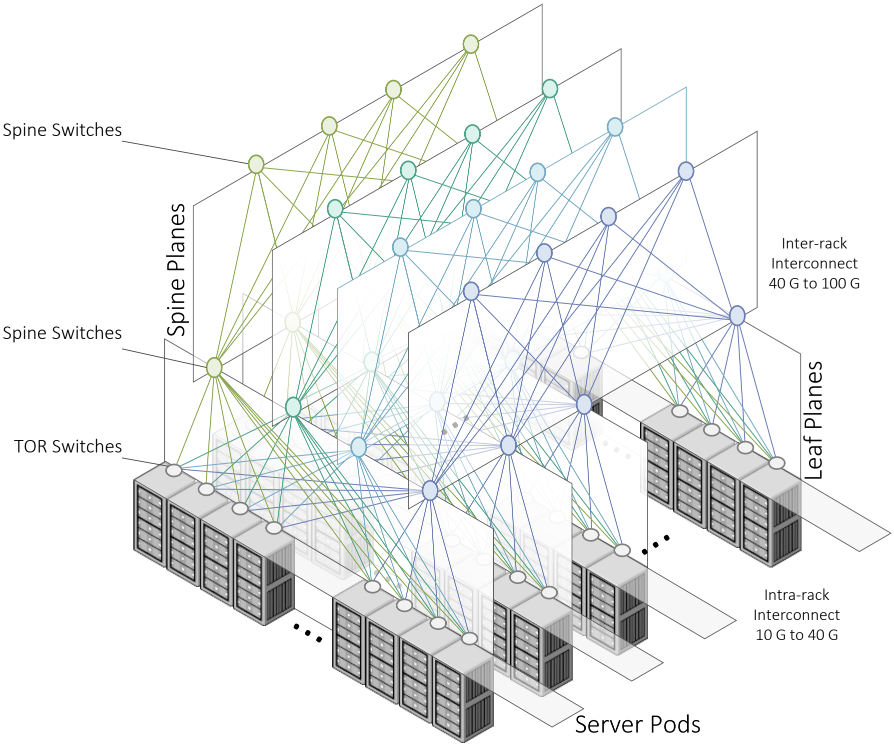

Figure 1.1: The typical network topology of a modern mega-datacenter.

the future. The interconnects with transmission distance from few meters to few kilometers, typically 2 km is the intra-datacenter case, which connects the top-of-rack (TOR) switch, edge switch, edge aggregation switch and the spine switch [3]. For interconnects with transmission distance <100 m, vertical-cavity surface-emitting laser (VCSEL) based multi-mode fiber (MMF) data links are used. It offers a comprehensive trade-off between performance and cost. Specifically, the cost of the VCSELs and VCSEL-to-MMF coupling, especially for 850 nm VCSELs, is relatively low, which balances the higher cost on the MMF. Beyond 100 m, single-mode fiber (SMF) becomes an exclusive solution. Moreover, the choices of lasers are beyond VCSEL only. External modulation schemes, e.g. Mach-Zehnder modulator (MZM) and electro-absorption modulator (EAM), with reasonable costs, also become the possible options. The reasons behind it include (1) the lower cost of SMF; (2) longer reach due to the lower dispersion, or equivalently higher bandwidth of SMF than MMF [3]. For distance beyond

Table 1.2: Physical layers of 40/100 Gigabit Ethernet standard in IEEE 802.3 [6].

Physcial layer	40 Gigabit Ethernet	100 Gigabit Ethernet
Backplane	n.a.	100GBASE-KP4
Improved Backplane	40GBASE-KR4	100GBASE-KR4
7 m over twinax copper cable	40GBASE-CR4	100GBASE-CR10
		100GBASE-CR4
100 m over OM3 MMF	40GBASE-SR4	100GBASE-SR10
125 m over OM4 MMF		100GBASE-SR4
500 m over SMF	-	100GBASE-DR
2 km over SMF, serial	40GBASE-FR	100GBASE-CWDM4
10 km over SMF	40GBASE-LR4	100GBASE-LR4
40 km over SMF	40GBASE-ER4	100GBASE-ER4

Table 1.3: Featured requirements for current and future datacenters [5].

Metric	**2012**	**2017**	**2022**
Line speed (Gbp)	10-100	100-1000	250-2500
Cost ($/Gbps)	1-5	0.5	0.025-0.15
Power inter-rack (pJ/bit, mW/Gbps)	20-100	10-50	10-20
Power inter-chip (pJ/bit, mW/Gbps)	2-10	1-5	1-2

the few km, it enters the territory of the inter-datacenter interconnects, where the aggregation of the data stream imposes a higher requirement on the data rate. Thus, WDM techniques will be used in this application scenario. The IEEE standards for 40/100 Gigbit Ethernet are partly listed in the Tab. 1.2, showing different requirements on transmitting distances for corresponding scenarios.

In the Tab. 1.3, some featured requirements of the current and future datacenter are listed [5]. Apart from the bandwidth needs (i.e. data rate), the other major requirements or limiting factors of the optical interconnect for the future datacenters, especially the mega-datacenters, include reach, cost, power consumption, latency, footprint, reliability, flexibility (or known as serviceability) [3].

1.1.2 Standards of the short-reach data interconnects

The typical protocols used for datacenter interconnects include Ethernet, InfiniBand, Fiber channel and etc. IEEE Ethernet standards 802.3 is the most widely accepted standards for 100 G interface. It covers all

Table 1.4: Physical layers of 200/400 Gigabit Ethernet standard in IEEE 802.3 [7].

Media	Wavelength	Gbit/s/lane	Standards
70 m OM3	850	26.5625	200GBASE-SR4
100 m OM4	850	26.5625	200GBASE-SR4
500 m SMF	1304.5-1317.5	26.5625	200GBASE-DR4
2 km SMF	4λ 1271-1331	26.5625	200GBASE-FR4
10 km SMF	4λ 1295.56-1709.14	26.5625	200GBASE-LR4
70 m OM3	850	26.5625	400GBASE-SR16
100 m OM4	850	26.5625	400GBASE-SR16
500 m SMF	1304.5-317.5	53.125	400GBASE-DR4
2 km SMF	8λ 1273.54-1309.14	26.5625	400GBASE-FR8
10 km SMF	8λ 1273.54-1309.14	26.5625	400GBASE-LR8

of the datacenter application scenarios, ranging from backplane (< 1 m, e.g. 802.3bj or 100GBASE-KP4) to inter-mega-datacenter connections (~ 10 km, e.g. 802.3ba or 100GBASE-LR4). The some other non-IEEE standards are accepted and owns the impregnable market shares, including 100GBASE-CWDM4 MSA [8] for 2 km reach of wavelength division multiplexing (WDM) links over SMF with central wavelength at 1310 nm, 100GBASE-PSM4 [9] for 500 m reach, and 100GBASE-CWDM4 OCP [10] supporting 500 m reach with Reed-Solomon (RS) forward error correction (FEC).

Apart from the Ethernet, InfiniBand is another important communication standard for computer-networking in the high performance computing (HPC). Compared with IEEE standard, InfiniBand emphasizes higher throughput and low latency. It is now widely applied in data links between and within super-computers as well as servers and storage systems. It is standardized by the InfiniBand Trade Association (IBTA) [11]. In the Tab. 1.5, the rate feature of some selected standards of InfiniBand is listed. For the high throughput and low latency, InfiniBand adopts coding schemes with short codes, e.g. 64b/66b [12].

1.1.3 Module standards

A multi-source agreement (MSA) is an agreement between multiple manufacturers to make products which are compatible across vendors, acting as de facto standards [14]. MSAs strictly define the features of the devices, so that system vendors may implement ports in their devices (e.g.

Table 1.5: Rate features of selected InfiniBand standard [13].

	FDR10	FDR	EDR	HDR	NDR	XDR
Bit-rate (Gbit/s)	10.3125	14.0625	25.78125	50	100	250
Throughput (Gbs)	10	13.64	25	50	100	250
Speeds 4x (Gbit/s)	40	54.54	100	200	400	1000
Speeds 8x (Gbit/s)	80	109.08	200	400	800	2000
Speeds 12x (Gbit/s)	120	163.64	300	600	1200	3000
Encoding (bits)	64/66	64/66	64/66	64/66	-	-
Latency (μs)	0.7	0.7	0.5	-	-	-
Year	2011	2011	2014	2017	2020	2023

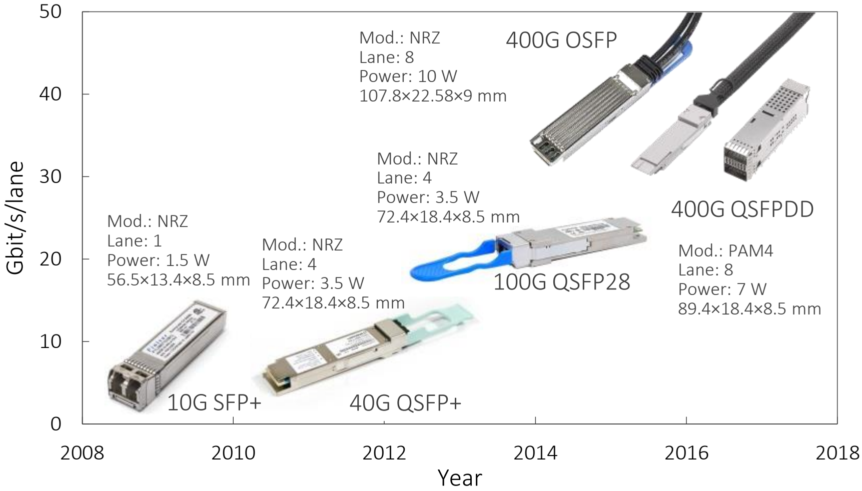

Figure 1.2: Optical transceiver module standards.

Ethernet switches and routers) that allow MSA compliant devices to function properly. The small form-factor pluggable (SFP) transceiver MSA include quad small form-factor pluggable (QSFP), quad small form-factor pluggable with 4×28 Gb/s interface (QSFP28), quad small form-factor pluggable double density (QSFP-DD), micro quad small form-factor pluggable (MicroQSFP) and octal small form-factor pluggable (OSFP). An intuitive illustration of the pluggable standards is shown in Fig. 1.2 with reference to [3]. The cutting-edge products from year 2018 on the market are the 400G QSFP-DD and OSFP.

1.2 Intensity-modulated direct-detection

Most of the optical interconnects used inside the datacenters are based on a so-called intensity-modulated direct-detection (IM-DD) transmission scheme. Cost and realizability are the primary considerations of adopting such technology. For the short-reach datacenter interconnects, e.g. rack-to-rack interconnects, the 850 nm VCSEL based IM-DD schemes are usually adopted, together with MMF as the data channel. At the receiver side, high-speed GaAs photodiodes are typically used to convert the optical signal into the electrical domain. In this paper, we focus on the configuration with 850 nm VCSELs. In the following, we clarify several general questions about the choice of such configuration and justify the research context of this thesis.

1.2.1 Why VCSELs?

As above mentioned, for the short-reach intra-datacenter interconnects, especially for the rack-to-rack interconnects, or known as the inter-TOR-switch interconnects, VCSELs coupled with MMF are dominantly adopted. It is the natural results based on comprehensive considerations. First of all, the directly modulated lasers are easier to implement and package. Compared with the externally modulated lasers, the laser cavity and the electrical interface are co-designed without considering the coupling between the laser and the external modulator, e.g. MZM and EAM. Thus, the designing and realization based on the intensity-modulated laser is straightforward. By doing so, integrated circuit (IC) designers can focus on designing the compatibility between the driver and laser, without considering additional port designs. Among the directly modulated lasers (the majority of them are intensity modulated.), the cost of VCSELs is relatively low, compared with other edge emitting lasers. This partly results from the lower expense on the fabrication process for the corresponding VCSEL structures and the scalability in the mass production. The other reason lays in the lower cost of the laser-fiber coupling. Furthermore, the directly modulated lasers appear to be more power efficient, i.e. J/bit than other external modulator schemes [15]. And, VCSEL seems to possess even higher power efficiency due to the lower threshold current and higher slope efficiency. Last but not least, VCSEL can operate without temperature controlling devices. It is because that the IM-DD systems are not frequency sensitive, as no phase of the carrier will be exploited. Meanwhile, the current modulation does not require high stability frequency. On the contrary, the external modulator usually imposes a high requirement on the frequency stability for the efficient signal modulation and stable power outputs. Concretely, if the wavelength of the laser output slips out of the effective absorption range of a EAM, no effective modulated signal will be guaranteed. Thus, the temperature controller is inevitable, brings additional power consumption and increases the overall power consumption; whereas the uncooled VCSEL based transceivers are typically and widely deployed in the current datacenters. For instance, Google is now deploying 4×10 Gb/s of uncooled coarse wavelength division multiplexing (CWDM) technology with directly modulated lasers [3].

1.2.2 Which wavelength 850 nm, 1310 nm or 1550 nm?

The choice of wavelength is a major topic in the short-reach datacenter interconnects. Configurations with different carrier wavelengths are a natural evolution result according to the concrete application scenarios. For interconnects short than 100 m, the 850 nm VCSEL is the dominating technology. Concretely, IEEE standards supporting 100 m transmission, e.g. 100GBASE-SR4, 200GBASE-SR4 and 400GBASE-SR16, adopt such framework. The primary supporting factor is the low-cost solution available by using the state-of-the-art VCSEL techniques, which can offer 25 GHz analogy bandwidth and support 26.5625 Gbps per lane transmission [6]. According to the recent IEEE standards, e.g. 100GBASE-DR, 200GBASE- DR4/FR4, 200GBASE- DR4/FR4, the wavelength range centered at 1310 nm becomes the first choice for the interconnects < 2 km using standard single-mode-fiber (SSMF), i.e. ITU-T G.652. Some non-IEEE standards, e.g. 100G PSM4 [9], also adopt 1310 nm as the standard wavelength for the optical carrier. The reason for using 1310 nm wavelength mainly comes from the dispersion. SSMF shows the lowest chromatic dispersion at a wavelength around 1310 nm. The performance degradation from inter-symbol interference (ISI) becomes increasingly serious when the baud rate scales up to 25 G or beyond over SSMF of few kilometers. The application of low dispersion wavelength implies lower pressure on the chromatic dispersion compensation and therefore reducing the cost of implementation, compared with the even longer wavelength, e.g. 1500 nm. However, one limiting factors of 1310 nm center wavelength applied in even longer links is the higher attenuation in the SSMF, i.e. $\leq$0.35 dB/km compare with $\leq$0.2 dB/km at 1550 nm for Corning SSMF28 [16] according to ITU-T G.652.D, and 0.33-0.35 dB/km, compared with 0.19-0.22 dB/km for Darka [17] according to ITU-T G.652.B. The other factors include the compatibility of the current standard telecommunication devices, e.g. erbium doped fiber amplifier (EDFA).

Yet, on the territory edges where the advantages of each technique are not obvious, the choice of products can be indecisive. For instance, with the development of 850 nm VCSEL and MMF, higher bandwidth and longer reach are available to support the commercial possibilities beyond 100 m. On the other hand, for 1310 nm techniques, with the improvement of the VCSEL output power, as so-called high power VCSEL, may also open the door towards the low-cost solution with longer transmission distance, entering the traditional territory for the 1550 nm technologies. Therefore, schemes with different wavelength are expected to co-exist long in the future. However, the market share of each technique will fluctuate while the techniques in the corresponding direction are advancing.

In this thesis, we will focus on the performance enhancement of the 850 nm VCSELs and explore the possibility of extending the territory of 850 nm techniques in the future datacenter interconnections.

1.2.3 Choice of FEC threshold

The performance criteria of a transmission system are often defined concerning a specific bit error rate (BER) threshold. Different IEEE standards for the short-reach Ethernet accept various FEC strategy. In optical transmission network (OTN) standard, hard-decision (HD) FEC with 7% overhead (OH) is adopted and BER below 3.8×10^{-3} is required as a criterion of successful transmission. However, it is not always reasonable to consider this BER threshold for the short-reach optical interconnect scenario because of high latency and large OH of OTN FEC. Applications such as the intra-datacenter (< 1000 m), the rack-to-rack interconnects (from several meters to hundreds of meters) and the board-to-board interconnects require the latency less than several hundred nanoseconds, e.g. 95∼105 ns for 100GBASE-KP4 and 85∼95 ns for 100GBASE-KR4 [18]. In addition, the high data exchange rates between datacenters are sensitive to the FEC OH. The newly accepted IEEE 802.3bm standard 100GBASE-SR4 adopts FEC with a lower BER threshold for transmission. The standard includes 2.7% OH Reed-Solomon code, RS (528, 514), with ∼45 ns latency. These requirements imply BER threshold at 1.42×10^{-5} for output BER lower than 10^{-15} [19,20]. In addition, 5.8% OH Reed-Solomon code, RS (544, 514), is compatible to the 100GBASE-KR4, requiring the latency of ∼70 ns [18,21].

Moreover, non-FEC transmission schemes are still preferred for many application scenarios with extreme latency requirements, e.g. the data exchange between supercomputers. BER lower than 10^{-12} or even 10^{-15} is required, which is mainly associated with the InfiniBand standards.

In this thesis, we place the research in the application scenarios of the mega-datacenters, emphasizing the performance of different techniques over 100 m$\sim$200 m MMF. Thus, we adopt, if without particular explanations, three different FEC thresholds, as the criteria for the performance comparison, i.e. 7% HD-FEC of required BER at 3.8×10^{-3}, the KP-4 standard 5.8% RS (544, 514) of the required BER at 2.2×10^{-4}, and the KR-4/SR-4 standard 2.7% RS (528, 514) for the required BER at 1.5×10^{-5}. These three FEC thresholds cover the most application scenarios of the short-reach applications. In addition, for comparing the performance of non-FEC transmissions, we use the BER at the accuracy limit. For most of the experiment, the value is chosen as 1.25×10^{-6}, if without specifically mentioning. The value is also used as the threshold for the comparison of the asymptotic performance.

1.3 Benchmarks of IM-DD transmission using 850 nm VCSEL

1.3.1 Single carrier

For the optical interconnect in the early stage of development, the simple modulation with non-return-to-zero (NRZ) is used. It is easy for implementation and offer a low-latency solution. The scale of the bit-rate then depends on the extension of the bandwidth of hardwares. Averagely, NRZ requires the analog bandwidth close to $\sim$0.75 of the the bit-rate. The data-rate can be boosted by using pulse shaping techniques. In the extreme case, the needs of analog bandwidth is half of the bit-rate desired.

Regarding the bit-rate, the current record for NRZ transmission is a 71 Gbit/s demonstration in the multi-mode (MM) VCSEL-based link over 7 m MMF [22], with two-taps feed-forward equalizer (FFE) and a 68 Gbit/s over 100 m MMF [23]. The highest bandwidth-distance product of NRZ error-free NRZ transmissions (i.e. BER below 10^{-12}) based on a 850 nm MM VCSEL is recored in [24] with 64 Gbit/s over 57 m OM4 and 60 Gbit/s over 107 m OM4. P. Westbergh and et al. reported a 43 Gbit/s NRZ over 100 m OM3 MMF without equalizations [25]. K. L. Chi and et al. reported a 54 Gbit/s on-off keying (OOK), i.e. NRZ, transmission over 1 km with respect to 7% FEC using 850 nm single-mode (SM) VCSEL together with a decision feedback equalizer (DFE) of 40 T/2 forward taps and 10 feedback taps [26]. Considering the thermal effects, D. M. Kuchta and et al. demonstrated a 50 Gbit/s error-free transmission with equalization up to 90 °C and without equalization up to 57 °C over few meters fiber [27]. Meanwhile, alternative investigations based on SM VCSEL have been conducted with benchmark works including a 54 Gbit/s NRZ transmission over 1000 m OM3 MMF [28, 29].

For enhancing the spectral efficiency and boosting the bit-rate, multi-level modulations are adopted in recent development. Among which, PAM-4 is the most realistic and promising formats for next-generation optical interconnects. The proof-of-concept demonstrations have been reported recently with the following benchmark works based on 850 nm VCSELs. In 2017, J. Lavrencik and et al. reported an error-free (i.e. $< 10^{-12}$) PAM-4 transmission over 100 m wideband fiber using 850 nm VCSELs with transmitter equalization [23]. In 2016, a 112 Gbit/s PAM-4 transmission over 100 m OM4 MMF was demonstrated supported by the equalization with FFE and maximum likelihood sequence estimation (MLSE), with respect to the BER threshold for the standard 7% HD FEC [30]. T. Zuo and et al. reported PAM-4 demonstrations of 150 Gbit/s, 100 Gbit/s and 70 Gbit/s over 100 m, 300 m and 500 m OM4 respectively using digital signal processing (DSP) [31]. G. Stepniak and et al. demonstrated PAM-4 transmissions of pre-FEC 80 Gbit/s over 100 m OM4 using 850 nm MM VCSEL and pre-FEC 108 Gbit/s over 100 m and pre-FEC 90 Gbit/s over 600 m OM4 using 850 nm SM VCSEL [32]. The demonstrations use equalizers with 40 FFE and 10 DFE taps. Similar work was also reported in [33] with a 107 Gbit/s PAM-4 over 105 m OM4 with respect to a BER threshold at 4.2×10^{-4} using offline equalizations. S. M. R. Motaghiannezam and et al. extended the aggregated pre-FEC rate of PAM-4 to 180 Gbit/s, i.e. 45 Gbit/s per lane, over 300 m OM4 in a shortwave division multiplexing (SWDM) system [34, 35]. Similar works include [36] and [37]. J.M. Castro and et al. demonstrated 48.7 Gbit/s PAM-4 transmission over 200 m MMF using 850 nm VCSEL and a 6-tap DFE [38, 39]. The other PAM-4 works include net 50 Gbit/s over 200 m [40], 96 Gbit/s over a few meter MMF [41], 70 Gbit/s over 2 m MMF [42] and earlier benchmarks with 60 Gbit/s over 2 m MMF [43] and 30 Gbit/s over 200 m MMF [44].

1.3.2 Multi-subcarrier

To further enhance the spectral efficiency, we can use multi-subcarrier modulation schemes. Typical sub-carrier modulations for IM-DD systems include discrete multi-tone modulation (DMT) and carrier-less amplitude phase modulation (CAP). DMT is a real-value version of orthogonal frequency division multiplexing (OFDM). J. Lee and et al. suggested of using DMT in the MMF based IM-DD system and demonstrated a 25-Gbit/s DMT over 1 km OM4 MMF using a 10 G 850 nm MM VCSEL [45]. Recently, more applications of DMT to enhance the VCSEL based systems have been reported. The benchmarks include a 115 Gbit/s DMT transmission using 1550 nm VCSEL and covering 500 m to 4 km SSMF with 95 Gbit/s to 105 Gbit/s respectively [46]. A 50 Gbit/s DMT transmission using 25 G class 850 nm VCSEL and an approaching 100 Gbit/s hybrid QAM-DMT transmission were demonstrated through 100 m OM3 MMF [47]. A world record of DMT was reported in [48, 49] using a 26-GHz 850 nm VCSEL with 161 Gbit/s, 152 Gbit/s, 135 Gbit/s over 10 m, 300 m, 550 m OM4 MMF respectively with respect to the soft-decision (SD) FEC BER limit at 1.5×10^{-2}. In [50], a record bit-rate distance product of 107.6 Gbit/s·km was presented. It used an 850 nm SM VCSEL at 50 Gbit/s under 7%FEC threshold (BER$< 3.8 \times 10^{-3}$) through 2 km OM4 MMF. Earlier attempt of 100 G DMT include a close 100 Gbit/s DMT transmission in [51] using 850 nm MM VCSEL over 100 m OM4, and a successful 100 G transmission using a 850 nm SM VCSEL over 300 m OM4 [52] reported from the same group. Other famous early work include a 56 Gbit/s DMT over 100 m OM3 using 25 G class VCSEL [53].

Apart from DMT, another multi-subcarrier modulation, CAP, is recently presented in the applications using vertical-cavity surface-emitting lasers (VCSELs). The benchmark works include an attempt to 100 G per lane transmission using 850 nm MM VCSEL over 100 m MMF [54]. It is followed by a similar work with net 100 Gbit/s CAP using SM VCSEL through MMF.

1.3.3 Multi-dimensional coded modulation

Multi-dimensional modulation (MD) formats have already been theoretically and experimentally investigated in coherent detection systems, e.g. the four-dimensional (4-D) formats [55–62]. Besides, formats optimized with D_4 lattice can be equivalently obtained from the conventional PDM-mQAM by applying a 4-D set partitioning scheme [63]. Eight-dimensional (8-D) formats have also been investigated recently [64–66]. A higher dimensional one, binary 24-dimensional modulation format, is also discussed in [67].

The pioneer theoretical works on the multi-dimensional (MD) modulation formats for IM-DD systems include the optimized constellations for single-subcarrier intensity-modulated (IM) transmission [68] and lattice code [69]. Recently, MD coded modulation has been experimentally validated in IM-DD systems. A two-dimensional (2-D) coded modulation scheme with external modulators is discussed in [70]. A 4-D version was reported in [71]. A 4-D trellis coded modulation (TCM) is experimentally analyzed in [72] and [73].

In this thesis, we place emphasis on extending the application of the MD modulation, or known as the MD formats in the IM-DD systems, with both single carrier and multi-subcarrier modulation schemes.

1.4 Outline of this thesis

This thesis is the summary of a three-year Ph.D. research work, which emphasizes the novel modulation schemes for current and future datacenter interconnect, especially the so-called multi-dimensional modulation formats used for the IM-DD systems.

In chapter 4, the multi-dimensional formats with the fixed spectral efficiency are introduced subject to two different optimization principles. With the cost function of minimum power, one 4-D format (D_4TS-4) and one eight-dimensional (8-D) format (E_8TS-4) are proposed and investigated numerically. Various benefits from different aspects are observed, including the reach extension and enhanced thermal performance, compared with the pulse amplitude modulation (PAM) signal. Meanwhile, with the cost function of minimum amplitude, together with the additional considerations on the simplicity, a block-based 8-D format, i.e. BB8, is theoretically proposed and experimentally investigated. The simplified mapping and de-mapping algorithms are devised by taking the advantages of the geometric features of the 8-D lattice. Two different types of the decision schemes are introduced briefly. It shows that the new format possesses better BER performance in cases of optical back-to-back (OBTB) and different types of MMF.

In chapter 5, a twenty-four-dimensional (24-D) PAM signal is designed with the similar principle as its 8-D equivalence. It relies on the geometric structure of the 24-D densest lattice, i.e. Λ_{24}. The bit-stream based modulation and corresponding demodulation are elaborated. The performance benefits are verified in a 100 G IM-DD link using an 850 nm SM VCSEL.

In chapter 6, we introduce a family of 8-D formats, which have a fractional number of bits per symbol with steps of 0.125 bit. Such format family is constructed by a serial of set bipartition on certain subsets of E_8 lattice grids. Based on the concise geometry, a uniformed bit-wise (de)modulation with the flexible bit transition is proposed, together with the hierarchical decision schemes. A transceiver with net 100 Gbit/s equipped with the 8-D rate-flexible format is demonstrated based on 850 nm VCSEL. The benefits of such format family compared with its conventional PAM counterpart is investigated. Following the 8-D rate-flexible format family, we extend such possibility to the 24-D version, based on the 24-D lattice. It is applied in a 120-subcarrier CAP transmission in Chapter 8.

In chapter 7, we explore the potentials of the 8-D rate flexible format family in a DMT transmission system. The finer granularity of the bit adjustment enables a fast bit and power loading algorithm for the DMT transmission. It offers the possibility for a flexible bandwidth resource management. Besides, the intrinsic benefit of the 8-D lattice geometry is converted into the performance enhancement in various aspects, e.g. the reach extension, the enhanced tolerance for the insertion loss and thermal degradation.

In chapter 8, another multi-subcarrier transmission system loaded by the rate-flexible 24-D format is reported. The format is modified from the rate-fixing format discussed in Chapter 5 and combined with a so-called extending and re-mapping algorithm. By loading a 12-subcarrier CAP transmission with such format, better transmission performances with different aspects have been demonstrated.

In chapter 9, we introduce briefly two other link enhancement schemes which are involved in the Ph.D. of past three years. One is so-called the mode selective launching techniques. It excites the vortex modes with different topological charge number rather than the fundamental mode. Such scheme brings better transmission performance and is reported with reach extensions approaching the dispersion limits. The other scheme is the all-optical compensations of the vortex modes after fiber propagation. Such scheme is expected to enable a mode division multiplexing (MDM) scheme for mega-datacenter transmissions.

Chapter 2

VCSEL based IM/DD Links

A typical intensity-modulated direct-detection (IM-DD) optical transport module consists of:

- *Transmitter*, including transmitter optical sub-assembly (TOSA) (incl. laser source and modulator), electric-optical interface (e.g. laser driver, analog signal process circuit, e.g. feed-forward equalizer (FFE)[1]) and transmitter integrated circuit (IC).
- *Data links*, including the laser-link pigtails connecting the transmitter and transmitting fiber.
- *Receiver*, including receiver optical subassembly (ROSA) (incl. photodiode (PD), trans-impedance amplifier (TIA)), equalizers (e.g. continuous time linear equalization (CTLE), decision feedback equalizer (DFE)[2]), clock and data recovery (CDR) and receiver IC.

The illustration of a typical optical transceiver is shown in Fig. 2.1.

In this chapter, We place emphasis on the principle and physics fundamentals of blocks, including vertical-cavity surface-emitting laser (VCSEL), multi-mode fiber (MMF), receiver and connectors.

---

[1] Note we do not indicate amplifiers explicitly, as FFEs are normally realized with amplifiers.

[2] We do not explicitly indicate the limiting amplifiers, as they are designed together with DFE.

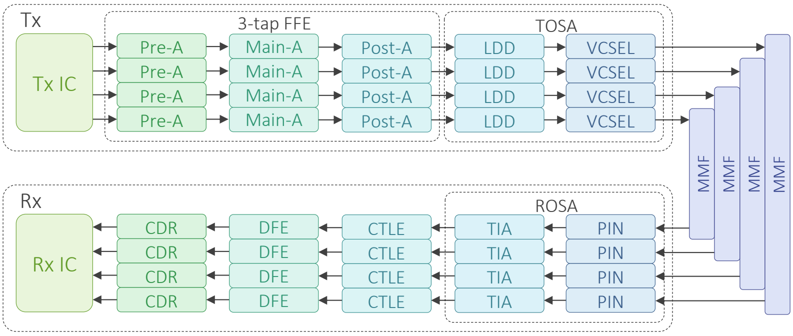

Figure 2.1: A typical VCSEL based 4-lane optical interconnect.

2.1 VCSEL

Compared with the edge emitting lasers, VCSELs have unique and decisive advantages in the applications of optical interconnects. The merits of VCSEL include:

- Lower threshold current and thus lower power consumption due to the high current density from the small cavity volume;
- Higher differential efficiency slop due to the low internal and mirror loss;
- Higher thermal stability due to the relatively lower frequency shift resulting from the change of cavity length compared with the shift of gain spectrum resulting from the change of the band gap energy of active material [74];
- High speed direct modulations due to relatively low parasitics;
- Low cost due to cheap package, easy manufacturing and scalability of mass production;
- Compatibility to MMF due to the spot size and shape. A circular beam with small divergent angle rooting in the circular mesa and oxide aperture design;
- Stable power and spectrum output due to the high stability from the physical properties of the laser cavity [74];
- Near infrared and long wave solutions are available;
- High density of integration, e.g. VCSEL array.

2.1.1 VCSEL structure

The structure of a typical VCSEL is shown in Fig. 2.2. Compared with the edge-emitting lasers, VCSELs have a vertical cavity with the orientation of output beam perpendicular to the laser surface and parallel to the current direction.

VCSELs adopt p-i-n heterojunction or multi-quantum well (MQW) [75] structure as the active layer and have a very short cavity with the thickness around 1-3λ. The diameter of the oxide aperture is usually $< \mu$m. Thus, the active layer of a VCSEL can be modeled as a thin plate, compared with a strip waveguide liked active region in an edge-emitting laser with dimensions typically $\sim 100\ nm \times \sim \mu \times 100\ \mu m$.

A distributed Bragg reflector (DBR) structure are fabricated on both sides of the active layer, known as top DBR and bottom DBR to form a optical cavity offering optical feedback [74,76,77]. For obtaining low threshold currents, the DBR is designed to have a high reflectivity, e.g. 99.9% for the bottom DBR and 99.5% for the top DBR, by using a multi-layer structure of thin films with alternative high and low refractive index. While on the other hand, high reflectivity leads to a lower quantum efficiency, leading to a lower output, which is seen as one of the drawbacks of VCSELs. Meanwhile, the DBR pair for a VCSEL is also conductive to perform the current injection [74, 76–79]. For enhancing current density, specifically designed carrier barriers are also deposited close to the active layer.

A oxide layer is fabricated to confine the carriers and photons, i.e. optical modes, in the transverse direction and enhance the modulation efficiency [74, 76, 77].

According to the structure, it is reasonable to treat the laser cavity as a cylindrical step-index waveguide, where the photons are recombined in a cylinder oxide-confined active region. The field output from the laser can be numerically estimated from the solution of the Maxwell equations with the standard cylindrical boundary conditions, i.e. waveguide. The linearly polarized (LP) modes are linear combination of eigenmodes of the field distribution in the cavity, which gives easier description of the field.

To enhance the bandwidth of VCSELs, the DBRs are designed to be short enough to reduce the parasitics and increase the confinement factor Γ. Typically, the cavity length of $3/2\lambda$ is adopted in the conventional design. Due to the short cavity, the free spectral range is large. Thus, VCSELs are usually longitudinally single-mode; whereas the aperture diameter of the active layer is much larger than the wavelength, typically several times of λ, for boosting the carrier-photon interactions and increasing the output

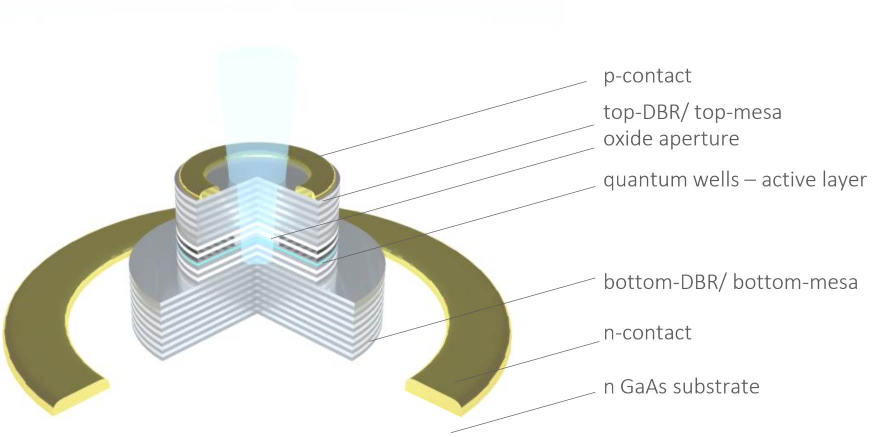

Figure 2.2: The structure of a typical VCSEL.

power. Concretely, for 850 nm VCSEL with oxide aperture of diameter $\sim 10\mu m$, the value can be 10. Thus, VCSELs usually show a transversally multi-mode feature with a specific design, i.e. operational wavelength and geometry of laser cavity. In other words, it accommodates more than one eigenmodes, leading to an output light field of a linear combination of its eigenbasis. It implies that to control the transversal modes, there are at least two major ways, namely using longer wavelength, e.g. 1550 nm or reducing the oxide aperture. Alternative methods to generating the single-mode (SM) transversal mode include introducing the depletion layer for a specific transversal mode, which will be discussed later.

For modes with the different order, the effective cavity lengths are different. The resonance frequency for a specific transversal mode, therefore, is different. This is observable from a serial of peaks in the optical spectrum.

The first VCSEL is proposed in 1988 [80]. GaInAsP/InP and AlGaAs/GaAs were the active material for VCSELs in the early development stages, which support the wavelength from 750 nm to 980 nm. InGaAs has been introduced in the long wavelength VCSEL, e.g. 1550 nm and 1310 nm, in 1990's [81]. The 850 nm VCSELs were then commercialized [82, 83] and deployed in the actual products. Today, the 850 nm VCSELs dominate 95% commercial products for short-reach interconnects with reach of few hundred meters [84].

2.1.2 VCSEL models

The basic principle of the rate equation formulating the behaviors of carriers and photons in VCSELs is elaborated thoroughly in [76]. The concrete VCSEL model, however, may differ according to the needs and the emphasis of research. In [85], Gion Sialm classified the VCSEL model into 1-D, 2-D, 3-D spatio-temporal models for the applications ranging from circuit level, system level to component level. Here we briefly introduce the rate equation used in the practical simulations for [86].

Rate equation

We use the following spatially dependent rate equation is a start point to explain the carrier-photon relations of the VCSEL [87], which is expressed as:

$$\begin{aligned}\frac{\partial N(\mathbf{r},t)}{\partial t} =& \frac{\eta_i I(\mathbf{r},t)}{q} - \frac{N(\mathbf{r},t)}{\tau_n} - G(\mathbf{r},t)S(t)\Psi(\mathbf{r}) \\ &+ \frac{L_{eff}^2}{\tau_n}\nabla^2 N(\mathbf{r},t) - \frac{I_l(N,T)}{q} \qquad (2.1)\\ \frac{\partial S(t)}{\partial t} =& -\frac{S(t)}{\tau_p} + \frac{\beta}{\tau_n}\frac{1}{V}\int_v N(\mathbf{r},t)dv + \frac{1}{V}\int_v G(\mathbf{r},t)S(t)\Psi(\mathbf{r})dv \qquad (2.2)\end{aligned}$$

in which, I is the spatially dependent injection current, N is the carrier density within the actively layer of an effective volume V, S and Ψ are the total photon number and normalized transverse mode profile, T is the device temperature, G is the gain, I_l is the thermal leakage current, η_i is the current-injection efficiency, τ_n is the carrier lifetime, L_{eff} is the effective carrier diffusion length, and q is the elementary charge. β is the spontaneous emission coupling coefficient and τ_p is the photon lifetime. Note that the confinement factor Γ is implicitly included in Eq. 2.2 via the volume integral. This general form includes the effects of carrier diffusion, current leakage and spatial distribution of the related quantities. However, even though this form is general enough, it is not realistic for the actual simulation and analysis.

In practice, we first decompose the spatial dependence of the carriers. Assuming that the VCSELs have cylindrical geometry, we can use a two-term Bessel-series expansion to describe $N(\mathbf{r})$ [87]:

$$N_0 - N_1 J_0(\sigma_1 r/R) \qquad (2.3)$$

in which, σ_1 is the first nonzero root of $J_1(x)$ and R is the active layer effective radius. If without considering the spatial distribution of current, i.e. $I(\mathbf{r},t) = I(t)$ and linear gain, i.e. $G(\mathbf{r},t) = G(t)$, we can obtain the spatially independent rate equation in Eq. 2.4-Eq. 2.6 [87].

$$\frac{dN_0}{dt} = \frac{\eta_i I}{q} - \frac{N_0}{\tau_n} - \frac{G(T)[\gamma_{00}(N_0 - N_t(T)) - \gamma_{01}N_1]}{1+\varepsilon S}S - \frac{I_l(N_0,T)}{q} \tag{2.4}$$

$$\frac{dN_1}{dt} = -\frac{N_1}{\tau_n}(1+h_{diff}) + \frac{G(T)[\phi_{100}(N_0 - N_t(T)) - \phi_{101}N_1]}{1+\varepsilon S}S \tag{2.5}$$

$$\frac{dS}{dt} = -\frac{S}{\tau_p} + \frac{\beta N_0}{\tau_n} + \frac{G(T)[\gamma_{00}(N_0 - N_t(T)) - \gamma_{01}N_1]}{1+\varepsilon S}S \tag{2.6}$$

The spatial feature of gain are now summarized as the overlap coefficients γ_{00}, γ_{01}, ϕ_{100} and ϕ_{101}, and the diffusive effects as $h_{diff} = (\sigma_1 L_{eff}/R)^2$. The temperature dependent gain constant $G(T)$ and the transparency number $N_t(T)$ describe the thermal effects. ε gives the gain saturation. The leakage current I_l is now the function of the N_0, the average carrier number. The photon number S is converted to an output power via the output-power coupling coefficient k_f as [85, 87]:

$$P_{out} = k_f S = \frac{V}{\Gamma} \cdot h\nu \cdot v_g \cdot \alpha_m \cdot F_1 \cdot S \tag{2.7}$$

in which $v_g \cdot \alpha_m$ is the energy loss rate of the mirrors; F_1 is the ratio of the power emitted at the top facet of the VCSEL.

The thermal effects are characterized by the temperature dependent gain $G(T)$ and transparency number $N_t(T)$. It can be modeled and characterized with empirical rational function as Eq. 2.8-Eq. 2.9 [87]:

$$G(T) = \frac{a_{g0} + a_{g1}T + a_{g2}T^2}{b_{g0} + b_{g1}T + b_{g2}T^2} \tag{2.8}$$

$$N_t(T) = N_{tr}(c_{n0} + c_{n1}T + c_{n2}T^2) \tag{2.9}$$

where $a_{g0}, a_{g1}, a_{g2}, b_{g0}, b_{g1}, b_{g2}, c_{n0}, c_{n1}, c_{n2}$ are the empirical parameters.

Phase rate equation

The rate equation of the optical phase is included in the mode, according to , it is expressed as [76, 88]:

$$\frac{d\phi}{dt} = \frac{\alpha}{2}\frac{G(T)[\gamma_{00}(N_0 - N_{th}) - \gamma_{01}N_1]}{1+\varepsilon S} \tag{2.10}$$

where, ϕ is the optical phase, α is the linewidth enhancement factor, N_{th} is the room-temperature threshold carrier number.

Thermal carrier leakage

The temperature dependent carrier leakage is characterized by the empirical equation as [89]:

$$I_l(N_0, T) = I_{l0} \cdot exp\left[\frac{-a_0 + a_1 N_0 + a_2 N_0 T - a_3/N_0}{T}\right] \tag{2.11}$$

where, I_{l0} is the leakage current factor. a_0, a_1, a_2, a_3 are the empirical parameters.

Temperature rate equation

According to [87,90], a device temperature equation of the dissipate heat is included. Heat generation is assumed to arise from any power not dissipated as part of the optical power as [87, 90]:

$$T = T_0 + (I_{tot}V - P_{out}) \cdot R_{th} - \tau_{th}\frac{dT}{dt} \tag{2.12}$$

where T_0 is the ambient temperature, I_{tot} is the total current through the VCSEL, including the current through the intrinsic parasitic shunting capacitance C_p, R_{th} is the device thermal impedance, and τ_{th} is the thermal time constant.

Note that the above rate equations rely on the empirical parameters, which should be extracted from the experimental measurements. Especially, for the thermal empirical parameters, it might be more problematic, as the actual temperature value inside the active layer cannot be directly measured. In addition, here we implicitly assume that only one mode is considered. For a more rigorous analysis, photons from different transversal modes need to be differentiated with separated equations, as the confinement factor Γ and the photon lifetime τ_p are different for the corresponding transversal modes.

Besides, the polarization effects, the interactions between different modes and relative intensity noise (RIN), known as mode partition noise (MPN) effect, are beyond the scope of this thesis.

2.1.3 VCSEL characterization

For characterizing VCSELs, the typical measurements necessary for extracting critical system parameters, including the direct current (DC) light-current-voltage (L-I-V) determination under different ambient temperatures, the small signal frequency response, i.e. S-parameters (typically S_{11}

and S_{21}), large signal, optical spectrum, RIN spectrum. In the following, we discuss the typical parameter extractions with these measurements. Note that the real laser modeling that the complexity of parameters extractions are far beyond the following descriptions and, also, beyond the scope of this thesis.

Static L-I relation

For understanding and predicting the modulation features, the L-I-V curve is measured. It reveals the information, including the maximum optical output power, the threshold current value I_0, the slope efficiency of the linear regime, input impedance and rollover region. The temperature variation of the L-I-V curves reflects the thermal impact of a specific VCSEL. With the increase of the temperature, the linear modulation regime of a VCSEL shrinks, meaning that the modulation amplitude with the same current modulation decreases. The DC light-current (L-I) relation is expressed as [76]:

$$P_{opt} = \eta \frac{h\nu}{q}(I - I_{th}) \tag{2.13}$$

in which P_{opt} is the output optical power; η is the quantum efficiency; $h\nu$ is the photon energy; q is the elementary charge; I_{th} is the threshold current.

Small signal frequency response

The small signal frequency response curve, known as S_{21} curve, is used for understanding the high-speed signal generation. It is one of the important parameters to predict the performance of a VCSEL at a specific bit-rate. -3 dB f_{-3dB} and -6 dB f_{-6dB} bandwidths are two criteria for estimating the performance. The curve needs to be flat and smooth. Overshoots on S_{21} generate spikes of the signal pulse, adding distortion. Such distortion will affect the eye quality. S_{21} curves changes with the bias current I_{bias}. The large the I_{bias} reaches, the flatter the S_{21} become. It is because that the resonances of VCSELs are proportional to the bias current and inversely proportional to the carrier and photon lifetime in the cavity. While the increase of I_{bias} will, in turn, constrain the useful linear modulation regime.

Even though the S_{21} is dependent on the parasitics of VCSEL as well as the external circuits, we can expect a simply two-polar relation between the drive current and output power in the active layer, which behaves as a second-order damping system [85]. It is expressed with the modulation transfer function (MTF) $H(\omega)$ as following:

$$H(\omega) = \frac{\omega_r}{\omega_r^2 - \omega^2 + j\gamma\omega} \tag{2.14}$$

where $H(\omega)$ is the MTF; γ is the damping factor; ω_r is the relaxation oscillation frequency, i.e. $\omega_r = 2\pi \cdot f_r$. f_r is proportional to $\sqrt{(I - I_{th})}$:

$$f_r = D \cdot \sqrt{(I - I_{th})} \tag{2.15}$$

where D denotes the damping. A higher value D implies a lower operation bias current to achieve the same frequency, meaning a higher modulation efficiency. The damping factor γ meets the following relation [91]:

$$\gamma = K \cdot f_r^2 + \frac{1}{\tau_n} \tag{2.16}$$

in which K is the gain compression factor. It suppresses the relaxation oscillation peak. For a small K value, the signal might experience a significant overshoot.

S_{11} is another useful S parameter measurement. It gives deep information on the electrical feature, from which the impedance of the laser varying with the frequency can be extracted. It is crucial for estimating the parasitics of the laser chip and further the design of the opto-electrical interface. For IC designers, a well-rounded model of chip, which describes the electrical behavior is more essential.

Optical spectrum

From the optical spectrum structure, e.g. linewidth for each mode and modes spacing, the laser features, especially the cavity feature can be deferred. Optical spectrum with and without modulated signal is an indicator showing the stability of the transmission condition. The relative intensity of the spectral peaks of different modes gives the information on the modes excitation and competition. And the shift of the spectral peak while the temperature varying implies the feature of the active layer and estimate the thermal stability of the laser. It can be also used to calibrate the difference between the core temperature and the ambient temperature.

Relative intensity noise

RIN describes the intensity fluctuations with respect to a desired constant output. It can be defined as:

$$\mathrm{RIN} = \frac{\delta P(t)^2}{P_0^2} \tag{2.17}$$

Usually, we measure the RIN(F) spectrum, which follows the form as [76]:

$$\mathrm{RIN}(f) = \frac{Af^2 + B}{(f_r^2 - f^2)^2 + (\frac{\gamma}{2\pi})^2 f^2} \tag{2.18}$$

The other useful characterizations include the higher order harmonics analysis, polarization state analysis, near-field and far-field mode profiles and etc. Limited by space, they are not explained in detail.

It is worth of mentioning that the typical VCSEL characterizations give the general understanding of a laser chip. While it not sufficient for a more comprehensive design together with the laser drive. And some important feature of lasers can not be directly extracted from the above-mentioned measurements. Concretely, the static L-I-V curve describes only the power-current relations for DC condition. It is not reasonable to determine the actual radio frequency (RF) signal range.

Moreover, the S-parameter measurement normally based on the small signal response. However, it is not enough to give a deeper understanding of the frequency responses when the input amplitude is large, for that the laser is nonlinear. Therefore, more rigorously, the higher order harmonics should be measured within the electrical domain. And simply using vector network analyzer (VNA) is not sufficient, as the output signal of VNA will be filtered by a narrow bandwidth filter internally.

Further, a deeper understanding of the temperature should be placed under attention. The reason is two-fold. First, the core temperature of the laser active layer is not the same as the ambient temperature, even though they have certain dependencies. Second, the definition of temperature inside the active layer is unclear when the RF modulation has large amplitudes. The interaction between carriers and the lattice and the thermal carrier effects change the exact definition of the temperature, and therefore change the system parameter extractions of the laser behavior.

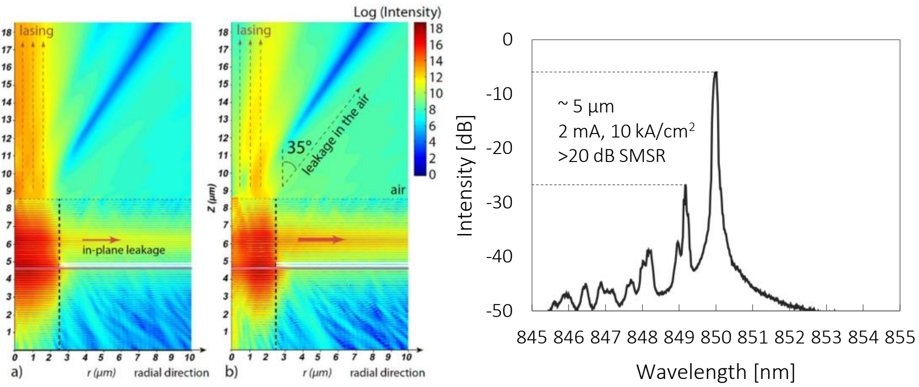

Figure 2.3: An 850 nm SM-VCSEL: the lateral leakage of (a) fundamental mode and (b) the higher order modes; The optical spectrum of the 850 nm SM VCSEL [92].

2.1.4 850 nm SM VCSEL

As mentioned in Section 2.1.1, to control the transversal modes, we can either increase the laser operation wavelength or use a smaller size of the aperture. However, both of them have major drawbacks: increasing the wavelength implies the change of laser structure and even the gain material; whereas shrinking the oxide aperture reduces the maximum optical output power, which is critical for the application of data transport. An alternative mode controlling techniques has been developed using two selectively oxidized aperture layers to produce a high lateral leakage of the high-order transverse modes of the vertical cavity [92, 93].

In Fig. 2.3.(a) and (b), the leakage effects with the numerical results can be clearly observed [92]. The optical spectrum of such laser is also shown in Fig. 2.3.(c) [93]. Such SM 850 nm VCSEL has been used for some of the experiments mentioned in this thesis.

2.2 Multi-mode fiber

For inter-mega-datacenter optical interconnects, both MMF and single-mode fiber (SMF) are used according to the concrete application, e.g. transmitting distances. In this section, the features of MMF are introduced. For more details of standard single-mode-fiber (SSMF), readers can refer to [94].

For conventional MMF, whose core diameter is round 50 μm, which is much larger than SSMF, it is more tolerant to the imperfect coupling and easier for the laser-fiber coupling. The typical numerical aperture of MMF ranges from 0.2 to 0.3.

The light field propagating in the MMF can be derived from the solution of the scalar-wave equation under weakly guiding assumption in order to calculate the LP modes with their respective propagation constants from the refractive index profile as:

$$\left(\frac{d^2}{dr^2}+\frac{1}{r}\frac{d}{dr}+\frac{4\pi^2{}^2}{\lambda}n^2(r)-\beta^2-\frac{l^2}{r^2}\right)F_{l,m}(r)=0 \tag{2.19}$$

The x- and y- electric field components of the LP modes are then expressed as in Eq. 2.20-Eq. 2.20.

$$\mathbf{E}_{l,m}^{(1)} = F_{l,m}(r)\begin{pmatrix}\cos l\theta\\ \sin l\theta\end{pmatrix} \qquad \mathbf{E}_{l,m}^{(2)} = F_{l,m}(r)\begin{pmatrix}-\sin l\theta\\ \cos l\theta\end{pmatrix} \tag{2.20}$$

$$\mathbf{E}_{l,m}^{(3)} = F_{l,m}(r)\begin{pmatrix}-\cos l\theta\\ \sin l\theta\end{pmatrix} \qquad \mathbf{E}_{l,m}^{(4)} = F_{l,m}(r)\begin{pmatrix}\sin l\theta\\ \cos l\theta\end{pmatrix} \tag{2.21}$$

By doing this, the field is separated into independent radial and azimuthal components. l is the azimuthal index number. An arbitrary spatial field can be decomposed into a weighted sum of n supported modes, like:

$$E_{in}(r,\phi)=\sum_{i=1}^{n}c_iE_i(r,\phi) \tag{2.22}$$

It is important that the above relation is only valid when the fiber modes form a complete basis. The modes in fiber are guided modes and unguided modes, including radiation modes and leaky modes. It is more accurate to rewrite the above relation as [95]:

$$E_{in}(r,\phi)=\sum_{i=1}^{n}c_i^{guided}E_i^{guided}(r,\phi)+\sum_{j=1}^{m}c_j^{unguided}E_j^{unguided}(r,\phi) \tag{2.23}$$

The coupling coefficient c_i between the input spatial field and each of the spatial fiber modes as Eq. 2.24

$$c_i=\int_0^{2\pi}\int_0^{\infty}E_{in}(r,\phi)E_i^*(r,\phi)rdrd\phi \tag{2.24}$$

It is clear that $|c_i|^2$ determines the proportion of the power coupled into a specific fiber mode. The signal transmitted in MMF is simulated then by n time-domain identical signals with different spatial fiber modes attached, scaled by their respective coupling coefficients. It is expressed as in Eq. 2.25.

$$E_{in}(r,\phi,t) = E_{in}(r,\phi)E_{in}(t) = \sum_{i=1}^{n}(c_iE_{in}(t))E_{in}(r,\phi) \tag{2.25}$$

2.2.1 Index profile

A typical OM3/OM4 fiber has a similar form as the following equation, with the core diameter a=50 μm, cladding diameter 125 μm and $\alpha \approx 2$ and the core-cladding index difference δ within the range 0.200 ± 0.015. The refractive index profile is expressed in Eq. 2.26.

$$n(r) = \begin{cases} n_0\sqrt{(1-2\Delta\left(\frac{r}{a}\right)^{\alpha})} & \text{for } r \leq a \\ n_0\sqrt{(1-2\Delta)} & \text{for } r \geq a \end{cases} \tag{2.26}$$

where Δ is a parameter quantifying the index step, as:

$$\Delta = \frac{n_1^2 - n_2^2}{2n_1^2} \tag{2.27}$$

which n_1 is the peak index at the fiber center, n_2 is the refractive index in the cladding, r is the radial distance form the fiber axis, a is the radius of the fiber core.

The waveguide with such refractive index profile accommodates hundreds of modes. Each mode has it own group velocity, chromatic dispersion, attenuation, and bending losses. The way of coupling light into MMF is critical, known as the launch condition.

$LP_{l,m}$ modes with the same principle mode number $2m + l - 1$ show the same effective index, and share the same group velocity, known as the mode delay group, except for the highest order mode groups, which are disturbed by the non-optimal core-cladding interface [95]. The probability of mode coupling between modes in the same group are higher than ones in different group. Yet, modes in different delay group are the main reason for the inter-modal dispersion.

2.2.2 Differential mode delay

Different fiber modes have different propagation speeds. It leads to the different arrival time of signal in different mode group, known as the differential mode delay (DMD), equivalently known as inter-modal dispersion. It is regarded as the main reason of the pulse broadening and the signal inter-symbol interference (ISI) through MMF, also the source of bandwidth limitation. It is worth noting that the degenerated modes have the same propagation speed. The effective index is proportional to the propagation constant as Eq. 2.28:

$$N_{eff,i} = \frac{\beta_i}{k_0} \tag{2.28}$$

where k_0 it the free-space wave number ($2\pi/\lambda_0$) and β_i is the modal propagation constant. The delay of the mode τ_i is proportional to the propagation length as Eq. 2.29:

$$\tau_i = \frac{L}{v_{g,i}} = L \cdot \frac{d\beta_i}{d\omega}, \quad v_{g,i} = \frac{d\omega}{d\beta_i} \tag{2.29}$$

Therefore, the output signal is the superposition of fiber modes with the same waveform with a delay τ_i, which is expressed as [95]:

$$E_{out}(r, \phi, t) = \sum_{i=1}^{n} (c_i E_{in}(t - \tau_i)) E_i(r, \phi) \cdot e^{j\beta_i z} \tag{2.30}$$

The time delay can be calculated by differentiating the effective index or propagation constant as [95]:

$$\tau = \frac{L}{c} \left(N_{eff} - \lambda_0 \frac{dN_{eff}}{d\lambda_0} \right) \tag{2.31}$$

The standard full characterization of the modal bandwidth used by fiber manufacturers is the DMD measurement. It consists in measuring the pulse response of an MMF for the single-mode launches scanned across its core radius. The measurements of DMD provides an accurate cartography figure the modal dispersion of an MMF, called the DMD plot. DMD values and effective modal bandwidth (EMB) of OM3/OM4 fiber can be derived from such plot.

2.2.3 Differential mode attenuation

The fiber modes will experience differential mode attenuation and have different power output after propagating over the fiber. It is expressed as [95]:

$$\rho = \rho_0 \cdot \left\{ 1 + I_\rho \left[\eta \cdot \left(\frac{(|l| + 2m)\lambda}{2\pi a n_1} \cdot \sqrt{\frac{\alpha + 2}{\alpha \Delta}} \right)^{\frac{2\alpha}{\alpha+2}} \right] \right\} \tag{2.32}$$

in which α is the profile alpha parameter, Δ is the profile delta, I_ρ is the ρth-order modified Bessel function of the first kind, and η is a scaling factor.

2.2.4 Parabolic configuration

MMF with parabolic index profile is designed to reduce the DMD. The modes and propagation constants can be represented analytically and achieved numerically. The analytical field solutions in the core are described as [96–102]:

$$E_{l,m}(r,\phi) = E_{0,core}\rho^{1/2}L_l^m(\rho)e^{-\rho/2}\begin{Bmatrix}\sin l\phi \\ \cos l\phi\end{Bmatrix}, \quad \rho = \frac{k_0 n_1 r^2\sqrt{2\Delta}}{a} \tag{2.33}$$

The field solutions in the cladding are then given as:

$$E_{l,m}(r,\phi) = (-1)^m E_{0,clad}K_l\left(r\sqrt{\beta_{l,m}^2 - k_0^2 n_2^2}\right)\begin{Bmatrix}\sin l\phi \\ \cos l\phi\end{Bmatrix} \tag{2.34}$$

The propagation constant $\beta_{l,m}$ is approximated as:

$$\beta_{l,m} = k_0 n_1\sqrt{1 - Q_{l,m}}, \quad Q_{l,m} = \frac{(1 + 2m + 1)\sqrt{8\Delta}}{k_0 n_1 a} \tag{2.35}$$

The corresponding group velocities are expressed in Eq. 2.36, so that the signal delay can be calculated with respect to the mode group delay.

$$\nu_{g,lm} = \left(\frac{d\beta_{l,m}}{d\omega}\right)^{-1} = \frac{c}{n_1}\left(\frac{2\sqrt{1 - Q_{l,m}}}{2 - Q_{l,m}}\right) \tag{2.36}$$

A well designed grade index fiber can have much better performance than the step-index fiber [103]. OM3 and OM4 fiber are the cases with optimal design of the index profile to enhance the performance cooperating with 850 nm multi-mode (MM) VCSEL.

2.2.5 Delay due to chromatic dispersion

For chromatic dispersion in general, we can summary the effect on the signal as the follow Eq. 2.37

$$\tau = DL\delta\lambda \tag{2.37}$$

in which τ is the time delay, or known as the pulse broadening, resulting from the chromatic dispersion; D is the chromatic dispersion coefficient (ps/(km· nm)); L is the fiber length; and $\delta\lambda$ is the difference on the wavelength. The chromatic dispersion is dependent on the waveguide material, which is similar in both MMF and SSMF. The dispersion coefficient is wavelength dependent, with typical value as 17 ps/(km· nm) for 1550 nm, 0 ps/(km· nm) for 1300 nm and -105 ps/(km· nm) for 850 nm. Compared with the modal dispersion, the chromatic dispersion in MMF is relatively small. Thus, for most of the cases in the practical research and in this thesis, we ignore the impact from the chromatic dispersions.

2.2.6 Loss in fiber

The propagation of optical signals in the actual fiber is always lossy, which is described by the Beer's law as Eq. 2.38.

$$P_{out} = P_{in} e^{-\alpha_L L} \tag{2.38}$$

in which P_{in} and P_{out} are the optical power of input and output signal for a piece of fiber; α_L is the attenuation coefficient (dB/km); and L is the length of fiber. The attenuation coefficient α_L depends on the material, wavelength, fiber geometry and etc. The typical values for different wavelength include: 0.2 dB/km for 1550 nm, 0.37 dB/km for 1300 nm and 2.89 dB/km for 850 nm. The practical value for standard MMF, i.e. OM3/OM4 fiber, reaches 3.5 dB/km [104].

2.2.7 Bandwidth of MMF

The bandwidth of the MMF is limited by its group-velocity spreading and the launching conditions. EMB is an effective metric describing the capacity of MMF in presence of inter-modal dispersion [105]. It is defined as the product of the maximum achievable data rate and the transmitting distance with a unit of MHz·km.

For characterizing the EMB of MMFs, TIA regulates a method in TIA FO 4.2.1 [106]. It is characterized by measuring the DMD with single pulses and plotting DMD v.s. radial position of the input light beam on the fiber surface.

Effective bandwidth (EB) takes into account both inter-modal and chromatic dispersion [107] and is proven better than EMB [108]. Similar to EMB, it uses the unit of MHz·km.

Another metric for describing the bandwidth of MMF is to measure the DMD under the launch condition, so-called over-filled launching (OFL), where the input light beam covers the whole core region. The bandwidth measured is known as OFL bandwidth. Such methods are widely used for light-emitting diode (LED) based data links.

2.2.8 OM3 and OM4 MMF

By using a specific design with the 850 nm MM VCSEL, the performance of MMF, e.g. OM3 and OM4, can be improved for the applications of datacenter optical interconnects. The typical effective bandwidth (EB) of OM3 fiber reaches 2 GHz·km and OFL of 2 GHz·km [104] for light wavelength ranging 780 nm-920 nm, with loss of 3.5 dB/km and 50 μm core diameter; whereas the EB for OM4 reaches 4.7 GHz·km and OFL of 3.5 GHz·km [109] with light wavelength centering at 850 nm.

OM5 MMF, regulated in ANSI/TIA-492AAAE, is newly standardized by TIA [110], known as wideband MMF. It is another case of specific optimal design on MMF, which aims to improving the performance of shortwave division multiplexing (SWDM) products, where carriers with a wide wavelength range e.g. >900 nm, will be used. More details of wideband MMF refer to [111–114].

2.3 VCSEL-to-MMF coupling

Light output from VCSEL propagates in free space before coupled into fiber. Unlike the field distribution inside the waveguide, the light beam transmitted in free space is described as a superposition of Laguerre-Gaussian (LG) modes. The LG modes are mathematically described in Eq. 2.39-Eq. 2.43.

$$E^L_{n,m}(r,\theta,z,w_0) = \frac{e^{-in\theta}}{W(z)}\left(\frac{r}{W(z)}\right)^n \times L^n_m\left(f\frac{2r^2}{W^2(z)}\right)e^{\phi(r,\theta,z,w_0)} \tag{2.39}$$

$$\phi(r,\theta,z,w_0) = jkz - \frac{r^2}{w_0^2\left(1+i\frac{z}{z_R}\right)} - j(n+2m+1)\arctan\left(\frac{z}{z_R}\right) \tag{2.40}$$

$$W(z) = w_0\left(1+(z/z_R)^2\right)^{1/2} \tag{2.41}$$

$$z_R = \pi w_0^2/\lambda \tag{2.42}$$

$$k = 2\pi/\lambda \tag{2.43}$$

To describe the light field propagating in free-space, we decompose the VCSEL modes into the LG modes as Eq. 2.44:

$$E_{l,p}^{F}(r,\theta,z)=\sum_{m=0}^{M}a_{l,m}LG_{l,m}(r,\theta,z,w_0) \tag{2.44}$$

in which, $a_{l,m}$ are results of the scalar products between VCSEL modes and the LG modes of the interest defined over the VCSEL output surface [95]. From laser output $E_{l,p}^{F}(r,\theta,z)$ to the fiber ends $E'^{F}_{l,p}(r,\theta,z)$, the field is characterized rigorously by the diffraction theory.

To understand the light coupling into MMF, we expand the field distribution at the fiber end $E'^{F}_{l,p}(r,\theta,z)$ onto the orthogonal basis of the full set of the MMF guided modes [95]. The coupling efficiency of each fiber modes can be obtained by the overlap integrals between the incident field and the guided modes of MMF [115]. The encircled flux (EF) function calculates the fraction of the total power radiating into a MMF. It is expressed as in Eq. 2.45.

$$EF(r)=\int_0^r\int_0^{2\pi}|E(r,\theta)|^2\,d\theta r dr \tag{2.45}$$

As mentioned in [95], the IEEE 802.3 standards recommend for the source less than 30% EF at 4-5 μm and more than 86% EF at 19 μm.

2.4 ROSA

A typical receiver consists of a photodiode and a TIA as pre-amplifier. The photodetector converts optical signal to photocurrent, which then passes through the TIA, converted into a voltage. The signal is finally amplified by a post-amplifier combined with a baseband filter. The noise feature is one of the critical considerations

A photodiode is a semiconductor component for detecting the optical signal and convert the signal from the optical domain to the electrical domain. It generates electrons by absorbing the photons. The photocurrent is generated following:

$$I_{opt}=\Re P_{in} \tag{2.46}$$

in which, I_{opt} is the photocurrent, P_{in} is the input power and R is the responsivity. $\Re$ is positively related to the quantum efficiency η [116]. It follows Eq. 2.47.

$$\Re=\frac{e\lambda\eta}{hc} \tag{2.47}$$

in which, e is the electron charge, λ is the wavelength of the incident light, h is the Planck's constant, and c is the speed of light. The responsivity has a unit of A/W. Quantum efficiency measures the percentage of the incident photons that are converted to electrons. The relation between η and the thickness W of the absorption layer of PD is expressed as:

$$\eta = (1 - R_f)\left(1 - e^{-\alpha W}\right) \tag{2.48}$$

where α is the absorption coefficient, and R_f is the reflectivity of the photosensitive area. This relation implies a critical trade-off during the design of PD, namely the side of PD chip and bandwidth.

The responsivity is the critical parameter describing the conversion of the incident optical power into voltage. For increasing the responsivity of a PD, we can increase the quantum efficiency by enlarging the thickness of PD. Yet, larger chips have higher parasitic effects, which reduces the effective bandwidth. Therefore, for the high-speed photoreciver, PD chips with small size are usually adopted, which also become one of the major limiting factors for Si or Ge PD used in the 850 nm region.

The typical material for the high-speed photodiode including GaAs, InGaAs, Si, Ge and InP. According to the bandgaps, the responsivity of each material changes with the corresponding wavelength. In the region of 850 nm, GaAs have a relatively high responsivity. It is one of the main reasons why GaAs is widely used in the current generation of the short reach data links. GaAs is also a factor behind the low cost of 850 nm system, as GaAs is cheaper than InGaAs, which uses more expensive and strategically constrained rare-earth materials.

2.4.1 Frequency response

A photodiode has a frequency response, which filters the photocurrent generated. The intrinsic response is expressed as [116]:

$$\begin{gathered}\frac{i(\omega)}{i(0)} = 10^{G/20}\left(\frac{1}{1 + j\omega(R_d + R_s)C_p}\right)\left(\frac{1}{1 - e^{-\alpha L}}\right)\\ \left(\frac{1 - e^{-j\omega\tau_e}e^{-\alpha L}}{j\omega\tau_e + \alpha L} + e^{-\alpha L}\frac{e^{-j\omega\tau_e} - 1}{j\omega\tau_e} + \frac{1 - e^{-j\omega\tau_h}}{j\omega\tau_h} + e^{-\alpha L}\frac{1 - e^{-j\omega\tau_h}e^{\alpha L}}{\alpha L - j\omega\tau_h}\right)\end{gathered} \tag{2.49}$$

where, $\tau_e = L/\nu_e$ is the electron transit time and $\tau_h = L/\nu_h$ is the hole transit time. C_p is the parasitic capacitance of the PD, R_d is the load resistance, R_s is the series resistance.

2.4.2 Noise features

The noise model of PD include spontaneous emission noise, short noise, dark current noise and RIN. The noise of circuit is also included. It can be formally expressed as [116]:

$$\left\langle i_n^2 \right\rangle = \left\langle i_{circuit}^2 \right\rangle + \left\langle i_{shot}^2 \right\rangle + \left\langle i_{dark}^2 \right\rangle + \left\langle i_{S-SP}^2 \right\rangle + \left\langle i_{Sp-SP}^2 \right\rangle + \left\langle i_{RIN}^2 \right\rangle \tag{2.50}$$

Spontaneous emission noise

Spontaneous emission noise effects include signal-spontaneous (sig-spon) and spontaneous-spontaneous (spon-spon) beat noise arise from the action of the square law detection mixing the deterministic signal and random noise. Considering the optical field is analytically decomposed into two parts, i.e. signal and noise, as:

$$E(t) = E_s(t) + E_n(t) \tag{2.51}$$

The photocurrent is then generated as:

$$I_{ph} = \Re \left| E_s(t) + E_n(t) \right|^2 = \Re \left(\left| E_s(t) \right|^2 + 2 \left| E_s(t) E_n(t) \right| + \left| E_n(t) \right|^2 \right) \tag{2.52}$$

The spontaneous emission noise is modeled as a stochastic time series added to the sampled optical signal. The variance of the signal-spontaneous amplified spontaneous emission (ASE) beat noise is modeled in the literature essentially by multiplying the spontaneous emission at every frequency by the optical signal as [116]:

$$\left\langle i_{S-SP}^2 \right\rangle = 4\Re^2 (M^2 F)^2 B_{eff} \int_{f_{start}}^{f_{end}} P_{s-n}(f) \, \mathrm{d}f \tag{2.53}$$

in which f_{start} and f_{end} represent the beginning and end frequencies of the ASE noise spectrum. The variance of the spontaneous-spontaneous ASE beat noise is expressed as [116]:

$$\left\langle i_{SP-SP}^2 \right\rangle = 4\Re^2 (M^2 F)^2 B_{eff} \int_{f_{start}}^{f_{end}} \int_{f_{start}}^{f_{end}} P_n(f_1) P_n(f_2) \, \mathrm{d}f_1 \mathrm{d}f_2 \tag{2.54}$$

Noise of other types is described by the variances of each effect and adding a Gaussian random variable photocurrent as:

$$N(t_i) = \xi_i \sqrt{\left\langle i_{shot}^2 \right\rangle + \left\langle i_{dark}^2 \right\rangle + \left\langle i_{RIN}^2 \right\rangle} \tag{2.55}$$

in which, ξ_i is a Gaussian random variable of zero mean and unit variance. It is reasonable to choose an effective bandwidth for the noise, for the noise is assumed to be white noise. The one-side bandwidth is $B_{eff} = 1/(2\delta t$, where δ is the sampling rate. The noise variance is expressed with the associated spectral density function $S(f)$, following [116]:

$$\left\langle i_n^2 \right\rangle = \sum_0^{B_{eff}} S_n(f)df \tag{2.56}$$

Shot noise derives from the random distribution in arrival times of the photons at the PD as [116]:

$$\left\langle i_{shot}^2 \right\rangle = 2qI(t)B_{eff} \tag{2.57}$$

Dark current noise is short noise associated with leakage currents in the active region of the photodetector which flow even in the absence of incident optical power, and is described as [116]:

$$\left\langle i_{dark}^2 \right\rangle = 2qI_{dark}M^2FB_{eff} \tag{2.58}$$

The dark current is time-independent. For PIN, the factors F and M are unity. For APD, M is the multiple gain factor and $F = kM + (1-k)(2 - 1/M)$ is an excess noise factor associated with the ratio $k = \alpha/\beta$ of the electron and hole ionization coefficients.

RIN is described with the variance given by [116]:

$$\left\langle i_{RIN}^2 \right\rangle = (M^2FI)^2 N_{RIN}B_{eff} \tag{2.59}$$

in which, N_{RIN} is the RIN parameter specified in the source model.

Circuit noise describes the thermal contribution of the feedback resistor in the transimpedance amplifier and the thermal channel noise in the pre-amplifier input transistor. The circuit noise is described as [116]:

$$\left\langle i_{circuit}^2 \right\rangle = \left(\frac{4kT}{R_f} + 4kT\Gamma \frac{(2\pi C_T)^2}{g_m} f^2 \right) B_{eff} \tag{2.60}$$

where k is the Boltzmann's constant, T is the temperature, R_f is the amplifier feedback resistance, g_m is the transconductance of the pre-amplifier input transistor, Γ is the excess channel noise factor, and C_T is the total input capacitance.

Chapter 3

Hyperspace, Lattice and Modulation Formats

3.1 Hyperspace

The construction of the multi-dimensional (MD) signal space is equivalent to find an orthogonal basis which consists of the degree of freedom provided by different physical quantities. These quantities should exist independently or be able to express the orthogonal relations, from where the virtual independence can be extracted. For systems with different realizations, the independent quantities may differ. Orthogonal basis is adopted both naturally and artificially. Concretely, for a single carrier single lane coherent system, four natural degrees of freedom as a four-dimensional (4-D) orthogonal basis can be naturally found in different components of the electromagnetic fields, namely the in-phase (I) and quadrature (Q) components existing in both polarizations, i.e. x- and y-polarization. For the multi-carrier systems, e.g. wavelength division multiplexing (WDM) systems, carriers with different wavelength is then the natural degree of freedom. Similarly, the sub-carrier on one optical carrier can also act as independent channels [68]. In the spatial division multiplexing (SDM) systems, degrees of freedom can be found in different modes of multi-mode fiber (MMF) or few mode fiber (FMF) [117–121] or signal in different cores of multi-core fiber (MCF) [122–124]. These modes are orthogonal ideally, if the modes coupling effects are not taken into account.

For a single-wavelength single-lane intensity-modulated direct-detection (IM-DD) system, however, is naturally one-dimensional, for that the only physical quantity that we can easily utilize as the degree of freedom is the amplitude of each pulse, i.e. symbol. However, a virtual degree of freedom is found between different temporally adjacent time-slots, which forms the orthogonal basis, provided the inter-symbol interference (ISI) is negligible. Alternatively, an orthogonal basis can be found in parallel optical channels, like separated fiber lanes for the 4-lane quad small form-factor pluggable (QSFP) or 8-lane octal small form-factor pluggable (OSFP) transceivers. Such channels are inherently multi-dimensional.

An n-element orthogonal basis spans an n-dimensional signal space. The signal space can be constructed by homogeneous degrees of freedom. For example, the single carrier coherent channel is inherently 4-D, considering four homogeneous orthogonal basis, e.g. $\mathrm{I_x}$, $\mathrm{I_y}$, $\mathrm{Q_x}$, and $\mathrm{Q_y}$.

However, the MD space can be also constructed with heterogeneous basis which combining different types of physical quantities, i.e. hybrid basis. For example, an eight-dimensional (8-D) signal space can be constructed by using all four components on two carriers. All the eight components are mutually independent, which form a hybrid 8-D orthogonal basis. Such techniques have been adopted and investigated in [64, 67, 119, 125–128] to increase the dimensionality of the signal space.

For a IM-DD system, by combining every n regular symbols into a sequence of super symbols, we can artificially construct an n-dimensional signal space. Further, IM-DD links using 4λ shortwave division multiplexing (SWDM) over 4-lane parallel channels are sixteen-dimensional.

In this thesis, we construct the n-dimensional signal space using various types of the degrees of freedom. For the single carrier MD pulse amplitude modulation (PAM), we treat the individual time slots as the degree of freedom. By combining n temporally adjacent symbols in a single channel, an n-dimensional signal space can be constructed. It is also an emulation of the independent channel for the physically parallel lanes. Later, we apply the MD constellations in the multi-subcarrier systems. In such a system, the construction of MD signal space is mainly based on the so-called inter-symbol super-channel and intra-symbol super-channel. The former one combines multiple subcarrier channels in different multi-subcarrier symbols, usually adjacent ones, into one MD super-channel, or MD super-symbol. Normally, we use the symbol from the subcarrier with the same frequency. The reason is that the channel condition keeps similar, especially for the colorful physical channels. For the later construction principle, super-symbols are constructed using the subcarriers within the single multi-subcarrier symbol.

3.2 Lattice

A lattice $\mathbf{L}$ is a subset of $\mathbb{R}^n$ which is isomorphic to $\mathbb{Z}^n$. Concretely, it follows the following the condition[1]:

$$\mathbf{L} = \left\{ \sum_{i=0}^{n-1} a_i \mathbf{v}_i \mid a_i \in \mathbb{Z} \right\} \tag{3.1}$$

in which $\mathbf{v}_i$ is a basis vector.

Lattices have specific symmetry or known as the invariance under specific operation, e.g. translation, rotation and reflection. In crystallography, a specific symmetry can be described as a certain group. Group is the set of elements $\mathcal{E}$ and operation, denoted as $\circ$, when the following requirements are satisfied [66]:

- *Closure* $\forall \mathbf{l}_a, \mathbf{l}_b \in \mathcal{E},\ \mathbf{l}_a \circ \mathbf{l}_b \in \mathcal{E}$;
- *Associativity* $\forall \mathbf{l}_a, \mathbf{l}_b, \mathbf{l}_c \in \mathcal{E},\ (\mathbf{l}_a \circ \mathbf{l}_b) \circ \mathbf{l}_c = \mathbf{l}_a \circ (\mathbf{l}_b \circ \mathbf{l}_c)$;
- *Identity* $\forall \mathbf{l}_a \in \mathcal{E},\ \exists\ \mathbf{l}_0 \in \mathcal{E}$, st. $\mathbf{l}_0 \circ \mathbf{l}_a = \mathbf{l}_0 \circ \mathbf{l}_a = \mathbf{l}_a$;
- *Inevitability* $\forall \mathbf{l}_a \in \mathcal{E},\ \exists\ \mathbf{l}'_a \in \mathcal{E}$, st. $\mathbf{l}_a \circ \mathbf{l}'_a = \mathbf{l}_0$.

The constellation designed in this thesis rely on the lattice structure in MD space, especially the densest lattice in the corresponding dimension. The densest lattice for two-dimensional (2-D), three-dimensional (3-D) and 4-D have been found since long. But the rigorous mathematic proofs of the densest lattice even for 3-D space has just been achieved at the end of last century [129]. And until recently, 8-D and twenty-four-dimensional (24-D) signal space are achieved by Maryna Viazovska [130] and by Henry Cohn and et al. in 2016 [131] respectively.

Two-dimensional

The densest lattice in 2-D is the hexagonal lattice known as honeycomb, or mathematically A_2, as shown in Fig. 3.2.(a). It can be expressed as the group D_{12}, which means it is the combination of group C_2 and S_3, which indicate symmetries of translation in two directions and rotation of angles. Z_2 is, however, the simplest lattice in 2-D, which has a cubic

---

[1] In the rest of this thesis, we reserve $\mathbf{L}$ as a notation for the set of the whole lattice with specific structure. Note that for avoiding confusion, the bold $\mathbf{L}$ and L have different meaning.

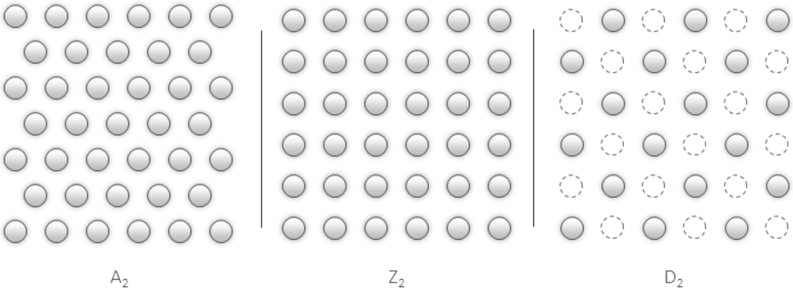

Figure 3.1: Typical 2-dimensional lattices. (a) A_2 lattice; (b) Z_2 lattice; (c) D_2 lattice.

configuration as shown in Fig. 3.2.(b). It is noteworthy that the normal quadrature amplitude modulation (QAM) formats are the subsets of Z_2 lattice. Another lattice worth mentioning is the D_2, which is nothing but a A_2 rotated by $\pi/4$ and scaled by a factor of $\sqrt{2}$, shown as Fig. 3.2.(c). A Z_2 can be divided into two independent subsets of D_2. It is expressed formally as:

$$\mathbf{L}_{Z_2} = \mathbf{L}_{D_2} \cup \mathbf{L}_{D_2}^{\perp} \tag{3.2}$$

in which $\mathbf{L}_{D_2}^{\perp}$ is the coset of $\mathbf{L}_{D_2}$[2]. From that we can further divide a D_2 into two A_2 independent subsets as:

$$\mathbf{L}_{D_2} = \mathbf{L}_{Z_2} \cup \mathbf{L}_{Z_2}^{\perp} \tag{3.3}$$

Three-dimensional

The densest lattice of 3-D space is known as lattice A_3 or D_3. D_3 is known as the face-centered cubic (f.c.c.) lattice. And as the 2-D case, Z_3 is the cubic lattice, or known as simple cubic in crystallography. The formats follows the 3-D lattice is reported in the subcarrier modulation for IM-DD systems [132].

Four-dimensional

Typical 4-D lattices include the simple hypercubic structure lattice A_4 and the densest lattice D_4.

---

[2] Note that the scaling factor is omitted here for not distracting the reader from the beauty of geometry.

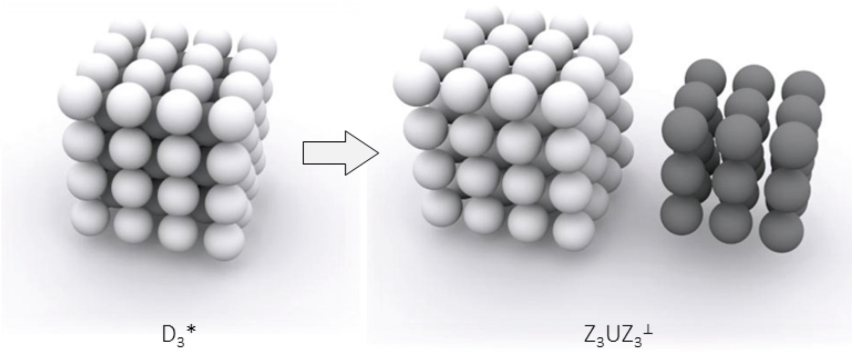

Figure 3.2: Illustration of lattice partition with the help of 3-D analogy. (a) D_3^* lattice; (b) $Z_3 \cup Z_3^{\perp}$ lattice. Note that D_3^* is the formal mathematic notation of the body centered cubic lattice.

Z_4 is the simple hypercubic structure, where the coordinators are chosen arbitrarily from $\mathbb{Z}^4$. The typical formats belong to the $\mathbb{Z}^4$ are the well-known polarization-division-multiplexing QAMs, e.g. PDM-QPSK and PDM-16QAM.

The densest lattice in 4-D space is known as D_4 or $W(F_4)$ with the context of group theory [133]. The formal expression is given as following [134, 135]:

$$D_4 = \left\{ (x_i) \in \mathbb{Z}^4 : \sum_i x_i \equiv 0 \ (\mathrm{mod} 2) \right\} \tag{3.4}$$

The lattice can be also constructed by the generation matrix [134]:

$$\widetilde{\mathbf{G}}_{D_4} = \begin{bmatrix} 1 & 0 & 0 & 0 \\ 0 & 1 & 0 & 0 \\ 0 & 0 & 1 & 0 \\ 1/2 & 1/2 & 1/2 & 1/2 \end{bmatrix} \tag{3.5}$$

where a D_4 lattice set can be constructed as:

$$\mathbf{L}_{D_4} = \widetilde{\mathbf{G}}_{D_4} \cdot \xi \tag{3.6}$$

where $\xi = [\ \xi_0 \ \cdots \ \xi_i \ \cdots \ \xi_3 \ ]^{\mathrm{T}}$, $\xi_i \in \mathbb{Z}$.

The typical formats rooting in D_4 lattice include polarization switching quadrature phase shift keying (PS-QPSK) and polarization division multiplexing quadrature amplitude modulation (PDM-QAM) applied with the set-partitioning, e.g. 128-SP-16QAM.

As the rules of division on the 2-D lattice, the 4-D lattices have similar features. Concretely, D_4 can be divided into two independent subsets, which belong to Z_4, as formally expressed as:

$$\mathbf{L}_{D_4} = \mathbf{L}_{Z_4} \cup \mathbf{L}_{Z_4}^{\perp} \tag{3.7}$$

in which $\mathbf{L}_{Z_4}^{\perp}$ is the coset of $\mathbf{L}_{Z_4}$. Similarly, it can be further divided as:

$$\mathbf{L}_{Z_4} = \mathbf{L}_{D_4} \cup \mathbf{L}_{D_4}^{\perp} \tag{3.8}$$

Such hierarchical partitioning is reflected in the construction of the set-partitioning formats [60]. It also offers deeper understanding of the formats, which is originally designed from a more physical perspective. For instance, H. Bülow proposed a format so-called POLQAM from the perspective of manipulations of the polarization states [58]. The format is actually bonded on the D_4 lattice and can be separated into two formats which are constructed in the Z_4 lattice. These two are now known as a polarization division multiplexing quadrature phase shift keying (PDM-QPSK) and a PS-QPSK, both of which root in the Z_4 lattice. We will elaborate these in detail in the later chapters.

Eight-dimensional

Entering the 8-D signal space, the densest lattice is called E_8. It can be expressed as [136],

$$E_8 = \left\{ (x_i) \in \mathbb{Z}^8 \cup (\mathbb{Z} + 1/2)^8 : \sum_i x_i \equiv 0 \ (\mathrm{mod} 2) \right\} \tag{3.9}$$

We can also use the generation matrix to present the construction of the lattice.

$$\widetilde{\mathbf{G}}_{E_8} = \begin{bmatrix} 2 & 0 & 0 & 0 & 0 & 0 & 0 & 0 \\ -1 & 1 & 0 & 0 & 0 & 0 & 0 & 0 \\ 0 & -1 & 1 & 0 & 0 & 0 & 0 & 0 \\ 0 & 0 & -1 & 1 & 0 & 0 & 0 & 0 \\ 0 & 0 & 0 & -1 & 1 & 0 & 0 & 0 \\ 0 & 0 & 0 & 0 & -1 & 1 & 0 & 0 \\ 0 & 0 & 0 & 0 & 0 & -1 & 1 & 0 \\ 1/2 & 1/2 & 1/2 & 1/2 & 1/2 & 1/2 & 1/2 & 1/2 \end{bmatrix} \tag{3.10}$$

E_8 lattice is the start point and foundation of the 8-D formats to be discussed in this thesis. We will elaborate more details on the geometric structure of E_8 lattice in later chapters.

Twenty-four-dimensional

The densest lattice for the 24-D space is known as the Leech lattice, which is an even unimodular lattice, Λ_{24}. The Leech lattice is closely related to the (24,12) extended Golay code. There are various ways of constructing the Leech lattice. Here we just quote the expression given by [137]. A more formal expression will be given in Chapter 5 when we discuss the Leech lattice based 24-D PAM.

"The Leech lattice can be explicitly constructed as the set of vectors of the form $2^{-3/2}[\, c_0\ a_1\ \cdots\ c_{23}]^{\mathrm{T}}$ where $\forall c_i \in \mathbb{Z}$ are integers such that

$$c_0 + c_1 + \cdots + c_{23} \equiv 4c_0 \equiv 4c_1 \equiv \cdots \equiv 4c_{23} \pmod 8 \tag{3.11}$$

and for each fixed residue class modulo 4, the 24 bit word, whose 1s correspond to the coordinates i such that c_i belongs to this residue class, is a word in the binary Golay code."

3.3 Multi-dimensional formats

3.3.1 Notation and formalization of multi-dimensional formats

Let us consider, without loss of generality, a L-element set of n-dimensional vectors[3], denoted as $\mathbf{C}$. It can be expressed as $\mathbf{C} = \{\, \mathbf{C}_0,\, \mathbf{C}_1,\, \cdots,\, \mathbf{C}_l,\, \cdots,\, \mathbf{C}_{L-1} \,\}$, where L is the scale of the constellation, e.g. $L = 4$ for PAM, $L = 256$ for D$_4$TS-4 and $L = 65536$ for E$_8$TS-4 and BB8, which will be mentioned in next chapter, with each n-dimensional real vector $\mathbf{C}_l \in \mathbb{R}^n$, $\mathbf{C}_l = [\ c_l^0\ c_l^1\ \cdots\ c_l^i\ \cdots\ c_l^{n-1}\ ]^{\mathrm{T}}$, $c_l^i \in \chi$. χ is the alphabet of each regular symbol, i.e. the set of the possible amplitude level, e.g. for pulse amplitude modulation with 4 levels (PAM-4), $\chi = \{\, 0,\, 1,\, 2,\, 3 \,\}$. We denote L_χ as the length of χ.

The Euclidean distance, or Euclidean norm, between the constellation points is defined as $d_{l,l'} = \|\mathbf{C}_l - \mathbf{C}_{l'}\|$, the minimum value of which $\forall l, l' \in$

---

[3] If without specifically indicating, we use $\mathbf{C}$ as the notation of certain constellation set in the rest of this thesis. If there is superscript m, like $\mathbf{C}^m$, it indicates the number of bit carried by per super-symbol.

$[\,0, n-1\,]$ is defined as

$$d_{min} = \min_{l \neq l'} d_{l,l'} \tag{3.12}$$

We denote d_{min} as the minimum mutual Euclidean distance (MMED) [55]. As d_{min} determines the overlapping region of the noise expansion, which is the source of error bits during the transmission, it is essential for estimating the performance of the constellation, and some other metrics of constellations are based on this value.

We need also to define the average energy per symbol, E_s. There are two different definition of E_s [138].

Average symbol energy is defined as[4]:

$$\frac{1}{L}\sum_{l=0}^{L-1} \mathbf{C}_l \cdot \mathbf{C}_l{}^{\mathrm{T}} \tag{3.13}$$

in which, $\mathbf{C}_l \in \mathbf{C}$ is one constellation in the constellation set $\mathbf{C}$.

Peak symbol energy is defined with the maximum amplitude, as:

$$\max \| \mathbf{C}_l \|^2 \tag{3.14}$$

Peak symbol energy is more natural for formats used in IM-DD systems. However, for keeping the consistency with the convention, we adopt the former definition through the whole thesis.

Based on E_s, we can also define the average energy per bit, E_b, which is defined as:

$$E_b = E_s/\log_2 L \tag{3.15}$$

3.3.2 Sphere packing

As mentioned above, the bit error rate (BER) performance, or more precisely the symbol-to-noise ratio (SER) performance of a certain constellation is determined by the d_{min}. If assuming that the noise distribution follows the additive white Gaussian noise (AWGN), we can visualize the impact of noise as the n-dimensional hypersphere expending from the constellation points. The design of a constellation in the MD space, therefore, is actually equivalent to the sphere packing problem defined in the hyperspace [134].

The sphere packing problem can be solved by searching the optimal configuration of the constellation set with the help of computers, as the case

---

[4] We keep the consistency of the notation in the following chapter. See more details of the notation in the following chapter.

of 3-D space [139] and the case of 4-D space [140]. The desired constellation can be constructed based on the database of the cluster. Such computer-based greedy searching algorithm works well for the constellations of small scales, i.e. fair number of constellation points. However, with the increase of dimensionality, i.e. n and the number of elements in the constellation set, i.e. L, such searching algorithm becomes unrealistic. It is discussed in [55, 134, 139–142]. Additionally, the cluster based algorithm normally offers irregular constellations. This will impose the complexity of the actual realization and the bit-to-symbol mapping. An inappropriate bit-mapping will spoil the benefits earned from the careful design of the constellation.

Apart from the cluster based algorithm, the densest lattice structure can help the design when the number of constellation set is large. Such an algorithm is sometimes also known as the lattice packing. For a concrete example, H. Bülow and et al. reported in 2014 an optimized 4-D with an equivalent spectral efficiency (SE) with PDM-16QAM using the lattice packing based on the densest lattice D_4 [59]. One major merit of lattice packing based constellations is the symmetry inherited from the lattice, which is reflected as the concise structure on each dimension as the reduced number of amplitude levels and more evenly distributed levels; or simpler structure for 2-D projections. Meanwhile, extra operations on a certain constellation set can create simpler structures without changing the internal structure. One appropriate instance follows the work mentioned above, in [143], T. Eriksson and et al. applied extra operations like 4-D rotations on the initial obtained constellation set and achieved a more symmetric constellation.

The above-mentioned constellation design is based on a Gaussian noise assumption. However, in many cases or even with an insight into a concrete case where the AWGN seems well enough, it does not always follow the fact. However, in this thesis, we assume such noise assumption is applicable in most of the scenarios.

3.3.3 Formalization of the optimization problem

In this section, we introduce the general formalization of the constellation optimization problem, namely finding the optimal constellation, with the cost function of minimum power or minimum amplitude. A comprehensive optimization of the constellation with the cost of power is formalized as

Eq. 3.16:

$$\arg\min_{\mathbf{C}} \frac{1}{L}\sum_{l=0}^{L-1} \mathbf{C}_l \cdot {\mathbf{C}_l}^{\mathrm{T}} \; + \; \alpha \cdot \frac{1}{L \cdot n}\sum_{l=0}^{L-1}\sum_{i=0}^{n-1} c_l^i \; + \; \beta \cdot L_\chi \tag{3.16}$$

The first term indicates the energy per symbol as mentioned before, or more concretely the average power the drive signal should have if it is selected evenly from the constellation set. The rest two terms are the regularization terms. The first one imposes the symmetry of the constellation, while the second one limits the number of amplitude levels. Generally, the optimal constellation, i.e. the most efficient constellation with the minimum cost, projects more power levels in each symbol than PAM-4 does, leading to the difficulty in the implementation of practical modulation and demodulation. During the allocation of the grid points, the number of amplitude levels on each symbol will be taken into account as a constraint of the optimization problem. Therefore, we add the last regularization term. The coefficients α and β give the weight of constraints. Concretely, if choosing a large β, the constellation probably sacrifices the sensitivity for a simpler structure.

Meanwhile the principle of the optimization with the cost of modulation amplitude is similarly expressed as Eq. 3.16:

$$\arg\min_{\mathbf{C}} \; \|\max \chi - \min \chi\| \; + \; \alpha \cdot \frac{1}{L \cdot n}\sum_{l=0}^{L-1}\sum_{i=0}^{n-1} c_l^i \; + \; \beta \cdot L_\chi \tag{3.17}$$

Here the first term is replaced by the one reflecting the range of modulation amplitude. The regularization terms, however, are kept as the same.

The above-mentioned algorithm is only in generalized formalization. The concrete design of the constellations, on the contrary, may be more complicated.

3.3.4 Metrics for multi-dimensional formats

To analyzing and estimating the performance of MD formats, we introduce several conventional metrics.

Spectral efficiency

The SE is used to describe the effective bit-rate. Following the convention, it counts the number of bit per complex channel, which actually contains two independent dimensions. Thus, the SE is formally defined as [138,144, 145]:

$$\mathrm{SE} = \frac{\log_2 L}{n/2} \tag{3.18}$$

where L is the number of symbols in the constellation set, i.e. the number of constellation points; n is the dimensionality of the signal space. Notice as the convention, n is divided by factor of 2. In the following chapter, we normally use bits per (regular) symbol, or denoted as bit/sym to indicate the effective bits carried by per regular symbol, for avoiding the confusion of above formal definition. While, since the SE is essential for calculating other metrics, it is necessary to keep the consistency with the conventions.

Asymptotic power efficiency

Asymptotic power efficiency is used to estimate the shaping gain for the regime of low noise, i.e. high signal-to-noise ratio (SNR). It is formally defined as:

$$\mathrm{APE} = \frac{d_{min}^2}{4E_b} \tag{3.19}$$

in which d_{min} is the MMED; E_b is the energy per bit.

We usually use dB as the unit of asymptotic power efficiency (APE). Typical APE values include 0 dB for non-return-to-zero (NRZ), -3.98 dB for PAM-4 and 0 dB for quadrature phase shift keying (QPSK).

Constellation figure of merit

The constellation figure of merit (CFM) is defined as [144,145]:

$$\mathrm{CFM} = \frac{n \cdot d_{min}^2}{2E_s} \tag{3.20}$$

Like APE, CFM characterizes the difference of sensitivity between two formats in high SNR regime. It conventionally uses dB as the unit of CFM. Some typical CFM values include 3.01 dB for NRZ and -3.98 dB for PAM-4 and 3.01 dB for QPSK.

3.4 Typical multi-dimensional formats

The multi-dimensional formats have been theoretically and experimentally investigated in the coherent optical communication systems, such as two-dimensional formats, three-dimensional formats, four-dimensional formats

[55–62], eight-dimensional formats [64–66] and twenty-four-dimensional formats [67, 146]. We emphasize, however, in this section the classical four-dimensional and eight-dimensional formats.

3.4.1 Four-dimensional formats

4-D signal space is inherently spanned by the four-components of the electromagnetic (EM) field, i.e. quadratures of the optical signal and the two orthogonal polarization states. Thus, the PDM-QPSK is naturally 4-D. By shaping the constellation set in the signal space, multiple 4-D formats are designed. The optimization process can be applied to the 4-D space. The 4-D formats are traced back to the pioneering theoretical works of G. Welti and Jhong Lee [147], and L. Zetterberg and H. Brändström [148] for the 4-D signaling in a general coherent communication system and the work of S. Betti and et al. [149, 150], who proposed the concept of the 4-D format of the coherent optical transmission for its early development stage. R. Cusani and et al. developed the concept [151]. S. Benedetto and P. Poggiolini proposed the PS-QPSK [152]. The other early works in the area include [153].

In 2009, when the digital signal processing (DSP) is widely applied in the coherent digital systems, M. Karlsson and E. Agrell systematically investigated the 4-D formats under the context of a coherent digital system [56, 154], with emphasis on the power efficiency.

POLQAM

H. Bülow invented a novel 4-D format, i.e. POLQAM, from the perspective of utilizing the polarization states [58]. From the point of view with the 4-D geometry, it is the format is a subset of the D_4 lattice, known as *24-cell* [134], which has 24 points in the set. We will elaborate later more 4-D formats rooting in the D_4 lattice. POLQAM does not have an integer number of bit per 4-D, but carries 9 bits for every two symbols. Therefore, it is sometimes treated as an 8-D format. F. Buchali and H. Bülow first experimentally verified the performance of POLQAM in a 28 GBaud coherent optical system [155]. Similar work was conducted by J. K. Fischer and et al. [156]. The performance of POLQAM was experimentally compared PS-QPSK [155] and OPT-16 [157]. POLQAM can be seen as a hybrid format of PDM-QPSK and a PS-QPSK.

PS-QPSK

PS-QPSK is another typical 4-D format which is investigated and studied in the coherent systems. It was theoretically investigated by L. Zetterberg and H. Brändström [148]. It has been thoroughly investigated with different schemes of PS-QPSK modulation, including the explicit selection of between optical branches for different polarization with a binary signal [158–161], using polarization modulator [162] and using the so-called single parity check (SPC) code [163–165]. The SPC operation can be simply expressed as following, if without loss of generality.

$$\mathrm{Q_y} = \mathrm{I_x} \oplus \mathrm{Q_x} \oplus \mathrm{I_y} \tag{3.21}$$

PS-QPSK can be also used in a format flexible transmission or a hybrid format modulation [60, 166–168]. Other important 4-D format is proposed and investigated, such as pulse position modulation (PPM) QPSK [169], and set-partitioning. It is noteworthy that PS-QPSK is also substantially a subset of D_4 lattice with 8 points. It is known as *16-cell.* PS-QPSK is equivalent to special cased for PPM as 2PPM-QPSK and a special case for the 4-D set-partitioning, known as 8-SP-QAM. We emphasize the 4-D set-partitioning in the following section.

4-D set-partitioning QAM

Ungerböeck first proposed the principle of the set-partitioning scheme [170, 171]. Such modulation scheme is extended by Coelho and Hanik [172], where a serial of 4-D formats have been introduced and investigated. The set-partitioning of their work is equivalent to select a subset based on D_4 lattice from the parent subset based on Z_4 lattice. Similar principles applied on the PDM-16QAM to 128-point and 32-point set can be found in [172, 173]. Following the convention, we denote the 4-D set-partition formats as k-SP-mQAM, representing a k-point subset selected from a PDM-mQAM. For instance, 128-SP-16QAM denotes a 128-point format selected from the 256-point PDM-16QAM. The modulation of the set-partitioning formats can be simply realized, in some cases, by the n_p-bit parity check code. A SPC code is special case when n_p=1. The set-partitioning Z_4 selection from D_2 with reduced half points can be simply realized by the SPC code. An example of n_i-bit SPC is shown as:

$$b_{spc} = b_0 \oplus b_1 \oplus b_2 \oplus \cdots \oplus b_k \oplus \cdots \oplus b_{n_i-1} \tag{3.22}$$

in which b_k is the k-th bit. More sophisticated parity check code schemes which enable the selection of even smaller subsets with fewer than half point of their parent sets, such as 32-SP-16QAM and 64-SP-16QAM are designed in [174].

Some typical works of 128-SP-16QAM include the investigations in a single carrier system [175], in a WDM system [176] and in a few-mode system [177] with different forward error correction (FEC) schemes [178] and comparison with other formats, e.g. POLQAM in [60, 63]. 32-SP-16QAM has been studied with different set-partitioning modulation schemes [172, 173], compare with other formats [174, 179]. The related experiments are reported in [60, 180]. 128-SP-16QAM has been given the attention in [181]. 4-D set-partitioning formats with higher order parent constellations are reported, like 512-SP-32QAM reported in [60, 182], 512-SP-64QAM reported in [173] and 2048-SP-64QAM in [60, 63].

The basic idea of the set-partitioning is the foundation of the rate-flexible PAM discussed in Chapter 6, where we apply the hierarchical subset selection on the 8-D densest lattice, known as E_8. We will also come back to such 4-D set-partitioning formats with half-set reduction in Chapter 7, where we load a serial of set-partitioning (SP) formats from 128-SP-16QAM to 8192-SP-128QAM in a discrete multi-tone modulation (DMT) transmission, to generate the half-integer steps between the larger steps created by PDM-mQAM.

Other 4-D formats

16-point constellation: the optimal 16-point 4-D format is proposed by M. Karlsson and E. Agrell [183], by applying the sphere packing in 4-D signal space, known as OPT-16. J. Karout and et al. investigated its performance in an orthogonal frequency division multiplexing (OFDM) system [184]. Another 16-point 4-D format is reported as the subset-optimized PM-QPSK (SO-PMQPSK) [185].

256-point set: the first attempt to optimize a 256-point 4-D constellation based on the D_4 lattice was conducted by H. Bülow and et al. in [59], which shows a better asymptotic performance compared with PDM-16QAM. T. A. Eriksson and et al. reported a format based on similar designing philosophy, known as 256-D_4 in [143]. It applies a 4-D rotation to search the optimal 2-D constellation projections, which have more concise configurations.

We will adopt the similar principle of designing the so-called optimal 4-D and 8-D formats for vertical-cavity surface-emitting laser (VCSEL) based

IM-DD systems. Yet, even though the basic ideas behind such optimal constellations are similar, ones designed for IM-DD systems need some further modifications, which will be elaborated in detail in Chapter 4.

3.4.2 Eight-dimensional formats

8-D formats for optical coherent systems have also been investigated recently. T. Koike-Akino and et al. reported three 8-D modulation formats constructed by two consecutive symbols [64]. Two of them are optimized by using the sphere packing one the E_8 lattice containing 128 and 256 points respectively. The third one applies a SPC to construct the format following the E_8 lattice grids. They are proven better in the asymptotic regime compared with PS-QPSK and PDM-QPSK. In [67], D. S. Millar and et al. reported 8-D formats constructed with the (8,4) extended Hamming code. H. Zhang and et al. reported an 8-D format combining a PDM-QPSK and a PS-QPSK rotated by $\pi/4$ [125]. It is substantially equivalent to POLQAM as discussed before, but with a different scaling factor on both subsets.

3.5 Multi-dimensional formats for IM-DD transmissions

The MD formats have been proposed for optical communication systems are even earlier than the coherent times. The lattice code is a pioneer theoretical work on the MD modulation formats for IM-DD systems, which was theoretically proposed by G. D. Forney and L. F. Wei in [144, 186] and systematically by S. Hranilovic and F. R. Kschischang in the optical IM-DD systems in [187]. The optical IM-DD systems which is theoretically proposed and systemically investigated by W. Mao and J. M. Kahn in [69]. J. Karout proposed to use multiple subcarrier as the basis of the MD signal space and studied the optimized constellations for single-subcarrier intensity-modulated (IM) transmission [68]. He and his colleagues formalized the 2-D signal space in [188]. K. Szczerba and et al. investigated into an optimal 8-level subcarrier format for a IM-DD using 850 nm VCSEL [189] and 16-ary constellation in a IM-DD based sub-carrier system [190]. J. Karout also studied theoretically the power efficient formats for the non-coherent systems [191].

Recently, MD coded modulation has been experimentally validated in IM-DD systems. A 2-D coded modulation scheme with external modulators is discussed in [70], to create multi-rate transceivers based on vertical-cavity surface-emitting lasers (VCSELs). A 4-D version was reported in [71] R. Rios-Müller and et al. They adopted a SPC scheme, where for every 7 bits one parity check bit is generated to output four PAM-4 symbols. Such modulation can earn a 2-dB asymptomatic gain compared with its PAM-m counterpart. A 4-D trellis coded modulation (TCM) is experimentally analyzed by N. Stojanovic and et al. in [72] and C. Prodaniuc and et al. investigated into the performance of a 4-D TCM compared with PAM-4 in the WDM system [73, 192]. Other works include a 2-D coded modulation based on pulse amplitude modulation with 8 levels (PAM-8) symbols [193], and 1-D PAM-8 and 2-D PAM-16 TCM based on 850 nm VCSEL in [32].

In this thesis, we place emphasis on extending the application of the MD coded modulation, or known as the MD formats in the IM-DD systems, with both single carrier and multi-subcarrier modulation schemes.

Chapter 4

Four and Eight-Dimensional PAM

Pulse amplitude modulations (PAM) are widely used in the current intensity-modulated direct-detection (IM-DD) systems. Specifically, non-return-to-zero (NRZ), i.e. known as pulse amplitude modulation with 2 levels (PAM-2), is most conventional format for current systems of 25 Gbit/s per lane; and pulse amplitude modulation with 4 levels (PAM-4) has been regarded as one of the most promising modulation formats for the next generation short-reach data-links beyond 50 Gbit/s for intra- and inter-datacenter interconnections [194], due to its higher spectral efficiency compared to NRZ and lower implementation complexity than higher order formats, such as quadrature phase shift keying (QPSK). However, the sensitivity of PAM-4 is much lower than NRZ for the same system configurations.

For increasing the receiver sensitivity, algorithms based on higher dimensional lattice grids have been investigated compared with the conventional quadrature amplitude modulation (QAM) in coherent detection systems [59,154,173]. The similar optimization approach can be introduced to IM-DD system by combining consecutive symbols (time slots) into temporal super-symbols based on the assumption that inter-symbol interference (ISI) is small and symbols are independent to each other, implying the orthogonality of basis in a n-dimensional signal space spanned by n temporally consecutive symbols.

In this chapter, we theoretically propose and experimentally investigated three different kinds of multi-dimensional PAM (MD-PAM) with various design principles. The principle of multi-dimensional signal space and pulse amplitude modulation (PAM) are formalized in Section 4.1 and

Section 4.2 respectively. In Section 4.3, we design and verify one four-dimensional (4-D) PAM, i.e. D_4TS-4, and one eight-dimensional (8-D) PAM, i.e. E_8TS-4, with 2 bits per symbol (bit/sym). They are optimized with 4 and 8 dimensional densest lattice grids, i.e. D_4 and E_8 respectively by applying geometric shaping on temporal super-symbols with the rule of minimum power. In the following section, we theoretically propose and experimentally investigate an alternative *Block-Based 8-dimensional/8-level* PAM, namely BB8, carrying 2 bit/sym, i.e. the same spectral efficiency as PAM-4. It takes the advantages of the geometry behind E_8, the densest 8-D lattice, and optimized with the rule of maximum amplitude, taking into account the trade-off between high performance and modulation simplicity. A simplified bit-to-symbol mapping and corresponding symbol-to-bit de-mapping algorithms, together with its decision schemes, i.e. hyper-space hard-decision (HD) and hierarchical soft-decision (SD), are designed specifically for its applications for short-reach data links.

4.1 Signal space for multi-dimensional PAMs

In general, the construction of the multi-dimensional (MD) signal space is equivalent to find an orthogonal basis which consists of the degree of freedom provided by different physical quantities. An n-element orthogonal basis spans an n-dimensional signal space, accommodating the modulation formats of corresponding dimension. Specifically, for MD-PAM, which based on a single-wavelength single-lane IM-DD system, the only physical quantity that we can easily utilize as the degree of freedom is the amplitude of each pulse, i.e. symbol. Ideally, consecutive symbol slots can be treated as independent basis, provided the ISI is negligible. It implies that by combining every n regular symbols into a sequence of super symbols, we can artificially construct an n-dimensional signal space.

Alternatively, an orthogonal basis can be found in parallel optical channels, like separated fiber lanes for the 4-lane quad small form-factor pluggable (QSFP) or 8-lane octal small form-factor pluggable (OSFP) transceivers. Such channels are inherently multi-dimensional.

In this chapter, n-dimensional signal space, i.e. $n = 4$ and 8, is constructed by combining n temporally adjacent symbols in a single channel. The modulated sequence of super-symbols is further interleaved into n blocks, emulating n independent channels and suppressing the deterioration of the orthogonality due to ISI.

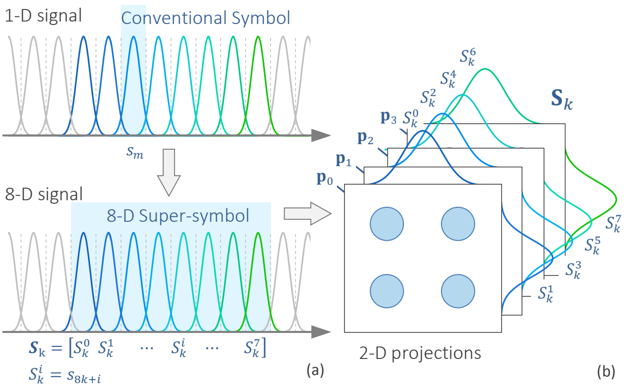

Figure 4.1: The schematic illustration of the construction of the multi-dimensional signal space. (a) Illustration of the principle of constructing the eight-dimensional super-symbols by combining the temporally adjacent symbols. (b) The construction of two-dimensional projections by using two symbols.

4.2 Multi-dimensional PAM for IM-DD systems

4.2.1 Formation of multi-dimensional PAM

Let us consider, without loss of generality, $\mathbf{s} = [\, s_0,\, s_1,\, \cdots,\, s_m,\, \cdots]^{\mathrm{T}}$ as a transmitting sequence. The subscript $m = 0,\ 1,\ \cdots$ as the position of a regular symbol s_m in the sequence. The sequence of n-dimensional super-symbols is denoted as $\mathbf{S} = [\, \mathbf{S}_0,\, \mathbf{S}_1,\, \cdots,\, \mathbf{S}_k,\, \cdots]^{\mathrm{T}}$. The subscript $k = 0,\ 1,\ \cdots$ is denoted as the position of a super-symbol $\mathbf{S}_k$ in the sequence $\mathbf{S}$. In the rest of the chapter, if without specific indication, the regular symbol sequence is denoted in lower case and the super-symbol sequence in upper case. For each super-symbol $\mathbf{S}_k = [\, S_k^0,\, \cdots,\, S_k^i,\, \cdots,\, S_k^{n-1}\,]^{\mathrm{T}}$. S_k^i is the individual symbol in the k-th super-symbol. $i = 0,\ 1,\ \cdots,\ n-1$ indicates its position in $\mathbf{S}_k$. S_k^i corresponds to the symbol $s_{n \cdot k+i}$ in $\mathbf{s}$, i.e. $m = n \cdot k + i$. Therefore, each symbol in one super-symbol gives the coordinate value of one point in n-dimensional signal space along a specific orthogonal direction. Specifically, for one-dimensional signal space when $n = 1$, the sequence of super-symbols $\mathbf{S}$ degenerates to the one of regular symbols $\mathbf{s}$. Concretely, a continuous pulse train with PAM signal modulated is naturally one-dimensional, i.e. $n = 1$, as shown in Fig. 4.1.(a).

4.2.2 Noise assumptions

We assume that the received super-symbols $\mathbf{R}_k = [\, R_k^0, \cdots, R_k^i, \cdots, R_k^{n-1} \,]^{\mathrm{T}}$ are affected by additive white Gaussian noise (AWGN). They can be visualized as hyper-spheres expanded from the ideal format points, like $\mathbf{R}_k = \mathbf{S}_k + \mathbf{N}_k$, where $\mathbf{N}_k$ are independent and identically distributed (i.i.d.) random variables. Notice that here the channel responses are not taken into account, i.e. each super-symbol is seen as independent. In fact, the Gaussian model is not naturally guaranteed in VCSEL based IM-DD links, that leads to the noise spheres shifted from the designed locations and apart from the hyper-sphere form, becoming more irregular and anisotropic. The impact of this effect on the performance is not straightforward and depends on the specific constellation configuration. In this chapter, we assume that the shift and distortion of the noise hyper-spheres are negligible and adopt a Gaussian noise model.

As mentioned in Sect. 3.3.1, since the errors mainly occur in the overlap regions between two noise hyperspheres, the performance of modulation formats can be improved by maximizing the minimum mutual Euclidean distance (MMED), denoted as d_{min}, between all pairs of the format points, to avoid the errors occurring in that region.

4.2.3 Block-wise interleaving

The proposed formats are designed for independent parallel channels, where the orthogonality of the basis is inherently guaranteed. Therefore, during the format design one can assume that the individual symbol is free of ISI. However, such an assumption is not sufficiently reasonable for the temporally adjacent symbols modulated by vertical-cavity surface-emitting laser (VCSEL) and transmitted through multi-mode fiber (MMF) because of two reasons: (1) the ISI resulting from the unavoidable inter-modal dispersion skews the basis; (2) the nonlinear transient line due to the complicated physical process inside the active layer of VCSEL reshapes the noise distribution from a pure Gaussian form to a mixed Gaussian distribution and bring the channel from memoryless to time-dependent. Hence we use a block-wise interleaving scheme to reduce such effects and emulate the parallel channels. By doing so, the ISI becomes the signal unrelated noise.

The general structure of block-wise interleaving is illustrated in Fig. 4.2. The transmitted sequence is fed into an interleaving matrix $\widetilde{\mathbf{M}}$ column-wisely. Each column corresponds to a single super-symbol $\mathbf{S}_k$ in the input sequence $\mathbf{S}_{input}$. Then n blocks $\mathbf{B}_i$ are generated row-wisely, with each

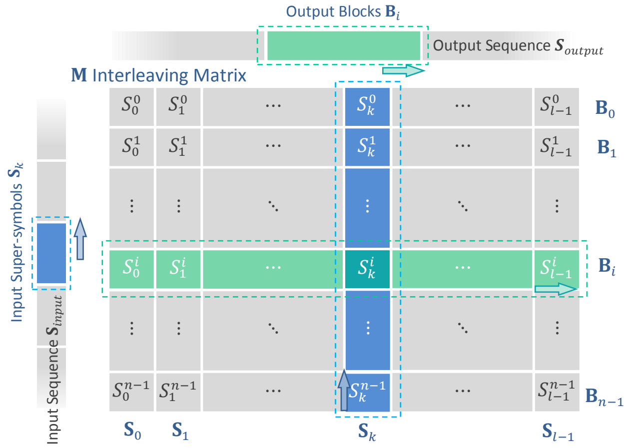

Figure 4.2: Schematics of a block-wise interleaving scheme.

block as an analogy of an independent channel. Symbols in each block correspond to the symbols with the same position, i.e. S_k^i with the same superscript i in $\mathbf{S}_k$. Formally, the interleaving matrix can be expressed as $\widetilde{\mathbf{M}} = [\,\mathbf{S}_0\ \mathbf{S}_1\ \cdots\ \mathbf{S}_k\ \cdots\ \mathbf{S}_{l-1}\,]$, in which $\mathbf{S}_k = [\,S_k^0\ S_k^1\ \cdots\ S_k^i \cdots\ S_k^{n-1}\,]^{\mathrm{T}}$ denotes the super-symbols with S_k^i the i-th symbol in the k-th super-symbol, and l gives the number of super-symbols that are processed in one batch, leading to the length of regular symbol sequence equal to $n \cdot l$ and the size of interleaver equal to $n \times l$. The matrix can be reformulated to a column matrix $\widetilde{\mathbf{M}} = [\,\mathbf{B}_0\ \mathbf{B}_1\ \cdots\ \mathbf{B}_i \cdots\ \mathbf{B}_{n-1}\,]^{\mathrm{T}}$, with row vectors $\mathbf{B}_i = [\,S_0^i\ S_1^i\ \cdots\ S_k^i\ \cdots\ S_{l-1}^i\,]$ as each block in output sequence $\mathbf{S}_{output} = [\,\mathbf{B}_0\,\mathbf{B}_1\ \cdots\ \mathbf{B}_i \cdots\ \mathbf{B}_{n-1}\,]$. Each block contains the symbols with the same position of all super-symbols.

It is noteworthy that for keeping the consistency, we applied the same interleaving scheme on all the formats we investigate in this work.

4.2.4 Designing philosophy

Multi-dimensional PAMs gain performance improvements via reshaping the configuration of the constellation set in hyperspace. The optimization of the constellation set is equivalent to find a subset selected from the grid set of a multi-dimensional densest lattice, for that the densest lattice occupies the minimum space for the same number of grid points compared with other lattice structures. Thus, for the same MMED, i.e d_{min}, the optimized constellation set, i.e. the MD-PAM, requires smaller occupancy in signal space, which is fenced by the actual physical quantities, e.g. the modulation amplitude or the signal power. Equivalently, with the same occupancy of the signal space, i.e. with the same maximum modulation amplitude or the power of the modulation signal, the densest lattice expands the MMED. As discussed before, the BER performance of a constellation is strongly related to the MMED, especially in the low noise regime, i.e. the high SNR regime. Therefore, the reshaping of MD constellations in hyperspace benefiting from the intrinsic geometric feature is expected to enhance the BER sensitivity.

However, compared with the design philosophy of MD formats for coherent detection systems, the one behind IM-DD systems is different. It is mainly because of the facts:

(1) The drive signal for a IM-DD system is positive, without containing phase information as the negative amplitude does, which leads to a half signal space.

(2) Non-FEC transmission schemes are widely adopted, especially for the high performance computing (HPC) applications, meaning that the channel is normally un-coded. Thus, the optimization priority should be given to the lower noise regime.

(3) The received signal is proportional to the incoming optical power rather than the amplitude. The criterion for optimization needs further modifications.

(4) Considerations on the trade-off between the sensitivity gain and the simplicity of transmitters are inevitable.

Basically, the minimum power and the minimum amplitude of the modulation signal are two major criteria of the optimization, i.e. the cost functions. The selection between these two options depends on the assumption of the signal modulation on vertical-cavity surface-emitting lasers (VCSELs). As shown in Fig. 4.3, for keeping the signal quality, the drive signal is applied in the linear regime according to the light-current (L-I) curve. However, the definition of the linear regime is normally ambiguous due to two major reasons.

(1) The linearity of output radio frequency (RF) signal is not exactly reflected on the static L-I curve which is characterized by a direct current (DC) signal. The nonlinear roll-off partly results from the temperature increase of in the active layer. However, the thermal relaxation of the lattice ($\sim \mu$s) is much slower than the modulation frequency ($\sim n$s, i.e. GHz). This implies that the linear regime may extend into the nonlinear

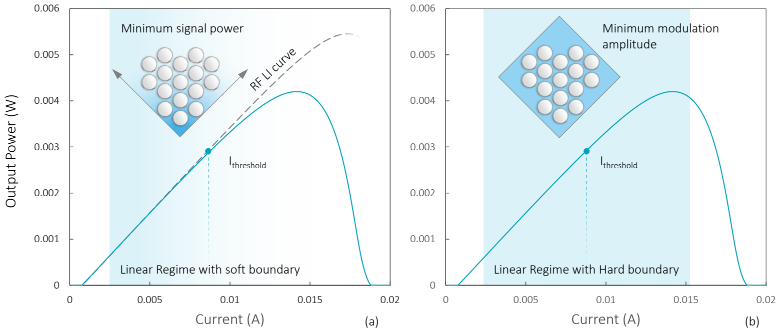

Figure 4.3: Schematics of two different modulation assumptions: (a) The modulation with the soft boundary, corresponding to the optimization with minimum signal power. (b) The modulation with the hard boundary, corresponding to the optimization with minimum modulation amplitude.

roll-off regime.

(2) As shown later, the peak-to-average power ratio (PAPR) of the MD-PAM optimized with the cost of minimum power is usually high, with high peaks of low occurrence. However, normally, VCSELs are tolerant for the occasional peaks cross the linear regime, even though it may impact on the lifetime in a long run.

Therefore, the cost function for the optimization process is different, depending on these facts and the actual operations of lasers.

The formats proposed in this chapter are designed based on these two criteria respectively, i.e. D$_4$TS-4 and E$_8$TS-4 using the minimum power and BB8 using the minimum amplitude.

4.3 Four- and eight-dimensional PAMs: D$_4$TS-4 and E$_8$TS-4

4.3.1 Optimization process

The actual optimization process in general with the cost of power is listed as following:

(1) Constructing the lattice grid with the corresponding dimension, i.e. list the coordinators as well as the square of norm of the grid points with a sufficient range.

(2) Selecting the positive half-space of the lattice grids and giving proper and necessary operations, i.e. translating, scaling and rotating, on the

lattice grids in the positive half-space.

(3) Sorting the list with respect to the power from small to large.

(4) Selecting first L points to minimize the total/average power.

(5) For extra points with the same power, selecting necessary ones according to the symmetry of the hyperspace.

(6) Obtaining the bit-to-symbol mapping scheme by using the modified Gray-mapping algorithm, similar to [59].

(7) Running Monte-Carlo simulation and checking the performance in the regime of interest.

(8) Repeating from step 2 until the results are satisfying.

4.3.2 Four-dimensional format: $\mathrm{D_4}$TS-4

$\mathrm{D_4}$TS-4 is designed based on the 4-D densest lattice, i.e. D_4. The lattice grids can analytically expressed as in [135]:

$$D_4 = \left\{ (x_i) \in \mathbb{Z}^4 : \sum_i x_i \equiv 0 \ (\mathrm{mod} 2) \right\} \tag{4.1}$$

The vertex diagram of D_4 is shown in Fig 4.4.(a). As a comparison, from a 4-D perspective, PAM-4 can be compared to the conventional PDM-16QAM in the dual-polarization coherent detection system, which geometrically occupies the corner of a hypercube, as all four levels can be chosen arbitrarily. Such 4-D lattice is known as Z_4.

Fig. 4.4.(b) illustrates the two-dimensional (2-D) facet, i.e. one 2-D projection of $\mathrm{D_4}$TS-4. The size of each circle indicates the probability of occurrence. The constellation has uneven probability, implying a more complicated geometric relation behind its low dimensional appearances. Such complicated intrinsic geometric dependency is also reflected by the uneven distribution of the amplitude in each regular symbol. Concretely, symbols for each dimension of $\mathrm{D_4}$TS-4 have 6 levels, which shown as the histogram in Fig. 4.4.(c). Due to the intrinsic feature of D_4, theoretically, $\mathrm{D_4}$TS- offers a 1.01 dB asymptotic improvement of sensitivity compared with PAM-4, if the signal is modulated with the same peak-to-peak amplitude.

4.3.3 Eight-dimensional format: $\mathrm{E_8}$TS-4

$\mathrm{E_8}$TS-4 relies on the densest geometry of the so-called E_8 lattice, which can be expressed analytically as in Eq. 4.2. The vertex diagram of E_8 is shown in Fig 4.5.(a).The 2-D appearance of $\mathrm{E_8}$TS-4 is shown in Fig. 4.5.(b).

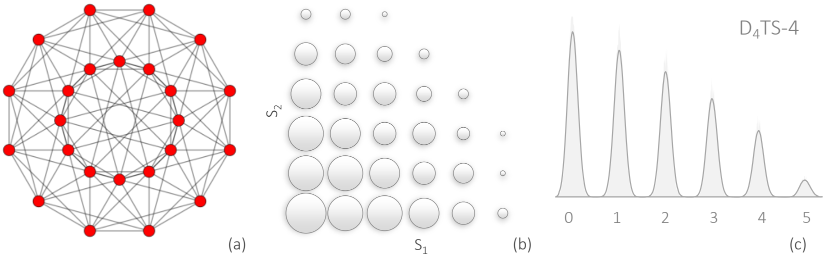

Figure 4.4: D$_4$Ts-4. (a) Vertex diagram of D_4 lattice. (Imaging source: [135]) (b) The virtual 2-D projections of D$_4$TS-4 consisting of two symbols. Size of each dot indicates the probability. (c) Histogram of 6-level D_4 with un-even distribution.

The mutual distance looks shorter and whole constellation seems denser. However, the actual MMED in 8-D space is larger, which leading to an asymptotic increase by 1.98 dB, compared with PAM-4 with the same peak-to-peak modulation amplitude.

The optimization process for E$_8$TS-4 is similar to the one for D$_4$Ts-4. The results of the optimal selection shows a 16-level unevenly distributed amplitude structure in each regular symbol as the histogram in Fig. 4.5.(c), with the reduced complexity at the cost of a sensitivity penalty from the optimal structure.

$$E_8 = \left\{ (x_i) \in \mathbb{Z}^8 \cup (\mathbb{Z} + 1/2)^8 : \sum_i x_i \equiv 0 \ (\text{mod}2) \right\} \tag{4.2}$$

4.3.4 Mapping, de-mapping and decision

Due to the complicated structure of the constellation configuration, the modulation and demodulation become tedious. The bit-to-symbol mapping and the symbol-to-bit de-mapping are based on the bit-symbol relation obtained from a heuristic algorithm, where no further clear and deterministic geometric relation can be utilized to further simplify the modulations. Here we adopt a look-up table (LUT) for the mapping and de-mapping.

For decisions, as the lower dimensional projections contain more complicated dependence, simple hard decisions are not applicable in this case. We use the minimum mean square error (MMSE) based SD. It is worth

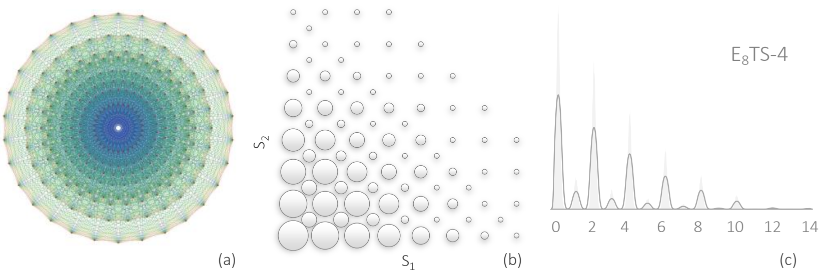

Figure 4.5: E_8Ts-4. (a) Vertex diagram of E_8 lattice. (Imaging source: [136]) (b) The virtual 2-D projections of E_8TS-4 consisting of two symbols. Size of each dot indicates the probability. (c) Histogram of 16-level E_8 with un-even distribution.

mentioning that for the fairness of comparison, we applied such decision scheme to all formats to be compared, including the simple PAM-4, with the corresponding dimensions.

4.3.5 Numerical setups

For setting up the numerical analysis on D_4Ts-4 and E_8TS-4, a 2^{15}-bit pseudo random bit sequence (PRBS) at 50 Gbit/s was generated and extended by repeating the section to form a transmitting sequence 2^{20} bits. Every two bits were combined into a regular symbol and every four conventional symbols were loaded into a super-symbol. The super-symbol sequence was mapped to a three-channel bit sequence and converted into a 6-level signal via a digital-to-analog converter (DAC). Imperfections of drive integrated circuit (IC) (e.g. bandwidth and noise) were considered. A VCSEL was used as light source, biased at 10 mA and modulated by modulation signal with peak-to-peak amplitude of 0.5 V. The properties (e.g. bandwidth, thermal effects) of laser were characterized by L-I curves, shown in Fig. 4.6.(a) and S_{21} curves 4.6.(b). The signal propagation on standard single-mode-fiber (SSMF) was simulated with the software kit: SSPROP from the University of Maryland, using the parameters as: α=0.2 dB/km, D=17 ps/(nm·km), γ=1.317 (1/W·km). The properties of photodiode was modeled in similar method to [195], with parameters R=0.4 W/A, T=298 K, F_n=5 dB, R_L=50 Ω, RIN=-155 dB/Hz. For more detailed parameters, also see Tab. 4.1. A Gaussian matched filter was used to improve the performance after sampling. The diagram of simulation

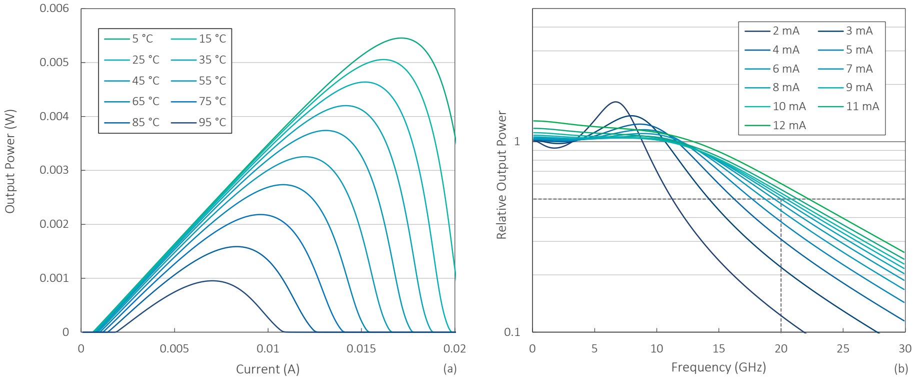

Figure 4.6: Simulation results of VCSELs for numerical investigations: (a) L-I-V curve of the simulated VCSEL under different ambient temperature. (b) S_{21} response of the simulated VCSEL varying with various bias current.

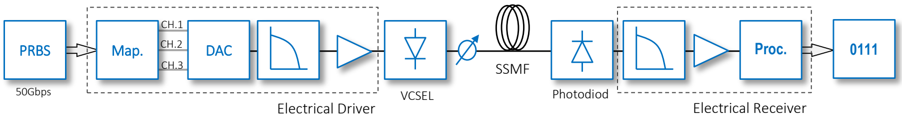

Figure 4.7: Numerical setups for performance measurements between PAM-4, D_4TS-4 and E_8TS-4.

blocks are shown in Fig. 4.7. After pre-processing (e.g. re-sampling, centralization, normalization, sequence alignment), signal was de-mapped by MMSE algorithm and sent to bit error rate (BER) evaluation. Simulation on E_8TS-4 is similar, but with a modified HD based de-mapping algorithm, since MMSE is no more practical for such too many candidate points in 8-D format.

4.3.6 Numerical results

Optical back-to-back

As shown in Fig. 4.8, D_4TS-4 and PAM-4 perform similarly at required BER=3.8×10^{-3} for 7% hard-decision feed-forward error correction (HD-FEC). Yet, the former outperforms by 1 dB asymptotically when increasing optical power and earns 0.9 dB at the required BER at 1×10^{-6},

Table 4.1: The parameters in the simulation for comparison between D_4Ts-4, E_8TS-4 and PAM-4.

Parameter	**Symbol**	**Value**	**Unit**
PRBS length	-	2^{15}	-
Symbol rate	-	25	Gbaud
Bit rate	-	50	Gbit/s
Driver SNR	-	30	dB
Driver Rising time	-	0.3	UI
Bias current	I_{bias}	10	mA
Modulation amplitude	V_{pp}	0.5	V
Laser 3 dB bandwidth	$f_{-3\ dB}$	20	GHz
Laser wavelength	λ	1550	nm
Laser RIN density		-145	dB/Hz
Fiber type	-	SSMF	-
Fiber attenuation coff.	α	0.2	dB/km
Fiber dispersion coff.	D	17	ps/(nm·km)
Fiber effective nonlinearity coff.	γ	1.317	1/W·km
Fiber length	L	0-10	km
PD Responsivity	R	0.4	W/A
Amplifier noise figure	F_n	5	dB
Load resistance	R_L	50	Ω
Ambient temperature	T	20-100	°C

where the simulation accuracy is just guaranteed, compared with even further 1 dB improvement earned by E_8TS-4 at cost of increased complexity. The summary of the results are shown in Tab. 4.3.

Extension of reach using D_4TS-4

The benefit of the extended transmission length over SSMF with D_4TS-4 is illustrated in Fig. 4.9. Under the required BER=1×10^{-6} for the uncoded, non-dispersion compensated channel, a 2-km-extension is achieved by using D_4TS-4 when the received optical power is fixed at -12 dBm. We can also assume the optical back-to-back (OBTB) BER difference remains approximately constant when power increasing. Therefore, from the curve in Fig. 4.9, an reach extension of 3 km remains in the short-reach regime when the optical launch power is higher than -12 dBm. Such reach benefit

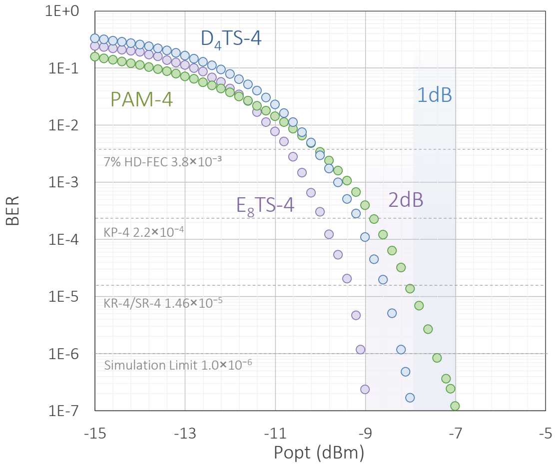

Figure 4.8: Numerical results for optical back-to-back BER sensitivity with D_4TS-4 (azure), E_8TS-4 (lavender) PAM-4 (lemon grass) in 25 GBaud data-links.

Table 4.2: The comparison between D_4Ts-4, E_8TS-4 and PAM-4 in terms of the optical back-to-back performance with the required optical power (unit dBm).

FEC threshold	**PAM-4**	**D_4TS-4**	$\Delta_{D_4TS/PAM}$	**E_8TS-4**	$\Delta_{E_8TS/PAM}$
7% HD-FEC	-10.1	-10.2	0.1	-10.7	0.6
KP-4	-8.8	-9.2	0.4	-10.0	1.2
KR-4/SR-4	-8.1	-8.6	0.5	-9.4	1.3
Asymptotic	-7.0	-7.9	0.9	-8.8	1.8

is an interesting feature for short-reach applications (i.e. from ∼m to ∼km).

Enhanced tolerance for thermal degradation using D_4TS-4

The BER performance under different room temperatures with -12 dBm launch power and the ideal transmission condition is shown in Fig. 4.10.(a). For required BER at 1×10^{-6}, D_4TS-4 gives a wider operational range of temperature. Meanwhile, the new formats are proven more tolerant for thermal effects on VCSELs when the temperature increase is limited as in Fig. 4.10.(b). The system parameters, e.g. launch power, are set to meet BER requirement at 1×10^{-6} while the room temperature is set to 20 °C.

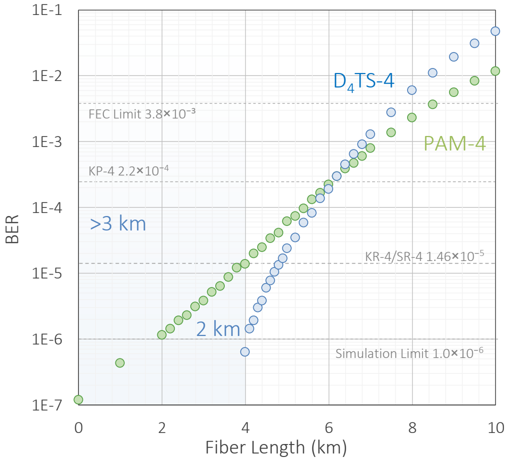

Figure 4.9: Numerical results for BER v.s transmission distance with D_4TS-4 and PAM-4 with increasing transmission length up to 10 km.

The BER degradation is recorded with the fixed parameter setting while increasing temperature for emulating thermal effects. A penalty of thermal tolerance can be observed up to 18 °C at the low noise regime. Such benefit vanishes when the increased temperature is over 30 °C. The thermal effects of laser and photodiode generate extra noise, which counteract the benefits gained from the densest structure. The clipping effects of VCSEL also generate additional degradations of the tighter arranged formats. However, an approximate 20 °C temperature variation can be treated as sufficient for most application scenarios, especially the temperature controlled systems.

4.3.7 Summary

Two modulation formats based on 4-D and 8-D densest lattice used in short-reach interconnections are proposed and investigated numerically. In the optical back-to-back measurement of un-coded 25 GBaud/s links, D_4TS-4 and E_8TS-4 outperform PAM4 when the received optical power is higher than -10 dBm and gain 1 dB and 2 dB asymptotic sensitivity improvement respectively. Under the same BER requirement, i.e. 10^{-6}, D_4TS-4 earns a 3-km-extension of reach and tolerance of 18 °C for thermal effects.

The potential benefits of these formats lay in the facts: (i) the low latencies from the non-redundant un-coded schemes; (ii) reach extensions

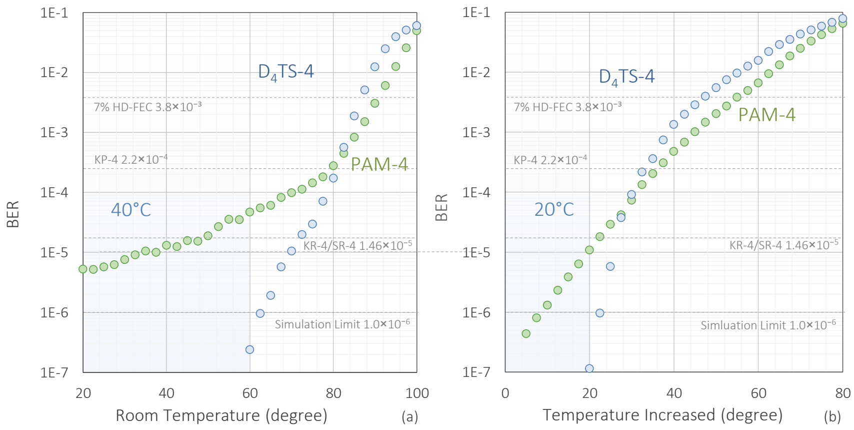

Figure 4.10: Numerical results for the thermal tolerance with D$_4$TS-4 and PAM-4. (a) BER v.s. room temperatures with D$_4$TS-4 and PAM-4. (b) BER v.s. temperature variation up to 80 °C with D$_4$TS-4 and PAM-4, with optimal system settings at room temperature = 20 °C.

at the same conditions; (iii) the higher stability from the higher tolerance for thermal effects and distortion; (iv) the lower power consumption because of higher sensitivity or power efficiency.

However, the drawbacks are also obvious: (i) the complex constellation structure leads to the unrealistic modulation and demodulation; (ii) the asymmetric configuration results in an inevitable LUT modulation scheme and further increases the latencies; (iii) the unevenly distributed amplitude level results in difficulties in the time recovery at the receiver side; (iv) ...

Due to all the limits, it is necessary to shift to a different designing paradigm, leading to a more practical version of the eight-dimensional PAM. It is discussed in the next section.

4.4 Simplified eight-dimensional PAM: BB8

In spite of the theoretical benefit, the practical implementation of the above mentioned MD formats is not straightforward due to the unrealistic bit-to-symbol mapping. LUTs may be a feasible solution for the MD formats with small-scale constellations in the cost tolerant applications, such as long-haul coherent systems. However, for the highly latency- and cost-sensitive short-reach data links, e.g. the rack-to-rack interconnects and the active optical cable (AOC)s for supercomputers, such modulation formats are no more

Table 4.3: The comparisons between D_4Ts-4 and PAM-4 in terms of the reach extension (unit m) and the enhanced tolerance for thermal degradations (unit °C).

	PAM-4	**D_4TS-4**	Δ	Δ (%)
Reach @ 7 % HD-FEC (km)	8.5	7.8	-0.7	-8.3%
Reach @ KP-4 (km)	6.2	6.2	0.0	0.0%
Reach @ KR-4/SR-4 (km)	4.0	4.8	0.8	20%
Reach @ Asymptotic (km)	2.0	4.0	2.0	100%
Temperature @ 7 % HD-FEC (°C)	90	87	-3	-3.3%
Temperature @ KP-4 (°C)	80	81	1	1.25%
Temperature @ KR-4/SR-4 (°C)	50	72	22	44%
Temperature @ Asymptotic (°C)	n.a.	60	n.a.	n.a.
Temp. Var. @ 7 % HD-FEC (°C)	55	48	-7	-12.7%
Temp. Var. @ KP-4 (°C)	36	32	-4	-11.1%
Temp. Var. @ KR-4/SR-4 (°C)	22	26	4	18.2%
Temp. Var. @ Asymptotic (°C)	10	22	12	120%

practical. In this section, we propose a *block based eight-dimensional/eight-level* PAM, named as **BB8**. Based on its symmetric intrinsic geometry, a specially designed simplified bit-to-symbol algorithm is proposed, which enables the symbol-wise modulation. It is expected to enable the real-time bit-to-symbol mapping and its corresponding de-mapping.

Like E_8TS-4, BB8 roots in the eight-dimensional densest lattice, i.e. E_8. Yet, BB8 stems from a different assumption of modulations, that the linear modulation regime is rigorously constrained, namely hard boundary as shown in Fig. 4.3.(b), rather than the soft boundary, as in Fig. 4.3.(a), where D_4TS-4 and E_8TS-4 are based on. In such assumption, the signal space is limited within a fixed-size eight-dimensional hypercube, instead of an open positive-half space, where the format sets $\mathbf{C}_{BB8}$ (or simply $\mathbf{C}$, for concise expressions) can select from. Therefore, the construction of BB8 equals to searching and selecting a subset from E_8 lattice grids within a fixed-size eight-dimensional hypercube. Such subset has the maximum d_{min} and an optimal orientation, offering the simplest level structure in each symbol.

4.4.1 Geometry

BB8 has 8 equally probable amplitude levels. The format point set $\mathbf{C}$ is defined in Eq. 4.3:

$$\mathbf{C} = \left\{ (c^i) \in \mathbf{U}_e^8 \cup \mathbf{U}_o^8 : \sum_i c^i \equiv 0 \ (\mathrm{mod} 4) \right\} \tag{4.3}$$

where c^i is the amplitude of each symbol, $i = 0, 1, \cdots, 7$ is the position of individual symbol in a super-symbol.[1] $\mathbf{U} \subset \mathbb{Z}$ indicates the alphabet of symbols, namely a discrete set where the amplitude of each symbol can be chosen from. Superscript n indicates the dimensionality of the super-symbol, here obviously $n = 8$, and the subscripts, e and o, bipartition the alphabet into *even* and *odd* subsets, namely $\mathbf{U} = \mathbf{U}_e \cup \mathbf{U}_o$ and $\mathbf{U}_e \cap \mathbf{U}_o = \emptyset$, where $\mathbf{U}_e \in \{0\,,2\,,4\,,6\}$ and $\mathbf{U}_o \in \{1\,,3\,,5\,,7\}$ are corresponding alphabets.

It is also obvious that $\mathbf{C} \subset \mathbf{L}_{E_8}$, in which $\mathbf{L}_{E_8}$ is the whole set of the lattice grids of E_8.

Subgroups

We can use the representation of 2-D projections, i.e. 2-D facets, to better understand the format structure in an 8-D space. As shown in Fig. 4.11, an 8-D super-symbol forms four 2-D projections by artificially projecting every two vector components, i.e. regular symbols, in one constellation diagram. Without loss of generality, we define the projections as $\mathbf{P}_j = [\,c^{2j}\ \ c^{2j+1}\,]^{\mathrm{T}}, \forall j \in \{0,\ 1,\ 2,\ 3\}$ with a symbol-wise sequence. Thus, the constellation set $\mathbf{C} = \{\ [\ \mathbf{P}_0\ \mathbf{P}_1\ \mathbf{P}_2\ \mathbf{P}_3\ ]^{\mathrm{T}}\ \}$.

According to the expression in Eq. 4.3, the set of format $\mathbf{C}$ is divided into two independent subsets, i.e. even and odd subsets, with the expression Eq. 4.4 and Eq. 4.5.

$$\mathbf{C}_e = \left\{ (c^i) \in \mathbf{U}_e^8 : \sum_i c^i \equiv 0 (\mathrm{mod} 2) \right\} \tag{4.4}$$

$$\mathbf{C}_o = \left\{ (c^i) \in \mathbf{U}_o^8 : \sum_i c^i \equiv 0 (\mathrm{mod} 2) \right\} \tag{4.5}$$

---

[1] Note that we use c^i instead of c_l^i, omitting the subscript l, to keep the generality.

Format points in each projection $\mathbf{P}_j$ are then divided into four sub-groups sub-group (SG), as express in Eq. 4.6 - Eq. 4.9.

$$\boldsymbol{\Theta} = \left\{\mathbf{P}_j \in \mathbf{U}_e^2 : c^{2j} + c^{2j+1} \equiv 0 \ (\mathrm{mod}4)\right\} \tag{4.6}$$

$$\boldsymbol{\Omega} = \left\{\mathbf{P}_j \in \mathbf{U}_e^2 : c^{2j} + c^{2j+1} \equiv 1 \ (\mathrm{mod}4)\right\} \tag{4.7}$$

$$\boldsymbol{\Phi} = \left\{\mathbf{P}_j \in \mathbf{U}_o^2 : c^{2j} + c^{2j+1} - 1 \equiv 0 \ (\mathrm{mod}4)\right\} \tag{4.8}$$

$$\boldsymbol{\Psi} = \left\{\mathbf{P}_j \in \mathbf{U}_o^2 : c^{2j} + c^{2j+1} - 1 \equiv 1 \ (\mathrm{mod}4)\right\} \tag{4.9}$$

in which $\forall j \in \{0, 1, 2, 3\}$. Like in Fig. 4.11, these sub-groups are represented by points of four different colors. The even subset is constructed with a conditional combination of pairs in $\boldsymbol{\Theta}$ and $\boldsymbol{\Omega}$, following:

$$\mathbf{C}_e = \left\{ [\, \mathbf{P}_0 \, \mathbf{P}_1 \, \mathbf{P}_2 \, \mathbf{P}_3 \,]^{\mathrm{T}} \;\middle|\; \pi_j = \begin{cases} 0 & \mathbf{P}_j \in \boldsymbol{\Theta} \\ 1 & \mathbf{P}_j \in \boldsymbol{\Omega} \end{cases}, \sum_{j=0}^{3} \pi_j \equiv 0 \, (\mathrm{mod}2) \right\} \tag{4.10}$$

Correspondingly, the odd subset is constructed with a conditional combination following:

$$\mathbf{C}_o = \left\{ [\, \mathbf{P}_0 \, \mathbf{P}_1 \, \mathbf{P}_2 \, \mathbf{P}_3 \,]^{\mathrm{T}} \;\middle|\; \pi_j = \begin{cases} 0 & \mathbf{P}_j \in \boldsymbol{\Phi} \\ 1 & \mathbf{P}_j \in \boldsymbol{\Psi} \end{cases}, \sum_{j=0}^{3} \pi_j \equiv 0 \, (\mathrm{mod}2) \right\} \tag{4.11}$$

Note that the concept of sub-groups is based on the 2-D visualization, which is constructed for the convenience of understanding. It implies that the selections of the sub-groups depend on the concrete projections, rather than an absolute division in the hyperspace. More intuitively, the possible combinations are listed in Tab. 4.4. There are 16 different combinations of the point from the sub-groups.

Hierarchy of subsets

For a more rigorous analysis, we formalize a hierarchy of the orthogonal set division, also known as set bipartition or set-partitioning [170, 171, 196], in the eight-dimensional hyperspace. Note that even though it uses the sub-group language, such hierarchy is absolute, i.e. not dependent on specific representations.

We define the hierarchy of constellation set $\mathbf{C}$ with the subscript $\boldsymbol{\Upsilon}_\sigma$, $\boldsymbol{\Upsilon}_\sigma \in \boldsymbol{\Upsilon}$, into subsets $\mathbf{C}_{\boldsymbol{\Upsilon}_\sigma}$, in which $\boldsymbol{\Upsilon} = \{\boldsymbol{\Upsilon}_0, \boldsymbol{\Upsilon}_1, \cdots, \boldsymbol{\Upsilon}_\sigma, \cdots, \boldsymbol{\Upsilon}_{15}\}$.

Table 4.4: The combination of the sub-groups for constructing BB8.

$\mathbf{C}_e$	$\mathbf{C}_o$
$\boldsymbol{\Theta}\ \boldsymbol{\Theta}\ \boldsymbol{\Theta}\ \boldsymbol{\Theta}$	$\boldsymbol{\Phi}\ \boldsymbol{\Phi}\ \boldsymbol{\Phi}\ \boldsymbol{\Phi}$
$\boldsymbol{\Theta}\ \boldsymbol{\Theta}\ \boldsymbol{\Omega}\ \boldsymbol{\Omega}$	$\boldsymbol{\Phi}\ \boldsymbol{\Phi}\ \boldsymbol{\Psi}\ \boldsymbol{\Psi}$
$\boldsymbol{\Theta}\ \boldsymbol{\Omega}\ \boldsymbol{\Theta}\ \boldsymbol{\Omega}$	$\boldsymbol{\Phi}\ \boldsymbol{\Psi}\ \boldsymbol{\Phi}\ \boldsymbol{\Psi}$
$\boldsymbol{\Theta}\ \boldsymbol{\Omega}\ \boldsymbol{\Omega}\ \boldsymbol{\Theta}$	$\boldsymbol{\Phi}\ \boldsymbol{\Psi}\ \boldsymbol{\Psi}\ \boldsymbol{\Phi}$
$\boldsymbol{\Omega}\ \boldsymbol{\Theta}\ \boldsymbol{\Theta}\ \boldsymbol{\Omega}$	$\boldsymbol{\Psi}\ \boldsymbol{\Phi}\ \boldsymbol{\Phi}\ \boldsymbol{\Psi}$
$\boldsymbol{\Omega}\ \boldsymbol{\Theta}\ \boldsymbol{\Omega}\ \boldsymbol{\Theta}$	$\boldsymbol{\Psi}\ \boldsymbol{\Phi}\ \boldsymbol{\Psi}\ \boldsymbol{\Phi}$
$\boldsymbol{\Omega}\ \boldsymbol{\Omega}\ \boldsymbol{\Theta}\ \boldsymbol{\Theta}$	$\boldsymbol{\Psi}\ \boldsymbol{\Psi}\ \boldsymbol{\Phi}\ \boldsymbol{\Phi}$
$\boldsymbol{\Omega}\ \boldsymbol{\Omega}\ \boldsymbol{\Omega}\ \boldsymbol{\Omega}$	$\boldsymbol{\Psi}\ \boldsymbol{\Psi}\ \boldsymbol{\Psi}\ \boldsymbol{\Psi}$

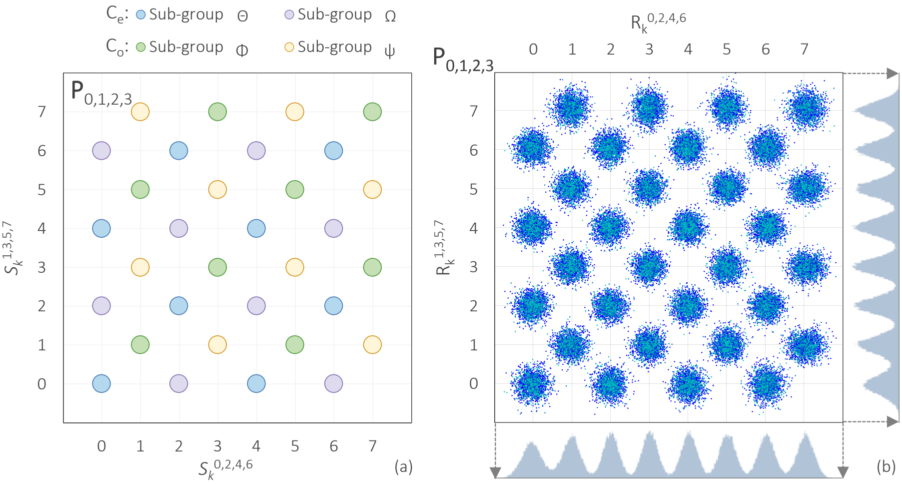

Figure 4.11: BB8 illustrated with aids of 2D projection in constellation diagram: (a) the illustration of the sub-groups $\boldsymbol{\Theta}$ and $\boldsymbol{\Omega}$ in the subset $\mathbf{C}_e$, $\boldsymbol{\Phi}$ and $\boldsymbol{\Psi}$ in the subset $\mathbf{C}_o$ on two-dimensional projections; (b) Experimentally measured symbol histogram and its 2-D projection.

$\mathbf{C}$ is divided uniquely into $\mathbf{C}_{\boldsymbol{\Upsilon}_\sigma}$, which follows:

$$\mathbf{C} = \bigcup_{\sigma=0}^{15} \mathbf{C}_{\Upsilon_\sigma}, \bigcap_{\sigma=0}^{15} \mathbf{C}_{\Upsilon_\sigma} = \emptyset \tag{4.12}$$

For each $\boldsymbol{\Upsilon}_\sigma = \left[\ \upsilon_\sigma^0\ \upsilon_\sigma^1\ \upsilon_\sigma^2\ \upsilon_\sigma^3\ \right]$, components $\upsilon_\sigma^j \in \{\,0,\ 1\,\}\,, \forall j \in \{\ 0,\ 1,\ 2,\ 3\ \}$, give the divisions on the j-th level. Therefore, the hierarchical division is expressed formally as in Eq. 4.13-Eq. 4.17.

$$\mathbf{Q}_0 = \begin{cases} \boldsymbol{\Theta} & \upsilon_\sigma^0 = 0 \\ \boldsymbol{\Phi} & \upsilon_\sigma^0 = 1 \end{cases}, \mathbf{Q}_1 = \begin{cases} \boldsymbol{\Omega} & \upsilon_\sigma^0 = 0 \\ \boldsymbol{\Psi} & \upsilon_\sigma^0 = 1 \end{cases}, \tag{4.13}$$

$$\mathbf{P}_0 \in \begin{cases} \mathbf{Q}_0 & \upsilon_\sigma^1 = 0 \\ \mathbf{Q}_1 & \upsilon_\sigma^1 = 1 \end{cases}, \tag{4.14}$$

$$\mathbf{P}_1 \in \begin{cases} \mathbf{Q}_0 & \upsilon_\sigma^2 = 0 \\ \mathbf{Q}_1 & \upsilon_\sigma^2 = 1 \end{cases}, \tag{4.15}$$

$$\mathbf{P}_2 \in \begin{cases} \mathbf{Q}_0 & \upsilon_\sigma^3 = 0 \\ \mathbf{Q}_1 & \upsilon_\sigma^3 = 1 \end{cases}, \tag{4.16}$$

$$\mathbf{P}_3 \in \begin{cases} \mathbf{Q}_0 & \upsilon_\sigma^1 \oplus \upsilon_\sigma^2 \oplus \upsilon_\sigma^3 = 0 \\ \mathbf{Q}_1 & \upsilon_\sigma^1 \oplus \upsilon_\sigma^2 \oplus \upsilon_\sigma^3 = 1 \end{cases} \tag{4.17}$$

The relation between the indices and the hierarchical structure is intuitively presented in Fig 4.12. A more rigorous formalization of the hierarchical set partitioning is going to be given in later chapter when discussing the rate flexible PAM.

Features

BB8 carries 2 bits per symbol, with the same spectral efficiency (SE) as PAM-4. Therefore the format set **C** has $4^8 = 65536$ points. The MMED of neighboring points reaches $d_{min} = 2\sqrt{2}$. Theoretically, BB8 has an asymptotic power efficiency (APE) -1.18 dB, with a gain of 2.8 dB compared to PAM-4. Similar, the constellation figure of merit (CFM) of BB8 reaches -1.18 dB with a gap of 2.8 dB outperforming its PAM-m counterparts. Practically, with the same maximum peak-to-peak modulation amplitude, the benefit is reduced to ∼1.5 dB.

Numerical results

A theoretical Monte-Carlo simulation is made based on AWGN assumption applied on the ideal constellations. Note that the simulation here only places emphasis on the theoretical performance on the constellation. No

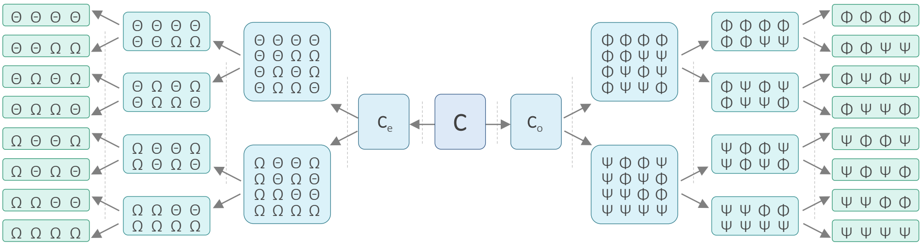

Figure 4.12: The hierarchy of BB8 subgroups.

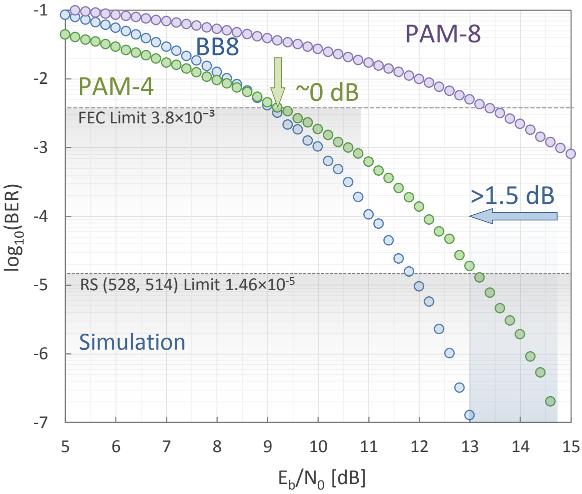

Figure 4.13: Theoretical Monte-Carlo simulations of BB8 (azure), PAM-4 (lemon grass), and PAM-8 (lavender) with varying signal-to-noise ratio.

extra actual physical factors are taken into account. The results are shown in the Fig. 4.13. The signal-to-noise ratio is given with respect to the received electrical signal. From the results, it is clear that PAM-4 and BB8 have an intersection point around the standard 7% FEC limit with required BER $\approx 3.8 \times 10^{-3}$. For low noise regime, BB8 outperforms PAM-4 and approaches the asymptotic gain larger than 1.5 dB.

4.4.2 Bit-to-symbol mapping

In spite of the theoretical benefit, the practical implementation of MD formats is not straightforward due to the indirect bit-to-symbol mapping. LUTs is a feasible solution for MD modulations with small scale constellations in coherent transmission systems. However, it cannot be applied for the highly latency- and cost-sensitive short-reach data links. A specially designed simplified bit-to-symbol algorithm is proposed in the following section. It is expected to enable the real-time bit-to-symbol mapping, and its corresponding de-mapping.

Formally, the input bit stream, $\mathbf{B}$, is first divided into bit blocks, $\mathbf{B}_k$, as $\mathbf{B} = [\ \mathbf{B}_0\ \mathbf{B}_1\ \cdots\ \mathbf{B}_k\ \cdots\ ]^{\mathrm{T}}$. For each input bit block $\mathbf{B}_k = [\ b_k^0\ b_k^1\ \cdots b_k^e\ \cdots\ b_k^{15}\ ]^{\mathrm{T}}$ and the mapped regular symbol sequence $\mathbf{S}_k = [S_k^0\ S_k^1\ \cdots\ S_k^i\ \cdots\ S_k^7]^{\mathrm{T}}$, a bit-to-symbol mapping is defined as, $\mathcal{M}\ :\ \mathbf{F}_2^{16} \rightarrow \mathbb{R}^8$ and the corresponding symbol-to-bit de-mapping is $\mathcal{M}^{-1}\ :\ \mathbb{R}^8 \rightarrow \mathbf{F}_2^{16}$. $\mathbf{F}_2^{16}$ means the 16-dimensional binary field. The superscript e indicates the position of the individual bit in $\mathbf{B}_k$. The simplified mapping algorithm is expressed as in Eq. 4.18 - Eq. 4.25, $\mathcal{M}$:

$$S_k^0 = b_k^0 + 2b_k^1 + 4b_k^2 \tag{4.18}$$

$$S_k^1 = b_k^0 + 2b_k^3 + 4b_k^4 \tag{4.19}$$

$$S_k^2 = b_k^0 + 2b_k^5 + 4b_k^6 \tag{4.20}$$

$$S_k^3 = b_k^0 + 2b_k^7 + 4b_k^8 \tag{4.21}$$

$$S_k^4 = b_k^0 + 2b_k^9 + 4b_k^{10} \tag{4.22}$$

$$S_k^5 = b_k^0 + 2b_k^{11} + 4b_k^{12} \tag{4.23}$$

$$S_k^6 = b_k^0 + 2b_k^{13} + 4b_k^{14} \tag{4.24}$$

$$S_k^7 = b_k^0 + 2P_k + 4b_k^{15} \tag{4.25}$$

$$P_k = b_k^1 \oplus b_k^3 \oplus b_k^5 \oplus b_k^7 \oplus b_k^9 \oplus b_k^{11} \oplus b_k^{13} \tag{4.26}$$

In the mapping stage, every 16 bits are mapped into one 8-symbol super-symbol, with each symbol modulated into eight levels. The first bit (b_k^0) controls the selection of the candidate points from the even subsets (when $b_k^0 = 0$) or from odd ones (when $b_k^0 = 1$). Bits $b_k^1 ... b_k^{14}$ are simply mapped as PAM-4. It is noteworthy that they are not Gray mapped, since Gray mapping is not optimal in an 8-D perspective. The last symbol is generated from bits b_k^0, b_k^{15} and a parity bit, P_k, which is calculated according to Eq. 4.26.

The merits of such bit-to-symbol mapping include: (i) minimizing the alteration from conventional PAM-4 mapping and therefore reducing the cost of IC design and implementation; (ii) minimizing extra computational resources required, as only additional calculation of parity bit P_k is needed;

(iii) enabling real-time solution with lower latency relative to the other mapping schemes, e.g. LUT.

4.4.3 Symbol-to-bit de-mapping

The corresponding de-mapping algorithm is then written as:

$$\widehat{b}_k^0 = \mathrm{mod}(\widehat{R}_k^{0-7}, 2) \tag{4.27}$$

$$\widehat{b}_k^1 = \mathrm{mod}((\widehat{R}_k^0 - \widehat{b}_k^0)/2, 2) \tag{4.28}$$

$$\widehat{b}_k^2 = \mathrm{mod}((\widehat{R}_k^0 - \widehat{b}_k^0)/4, 2) \tag{4.29}$$

$$\dots$$

$$\widehat{b}_k^{13} = \mathrm{mod}((\widehat{R}_k^6 - \widehat{b}_k^0)/2, 2) \tag{4.30}$$

$$\widehat{b}_k^{14} = \mathrm{mod}((\widehat{R}_k^6 - \widehat{b}_k^0)/4, 2) \tag{4.31}$$

$$\widehat{b}_k^{15} = \mathrm{mod}((\widehat{R}_k^7 - \widehat{b}_k^0)/2, 2) \tag{4.32}$$

in which, $\widehat{R}_k^{0-7}$ means an arbitrary symbol from $\widehat{R}_k^0$ to $\widehat{R}_k^7$. During the de-mapping phase, a 16-bit block is recovered from one super-symbol, i.e. 8 received and aligned symbols. The first bit $\widehat{R}_k^0$ is decoded according to the parity of the subset that the received super-symbol belongs to, i.e. either even subset (when $\widehat{R}_k^{0-7}$ is even, $\widehat{b}_k^0 = 0$) or odd subset (when $\widehat{R}_k^{0-7}$ is odd, $\widehat{b}_k^0 = 1$). Then, the symbols $\widehat{R}_k^{0-7}$ are shifted, i.e. subtracted by $\widehat{b}_k^0$, as described by Eq. 11-16. After doing that, $\widehat{R}_k^{0-7}$ are degenerated from PAM-8 into PAM-4 signal. The remaining bits $\widehat{b}_k^1 ... \widehat{b}_k^{15}$ are simply calculated from $\widehat{R}_k^{0-7}$ with PAM-4 de-mapper. The parity bit (P_k) is not used during the de-mapping and therefore discarded.

4.4.4 Hyper-space based hard decision

A maximum likelihood (ML) SD algorithm is used in coherent MD modulation systems. It is combined with forward error correction (FEC) to maximize the achievable data rate [61]. However, considering the computational complexity, it is unrealistic to apply ML-SD to the 8-D modulation. It would be overloaded by the number of possible states. In this work we propose a hyperspace based hard decision (HS-HD) algorithm.

A lattice is filled with primitive cells, the smallest symmetric units. All positions inside the cell are closer to the center than to the rest of the lattice.

Hence, the central lattice point in each primitive cell gives a decided symbol. All received symbols in one primitive cell have the same decision. We can separate an 8-D primitive cell by determining all the perpendicular bisecting hyperplanes between the neighbors, as shown in Fig. 4.14. The perpendicular bisecting hyperplane is also seen as the decision threshold hyperplane. Generally, the (n-1)-dimensional boundaries of primitive cells work as hard-decision thresholds in an n-dimensional signal space. Hence, 7-dimensional hyperplanes $\mathbf{H}$ ($\mathbf{H} = \left\{\mathbf{x} \in \mathbb{R}^8 \mid \mathbf{a}^{\mathrm{T}}\mathbf{x} = d\right\}, \mathbf{a} = (a_1, a_1, \cdots, a_8)^{\mathrm{T}}$) divide the 8-D signal space into cells of symbols. Here $\mathbf{x}$ represents the points on the hyperplane and $\mathbf{a}$ is its normal vector.

We use a 2-D honeycomb (A_2 lattice) as the analog of the E_8 lattice to illustrate the principle of the algorithm (Fig. 4.14). Generally, the normal vector of the threshold plane between the j-th lattice point $\mathbf{l}_j \in \mathbf{L}$ and its z-th neighbor $\mathbf{l}_j^z \in \mathbf{L}$ is expressed as $\mathbf{a}^z = \mathbf{l}_j^z - \mathbf{l}_j$, where $\mathbf{L}$ is the set of the whole lattice. The unit normal vector is then given as $\mathbf{a}_0^z = \mathbf{a}^z / d_{min}$. The perpendicular bisector of the line connecting these two points is described as $\mathbf{P} = \mathbf{l}_j + \mathbf{a}^z/2$. The hyperplane function is written as $(\mathbf{a}_0^z)^{\mathrm{T}}\mathbf{x} = d$, in which $d = (\mathbf{a}_0^z)^{\mathrm{T}}\mathbf{P} = (\mathbf{a}_0^z)^{\mathrm{T}}(\mathbf{l}_j + \mathbf{a}^z/2) = D_j^z + d_{min}/2$. Here, d is the characteristic number, which equals to the perpendicular distance between the decision plane and the origin of the coordinate; it consists of $d_{min}/2$, half of the MMED, and D_j^z, the perpendicular distance from the origin of the coordinate to the hyperplane containing $\mathbf{l}_j$. $D_j^z \in \mathbf{D}^z$ is inherent for a specific lattice structure. $\mathbf{D}^z = (\mathbf{a}_0^z)^{\mathrm{T}}\mathbf{L}$ is the set of all possible D_j^z. Normally, due to the symmetry of the lattice, $\mathbf{D}^z$ degenerates to a smaller discrete set. It is evident that $\mathbf{D}^z$ consists of identical subsets equally spaced by distance d_{min} and expressed as $\mathbf{D}^z = \bigcup_{\mu=-\infty}^{\infty}(\mathbf{D}_0^z + \mu \cdot d_{min})$, $\mu \in \mathbb{Z}$. Specifically, the number of possible direction vectors $\mathbf{a}_0^z$ in E_8 reaches 120, because each E_8 lattice point is surrounded by 240 neighbors, and each direction has a conjugate counterpart, i.e. $\mathbf{a}_0^z = -\mathbf{a'}_0^z$, which reduces the number by half.

We use a 'cake-cutting' algorithm to implement the HS-HD. $d_k^z = (\mathbf{a}_0^z)^{\mathrm{T}}\mathbf{R}_k$ generates a characteristic number, which equals to the projection of $\mathbf{R}_k$ along the direction $\mathbf{a}_0^z$. The same procedure is applied on the lattice set $\mathbf{L}$ and generates a set of characteristic numbers, $\mathbf{D}^z$, as described above. By comparing the characteristic value d_k^z of the received super-symbol with the lattice characteristic values $D_\mu^z \in \mathbf{D}^z$, we obtain the difference $\delta = d_k^z - D_\mu^z$. Therefore, a HD selects a subset $\mathbf{L}^z$ of lattice from the whole set $\mathbf{L}$, where $|\delta| \leq d_{min}/2$. The selection starts from an arbitrary direction and goes through all possible 120 directions. The ergodic process

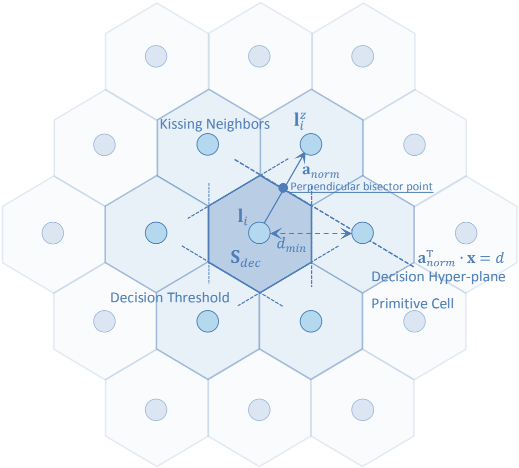

Figure 4.14: Division of a signal space by using the decision threshold given by the perpendicular bisecting hyperplane between a lattice point and its neighbors, apart from the origin of the coordinate by d_{min}, with the analogy of two-dimensional honeycomb structure (A_2 lattice).

stops when one element only remains in the candidate set. The procedure looks like cutting the cake (signal space) until the last piece containing the cherry (the decided symbol) is found.

The major difference between HS-HD and the conventional hard-decision used for PAM-m are extra linear transforms required before the decision. Such operations are expected to be serialized with electrical analog circuits. As the decision can be implemented in an analog domain, analog-to-digital converter (ADC) is dispensable, whereas it is required in the case of digital ML algorithms.

4.4.5 Hierarchical soft-decision

The soft-decision is defined formally as Eq. 4.33.

$$\widehat{\mathbf{R}}_k = \underset{\mathbf{C}_l \in \mathbf{C}}{\arg\min} \parallel \mathbf{R}_k - \mathbf{C}_l \parallel \tag{4.33}$$

in which $\mathbf{R}_k$ is the k-th received super-symbol, and $\mathbf{C}_l$ is one constellation point from the constellation set $\mathbf{C}$, minimizing the Euclidean distance to $\mathbf{R}_k$. For the convenience and simplicity of computation, we can also use the form as:

$$\widehat{\mathbf{R}}_k = \arg\min_{\mathbf{C}_l \in \mathbf{C}} \; \| \, \mathbf{R}_k \; - \; \mathbf{C}_l \, \|^2 \tag{4.34}$$

Yet, for constellations with the scale like BB8, which contains 65536 constellation points, the MMSE rooted SD is not realistic. Concretely, 65536 times of 8-D distance calculations are inevitable for just deciding one super-symbol. However, taking advantages of the intrinsic symmetry of BB8 and the hierarchical structure of set partition, we can devise a simplified hierarchical SD.

Basics

The simplified decision benefits from the symmetry of the lattice. It can be clearly seen from the hierarchical division of constellation sets as discussed in Section 4.4.1 that points in the same subgroup are independent, meaning that the selection of points in one projection is not constrained by the selections on the other 2-Dfacets. In other words, we can make independent decisions on one projection within the same sub-group. Hence, we can run a coarse decision to select the possible decided points in each subgroup, denoted as $\theta_k^j \in \mathbf{\Theta}$, $\omega_k^j \in \mathbf{\Omega}$, $\phi_k^j \in \mathbf{\Phi}$, and $\psi_k^j \in \mathbf{\Psi}$. For the k-th super-symbol, on j-th projection, $j = 0,\, 1,\, 2,\, 3$, we can obtain four selected points, total 16 points selected in one super-symbol. Without loss of generality, we omit the subscript k in the rest of this chapter. By applying the combination rule discussed in Section 4.4.1, 16 candidate super-symbols can be enumerated, which is listed in the Tab. 4.5, and grouped into the candidate set, denoted as $\mathbf{\Gamma}$. More specifically, $\mathbf{\Gamma}_\sigma \in \mathbf{\Gamma} = \{\mathbf{\Gamma}_0, \mathbf{\Gamma}_1, \cdots, \mathbf{\Gamma}_\sigma, \cdots, \mathbf{\Gamma}_{15}\}$. And further, for each candidate, $\mathbf{\Gamma}_\sigma = \left[\, \Gamma_\sigma^0 \, \Gamma_\sigma^1 \, \cdots \, \Gamma_\sigma^i \, \cdots \, \Gamma_\sigma^7 \,\right]^{\mathrm{T}}$. We can further divide $\mathbf{\Gamma}$ into the even subset $\mathbf{\Gamma}_e$ and the odd subset $\mathbf{\Gamma}_o$.

Via coarsely selecting and enumerating the candidate decision points, we reduce the number of the points requiring further comparisons from 65536 to 16, with 4096 times reduction. However, the comparison between the received symbols and the candidate points requires 16×8 multiplications, which might be feasible for the digital systems, but not for analog systems without using ADC and digital signal processing (DSP). Thus, further simplifications for the possible analog transmission is desirable.

Table 4.5: The enumeration of the BB8 candidate points.

$\boldsymbol{\Gamma}_e$	$\boldsymbol{\Gamma}_o$
$\theta^0\ \theta^1\ \theta^2\ \theta^3$	$\phi^0\ \phi^1\ \phi^2\ \phi^3$
$\theta^0\ \theta^1\ \omega^2\ \omega^3$	$\phi^0\ \phi^1\ \psi^2\ \psi^3$
$\theta^0\ \omega^1\ \theta^2\ \omega^3$	$\phi^0\ \psi^1\ \phi^2\ \psi^3$
$\theta^0\ \omega^1\ \omega^2\ \theta^3$	$\phi^0\ \psi^1\ \psi^2\ \phi^3$
$\omega^0\ \theta^1\ \theta^2\ \omega^3$	$\psi^0\ \phi^1\ \phi^2\ \psi^3$
$\omega^0\ \theta^1\ \omega^2\ \theta^3$	$\psi^0\ \phi^1\ \psi^2\ \phi^3$
$\omega^0\ \omega^1\ \theta^2\ \theta^3$	$\psi^0\ \psi^1\ \phi^2\ \phi^3$
$\omega^0\ \omega^1\ \omega^2\ \omega^3$	$\psi^0\ \psi^1\ \psi^2\ \psi^3$

Hierarchical decision

Considering the two candidate symbol[2] $\boldsymbol{\Gamma}$ and $\boldsymbol{\Gamma}'$, according to Eq. 4.34, we make a decision between them by calculating Eq. 4.35. If $\Delta \leq 0$, the candidate symbol $\boldsymbol{\Gamma}$ is more likely to be the estimated symbol. Other wise, the candidate $\boldsymbol{\Gamma}'$ is preferred.

$$\Delta = \parallel \mathbf{R} - \boldsymbol{\Gamma} \parallel^2 - \parallel \mathbf{R} - \boldsymbol{\Gamma}' \parallel^2 \tag{4.35}$$

If we expand Eq. 4.35, we can achieve Eq. 4.37.

$$\Delta = \sum_{i=0}^{7}(R_i - \Gamma_i)^2 - \sum_{i=0}^{7}(R_i - \Gamma_i')^2 \tag{4.36}$$

$$= \sum_{i=0}^{7}(\Gamma_i - \Gamma_i')(\Gamma_i + \Gamma_i' - 2R_i) \tag{4.37}$$

We know that $\boldsymbol{\Gamma} \in \mathbf{C}$, meaning that that $\boldsymbol{\Gamma} \in \mathbb{Z}^8$. It hides the convenience behind Eq. 4.37 for the actual realization that only after simple signal processing, e.g. voltage elevation, amplification, and summation, the received analog signal can be directly used as the criteria of decision, without being converted into the digital forms.

Applying such decision scheme into the hierarchical structure of the set partitions described in Sect. 4.4.1, i.e. the hierarchical structure for

---

[2] Note that for convenience, we omit the superscript k for $\mathbf{R}_k$ and σ for $\boldsymbol{\Gamma}_\sigma$ and shift the superscript i as subscript if not confusing.

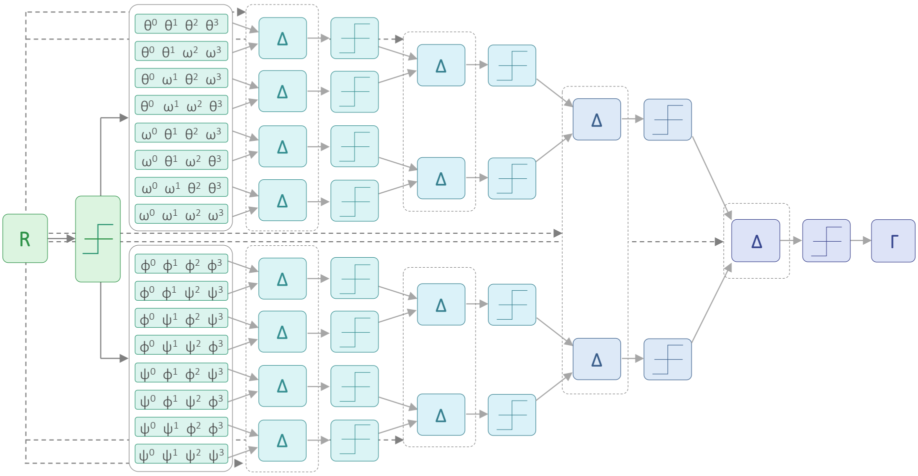

Figure 4.15: The hierarchical decision for decoding BB8.

the candidate set, the direct comparisons with the 16-candidate list can be converted to a serial of 4-level hierarchical decisions, with a candidate-candidate, i.e. $\mathbf{\Gamma} - \mathbf{\Gamma}'$, comparison for each level. If we well design such SD using the sample and hold circuit together with a mixed-signal IC design, the whole decision can be obtained in a few clock cycles. The output of the decision according to Eq. 4.37 has very low latency and is almost instantaneous. The principle is schematically illustrated as Fig. 4.15

Pros and cons

The above-mentioned decision scheme roots in the processing of the input analog signal, without being converted into digital signals with ADCs. This is essential for the low-cost data links if the ADCs can be avoided. Further, it is fundamentally a real-time solution. Meanwhile, the drawback lays in a more complicated mixed-signal design with both the analog and digital circuit. The increase in power consumption during the actual operation also remains unknown.

In fact, from Eq. 4.37, we can see that the second process phase of the hierarchical SD is equivalent to the hyperspace based HD. The difference is that it utilizes a priori information, which is obtained by applying the coarse HD in the form of digital signal, to simplify the actual computation, i.e. analog signal processing for the received signal. Today, the sample and hold circuit for the analog signal is getting popular. Thus, such technique may open a window to the actual adoption of the MD modulations in future IM-DD systems.

4.4.6 Experiment setup

The experimental setup is presented in Fig. 4.16. An 850 nm multimode VCSEL, biased at 8 mA, was directly modulated by a 520 mV peak-to-peak differential electrical signal. The L-I-V curve, the small-signal frequency response and the optical spectrum are shown in Fig. 4.17 (a), (b), and (c) respectively.

The electrical signal was generated from 28 GBaud sequences of 256K symbols by a 65 GSa/s 8-bit arbitrary waveform generator (AWG). The sequences were pre-processed with a raised cosine (roll-off factor $\alpha = 0.5$) pulse shaping and repeatedly transmitted. A pre-equalization on the electrical signal was included to mitigate the spectral roll-off of the AWG. The VCSEL used in this experiment has a -3 dB bandwidth of 17 GHz. The maximum output optical power from the transmitter optical sub-assembly (TOSA) reaches -0.61 dBm. A variable optical attenuator (VOA) was employed, which has an insertion loss of 0.52 dB, reducing the maximum launched optical power to -1.13 dBm. The signal was received by a commercially available VI-Systems photodiode package which includes a trans-impedance amplifier (TIA). The detected electrical signal was improved with a low-noise amplifier (LNA) and a low-pass filter (LPF). Signal traces were captured with a 33 GHz, 80 GSa/s digital storage oscilloscope (DSO). A back-to-back BER measurements were taken for a primary characterization. Then link measurements were performed with one spool of 100 m OM3 MMF and one of OM4 MMF. They introduced the losses of 0.69 dB and 0.85 dB respectively, giving the maximum received optical power -1.82 dBm and -1.98 dBm correspondingly. For the convenience of comparison, we set -2 dBm as the maximum power for BER measurements in the following experiments and treat it as the maximum achievable received optical power.

The received digital signal was processed offline. The traces were resampled from 80 GSa/s to 56 GSa/s, i.e. two samples per symbol, processed with a T/2 fractional infinite impulse response (IIR) filter with 11 and 5 taps in the feed-forward and feedback parts, respectively. Training sequences with an adaptive process using the least-mean-square (LMS) algorithm were applied to train the coefficients of the filter taps. The first 2048 samples of the traces were used as the training sequences. The training process was executed iteratively 10 times with different step sizes varying

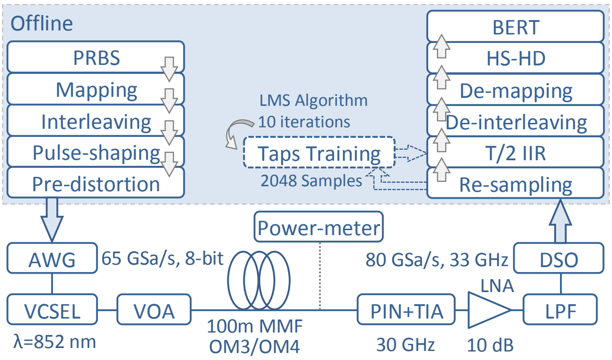

Figure 4.16: Experimental setup used for performance verification of BB8.

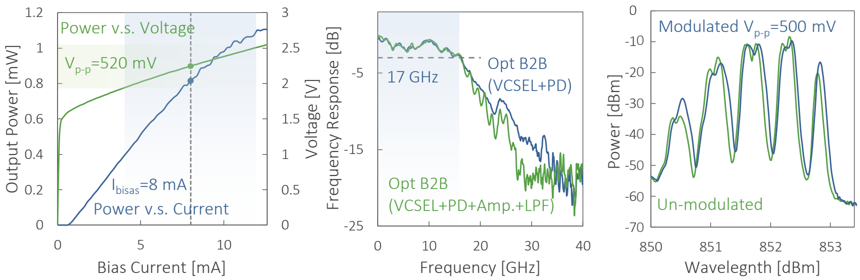

Figure 4.17: Characterizations of 850 nm MM-VCSEL: (a) DC L-I-V measurement. (b) The end-to-end frequency response, with (lemon grass) and without (azure) post-amplifier and low pass filter. (c) The optical spectrum of VCSEL, with (azure) and without (lemon grass) electrical signal modulation.

from 0.03 to 0.003. After the coefficients were trained during the initialization stage, they were kept constant for the whole payload. We used IIR filter instead of decision feedback equalizer (DFE) because the decision of BB8 is not straightforward, where no instant symbol-wise decision can be made. Therefore, we set the decision phase after the equalization and used the IIR filter, where no decision is required in advance. It is noteworthy that for keeping the results comparable, we apply the same signal process on all the formats studied in this work.

Data collections were treated differently in different transmission regimes. 100 traces with 2 million samples (25 μs) were stored for each transmission condition in critical regime; for the received optical power which generates BER approximately lower than 10^{-3} to the maximum received optical power, where the accuracy of BER is easily influenced by the number and length of the traces. 10 traces with 1 million samples (12.5 μs) were stored for the remaining power regime, because the trend was well displayed in the higher noise conditions.

4.4.7 Experimental results

Back-to-back measurements

Fig. 4.18 shows the back-to-back (BTB) BER sensitivity of BB8, PAM-4, and PAM-8. The last one is used as a reference. Substantially, BB8 and PAM-4 perform similarly at the 7% OH FEC level, predicted by simulation shown in Fig. 4.13. However, in the experiment BB8 has a minor degradation of 0.2 dB to PAM-4. It is reasonable that BB8 degrades faster due to the system imperfection in the low signal-to-noise ratio (SNR) regime, as it is constructed by more neighboring points. With the increase of received optical power, BB8 outperforms PAM-4 by an asymptotic gain larger than 1 dB. An apparent error floor can be observed for the PAM-4's curve due to the limited bandwidth, relative intensity noise (RIN) and laser nonlinearities. Its new counterpart, BB8, provides a potential to achieve BER=10^{-12} before reaching the maximum laser optical output power, as can be concluded from the fitted trend line in Fig. 4.18. It is also possible that BB8 conceals the error floor below the measurement accuracy limit at BER=10^{-7}. In contrast, PAM-8 displays an unsuccessful transmission with 7% FEC. BB8 gives a 2 dB power margin (maximum optical power -2 dBm) at the 2.7% overhead (OH) FEC of RS (528, 514) which gives the output BER$< 10^{-15}$. PAM-4 has a BER gap larger than one order of magnitude.

MMF links

Transmissions of BB8 over 100 m OM3 and OM4 MMFs result in a <1 dB penalty at 7% FEC as compared to the BTB scenario (100 m OM3 in Fig. 4.19 and 100 m OM4 in Fig. 4.20). PAM-4 experiences a major degradation in OM3 and OM4. Unlike the simulation analysis in Fig. 4.13, the receiver sensitivity for BB8 is improved as compared to PAM-4 by 0.6 dB and 1 dB for OM3 and OM4, respectively. BB8 has a successful transmission at the FEC threshold of lower required BER and an improved power margin for both 100 m OM3 and 100 m OM4, whereas for PAM-4 the error floor close to the maximum received optical power makes 56 Gbit/s

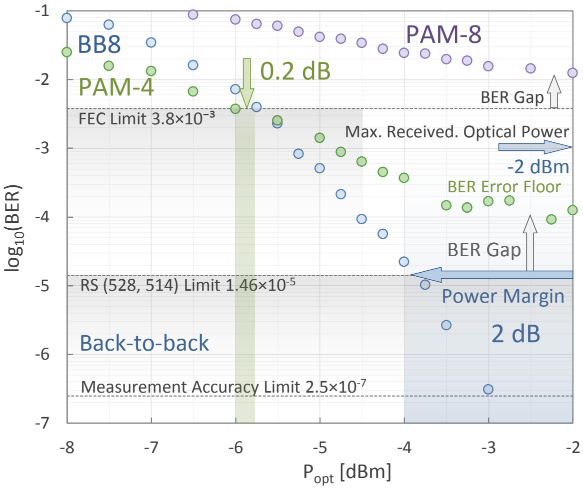

Figure 4.18: Comparison of the optical back-to-back BER sensitivity for BB8 (azure), PAM-4 (lemon grass), and PAM-8 (lavender) in 28 GBaud/s data-links.

transmission unsuccessful. Apparently, PAM-4 degrades faster than BB8 in MMF links. We believe that it stems from the fact that BB8 has larger MMED than PAM-4, which is more tolerant to the signal distortion from the nonlinearities of components and the limited bandwidth of fiber links. It is also noteworthy that the increased gap doesn't imply the inevitable relations with the differences in specifications between OM3 and OM4. In principle, OM4 is further optimized based on OM3, which theoretically should have the larger modal bandwidth. However, due to the different design and implementation of vendors, batches, conservation conditions of fiber spools or even launching conditions, it is difficult to provide a direct comparison of the performance with different fiber spools.

Since 100 m links are typical in commercial products, these results imply the potential of BB8 for MMF data transmission links scenarios.

4.5 Summary and discussion

An 8-D modulation format based on E8 lattice was proposed for short-reach data transmission links. The experimental performance shows a 2 dB power margin in BTB measurements and $\sim$ 1.5 dB for a transmission over 100 m OM3/OM4 MMF measured at 2.7% 100BASE-SR4 FEC. It implies the potential advantages of BB8 in intra-datacenter and other short-reach ap-

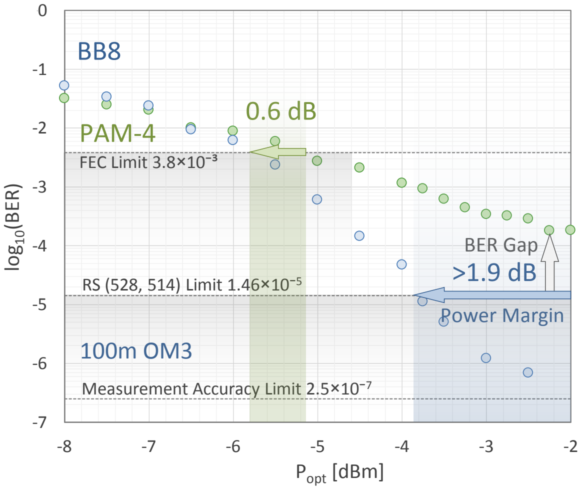

Figure 4.19: BER performances of BB8 and PAM-4 with varying received optical power measured for transmission over 100 m OM3 MMF.

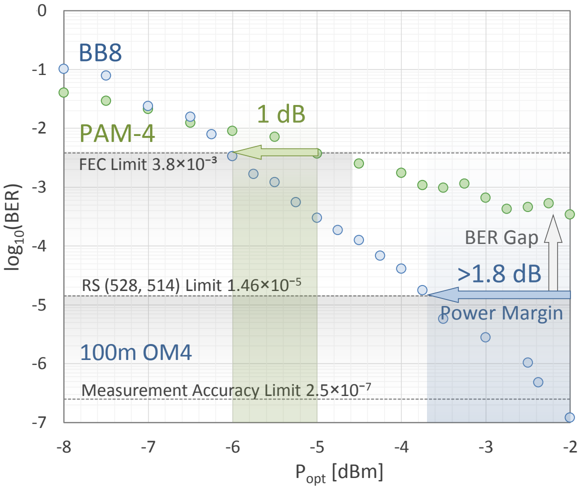

Figure 4.20: The BER performance of BB8 and PAM-4 with varying received optical power measured for transmission over 100 m OM4 MMF.

plications. Due to a better asymptotic BER performance, BB8 relieves the requirement on maximum received optical power, and hence the maximum laser output power. Potential non-FEC transmission of BB8 down

Table 4.6: The performance comparison between BB8 and PAM-4 in terms of the optical back-to-back, 100 m OM3 and 100 m OM4 with the required optical power (unit dBm).

FEC threshold	**BB8**	**PAM-4**	$\Delta_{BB8/PAM-4}$
7 % HD-FEC OBTB	-5.8	-6	-0.2
KR-4/SR-4 OBTB	-3.9	-	-
2.5×10^{-7} OBTB	-3	-	-
7 % HD-FEC 100 m OM3	-5.8	-5.2	0.6
KR-4/SR-4 100 m OM3	-3.8	-	-
Asymptotic 100 m OM3	-2.1	-	-
7 % HD-FEC 100 m OM4	-6	-5.0	1.0
KR-4/SR-4 100 m OM4	-3.7	-	-
Asymptotic 100 m OM4	-2.2	-	-

to BER=10^{-12} without extra redundancy can provide reduced latency and complexity of the transceivers. Moreover, it is inherently compatible with the 8-lane octal small form-factor pluggable (OSFP) links. BB8 is also attractive for future modulation flexible transceivers, because of the possible smooth transition between BB8 and PAM-m provided by the simplified mapping and de-mapping schemes. Considering the requirements on capacity, power efficiency, latency, reliability and flexibility, BB8 is a possible candidate for the next generation IM-DD optical interconnections.

The works summarized in this chapter are presented in **PAPER6**, **PAPER7** and **PAPER8**[3].

---

[3] Note that some charts presented in this thesis from **PAPER6** have been updated.

Chapter 5

Twenty-Four-Dimensional PAM

In the previous chapter, we discussed three four and eight-dimensional pulse amplitude modulation (PAM) with different optimization principles. They rely on the four and eight-dimensional densest lattices, namely D_4 and E_8 respectively. By applying the similar principle, combining more regular symbols and designing with the lattice in the corresponding dimension, a multi-dimensional (MD) PAM with higher dimension can be constructed. In this chapter, we introduce an MD-PAM when $n = 24$, i.e. a twenty-four-dimensional PAM, by packing 24 regular symbols in a super-symbol and designing the constellation according to the densest lattice in 24-D space, i.e. the Leech lattice, denoted as Λ_{24}. It carries 48 bits per super-symbol, equivalent to 2 bits per symbol (2 bit/sym), equal to pulse amplitude modulation with 4 levels (PAM-4). It is named as Leech24D-m[1], and obviously here m=2.

In the following sections, we start with the formalization, geometry, and construction of the constellation set. They are followed by the elaboration of modulation and demodulation, as well as the corresponding decision strategy. The new MD member is investigated in an intensity-modulated direct-detection (IM-DD) system using 850 nm single-mode (SM) vertical-cavity surface-emitting laser (VCSEL) and multi-mode fiber (MMF) spans. The performance is compared with the conventional PAM-4 and the eight-dimensional PAM investigated in the last chapter, namely BB8. The proposed modulation format is proven to have additional benefits compared

---

[1] Note that for convenience the representation in this chapter, m here represents the number of bits carried by each regular symbol instead of each super-symbol.

with its counterparts of other dimensions in different transmission scenarios.

5.1 24-dimensional space, lattice and Leech24D-m

5.1.1 24-D signal space

In this chapter, we construct the 24-D signal space by combining 24 time slots, i.e. regular PAM symbols. Following the notation in the last chapter, let us consider, $\mathbf{s} = [s_0, s_1, \cdots, s_m, \cdots]^{\mathrm{T}}$ is a transmitting sequence. The subscript $m = 0, 1, \cdots$ as the position of a regular symbol s_m in the sequence. The sequence of n-dimensional super-symbols (n=24) is denoted as $\mathbf{S} = [\ \mathbf{S}_0\ \mathbf{S}_1\ \cdots\ \mathbf{S}_k\ \cdots]^{\mathrm{T}}$. The subscript $k = 0, 1, \cdots$ is denoted as the position of a super-symbol $\mathbf{S}_k$ in the sequence $\mathbf{S}$. For each super-symbol $\mathbf{S}_k = [\ S_k^0\ \cdots\ S_k^i\ \cdots\ S_k^{23}\ ]^{\mathrm{T}}$. S_k^i is the individual symbol in the k-th super-symbol. $i = 0, 1, \cdots, n-1$ indicates the position in $\mathbf{S}_k$. S_k^i corresponds to the symbol $s_{n\cdot k+i}$ in $\mathbf{s}$, i.e. $m = n \cdot k + i$.

The twenty-four-dimensional (24-D) space has been rigorously proven the space with the highest dimension known so far, which has the densest lattice close to the theoretical limits, followed by the eight-dimensional E_8 [130, 131]. Thus, we can expect that a MD PAM designed based on the 24-D densest lattice, i.e. Λ_{24}, outperforms all its counterparts in other dimensions as previously mentioned. A similar interleaving technique is adopted as it was done in the previous chapter, so that the orthogonality of the basis is guaranteed.

5.1.2 Λ_{24}

Leech lattice set Λ_{24}, or more conveniently denoted as $\mathbf{L}_{\Lambda_{24}}$, can be constructed formally as:

$$\Lambda_{24} = \left\{ (x_i) \in \mathbb{Z}^{24} : \sum_{i=0}^{23} x_i \equiv 4x_i \,(\mathrm{mod}\, 8),\, \mathbf{P} \in \mathbf{W}_{\mathcal{G}} \right\} \tag{5.1}$$

in which $\mathbf{P} \in \mathbf{W}_{\mathcal{G}}$ and $\mathbf{P} = [\ P_0\ P_1\ \cdots\ P_i\ \cdots\ P_{23}\ ]^{\mathrm{T}}$ is a vectorial index, which imposes additional constraints and follows the Eq. 5.2

$$P_i = \begin{cases} 1 & \text{for } x_i \,(\mathrm{mod}\, 4) \equiv I \\ 0 & \text{otherwise} \end{cases} \tag{5.2}$$

in which, I is the index of the residue class modulo 4 and is an arbitrary value from set $\{\,0,\ 1,\ 2,\ 3,\ \}$; and $\mathbf{W}_{\mathcal{G}} = \{\,\mathbf{W}_0,\ \mathbf{W}_1,\ \cdots,\ \mathbf{W}_{4095}\,\}$ is the set of codewords of the binary Golay code.

In a different perspective, Λ_{24} can be seen as the union of two cosets of the Leech half-lattice, i.e. $\mathbf{L}_{\Lambda_{24}} = \mathbf{H}_{\Lambda_{24}} \cup \mathbf{H}^{\perp}_{\Lambda_{24}}$ [134]. Each of the cosets of $\mathbf{H}_{24}$ can be described with the (24,12) extended Golay code $\mathcal{G}_{24}$, combined with a one-bit parity check code.

Due to the symmetry of lattice, we can define the basic building blocks of Λ_{24}. It is denoted as $\mathbf{L}^0_{\Lambda_{24}}$, known as primitive cell. The whole lattice set $\mathbf{L}_{\Lambda_{24}}$ is the tessellation of the primitive cells, which is expressed formally as:

$$\mathbf{L}_{\Lambda_{24}} = \mathbf{L}^0_{\Lambda_{24}} + \mathbf{L}_{\Delta} \tag{5.3}$$

in which, $\mathbf{L}_{\Delta} = [\ L^0_{\Delta}\ L^1_{\Delta}\ \cdots\ L^i_{\Delta}\ \cdots\ L^{23}_{\Delta}\ ]^{\mathrm{T}}$, $L^i_0 = \beta_i D_i,\ \forall \beta_i \in \mathbb{Z}$. D_i is the occupancy of $\mathbf{L}^0_{\Lambda_{24}}$ in i-th dimension. Note that $\mathbf{L}_{\Delta} \cong \mathbf{L}_{Z_{24}}$, namely $\mathbf{L}_{\Delta}$ and the lattice Z_{24} are isomorphic.

Via an insight into the above structure, we find that the tessellation of $\mathbf{L}_{\Lambda_{24}}$ is equivalent to a nesting of the primitive cells, into a 24-D cubic lattice, known as Z_{24} lattice. The identical primitive cells are placed at every Z_{24} grids. By doing so, the construction of the lattice set is equal to construct the primitive cell $\mathbf{L}^0_{\Lambda_{24}}$ and extend the primitive cell to the Λ_{24} lattice via Z_{24} lattice.

5.1.3 Leech24D-m

The design of Leech24D-m equals to find a constellation set $\mathbf{C}^m_{\Lambda_{24}} \subset \mathbf{L}_{\Lambda_{24}}$, which is a subset of the lattice set. Averagely, m bits are carried by each regular symbol, meaning $24m$ bits for each Leech24D-m super-symbol, resulting in a constellation set of a 2^{24m}-element twenty-four vector set.

The tessellation of the primitive cell as Eq. 5.3 implies a convenient way of extending the scale of constellation set. As mentioned above, the Leech lattice is the nesting of the primitive cell $\mathbf{L}^0_{\Lambda_{24}}$ on to the Z_{24} lattice, which corresponds to the conventional PAM or quadrature amplitude modulation (QAM). The construction of Leech24D-m can be divided into the construction of the constellation set $\mathbf{C}^0_{\Lambda_{24}}$, which contains the geometry of Leech lattice, and a modulation of conventional PAM-m with Gray mapping, which extend the $\mathbf{C}^0_{\Lambda_{24}}$ to the desired $\mathbf{C}^m_{\Lambda_{24}}$. Obviously, when $m = 1$, the constellation degenerates to the primitive cell, where $\mathbf{C}^1_{\Lambda_{24}} = \mathbf{C}^0_{\Lambda_{24}}$. The 24 bits are coded by a $\mathcal{G}_{24}$ based encoder. When $m > 1$, besides the first 24

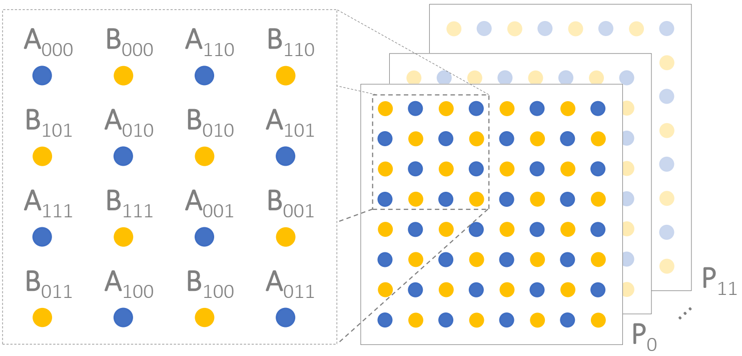

Figure 5.1: 2-D projections for Leech24D-m.

bit coded into $\mathbf{C}^1_{\Lambda_{24}}$, the rest uncoded bits are modulated by a PAM-(m-1) modulator.

For understanding the geometric feature of Leech24D-m, we can investigate its hierarchical relations of the subsets. The constellation set $\mathbf{C}^m_{\Lambda_{24}}$ can be partitioned into to orthogonal subsets, like Eq. 5.4.

$$\mathbf{C}^m_{\Lambda_{24}} = \mathbf{A}^m \cup \mathbf{B}^m, \mathbf{A}^m \cap \mathbf{B}^m = \emptyset \tag{5.4}$$

in which $\mathbf{A}^m \subset \mathbf{H}_{\Lambda_{24}}$ and $\mathbf{B}^m \subset \mathbf{H}^{\perp}_{\Lambda_{24}}$. We use one of the 12 two-dimensional projections to illustrate the higher dimensional structure, as in Fig. 5.1. All 12 points can be selected from either the blue ($\mathbf{A}_{x,y,z}$) or the yellow ($\mathbf{B}_{x,y,z}$) subset, in which the subscripts of x, y, z are the indices showing the relations of the subsets in deeper nesting levels. They are also used as bit positions in the modulation.

The orthogonal subsets can be further partitioned into subsets according to the lattice geometry.

According to the subsets in the last nesting level as shown in the Fig. 5.1, the theoretical minimum mutual Euclidean distance (MMED) is estimated as $\sqrt{2}$ times larger than the E_8 based formats, enabling the largest nominal coding gain (~6 dB) among the other MD formats. Concretely, The constellation figure of merit (CFM) of Leech24D-1, Leech24D-2 and Leech24D-3 reach 8.06 dB, 1.83 dB and -4.24 dB respectively, earning 5.05 dB, 5.81 dB and 5.97 dB apart CFM benefits from non-return-to-zero (NRZ), PAM-4 and pulse amplitude modulation with 8 levels (PAM-8) accordingly. The asymptotic power efficiency (APE) values of these three formats arrive 5.05 dB, 1.83 dB and -2.48 dB with the gaps of 5.05 dB, 5.81 dB and 5.97 dB with their corresponding PAM-m counterparts. It is noteworthy that the metrics calculated here are based on the average symbol energy calculated from randomly selecting from the constellation sets, as the scale of these constellation, e.g. 2^{72} points for Leech24D-3, which is unrealistic to have an ergodic result.

5.2 Bit-to-symbol modulation

For the input bit block $\mathbf{B}_k = [\ b_k^0\ b_k^1\ \cdots\ b_k^e\ \cdots\ b_n^{24m-1}]^\mathrm{T}$ and the mapped symbol sequence $\mathbf{S}_k = [\ S_k^0\ S_k^1\ \cdots\ S_k^i\ \cdots\ S_k^{23}]^\mathrm{T}$ the k-th super-symbol of Leech24D-m carrying $12m$ bits, a bit-to-symbol mapping is defined as, $\mathcal{M}\ :\ \mathbf{F}_2^{24m} \rightarrow \mathbb{R}^{24}$ and the corresponding symbol-to-bit de-mapping is $\mathcal{M}^{-1}\ :\ \mathbb{R}^{24} \rightarrow \mathbf{F}_2^{24m}$. $\mathbf{F}_2^{24}$ means the $24m$-dimensional binary field. The superscript e indicates the position of the individual bit in $\mathbf{B}_k$.

Specifically, 24 bits are used as coded bits to generate the finer structure of the Λ_{24} geometry and with the rest $24(m-1)$ bits as the uncoded one, which are used to extend the primitive cell via a Gray mapped PAM-(m-1) modulator. We can extract a parameter $\gamma = m - 1$, which indicates the depth of modulation for the uncoded bits.

For the modulator, a $24m$-bit section in the input bit stream is fed into a register $\mathbf{v}_k$, i.e. $\mathbf{v}_k = [\ v_k^0\ v_k^1\ \cdots\ v_k^e\ \cdots\ v_k^{24m-1}\ ]^\mathrm{T}$, as:

$$\mathbf{v}_k = [\ \mathbf{h}_k\ \mid\ \mathbf{g}_k\ ]^\mathrm{T} \tag{5.5}$$

in which an 24-bit section $\mathbf{h}_k = [\ h_k^0\ h_k^1\ \cdots\ h_k^i\ \cdots\ h_k^{23}\ ]^\mathrm{T}$ is used for the modulation of the coded bits. It reads as:

$$\mathbf{h}_k = [\ b_k^0\ \cdots\ b_k^{23}\ ]^\mathrm{T} \tag{5.6}$$

And $\mathbf{g}_k = [\ g_k^0\ g_k^1\ \cdots\ g_k^e\ \cdots\ g_k^{24m-25}\ ]^\mathrm{T}$ indicates the uncoded bit section for the integer bit modulation. It is expressed as:

$$\mathbf{g}_k = [\ b_k^8\ \cdots\ b_k^{24m-1}\ ]^\mathrm{T} \tag{5.7}$$

The overall bit-to-symbol mapping is formally expressed as:

$$S_k^i = t_k^i + \sum_{\nu=0}^{\gamma} 2^{\nu+1} g_k^{24\nu+i} \tag{5.8}$$

The modulation consists of two phases. The coded bits are first encoded and cached as the pre-processed symbols $\mathbf{t}_k = [\ t_k^0\ t_k^1\ \cdots\ t_k^i\ \cdots\ t_k^{23}\ ]^\mathrm{T}$.

Then, a PAM modulator sum up $\mathbf{t}_k$ with the modulated un-coded bits as output symbols, as Eq. 5.8.

For the mapping of the pre-processed symbols, the indices, i.e. $\mathbf{A}_{x,y,z}$ or $\mathbf{B}_{x,y,z}$, are first generated for each regular symbols; and then the output t_k^i are selected from the two-dimensional (2-D) digram, shown in Fig. 5.1. For the convenience for the expression of selection rules, we define a new index w_k, as in Eq. 5.9.

$$w_k = \begin{cases} 0 & \mathbf{S}_k \in \mathbf{A}^1 \\ 1 & \mathbf{S}_k \in \mathbf{B}^1 \end{cases} \tag{5.9}$$

Note that we omit the subscript k in the rest of this chapter for more concise expressions. Thus, based on above, each t^i is completely determined by a set of indices, i.e. (w^j, x^j, y^j, z^j), $\forall j \in \{0,\ 1,\ \cdots,\ 11\}$, where j is the index of the projection. It implies that the 24 output symbols t^i is determined by 12 points on the 2-D projections.

For each bit section $\mathbf{h}$, we divide the bits into three sections $\mathbf{q}^0 = [\ h^0\ h^1\ \cdots\ h^{11}\ ]^{\mathrm{T}}$, $\mathbf{q}^1 = [\ h^{12}\ h^{13}\ \cdots\ h^{22}\ ]^{\mathrm{T}}$, and $\mathbf{q}^2 = [\ h^{23}\ ]^{\mathrm{T}}$ and follows:

$$\mathbf{h} = [\ \mathbf{q}^0\ \mathbf{q}^1\ \mathbf{q}^2\ ]^{\mathrm{T}} \tag{5.10}$$

Let $w^0 = w^1 = \cdots = w^{11} = h^{23}$, which can be realized by a repetition encoder. The determination of index x and y is based on a (24,12) extended Golay $\mathcal{G}_{24}$ encoder. Formally, $\mathbf{P} = [\ x^0\ y^0\ x^1\ y^1\ \cdots\ x^{11}\ y^{11}\ ]^{\mathrm{T}}$, a vectorial index, is an codeword of $\mathcal{G}_{24}$, following:

$$\mathbf{P} = \mathbf{G} \cdot \mathbf{q}^0 \tag{5.11}$$

in which, $\mathbf{G}$ is the generator matrix of $\mathcal{G}_{24}$. For determining the index z, we use a parity check encoder. It is formally expressed as:

$$z^0 = h^{12} \tag{5.12}$$

$$z^1 = h^{13} \tag{5.13}$$

$$\cdots$$

$$z^{10} = h^{22} \tag{5.14}$$

$$z^{11} = h^{12} \oplus \cdots \oplus h^{22} \oplus h^{23} \tag{5.15}$$

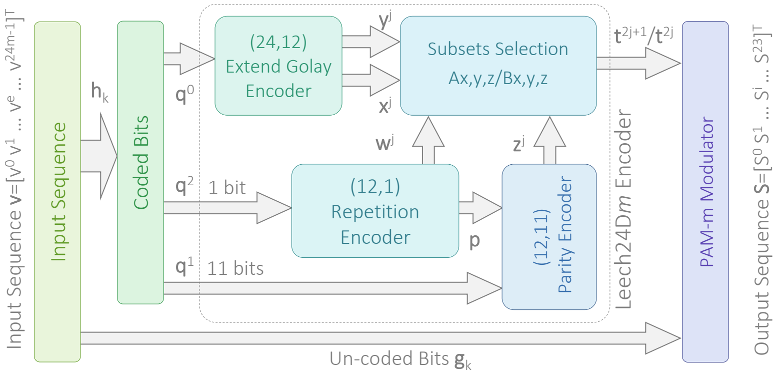

Figure 5.2: The schematic illustration of the bit-to-symbol modulator for Leech24D-m.

The selection of the output symbols based on the indices using the 2-D projections, as shown in Fig. 5.1, can be realized by the look-up table (LUT). However, to reduce the latencies, we adopt a bit-wise mapping, which only requires the bit-level operations. The mapping is formally shown from Eq. 5.16-Eq. 5.17.

$$t^{2j} = \mathrm{mod}(\ 2 \cdot ((x^j \wedge y^j) \oplus z^j) + w^j + x^j \oplus y^j,\ 4\ ) \tag{5.16}$$

$$t^{2j+1} = 2 \cdot ((x^j \wedge \overline{y^j}) \oplus z^j) + x^j \oplus y^j \tag{5.17}$$

in which $\forall j \in \{\, 0,\ 1,\ \cdots\ ,\ 11\,\}$. The schematic illustration of the Leech24D-m encoder is shown as Fig. 5.2.

5.3 Symbol-to-bit demodulation and decision

For decoding the Leech24D-m symbols, the pure maximum likelihood (ML) decoding scheme is not realistic. For a concrete instance of the case when $m = 2$, there are 2^{48} points in $\mathbf{C}^2_{\Lambda_{24}}$, and it requires comparisons of the same number to decoding one super-symbol, which makes the practical implementation unaffordable. However, we can take full advantages of the geometry features of the highly structured constellation set, to simplify the complexity of the decoding. The basic idea is to utilize the the symmetry of the lattice, i.e. invariance of translation, and the hierarchical subsets relations.

We can first simplify the decoding of the whole constellation set $\mathbf{C}^m_{\Lambda_{24}}$ to the primitive cell set $\mathbf{C}^0_{\Lambda_{24}}$, or known as $\mathbf{C}^1_{\Lambda_{24}}$. Utilizing the dependence of the primitive cells on each projection, such process can be easily realized by applying a pre-hard-decision in each dimension, i.e. each regular symbol, and selecting the four candidate values from each symbol.

The estimated symbol is decided among the candidate points with the cost function of the Euclidean distances. We adapt a ML soft-decoding scheme. The Golay decoder enumerates the candidate point set and the difference of Euclidean distance (ED) between the received signal and the candidate points, which is listed by using the Golay generation matrix. The point with the smallest distance difference is selected as the candidate point of one of the $\mathbf{H}_{\Lambda_{24}}$ decoders. And the final decided symbol is the one with the smaller distance difference between the two candidates from $\mathbf{H}_{\Lambda_{24}}$ and $\mathbf{H}^{\perp}_{\Lambda_{24}}$.

Formally, we can define the candidate set for each 2-D projection, denoted as $\mathbf{O}^j$. Such candidate set can be further partitioned into two orthogonal sets $\mathbf{O}^j_{\mathbf{A}}$, $\mathbf{O}^j_{\mathbf{B}} \subset \mathbf{O}^j$, according to the principle of Leech lattice construction. And they are following:

$$\mathbf{O}^j = \mathbf{O}^j_{\mathbf{A}} \cup \mathbf{O}^j_{\mathbf{B}}, \mathbf{O}^j_{\mathbf{A}} \cap \mathbf{O}^j_{\mathbf{B}} = \emptyset \tag{5.18}$$

It implies that the candidate values on each projection can be selected in dependently either from $\mathbf{O}^j_{\mathbf{A}}$ or from $\mathbf{O}^j_{\mathbf{B}}$. We can further partition each of the above subsets into four sub-groups according to the indices x^j and y^j, total eight sub-group. Specifically, without loss of generality, we can divide $\mathbf{O}^j_{\mathbf{A}}$ into $\mathbf{O}^j_{\mathbf{A}_{x^j,y^j}}$, namely,$\mathbf{O}^j_{\mathbf{A}_{0,0}}$, $\mathbf{O}^j_{\mathbf{A}_{1,0}}$, $\mathbf{O}^j_{\mathbf{A}_{0,1}}$, and $\mathbf{O}^j_{\mathbf{A}_{1,1}}$. Obviously, they follow Eq. 5.19

$$\mathbf{O}^j_{\mathbf{A}} = \bigcup_{x^j=0}^{1} \bigcup_{y^j=0}^{1} \mathbf{O}^j_{\mathbf{A}_{x^j,y^j}}, \bigcap_{x^j=0}^{1} \bigcap_{y^j=0}^{1} \mathbf{O}^j_{\mathbf{A}_{x^j,y^j}} = \emptyset \tag{5.19}$$

The subgroups are not independent, which is defined and constrained by the extended (24,12) Golay code. In each of the sub-group, there are two points, corresponding to the cases when $z^j = 0$ and $z^j = 1$.

We denote the received symbols, following the conventions from the previous chapter, $\mathbf{R}_k$ or for concision $\mathbf{R}$. For each, we can obtain 16 values for the difference of ED between $\mathbf{R}$ and 16 points in $\mathbf{O}^j$ on each 2-D projection. We denote the square of difference as Δ^j_μ, where $\mu = 0, 1, \cdots, 15$. It follows Eq. 5.20.

$$\Delta^j_\mu = (C^{2j}_\mu - R^{2j})^2 + (C^{2j+1}_\mu - R^{2j+1})^2 \tag{5.20}$$

According to the hierarchical nesting of the sub-groups, we can apply the similar partition to these 16 value. They are denoted as $\Delta^j_{\mathbf{A}_{x^i,y^j}}$ and $\Delta^j_{\mathbf{B}_{x^i,y^j}}$.

For convenience of the later process in the decoding, we need to define another serial of distance difference, denoted as δ^j_μ, which can be expressed as Eq. 5.21.

$$\delta^j_\mu = \bigcup_{x^j=0}^{1} \bigcup_{y^j=0}^{1} \delta^j_{\mathbf{A}_{x^i,y^j}} \cup \bigcup_{x^j=0}^{1} \bigcup_{y^j=0}^{1} \delta^j_{\mathbf{B}_{x^i,y^j}} \tag{5.21}$$

in which, $\delta^j_{\mathbf{A}_{x^i,y^j,z^j}}$ and $\delta^j_{\mathbf{B}_{x^i,y^j,z^j}}$ are expressed as:

$$\delta^j_{\mathbf{A}_{x^i,y^j}} = \Delta^j_{\mathbf{A}_{x^i,y^j,0}} - \Delta^j_{\mathbf{A}_{x^i,y^j,1}} \tag{5.22}$$

$$\delta^j_{\mathbf{B}_{x^i,y^j}} = \Delta^j_{\mathbf{B}_{x^i,y^j,0}} - \Delta^j_{\mathbf{B}_{x^i,y^j,1}} \tag{5.23}$$

We then select the candidate points as the estimation of $\mathbf{R}$ first regardless the index z^j and enumerate the possible distance difference between $\mathbf{R}$ and the constellation points according to the Golay codewords. We can enumerate a 4096-element set of distance difference. We denote such set as Ξ, where $\Xi = \Xi_\mathbf{A} \cup \Xi_\mathbf{B}$ .It follows Eq. 5.24.

$$\Xi_\mathbf{A} = \left\{ \xi^j_\mathbf{A} \in \mathbb{R} : \xi = \sum_{j=0}^{11} \min\left(\Delta^j_{\mathbf{A}_{x^i,y^j,0}}, \Delta^j_{\mathbf{A}_{x^i,y^j,1}} \right), \mathbf{P} \in \mathbf{W}_\mathcal{G} \right\} \tag{5.24}$$

where the extra constraint $\mathbf{P} \in \mathbf{W}_\mathcal{G}$ means that the indices array $\mathbf{P} = [\ x^0\ y^0\ x^1\ y^1\ \cdots\ x^{11}\ y^{11}\ ]$ is an codeword of $\mathcal{G}_{24}$. And similarly, we can obtain the set for $\mathbf{B}$, as Eq. 5.25.

$$\Xi_\mathbf{B} = \left\{ \xi^j_\mathbf{B} \in \mathbb{R} : \xi = \sum_{j=0}^{11} \min\left(\Delta^j_{\mathbf{B}_{x^i,y^j,0}}, \Delta^j_{\mathbf{B}_{x^i,y^j,1}} \right), \mathbf{P} \in \mathbf{W}_\mathcal{G} \right\} \tag{5.25}$$

We denote the minimum of $\Xi_\mathbf{A}$ as $\Xi^{min}_\mathbf{A}$.

Then, we do the parity check, as:

$$\Xi^{min}_\mathbf{A} = \begin{cases} \Xi^{min}_\mathbf{A} & \text{for } \bigoplus_{j=0}^{11} z^j = 0 \\ \Xi^{min}_\mathbf{A} + \xi^{min}_\mathbf{A} & \text{otherwise} \end{cases} \tag{5.26}$$

where $\xi^{min}_\mathbf{A}$ define as the minimum of $\xi_\mathbf{A}$, where $\xi_\mathbf{A}$ follows Eq 5.27.

$$\xi_\mathbf{A} = \left\{ \xi^j_\mathbf{A} \in \mathbb{R} : \xi = \sum_{j=0}^{11} \delta^j_{\mathbf{A}_{x^i,y^j}} \right\} \tag{5.27}$$

Following the similar principle, we can obtain the corresponding value for **B**, denoted as $\Xi_{\mathbf{B}}^{min}$. By comparing the $\Xi_{\mathbf{A}}^{min}$ and $\Xi_{\mathbf{B}}^{min}$, we can obtain the estimated symbol, following Eq. 5.28 as:

$$\widehat{R}^j = \begin{cases} \mathbf{A}_{x^i,y^j,z^j} & \Xi_{\mathbf{A}}^{min} < \Xi_{\mathbf{B}}^{min} \\ \mathbf{B}_{x^i,y^j,z^j} & \text{otherwise} \end{cases} \tag{5.28}$$

As we can see from the above discussion, in our work, for enhancing the efficiency, we calculate the MMED differences for each cell by applying a LUT which stores these MMED differences and their position indices on each symbol before the decoding. By doing this, we can avoid the redundant calculation during the decoding. And then the enumeration requires only the summations of the $\mathcal{G}_{24}$ code words. The other the fast decoding of the Golay code and the Leech lattice modulation have been well discussed [197].

5.4 Testbed

In the experiment setup illustrated in Fig. 5.3, we used an 850 nm SM VCSEL coupled with single-mode fiber (SMF) pigtails. Its -3 dB bandwidth reaches 20 GHz and the maximum output power reaches -1.7 dBm when biased at 2.8 mA. The laser was modulated by a 8-bit arbitrary waveform generator (AWG) of 65 GSa/s sampling rate and 22 GHz analog bandwidth with the modulation amplitude of 750 $\mathrm{mV_{pp}}$. The optical signal was detected by a 22 GHz calibrated photoreceiver module with the co-packaged trans-impedance amplifier (TIA). During the signal generation at the transmitter, streams with 19.2M bits were randomly generated and mapped into 9.6M symbols, 0.4M super-symbols accordingly. After interleaving, the symbol sequences were resampled to the desired baud rate, shaped into the root raised cosine pulses (α=0.6), and pre-distorted to compensate the electrical spectrum roll-off of the AWG. For the digital signal processing (DSP) at the receiver side, the electrical signal was first collected by a 256-level digital storage oscilloscope (DSO) of 33 GHz analog bandwidth at sampling rate of 80 GSa/s and resampled into two times of the baud rate, followed by the synchronization, equalization with a 16-tap T/2 fractional feed-forward equalizer (FFE) and an amplitude correction. After de-interleaving, the output bit streams were obtained by the Leech24D-m de-mapper. The value of each point was given by the average value of 10 traces, with 51.25M sampling points of each. The detailed parameters for the experimental testbed are listed in Tab. 5.1.

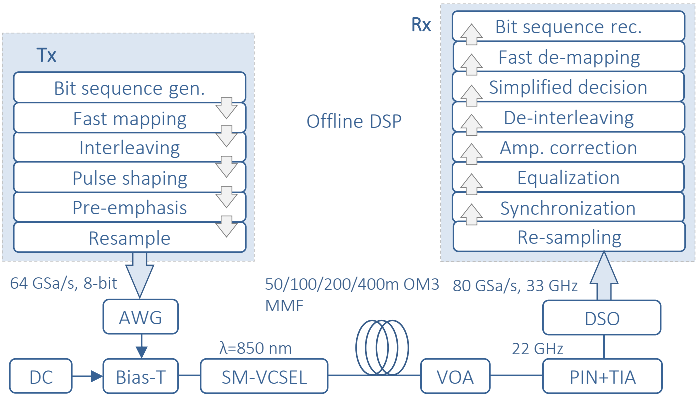

Figure 5.3: The experimental setup for investigating the performance of Leech24D-m.

5.5 Experimental results

We compare the performance of Leech24D-2 with the conventional PAM-4 and the eight-dimensional (8-D) format proposed in the last chapter, i.e. BB8, with different transmission aspects, including the bit error rate (BER) performance, pre-FEC rate and the tolerance for the insertion loss.

5.5.1 Pre-FEC bit-rate

Fig. 5.4. shows the BER performance of different modulation formats with respect to the received optical power in the case of optical back-to-back (OBTB) and 200 m OM3 MMF link. 24-D format provides a well recognizable gain at lower BER values over its 8-D counterpart, and significantly outperforms the standarded PAM-4. At 56 Gbit/s in OBTB regime, Leech24D-2 provides a 2 dB gain relative to PAM-4 in the low-latency KR-4 forward error correction (FEC) threshold. But, with the pre-FEC rate at 80 Gbit/s PAM-4 fails to provide the required BER value of 1.42×10^{-5} within the available power budget of the setup, while 24-D modulation guaranties operation under KR-4 FEC scheme with a 2 dB power margin. Moreover, 24-D modulation shows the possibility of 100 G transmission within the hardware limits of our setup, where the PAM-4 exhibits error floor above the standard 7 % overhead (OH) FEC threshold. The possibility of 100 Gbit/s transmission using the proposed 24-D format remains possible over up to 200 m MMF links. In case of 80 Gbit/s transmission over 200 m MMF link, 24-D format allows data transmission under the BER limit of KR-4 FEC with a 1.5 dB power margin, while both PAM-4

Table 5.1: The parameters of the experiment setup for a Leech24D-m supported 100 G IM-DD transceiver.

Parameter	Symbol	Value	Unit
Sequence length	-	2^{15}	-
Symbol rate	-	28/40/50	GBaud
Bit rate	-	56/80/100	Gbit/s
Formats	-	Leech24D-2/PAM-4/BB8	-
Bias current SM-VCSEL	I_{bias}^{sm}	2.8	mA
Output power	-	-1.7	dBm
wavelength	λ	850	nm
Modulation amplitude	V_{pp}	0.75	V
AWG analogy frequency	$f_{-3\ dB}^{AWG}$	$\sim$ 20	GHz
AWG sampling rate	-	64	GSa/s
AWG vertical resolution	-	8	bit
DSO analogy frequency	$f_{-3\ dB}^{DSO}$	$\sim$ 33	GHz
DSO sampling rate	-	80	GSa/s
DSO vertical resolution	-	8	bit
VCSEL pigtail	-	SMF	-
MMF length	L_{MMF}	200	m
PR bandwidth	$f_{-3\ dB}^{PR}$	22	GHz
PR Gain	G	-80/-70	V/W
PR Output noise	N_{PR}	590	μVrms
PR Impedance	Z_{PR}	50	Ω
Ambient temperature	T	22	°C

and 8-D modulation fail. The details are also listed in the Tab. 5.2 and Tab. 5.3

5.5.2 Bandwidth enhancement

In Fig. 5.5, the BER performance of the modulation formats is compared with respect to the bit-rate, defined by the modulation baud rate. A major capacity enhancement of 10 Gbit/s between Leech24D-2 and the conventional PAM-4 is observed with respect to the same BER value at KR-4/SR-4 threshold (1.42×10^{-5}), for both OBTB and over 200 m MMF. Meanwhile the pre-FEC rate enhancement keeps 8 Gbit/s at the FEC threshold for KP-4 (2.2×10^{-4}). Yet, the benefits generally vanishes at the 7 %

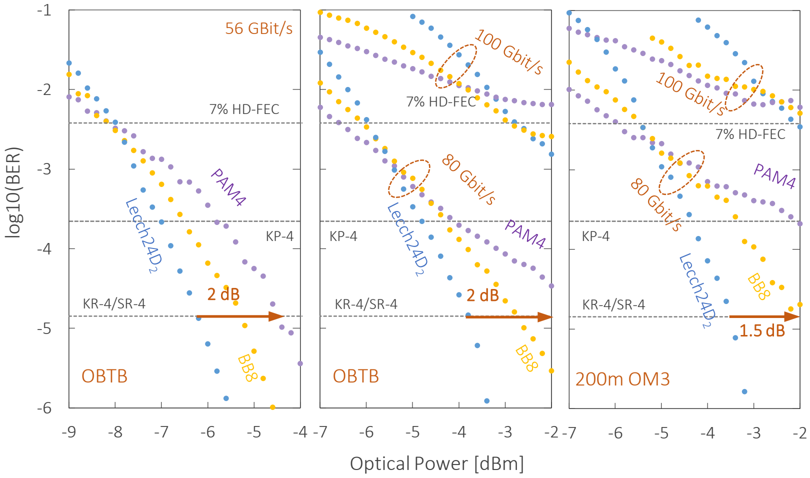

Figure 5.4: BER performance vs. received optical power with Leech24D-2, BB8 and PAM-4, in OBTB or over 200 m OM3 MMF using different baud rates.

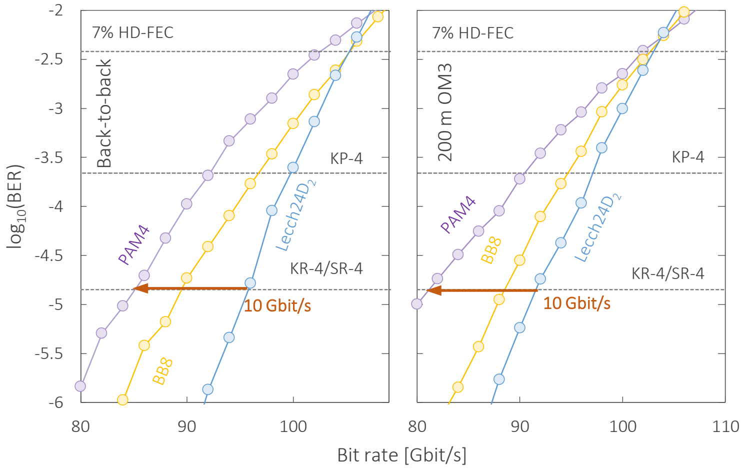

Figure 5.5: BER performance vs. channel bit rate with Leech24D-2, BB8 and PAM-4 in OBTB and over 200 m OM3 MMF.

hard-decision (HD) FEC. And the detailed comparison is summarized in Tab. 5.4.

Table 5.2: The comparison of the optical back-to-back performance, i.e. BER v.s. optical power, between Leech24D-2, PAM-4, and BB8 (unit dBm).

FEC threshold	**Leech24D-2**	**PAM-4**	Δ_{PAM-4}	**BB8**	Δ_{BB8}
7% HD-FEC (56 Gbit/s)	-8.0	-8.1	-0.1	-8.1	-0.1
KP-4 (56 Gbit/s)	-7.0	-5.8	1.2	-6.5	0.5
KR-4/SR-4 (56 Gbit/s)	-6.2	-4.4	1.8	-5.2	1
7% HD-FEC (80 Gbit/s)	-5.9	-6.7	-0.8	-6.0	-0.1
KP-4 (80 Gbit/s)	-5.8	-4.1	1.7	-4.3	1.5
KR-4/SR-4 (80 Gbit/s)	-3.8	-2.7	1.1	-	-
7% HD-FEC (100 Gbit/s)	-2.8	-	-	- 2.9	-0.1
KP-4 (100 Gbit/s)	-	-	-	-	-
KR-4/SR-4 (100 Gbit/s)	-	-	-	-	-

Table 5.3: The comparison of the BER performance, i.e. BER v.s. optical power, over 200 m OM3 MMF between Leech24D-2, PAM-4, and BB8 (unit dBm).

FEC threshold	**Leech24D-2**	**PAM-4**	Δ_{PAM-4}	**BB8**	Δ_{BB8}
7 % HD-FEC (80 Gbit/s)	-5.5	-5.9	-0.4	-5.5	0
KP-4 (80 Gbit/s)	-4.8	-4.4	0.4	-4.8	0
KR-4/SR-4 (80 Gbit/s)	-3.8	-	-	-2.8	1
7 % HD-FEC (100 Gbit/s)	-2.1	-	-	-	-
KP-4 (100 Gbit/s)	-	-	-	-	-
KR-4/SR-4 (100 Gbit/s)	-	-	-	-	-

5.5.3 Tolerance for insertion loss

The tolerance for the insertion loss is estimated in Fig. 5.6. For different modulation formats and bit rates (defined by corresponding baud rates) over a 200 m MMF link, we observe an obvious enhancement of the tolerance for the power loss, when keeping the same bit-rate. In general, a 2 dB tolerance margin for the insertion loss is earned between the Leech24D-2 and PAM-4, with a reduced but still obvious difference between Leech24D-2 and BB8 by averagely 1 dB. While all considered modulation formats show similar power loss tolerance at the standard 7 % hard-decision feed-

Table 5.4: The comparison of the BER performance vs. channel bit rate in OBTB (upper rows) and over 200 m OM3 MMF (lower rows) between Leech24D-2, PAM-4, and BB8 (unit Gbit/s).

FEC threshold	**Leech24D-2**	**PAM-4**	Δ_{PAM-4}	**BB8**	Δ_{BB8}
7 % HD-FEC (OBTB)	106.2	102.5	3.7	106.2	0
KP-4 (OBTB)	100.0	92.1	7.9	96.7	3.3
KR-4/SR-4 (OBTB)	96.2	85.0	11.2	89.2	7.0
7 % HD-FEC (200 m OM3)	103.9	102.1	1.7	103.2	0.7
KP-4 (200 m OM3)	97.8	90.6	7.2	94.9	2.9
KR-4/SR-4 (200 m OM3)	91.5	81.4	10.1	88.2	3.3

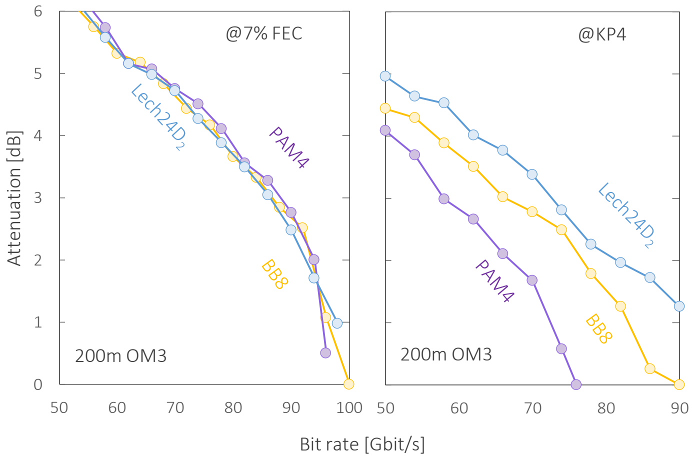

Figure 5.6: Tolerance for loss vs. channel bit rate with Leech24D-2, BB8 and PAM-4 in OBTB and over 200 m OM3 MMF.

forward error correction (HD-FEC) threshold, at the KP-4 FEC threshold (BER=2.2×10^{-4}) 24-D format outperforms both the PAM-4 and 8-D counterparts, especially for the higher bit rates.

5.6 Conclusion

In this chapter, we propose a new 24-D modulation format for IM-DD transmission systems. It shows a significant gain at the low BER values compared to the standard PAM-4 modulation and 8-D formats, which implies its potential in the high-speed short-reach communication scenarios, where the use of low OH FEC schemes with minimized latency is crucial. Meanwhile, the proposed modulation scheme enables a 100 Gbit/s transmission over 200 m OM3 MMF link within the hardware limits.

The complexity of the realization of Leech24D-m is a major drawback, where there are two main factors: (1) the decoding structure is complicated. The cost on the design and power of the operation is therefore increased; (2) it relies on a Golay en- and decoder. Even though the Golay codes are short and straightforward, it adds the latencies, which may spoil all the benefits earned from the complicated structure. The possible application scenario may hide among the short-reach Ethernet connection of transmission range from 100 m to kms, where low OH FEC scheme or even non-FEC scheme is adopted. One typical application may follow the regulations according to 100GBASE-DR, i.e. 802.3cd [6], which is under discussion.

Leech24D-m may be also used as a start point of constructing a rate-flexible format family, which will be given in Chapter 8, and its application in the sub-carrier system will be introduced in the same chapter. The (de)modulation principles used are all based on the discussion in this chapter.

The works presented in this chapter are summarized in the **PAPER 4**.

Chapter 6

Multi-dimensional Rate Flexible PAM

Optimizing the utilization of hardware resources and achieving a flexible transmission is a fundamental objective in the design of intensity-modulated direct-detection (IM-DD) transceivers using pulse amplitude modulation (PAM). The conventional PAMs may underuse the system resource, e.g. bandwidth or maximum output power. Besides, the rigid PAMs with 1 bit per symbol, i.e. bit/sym, granularity are flexible enough to support agile transmissions. However, by taking advantages of the geometric features inside the multi-dimensional PAM (MD-PAM) optimized with a certain multi-dimensional (MD) densest lattice, we propose two families of formats, which enable the flexible multi-rate transmissions and the smooth transition between different bit-rates.

In this chapter, we place the investigation on the performance of the new format families in single carrier systems. In Section 6.1, the formalization of the question is given, together with the principle of the rate-flexibility from two different perspectives, which lead to two different designs of the rate-flexible PAMs in different application scenarios. We discuss the formation of E_8Flex-m[1] and the corresponding modulation techniques in detail in Section 6.2. It enables a flexible transition of bit-rate with finer granularities down to 0.125 bit/sym. In the same section, a rate-flexible IM-DD transceiver with a software-defined bit-rate up to net 100 Gbit/s, using the newly designed format family E_8Flex-m, is experimentally veri-

---

[1] Note that we reserve the lowercase m after a name of format to indicate the number of bits per super-symbol regardless of the number of dimensions, if without specific indication.

fied. Such transceiver sufficiently utilizes the bandwidth resource and power budget and benefits from the simplicity of the hardware implementation of PAM-m modulators. By using fractional bit/sym[2], we demonstrate a net 100 Gbit/s transmission over 200 m OM4 multi-mode fiber (MMF) and gross 100 Gbit/s over 1 km standard single-mode-fiber (SSMF), where both pulse amplitude modulation with 4 levels (PAM-4) and pulse amplitude modulation with 8 levels (PAM-8) fail. In Section 6.3, we place emphasis on the design principle, constellation scaling and shaping techniques and numerical results of Jupiter-m. The possible advantages in multi-subcarrier systems will be explored in the later chapter.

6.1 Multi-dimensional rate flexible PAM

6.1.1 Motivation

PAM formats carry an integer bit/sym; and the multi-dimensional formats described in the previous chapters carry equivalent bits in each symbol. It implies the bit-rate is an integer multiple of system baud-rate, i.e. a granularity of 1 bit/symbol. One limitation of such formats lays in the fact that the hardware resources may not be fully utilized. Concretely, for a given link configuration, PAM-4 may underuse the available output power to support the required signal-to-noise ratio (SNR) which guarantees the successful transmission under a certain forward error correction (FEC) threshold, i.e. the required bit error rate (BER), and provide unnecessary power margin; whereas stepping to PAM-8 can be hindered by the insufficient power budget or insufficient SNR. Hence, we have to downscale the format to a smaller scale PAM-m, which implies a loss of bit-rate. A schematic is illustratively shown in Fig. 6.1, in which the yellow triangles in the left inset implies the areas where the system may underuse the resources. Another major constraint of the integer granularity is the rigidity to variations of transmission condition. It cannot provide agile re-adjustments of the bit-rate according to the channel SNR at a time instant. The (de)modulation for a fractional bit/sym is necessary for systems equipped with a rate-flexible PAM. In the right inset of Fig. 6.1, the idea is elaborated in principle. Equipped with constellations of fractional bits, i.e. finer granularity (here 0.5 bit/sym as a concrete example), the step of system requirement is reduced by half.

---

[2] Note that bit/sym indicates the number of bits per regular symbol, i.e. 1-D symbol and bit/sup-sym indicates the number of bits per super-symbol.

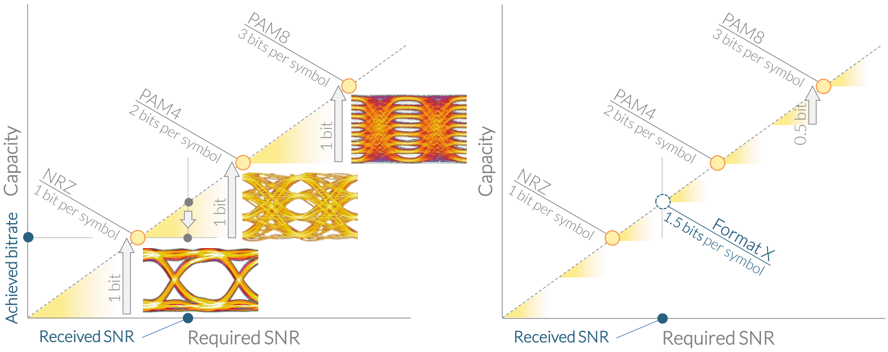

Figure 6.1: Schematic illustration of SNR vs bit-rate with the integer granularity of 1 bit/sym (left) and fractional granularity 0.5 bit/sym (right).

A solution to such gap is hidden in the modified multi-dimensional (MD) modulation formats [60,70]. Such formats carry fractional bits per symbol. In general, as discussed in Section 4.1, an n-dimensional PAM super-symbol consists of n regular symbols. Extra bits added and removed from one super-symbol are shared by n regular symbols, leading an average $1/n$-bit transition between bit-rate steps, namely finer granularity of $1/n$ bit/sym. Applying a certain principle of the scale shift on a MD constellation leads to a specific family of formats, which provides a serial of constellations with various bit-rates according to the required SNR. Furthermore, such MD formats enable rate-flexible transmissions. By fully utilizing the symmetry and concision of certain MD lattice, a fast bit-to-symbol modulation and its corresponding demodulation can be designed for a smooth transition of bit-rates with a uniformed modulation framework, leading to a flexible real-time bit-rate adjustment.

Two families of rate-flexible MD formats constructed with different principles of constellation scale-gearing are discussed in this chapter. One stems from the hierarchical partition of the constellation set, similarly as discussed in Section 4.4.1, which leads to an eight-dimensional (8-D) rate-flexible PAM, named as E_8Flex-m. It consists of an 8-D format family, which has a granularity of spectral efficiency down to 0.125 bit/sym and is equipped with a uniformed (de)modulation framework. Another format family, on the other hand, applies the so-called scaling and shaping techniques on the twenty-four-dimensional (24-D) constellation sets, named as Jupiter-m, which stems from the formats called Leech24D-m as discussed in Chapter 5.

6.1.2 Formalization

In mathematics, a *partition* of a set is a grouping of the set's elements into non-empty subsets, and every element is included in one and only one of the subsets. We define a partition of set $\mathbf{A}$, $\mathscr{P} \subseteq P(\mathbf{A})$, if:

(1) $\forall\, \mathbf{B} \in \mathscr{P}, \mathbf{B} \neq \emptyset$;

(2) $\forall\, \mathbf{B}, \mathbf{B}' \in \mathscr{P}, \mathbf{B} = \mathbf{B}' or \mathbf{B} \cap \mathbf{B}' = \emptyset$;

(3) $\bigcup_{\mathbf{B} \in \mathscr{P}} = \mathbf{A}$.

where P($\mathbf{A}$) is the set of the full enumeration of elements grouping for $\mathbf{A}$.

Specifically, a *bipartition* is denoted as $\mathscr{P}_2$, which separates a set into to two subsets. We denote the constellation set $\mathbf{C}^m$ as the n-dimensional PAM carrying m bits, $\mathbf{C}^m = \left\{ \mathbf{C}^m_0, \mathbf{C}^m_1, \cdots, \mathbf{C}^m_l, \cdots, \mathbf{C}^m_{L-1}, \right\}$, $m \in \mathbb{Z}$, and obviously $L = 2^m$. For removing one bit from the super-symbol, we can simply separate alphabet $\mathbf{C}^m$ two orthogonal subsets $\mathbf{C}^{m-1}_l$ and $\mathbf{C}^{m-1}_r$, equivalent to find partition $\mathscr{P}$ leading to $\mathbf{C}^m = \mathbf{C}^{m-1}_l \cup \mathbf{C}^{m-1}_r$ and $\mathbf{C}^{m-1}_l \cap \mathbf{C}^{m-1}_r = \emptyset$, in which the subscripts 'l' and 'r' indicate the '*left*' set and the '*right*' set, and normally $\mathbf{C}^{m-1}_l \cong \mathbf{C}^{m-1}_r$, It means $\mathbf{C}^{m-1}_l$ and $\mathbf{C}^{m-1}_r$ are isomorphic, implying that they keep the same intrinsic geometry, but may differ with a specific linear operation, e.g. translation, reflection, rotation, and scaling.

We define a format family $\mathscr{C} = \left\{ \mathbf{C}^1, \mathbf{C}^2, \cdots, \mathbf{C}^{m-1}, \cdots, \mathbf{C}^m, \cdots \right\}$, offering a serial of constellations with a scale $L = 2, 2^2, \cdots, 2^{m-1}, 2^m, \cdots$, carrying $1, 2, \cdots, m-1, m, \cdots$ bits. And the construction of a rate-flexible format family is then equivalent to find a set of bipartitions as Eq. 6.1.

$$\mathscr{P} = \left\{ \mathscr{P}^1_2, \mathscr{P}^2_2, \cdots, \mathscr{P}^{m-1}_2, \cdots, \mathscr{P}^m_2, \cdots \right\} \tag{6.1}$$

resulting in the hierarchy $\mathbf{C}^1 \subset \mathbf{C}^2 \subset \cdots \subset \mathbf{C}^m \subset \cdots$. Ideally, it is preferred that $\forall m$, $\mathbf{C}^m \subset \mathbf{L}$, meaning that constellations in any hierarchical level root in the same lattice. Yet, in the actual implementation, it is normally hard to realize. To relax the condition, we can regulate a periodical return to lattice $\mathbf{L}$. In form, $\forall m$, when m(modM_p)$\equiv 0$, $\mathbf{C}^m \subset \mathbf{L}$. In the case of E$_8$Flex-$m$, $M_p = 4$.

6.1.3 Bit-rate transition

Theoretically, for reducing the bit numbers, arbitrary bipartitions can be used. Yet, the concrete design of the rate-flexible formats takes into account

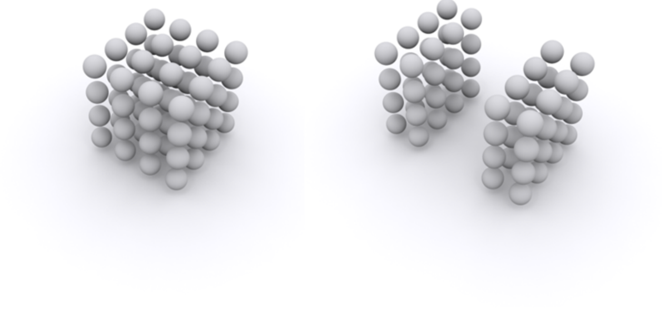

Figure 6.2: Constellation reduction via a direction bipartition.

more details on the way of constellation bipartitions, which results in two major principles for constructing constellation series.

In general, there are two factors to be considered. One is the matched geometric structures of constellation sets with the feature of signal space, or equivalently the SNR_n in each dimension, which keeps the optimal (maximum) utilization of the signal space for the followed subsets and guarantees the achievable BER performance through the whole bit shifts.

Another factor is that the selected subsets are expected to keep the symmetry of its parent set and the hierarchical structure of the lattice. It is essential for keeping the simplicity and uniformity of the (de)modulation schemes through the whole constellation family, which then enables the smooth bit transitions.

Constellation shaping

The most straightforward way of downscaling the constellation set is to select one of the subsets after a direct bipartition, which cuts the constellation set by half in a certain dimension. A schematic illustration is shown in Fig. 6.2 with the help of Z_3 lattice as the analogy of 3-D space to elaborate the direct bipartition. A major benefit of such brutal method lays in the fact that the intrinsic lattice structure remains in each subset, which enables the possible simple and uniform (de)modulation schemes. Such a set partition solution is natural for the cases where SNR_n are various at different orientations, i.e. dimensions. An example is the subcarrier transmission over a colorful channel. The SNRs for each subcarrier are different. We will elaborate the principle on the construction of a rate-flexible format, together with extra constellation shaping techniques on a specific lattice structure in later section. And we will discuss its application and performance in a multi-subcarrier system in the later chapter.

However, for a single carrier MD-PAM, the SNRs for the temporally adjacent symbols are theoretically equal, if we neglect the actual variations due to the nonlinearity of vertical-cavity surface-emitting laser (VCSEL). It is equivalent to visualize as filling hyperspheres into the signal space with the same size in each dimension, i.e. a hypercube. The direct bipartition in this case, therefore, is no more compatible. The reduction of occupancy in a certain dimension leaves unfilled space, implying the waster of system resources, e.g. power. Alternatively, we can scale the constellation in the corresponding dimension. It leads to the asymmetric minimum mutual Euclidean distance (MMED) in different dimensions and remains the overall MMED in the whole signal space. The impacts include (1) the whole constellation set is equivalently skewed in the signal space, apart from the original lattice set; (2) the impact from additive white Gaussian noise (AWGN) is then unequal in each dimension, transforming from hypersphere into hyperellipsoid; (3) and the BER is determined mainly by the dimension with the highest density, i.e. smallest MMEDs. Mathematically, the extra scaling operation breaks the symmetry of the lattice. The subset after scaling in one specific dimension, instead of the whole signal space, is not the subset of its parent constellation set, or isomorphic to its coset of bipartition.

Set-partitioning

One possible solution is to apply set partitions based on the intrinsic lattice geometry, or well known as set-partitioning (SP). Such principle can traces back to the famous set-partitioning algorithm on the conventional quadrature amplitude modulation (QAM) [170,171]. The four-dimensional (4-D) version for the bandwidth flexible transmission for coherent systems has been well discussed in [63]. In our previous works, we extend such scheme to an 8-D version, which utilizes the hierarchical topology of the set partition. An illustrative example is shown in Fig 6.3, where a three-dimensional (3-D) analogy is used to enhance the intuitive understanding. In Fig 6.3, a simple cubic lattice Z_3 is decomposed into two subsets, with the body-centered cubic lattice (b.c.c), i.e. D_3 of each. The occupancies on each dimension of the separated subsets are equal. However, the overall MMED is enlarged without scaling on a specific dimension. Note that such

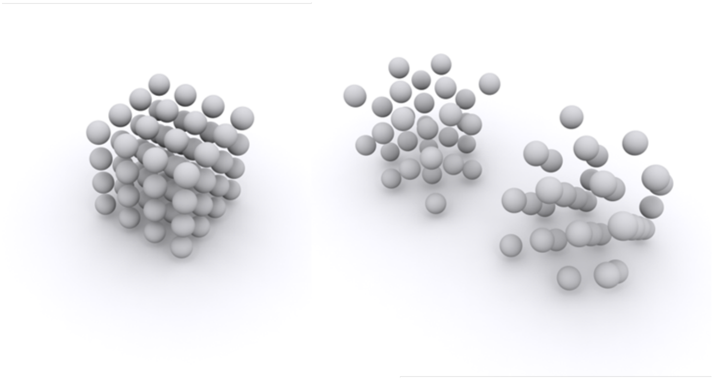

Figure 6.3: Constellation reduction via set-partitioning.

symmetric set-partitioning is not applicable for all kinds of lattices. While E_8 is one of these highly symmetric lattices.

6.2 Eight-dimensional rate-flexible PAM: E$_8$Flex

As discussed above, we apply an 8-D set-partitioning rules to construct a family of formats. It offers a 0.125-bit/sym granularity of the adjustment on the spectral efficiency, i.e. finer rate steps. The (de)modulation is based on the hierarchical nesting relations of E_8, and stems from an uniformed bit-stream based framework.

6.2.1 Formalization

Finer granularity

Formally, the input bit stream, $\mathbf{B}$, is first divided into bit blocks, $\mathbf{B}_k$, as $\mathbf{B} = [\ \mathbf{B}_0\ \mathbf{B}_1\ \cdots\ \mathbf{B}_k\ \cdots\ ]^{\mathrm{T}}$. For each input bit block $\mathbf{B}_k = [\ b_k^0\ b_k^1\ \cdots b_k^e\ \cdots\ b_k^m\ ]^{\mathrm{T}}$ is mapped into the regular symbol sequence $\mathbf{S}_k = [S_k^0\ S_k^1\ \cdots\ S_k^i\ \cdots\ S_k^7]^{\mathrm{T}}$. For each E$_8$Flex-$m$ super-symbol, $\mathbf{S}_k \in \mathbf{C}^m$, in which $\mathbf{C}^m$ is the corresponding constellation set. E$_8$Flex-m is geared to E$_8$Flex-(m-1) by reducing the scale of constellations from $\mathbf{C}^m$ to $\mathbf{C}^{m-1}$ via the bipartition, $\mathscr{P}_2^{m-1}$. The reduced bit is shared by 8 regular symbols, leading to a granularity equal to 0.125 bit/sym. The granularity of the data rate equals to 1/8 system baud rate. Two indicative parameters are extracted, i.e. γ, $\delta \in \mathbb{N}$, $\gamma = \lfloor m/8 \rfloor$, and $\delta = \mathrm{mod}(m, 8)$, in which $\lfloor \cdot \rfloor$ denoted as rounding down, i.e. floor function. Apparently, γ gives the integer part of bits per symbol, whereas δ for the fractional part.

Hierarchical set-division

In Section 4.4.1, we have elaborated the hierarchical structure of the subset division of E_8 lattice, i.e. $\mathbf{L}_{E_8}$. It offers a natural principle of the set-partitioning we desire. A four-level partition is given from the E_8 hierarchical lattice structure, equivalent to a 4-bit scale-reduction, namely 0.5 bit/sym. We start from E$_8$Flex-m, where $m = 8\gamma$, in which $\gamma \in \mathbb{N}$. Obviously, $\mathbf{C}^m \subset \mathbf{L}_{E_8}$. For applying the continuous set-partitioning, after every four-bit reduction, the constellation should return to $\mathbf{L}_{E_8}$ as discussed in Sect. 6.1.2, so that we can further applying the bipartition serial $\mathscr{P}_2^{m-1}$. Yet, rigorously $\mathbf{C}^m \not\subset \mathbf{L}_{E_8}$. To solve this, we applying extra operation on the lattice grids, when $\mathrm{mod}(m, 8) = 4$. The most intuitive way is rotating the grid set by $\pi/4$ and scaling by a factor of $\sqrt{2}$. However, normally we omit the scaling factor, as the normalization process will be anyways applied on in the later processing. Formally $\mathbf{C}^{m-4} \subset \mathbf{L}_{E_8}^{\pi/4}$. We simply denote $\mathbf{L}_{E_8}^{\pi/4}$ as $\mathbf{L}'_{E_8}$. And then we can apply the set-partitioning rule again to reduce the scale of constellation further. The relation shows like the following in Eq. 6.2.

$$\cdots \underset{(\mathbf{C}_{8\gamma})}{\mathbf{L}_{E_8}} \xrightarrow[(\,\mathbf{C}_{8\gamma-1},\mathbf{C}_{8\gamma-2},\mathbf{C}_{8\gamma-3}\,)]{\mathscr{P}_2^{8\gamma-1},\mathscr{P}_2^{8\gamma-2},\mathscr{P}_2^{8\gamma-3}} \underset{(\mathbf{C}_{8\gamma-4})}{\mathbf{L}'_{E_8}} \xrightarrow[(\,\mathbf{C}_{8\gamma-5},\mathbf{C}_{8\gamma-6},\mathbf{C}_{8\gamma-7}\,)]{\mathscr{P}_2^{8\gamma-5},\mathscr{P}_2^{8\gamma-6},\mathscr{P}_2^{8\gamma-7}} \underset{(\mathbf{C}_{8\gamma-8})}{\mathbf{L}_{E_8}} \cdots \tag{6.2}$$

Even though the subgroups for $\mathbf{L}_{E_8}$ and $\mathbf{L}'_{E_8}$ are differ from the orientation, by using the symmetry principle, we can treat them as equivalent, or isomorphic, i.e. $\mathbf{L}_{E_8} \cong \mathbf{L}'_{E_8}$. Thus, we can define a parameter $\eta = \mathrm{mod}(\delta, 4)$ to indicate the the level of hierarchy of the subgroup combination, and $\rho = \mathrm{mod}(m, 4)$ to indicate the cycle of the combinations. For a more concrete illustration, the subgroup combinations with a specific level η are shown Tab. 6.1-Tab. 6.4.

Groups of 2-D appearance

The hierarchy of the sub-group combinations shows that $\mathbf{C}^m$ with the same ρ can be grouped into one, which share the similar two-dimensional (2-D) projections, even though it may have more complicated temporal combinations. The illustration of the 2-D appearances are shown in Fig. 6.4.

Table 6.1: The combination of the sub-groups, $\eta = 4$, i.e. $\eta = 0$.

$\boldsymbol{\Theta}$	$\boldsymbol{\Theta}$	$\boldsymbol{\Theta}$	$\boldsymbol{\Theta}$	$\boldsymbol{\Phi}$	$\boldsymbol{\Phi}$	$\boldsymbol{\Phi}$	$\boldsymbol{\Phi}$
$\boldsymbol{\Theta}$	$\boldsymbol{\Theta}$	$\boldsymbol{\Omega}$	$\boldsymbol{\Omega}$	$\boldsymbol{\Phi}$	$\boldsymbol{\Phi}$	$\boldsymbol{\Psi}$	$\boldsymbol{\Psi}$
$\boldsymbol{\Theta}$	$\boldsymbol{\Omega}$	$\boldsymbol{\Theta}$	$\boldsymbol{\Omega}$	$\boldsymbol{\Phi}$	$\boldsymbol{\Psi}$	$\boldsymbol{\Phi}$	$\boldsymbol{\Psi}$
$\boldsymbol{\Theta}$	$\boldsymbol{\Omega}$	$\boldsymbol{\Omega}$	$\boldsymbol{\Theta}$	$\boldsymbol{\Phi}$	$\boldsymbol{\Psi}$	$\boldsymbol{\Psi}$	$\boldsymbol{\Phi}$
$\boldsymbol{\Omega}$	$\boldsymbol{\Theta}$	$\boldsymbol{\Theta}$	$\boldsymbol{\Omega}$	$\boldsymbol{\Psi}$	$\boldsymbol{\Phi}$	$\boldsymbol{\Phi}$	$\boldsymbol{\Psi}$
$\boldsymbol{\Omega}$	$\boldsymbol{\Theta}$	$\boldsymbol{\Omega}$	$\boldsymbol{\Theta}$	$\boldsymbol{\Psi}$	$\boldsymbol{\Phi}$	$\boldsymbol{\Psi}$	$\boldsymbol{\Phi}$
$\boldsymbol{\Omega}$	$\boldsymbol{\Omega}$	$\boldsymbol{\Theta}$	$\boldsymbol{\Theta}$	$\boldsymbol{\Psi}$	$\boldsymbol{\Psi}$	$\boldsymbol{\Phi}$	$\boldsymbol{\Phi}$
$\boldsymbol{\Omega}$	$\boldsymbol{\Omega}$	$\boldsymbol{\Omega}$	$\boldsymbol{\Omega}$	$\boldsymbol{\Psi}$	$\boldsymbol{\Psi}$	$\boldsymbol{\Psi}$	$\boldsymbol{\Psi}$

Table 6.2: The combination of the sub-groups, $\eta = 3$.

$\boldsymbol{\Theta}$	$\boldsymbol{\Theta}$	$\boldsymbol{\Theta}$	$\boldsymbol{\Theta}$
$\boldsymbol{\Theta}$	$\boldsymbol{\Theta}$	$\boldsymbol{\Omega}$	$\boldsymbol{\Omega}$
$\boldsymbol{\Theta}$	$\boldsymbol{\Omega}$	$\boldsymbol{\Theta}$	$\boldsymbol{\Omega}$
$\boldsymbol{\Theta}$	$\boldsymbol{\Omega}$	$\boldsymbol{\Omega}$	$\boldsymbol{\Theta}$
$\boldsymbol{\Omega}$	$\boldsymbol{\Theta}$	$\boldsymbol{\Theta}$	$\boldsymbol{\Omega}$
$\boldsymbol{\Omega}$	$\boldsymbol{\Theta}$	$\boldsymbol{\Omega}$	$\boldsymbol{\Theta}$
$\boldsymbol{\Omega}$	$\boldsymbol{\Omega}$	$\boldsymbol{\Theta}$	$\boldsymbol{\Theta}$
$\boldsymbol{\Omega}$	$\boldsymbol{\Omega}$	$\boldsymbol{\Omega}$	$\boldsymbol{\Omega}$

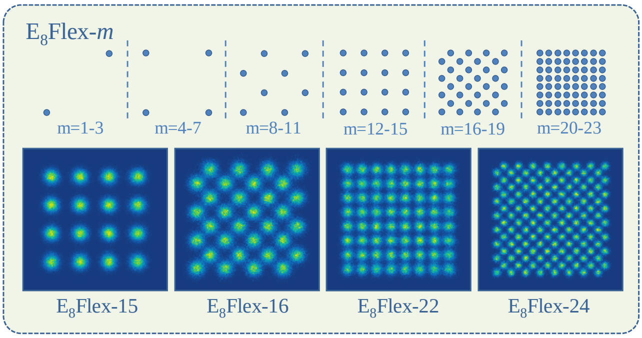

Figure 6.4: 2-D appearances of E_8Flex-m constellations.

Table 6.3: The combination of the sub-groups, $\eta = 2$.

$\mathbf{\Theta}$	$\mathbf{\Theta}$	$\mathbf{\Theta}$	$\mathbf{\Theta}$
$\mathbf{\Theta}$	$\mathbf{\Theta}$	$\mathbf{\Omega}$	$\mathbf{\Omega}$
$\mathbf{\Omega}$	$\mathbf{\Omega}$	$\mathbf{\Theta}$	$\mathbf{\Theta}$
$\mathbf{\Omega}$	$\mathbf{\Omega}$	$\mathbf{\Omega}$	$\mathbf{\Omega}$

Table 6.4: The combination of the sub-groups, $\eta = 1$.

$\mathbf{\Theta}$	$\mathbf{\Theta}$	$\mathbf{\Theta}$	$\mathbf{\Theta}$
$\mathbf{\Omega}$	$\mathbf{\Omega}$	$\mathbf{\Omega}$	$\mathbf{\Omega}$

Multi-granularity modulation

From the symmetry of lattice, we can straightforwardly extract a relation in Eq 6.3.

$$\cdots\ \mathbf{C}^{\delta} \subset \mathbf{C}^{\delta+8} \subset \mathbf{C}^{\delta+8\gamma}\ \cdots \tag{6.3}$$

More rigorously, the relation between $\mathbf{C}^{\delta+8\gamma}$ and $\mathbf{C}^{\delta+8(\gamma+1)}$ is expressed as Eq. 6.4.

$$\mathbf{C}^{\delta+8(\gamma+1)} = \mathbf{C}^{\delta+8\gamma} + \sum_{i=0}^{7} \beta_i \mathbf{L}_0^i \tag{6.4}$$

in which, $\beta_i \in \{0,\, 1\}$ and $\mathbf{L}_0^i = [0,\, 0, \cdots, L_0^i, \cdots,\, 0]^{\mathrm{T}}$, $L_0^i = 2^{\gamma+1}$.

$\mathbf{C}^{\delta+8(\gamma+1)}$ can be treated as the extension of $\mathbf{C}^{\delta+8\gamma}$ in the 8-D signal space. Based on that, we can extend it to a more general form as expressed in Eq. 6.5.

$$\mathbf{C}^{\delta+8\gamma} = \mathbf{C}^{\delta} + \mathbf{W}\mathbf{D} \tag{6.5}$$

where $\mathbf{W} = [\,\mathbf{W}_0\, \mathbf{W}_1\, \cdots\, \mathbf{W}_i\, \cdots\, \mathbf{W}_7\,]^{\mathrm{T}}$, $\mathbf{W}_i = [\, w_i^0\ w_i^1\ \cdots\ w_i^{\nu}\ \cdots\ w_i^{\gamma-1}\,]$, $w_i^{\nu} \in \{0,\, 1\}$; and $\mathbf{D} = [\ 2\ 2^2\ \cdots\ 2^{\gamma}\ ]^{\mathrm{T}}$. For an arbitrary $\mathbf{C}^m$, when $m(\mathrm{mod}8) \equiv \gamma$, is just an extension of $\mathbf{C}^{\gamma}$, or the tessellation of $\mathbf{C}^{\gamma}$ on a simple hypercubic lattce Z_8. Thus, it implies that the coded bits are used to adjust the spectral efficiency with finer granularity; whereas the uncoded bits modulate the signal like a regular PAM.

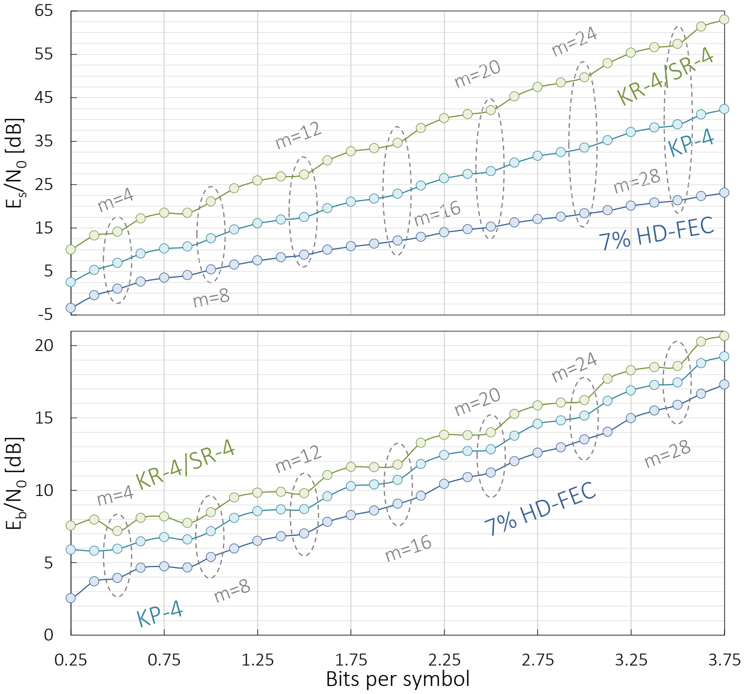

Figure 6.5: Monte-Carlo simulations of the theoretical SNR vs. bit per symbol for E$_8$Flex-m with different m with respect to three different FEC threshold, i.e. 7% HD-FEC, KP-4 and SR-4/KP-4. (upper) SNR defined with average power per (regular) symbol E$_\mathrm{s}$/N$_0$. (lower) SNR defined with average power per bit E$_\mathrm{b}$/N$_0$.

Monte-Carlo results

We verify the theoretical performance of E$_8$Flex-m by using the Monte-Carlo simulation. Fig. 6.5 shows the results. We define the SNR with both average power per regular symbol, i.e. E$_\mathrm{s}$/N$_0$ shown in the upper inset of Fig. 6.5, and the average power per bit, i.e. E$_\mathrm{b}$/N$_0$ shown in the lower inset of Fig. 6.5. We find that required SNR of E$_8$Flex-m for successful transmission with respect to 7% FEC changes linearly and smoothly with the increase of bit/sym, with the granularity of 0.125 bit/sym, reaching a slope of 6.9 dB·sym/bit[3] and 4.1 dB·sym/bit for E$_\mathrm{s}$/N$_0$ and for E$_\mathrm{b}$/N$_0$. For the transmission for FEC with lower overhead (OH), i.e. in the lower noise regime, the general tendency of the change is linear, reaching the slopes of 11 dB/bit and 14.5 dB·sym/bit for KP-4 and SR-4/KR-4 with

---

[3] dB·sym/bit comes from the dB for every bit per regular symbol i.e. dB/(bit/sym).

$\mathrm{E_s/N_0}$ respectively. The values are averaged by bits to 4.2 dB·sym/bit and 4.1 dB·sym/bit for KP-4 and SR-4/KR-4 accordingly. The general slopes for the required SNR defined as $\mathrm{E_b/N_0}$ are similar. It is noteworthy that there are plateau-liked structures with periods of every four bit/sym. It is especially obvious when the SNR is defined as $\mathrm{E_b/N_0}$. This structure comes from the lattice $\mathrm{E_8}$Flex-m of different m relies on. As discussed before, $\forall m (\mathrm{mod}\ 4) \equiv 0$, $\mathrm{E_8}$Flex-m returns to a subset of E_8, which offers the densest structure in 8-D space. It is known from the previous discussions that formats following the densest lattice possess the optimal asymptotic performance, which reflected as large improvements of sensitivity when entering the low noise regime with respect to the low OH FEC. Yet, for the standard 7% HD-FEC, due to the increase of neighbors, each constellation point is surrounded by more points and surfers from the server impact of noise. For $\forall m (\mathrm{mod}\ 4) \not\equiv 0$, the intrinsic structure of constellation points are apart from the densest one. Therefore the improvement gaps between spectral efficiency steps are not as large as ones for the E_8 based ones.

6.2.2 Symbol-wise modulations

Mapping

As mentioned before, for each super-symbol of $\mathrm{E_8}$Flex-m carrying m bits, two indicative parameters are extracted, i.e. γ, $\delta \in \mathbb{N}$, $\gamma = \lfloor m/8 \rfloor$, and $\delta = \mathrm{mod}(m, 8)$. Obviously, $m = 8 \cdot \gamma + \delta$, in which γ indicates the depth of modulation and a $2^{\gamma+1}$-level PAM modulator is required for each regular symbol, and δ indicates the number of bits shared by 8 regular symbols, resulting in a fractional number of bit per symbol, which equals to $\delta/8$ bits/sym.

A m-bit section in the input bit stream is fed into a register of $8(\gamma{+}1)$ bits, i.e. $\mathbf{a}_k = [\ a_k^0\ a_k^1\ \cdots\ a_k^e\ \cdots\ a_k^{8\gamma+7}\ ]^{\mathrm{T}}$, which consists of two sections as in Eq. 6.6.

$$\mathbf{a}_k = [\ \mathbf{h}_k\ \mid\ \mathbf{g}_k\ ]^{\mathrm{T}} \tag{6.6}$$

in which an 8-bit section $\mathbf{h}_k = [\ h_k^0\ h_k^1\ \cdots\ h_k^i\ \cdots\ h_k^7\ ]^{\mathrm{T}}$ is used for the modulation of fractional bits, which reads as Eq. 6.7.

$$\mathbf{h}_k = [\,\underbrace{0\ 0\ \cdots\ 0}_{8-\delta}\ \mid\ b_k^0\ \cdots\ b_k^{\delta-1}\ ]^{\mathrm{T}} \tag{6.7}$$

It is filled with bits b_k^0 to $b_k^{\delta-1}$ by pending $8-\delta$ zeros in front of them. And $\mathbf{g}_k = [\ g_k^0\ g_k^1\ \cdots\ g_k^e\ \cdots\ g_k^{8\gamma-1}\ ]^{\mathrm{T}}$ indicates the bit section for the integer bit modulation. It is expressed as Eq. 6.8.

$$\mathbf{g}_k = [\ b_k^{\delta}\ \cdots\ b_k^{m}\ ]^{\mathrm{T}} \tag{6.8}$$

Based on $\mathbf{h}_k$, we need also define a flag register, i.e. the controlling bits, $\mathbf{f}_k = [\ f_k^0\ f_k^1\ \cdots\ f_k^i\ \cdots\ f_k^7\ ]^{\mathrm{T}}$, which switches on/off the bit-stream according to the scale of constellation, i.e. the number of effective fed-in bit stream. It is expressed as in Eq. 6.9.

$$\mathbf{f}_k = [\,\underbrace{0\ 0\ \cdots\ 0}_{8-\delta}\ \mid\ \underbrace{1\ 1\ \cdots\ 1}_{\delta}\,]^{\mathrm{T}} \tag{6.9}$$

The bit-to-symbol mapping consists of two phases. The coded bits for the finer granularity are first processed and saved in the register, as the pre-processed bits $\mathbf{t}_k$. The register bit sequence reads $\mathbf{t}_k = [\ t_k^0\ t_k^1\ \cdots\ t_k^i\ \cdots\ t_k^7\ ]^{\mathrm{T}}$. The concrete mapping is indicated with Eq. 6.10-Eq. 6.17.

$$t_k^0 = h_k^7 \tag{6.10}$$

$$t_k^1 = h_k^3 \wedge f_2 + t_k^0 \wedge \overline{f_2} \tag{6.11}$$

$$t_k^2 = h_k^2 \wedge f_1 + t_k^0 \wedge \overline{f_1} \tag{6.12}$$

$$t_k^3 = h_k^6 \wedge f_5 + (\ t_k^0 \oplus t_k^1 \oplus t_k^2\ ) \wedge \overline{f_5} \tag{6.13}$$

$$t_k^4 = h_k^1 \wedge f_0 + t_k^0 \wedge \overline{f_0} \tag{6.14}$$

$$t_k^5 = h_k^5 \wedge f_4 + (\ t_k^2 \oplus t_k^3 \oplus t_k^4\ ) \wedge \overline{f_4} \tag{6.15}$$

$$t_k^6 = h_k^4 \wedge f_3 + (\ t_k^1 \oplus t_k^2 \oplus t_k^5\ ) \wedge \overline{f_3} \tag{6.16}$$

$$t_k^7 = t_k^0 \oplus t_k^1 \oplus t_k^2 \oplus t_k^3 \oplus t_k^4 \oplus t_k^5 \oplus t_k^6 \tag{6.17}$$

After that, the symbols are modulated as the regular PAM-m modulator, similar to the Eq. 6.18[4].

$$S_k^i = h_k^0 \wedge f_0 + 2t_k^i + \sum_{\nu=0}^{\gamma-1} 2^{\nu+2} g_k^{8\nu+i} \tag{6.18}$$

in which, $i = 0,\ 1,\ \cdots,\ n-1$.

Principles for IC design

Fig. 6.6 shows a schematic illustration of the proposed bit-wise modulation in a possible integrated circuit (IC) design. The left inset elaborates the

---

[4] Note that for convenience, the results of Eq. 6.18 is scaled by a factor of 2.

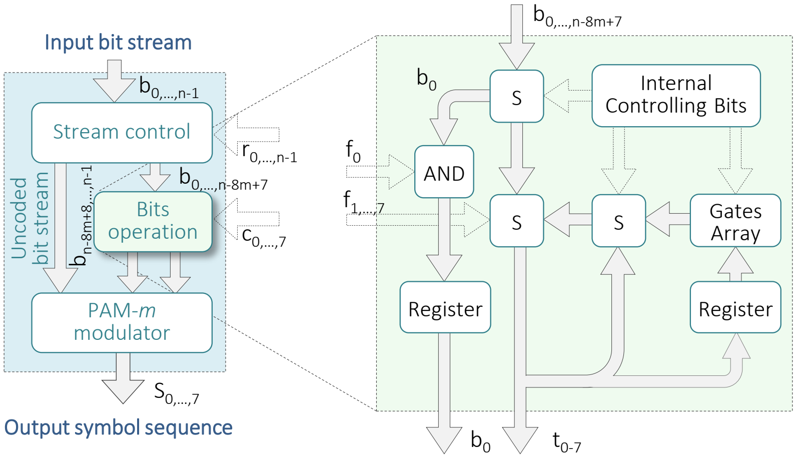

Figure 6.6: The principle diagrams of the IC design for decoding E$_8$Flex-m: (left) the schematic illustration of the bit-stream modulation. (right) the schematic flow chart for the bit operation. S-Switcher; b_i-information bits; f_i-controlling bits.

principle of the bit-wise modulation with multi-granularity. For the input bit-section, γ bits are used to generate finer granularity. They are pre-processed through a bit operation block and converted into pre-processed bits $\mathbf{t}_k$. They are fed, together with the reset of input bits, into a regular PAM-m modulator.

The right inset of Fig. 6.6 explains the details of the pre-processing block. The flag register $\mathbf{f}_k$ turns on/off the input ports. When it is on, i.e. $f_k^i = 1$, output ports directly use the bit streams from the corresponding input ports. When it is off, i.e. $f_k^i = 0$, the input port is prohibited and no input stream is accepted. The output ports use the bits generated and calculated by bits from other input ports and the bits saved in the caches.

6.2.3 Symbol-to-bit demodulation

According to the bit-to-symbol mapping rules, the corresponding demodulation is straightforward. We define the estimated bit sequence $\widehat{\mathbf{b}}_k = [\ \widehat{b}_k^0\ \widehat{b}_k^1\ \cdots\ \widehat{b}_k^e\ \cdots\ \widehat{b}_k^m\ ]^{\mathrm{T}}$ for the k-th E$_8$Flex-m super-symbol. The register sequence for the estimated bits is $\widehat{\mathbf{a}}_k = [\ \widehat{a}_k^0\ \widehat{a}_k^1\ \cdots\ \widehat{a}_k^e\ \cdots\ \widehat{a}_k^{8\gamma+7}\ ]^{\mathrm{T}}$, where the bit-section for the fractional bits is $\widehat{\mathbf{h}}_k = [\ \widehat{h}_k^0\ \widehat{h}_k^1\ \cdots\ \widehat{h}_k^e\ \cdots\ \widehat{h}_k^7\ ]^{\mathrm{T}}$ and the integer bits is $\widehat{\mathbf{g}}_k = [\ \widehat{g}_k^0\ \widehat{g}_k^1\ \cdots\ \widehat{g}_k^{8\gamma-1}\ ]^{\mathrm{T}}$, follows Eq. 6.19.

$$\widehat{\mathbf{a}}_k = [\ \widehat{\mathbf{h}}_k\ \mid\ \widehat{\mathbf{g}}_k\ ]^{\mathrm{T}} \tag{6.19}$$

And the estimated bit sequence can be extracted from the cached bits as Eq. 6.20.

$$\widehat{\mathbf{b}}_k = [\, \widehat{a}_k^{8-\delta}\ \widehat{a}_k^{9-\delta}\ \cdots\ \widehat{a}_k^{8\gamma+7}\,]^{\mathrm{T}} \tag{6.20}$$

The procedure of demodulation follows Eq. 6.21-Eq. 6.28.

$$\widehat{h}_k^0 = \mathrm{mod}(\widehat{R}_k^{0-7}, 2) \tag{6.21}$$
$$\widehat{h}_k^1 = \mathrm{mod}((\widehat{R}_k^4 - \widehat{h}_k^0)/2, 2) \tag{6.22}$$
$$\widehat{h}_k^2 = \mathrm{mod}((\widehat{R}_k^2 - \widehat{h}_k^0)/2, 2) \tag{6.23}$$
$$\widehat{h}_k^3 = \mathrm{mod}((\widehat{R}_k^1 - \widehat{h}_k^0)/2, 2) \tag{6.24}$$
$$\widehat{h}_k^4 = \mathrm{mod}((\widehat{R}_k^6 - \widehat{h}_k^0)/2, 2) \tag{6.25}$$
$$\widehat{h}_k^5 = \mathrm{mod}((\widehat{R}_k^5 - \widehat{h}_k^0)/2, 2) \tag{6.26}$$
$$\widehat{h}_k^6 = \mathrm{mod}((\widehat{R}_k^3 - \widehat{h}_k^0)/2, 2) \tag{6.27}$$
$$\widehat{h}_k^7 = \mathrm{mod}((\widehat{R}_k^0 - \widehat{h}_k^0)/2, 2) \tag{6.28}$$

And each element is expressed as in Eq. 6.29.

$$\widehat{g}_k^{8\nu+i} = \mathrm{mod}((\widehat{R}_k^i - \widehat{h}_k^0)/2^{\nu+2}, 2) \tag{6.29}$$

in which, $\nu = 0, 1, \cdots, \gamma - 1$ and $i = 0, 1, \cdots, 7$.

6.2.4 Hierarchical soft-decision for E$_8$Flex-m

As E$_8$Flex-m roots in the E_8 lattice and is derived from BB8 as discussed in Chapter 4, it can reuse the hierarchical soft-decision (SD) schemes. The schematic illustration of the hierarchical SD is shown in Fig. 6.7. The whole structure of a four-level soft-decision is used only when $\eta = 4$, as discussed in Sect. 4.4.5. As a special case, E$_8$Flex-16, i.e. BB8 in chapter 4, use the four-level SD. However, when $\eta = 3$, only half of such SD framework is used, namely the number of candidate points and decisions are reduced by half. Specially, when $\eta = 1$, only two candidate points are selected and one extra SD is required. Constellations in this special case are actually generated to a 4-D constellation based on D_4 lattice [60]. However, it is beyond the scope of this thesis.

The simplicity of the decision structure is also an important consideration when choosing between formats in the same family.

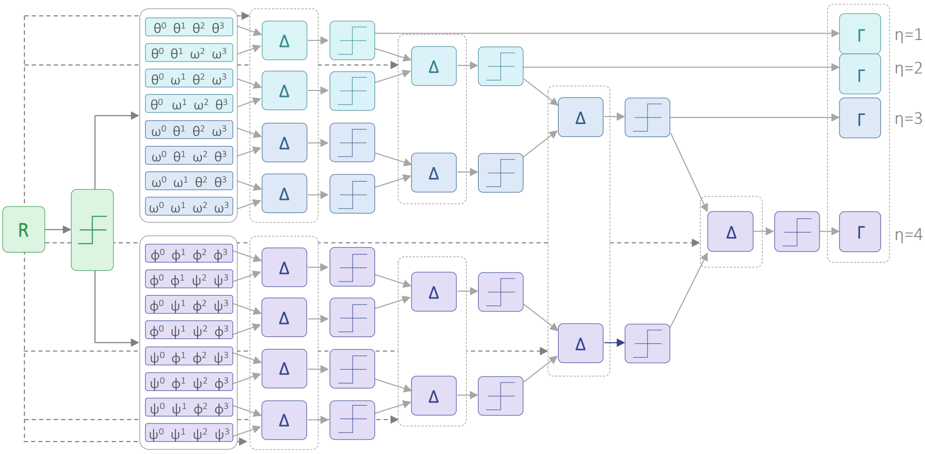

Figure 6.7: The principle of the hierarchical soft-decision for E_8Flex-m.

6.2.5 100 G transceiver

By applying the proposed 8-D format family, we demonstrated a rate-flexible transceiver which supports a 100 Gbit/s transmission. The details of the designing considerations and the performance regarding different system aspects are discussed in this section.

Experimental setups

Fig. 6.8 depicts the structure of the testbed. 850 nm VCSELs of different types, i.e. a multi-mode (MM) VCSEL, and two single-mode (SM) VCSELs coupled with MMF and 850 nm single-mode fiber (SMF) pigtails respectively, were used as optical signal sources. The -3 dB bandwidth of the MM-VCSEL and SM-VCSELs reach 18 GHz and 20 GHz respectively. The optical output power reaches 4 dBm for the MM-VCSEL when biased at 8 mA, 0.5 dBm for the MMF-coupled SM-VCSEL biased at 2.8 mA, and -1.7 dBm for the SMF-coupled SM-VCSEL biased at 2.8 mA. The lasers were modulated by the electrical signal of 0.75 $V_{\text{p-p}}$ from an 8-bit arbitrary waveform generator (AWG) of 64 Gsa/s and $\sim$ 22 GHz analog bandwidth. After transmitted through the fiber links of different lengths, the optical signal was received by a calibrated photoreceiver module with the co-packaged trans-impedance amplifier (TIA). Its -3 dB bandwidth reaches 22 GHz. The electrical signal was then sampled by an 8-bit digital storage oscilloscope (DSO) of $\sim$ 33 GHz analog bandwidth with the sampling rate of 100 GSa/s.

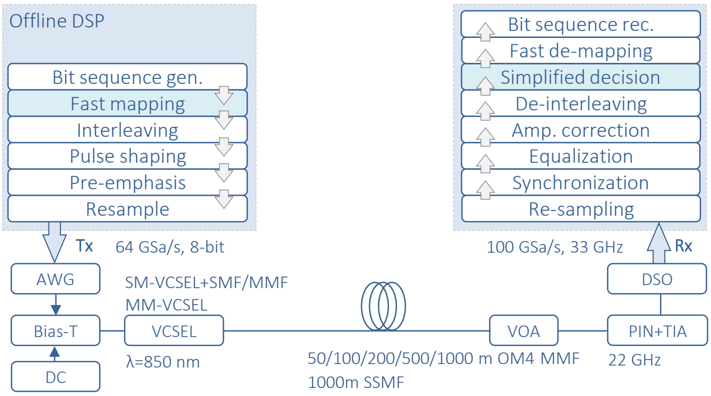

Figure 6.8: Schematics of the experimental setup for a E$_8$Flex-m supported 100 G IM-DD transceiver.

At the transmitter, for each measured trace, 30M-bit input streams were generated randomly for each measurement point for avoiding the pattern dependent effects and mapped with the fast E$_8$Flex-m mapper. After interleaving, the symbol sequences were resampled to the desired baud-rate and shaped into raised cosine/root raised cosine pulses ($\alpha = 0.32$). The output sequences were pre-emphasized, for compensating the electrical spectral roll-off of the transmitter. After transmitted through the physical channel, the signal is processed in the offline digital signal processing (DSP) at the receiver side. The received electrical signal was resampled into two times of the baud-rate, and after sequence synchronization it was equalized by a T-2 fractional feed-forward equalizer (FFE) of 16 taps, together with an amplitude correction. After de-interleaving, the output bit streams were decided by a hierarchical soft-decision and converted by the corresponding E$_8$Flex-m de-mapper. The detailed configuration of the experimental setup is listed in Tab. 6.5.

Choice of laser

For determining the best system configuration, we first placed the emphasis on the choice of lasers between MM VCSEL and SM VCSEL. It is clear from the upper inset of Fig. 6.9 that in the optical back-to-back (OBTB) case, the overall performance of an MM-VCSEL is worse than the SM-VCSELs with both MMF and SMF pigtailed. The capacity difference reaches 10 Gbit/s

Table 6.5: The parameters of the experiment setup for a E_8Flex-m supported 100 G IM-DD transceiver.

Parameter	Symbol	Value	Unit
Sequence length	-	2^{15}	-
Symbol rate	-	32-50	GBaud
Bit-rate	-	100	Gbit/s
Formats	-	E_8Flex-m/PAM-4	-
Bias current MM-VCSEL	I_{bias}^{mm}	8	mA
Bias current SM-VCSEL	I_{bias}^{sm}	2.8	mA
wavelength	λ	850	nm
Modulation amplitude	V_{pp}	0.75	V
AWG analogy frequency	$f_{-3\ dB}^{AWG}$	~ 20	GHz
AWG sampling rate	-	64	GSa/s
AWG vertical resolution	-	8	bit
DSO analogy frequency	$f_{-3\ dB}^{DSO}$	~ 33	GHz
DSO sampling rate	-	100	GSa/s
DSO vertical resolution	-	8	bit
VCSEL pigtail	-	SMF/MMF	-
SMF length	L_{SMF}	1000	m
MMF length	L_{MMF}	50/100/200/500	m
PR bandwidth	$f_{-3\ dB}^{PR}$	22	GHz
PR Gain	G	-80/-70	V/W
PR Output noise	N_{PR}	590	μVrms
PR Impedance	Z_{PR}	50	Ω
Ambient temperature	T	22	°C

at 7% hard-decision feed-forward error correction (HD-FEC) threshold; whereas the gap extends to 15 Gbit/s at KP-4. The comparison between the SM-VCSELs of SMF and MMF pigtails shows that the MMF-pigtailed VCSEL provides slightly better BER performance in case of OBTB. A detailed comparison between these two lasers with respect to the 7% HD-FEC through OM4 MMF of different lengths are shown provided in the lower inset of Fig. 6.9. For cases of OBTB and 100 m MMF link, because of higher output power at the biased current, the performance of MMF-pigtailed SM-VCSEL is slightly better. However, the SMF-pigtailed SM-VCSEL significantly outperforms the MMF-pigtailed one over fiber longer than 200 m.

Specifically, the difference is enlarged to one magnitude when the gross bit-rate reaches 100 Gbit/s.

It stems from the fact that the VCSEL-fiber coupling behaves like a mode filter. The SMF pigtail supports only the fundamental, filtering the higher order modes, performing as a single mode selector. At the pigtail-fiber coupling phase, in most of the cases, the pigtails are aligned with the center of the transmission fiber. The fundamental mode in the pigtail is mainly converted into the fundamental mode in the transmission line, with less power excited into other modes. The modes excitation in the MMF pigtail and the modes conversion during the pigtail-fiber coupling is, however, more complicated. The signal is normally carried by modes of different group velocities, resulting in server inter-modal dispersions. Meanwhile, the SMF-pigtailed SM-VCSEL provides a possibility of transmission over standard ITU-T G.652D compliant SMF, i.e. SSMF, where the SSMF performs as few mode fiber (FMF). Thus, for further investigations into the features of the proposed transceiver scheme, the SMF-pigtailed SM-VCSEL is used.

Bandwidth requirement

Fig. 6.10 shows the OBTB performance for different numbers of bits carried by each super-symbol, i.e. bit/sup-sym, with various baud-rates. The red dot curve gives the gross 108 G threshold with respect to the 7% HD-FEC threshold. The parameter combinations above the threshold enable a pre-FEC bit-rate faster than 108 Gbit/s. The parameters chosen from the shadowed area enable the net 100G transmission and beyond. From this area, it implies that 22 bit/sym in 40 Gbaud systems is a fair choice. It gives a trade-off between bit-rate and system bandwidth, providing a gross rate, i.e. pre-FEC rate, of 110 Gbit/s. In addition, the modulation and demodulation are easier for super-symbols with m=22, i.e. $\eta = 2$. Thus, in the later tests, we use 40 Gbaud for the system investigation and 32 Gbaud as a reference, which corresponds to 5 and 4 Gbit/s rate granularity respectively.

Achievable bit-rate

Fig. 6.11.(a) analyzes the achievable bit-rate of systems equipped with different formats from E_8Flex-m. The OBTB performance of SM-VCSEL shows a transmission potential up to 110 Gbit/s within the power budget of our experimental setup. THe achievable pre-FEC bit-rate starts to

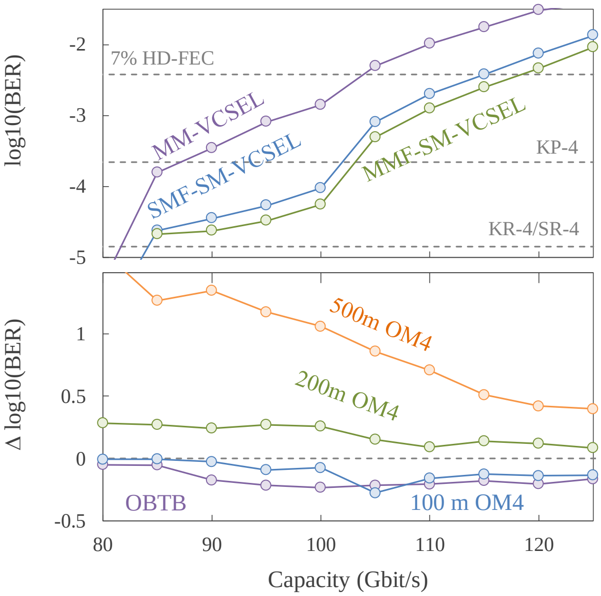

Figure 6.9: The performance comparison between different lasers and fiber links for 100 G IM-DD transceiver: (upper) BER performance vs. channel capacity for different types of VCSEL modules in OBTB mode; (lower) BER difference between MMF- and SMF-pigtailed SM-VCSELs vs. channel capacity for different MMF links at 40 Gbaud symbol rate with respect to the 7% HD-FEC threshold at 3.8×10^{-3}.

saturate at 23 bit/sup-sym because of the limited power as shown in the right inset of Fig. 6.11.(b). It implies that E_8Flex-22 has a near optimal utilization of the laser output power; and at 22 bit/sup-sym, the net 100 G transmission is possible. Another interesting point is E_8Flex-21. Even though it has a lower bit-rate and lower achievable bit-rate, it has the simplest hierarchical soft-decision structure among the formats from E_8Flex-16 to E_8Flex-23. Therefore, it can be also a good format candidate for the 100 G system that we desire.

6.2.6 Performances

After determining the specifications for investigations, we experimentally verify the performance of E_8Flex-m in various system aspects, including the reach extension and tolerance for the power penalty.

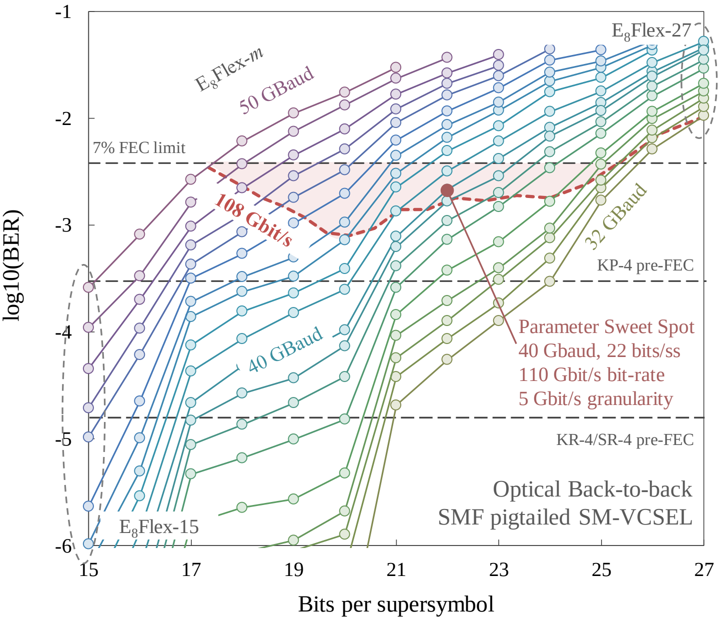

Figure 6.10: The pre-FEC bit-rate with different parameter combinations: numbers of bits per super-symbol and symbol rate.

Comparison between E$_8$Flex-m and PAM signal

Comparing with PAM signal as in Fig. 6.12, we believe that with both PAM-4 and PAM-8 at any symbol rate, the 100 G net transmission is hardly achievable, but it can be provided by 40 Gbaud E$_8$Flex-m, using fractional numbers of bits per symbol. Specifically, it is noteworthy that E$_8$Flex-16 and E$_8$Flex-24 formats, which have the same bit/sym as to PAM-4 and PAM-8, i.e. 2 bit/sym and 3 bit/sym respectively, outperform their conventional PAM counterparts due to the optimized geometrical features as discussed in Chapter 4. The details are listed in the Tab. 6.6.

Reach

Fig. 6.13 gives the maximum reach vs. the bit-rate under the BER limits of different FEC schemes. The maximum reach values are estimated by fitting the transmission results of over 50, 100, 200, 500 m and 1 km MMF links. It is worth mentioning that SSMF provides a gross 100 G transmission over 1 km link and outperforms the 500 m MMF link by the capacity distance

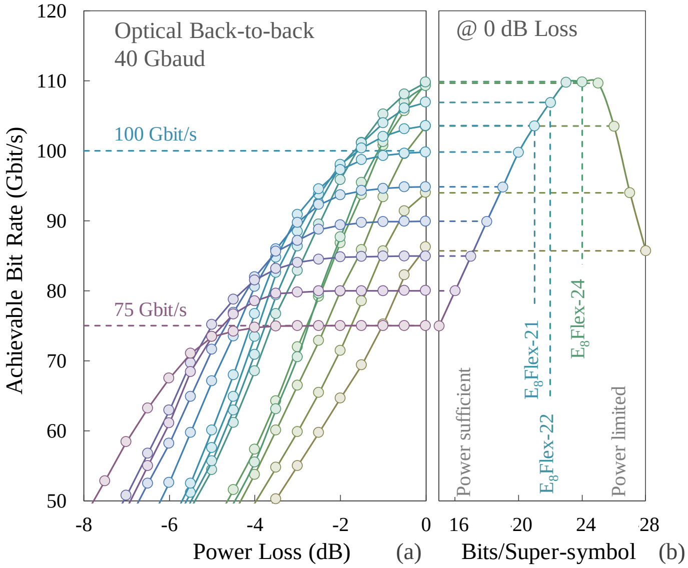

Figure 6.11: Achievable pre-FEC bit-rate for different numbers of bits per super-symbol.

Table 6.6: The comparison of the optical back-to-back performance, i.e. BER v.s. pre-FEC data rate, between E_8Flex-22, E_8Flex-24, E_8Flex-16, PAM-4, and PAM-8 (unit Gbit/s).

FEC threshold	**E_8Flex-22**	**E_8Flex-16**	**E_8Flex-24**	**PAM-4**	**PAM-8**
7 % HD-FEC	113.2	105.1	112.6	106.6	109.1
KP-4	98.3	97.2	96.5	90.2	-
KR-4/SR-4	80.8	89.1	-	81.0	-

product.

Power penalty

Power penalty is estimated in Fig 6.14 for different data rates over 100 m MMF (left) and 1 km SSMF (right) links respectively. The general linearity of power penalty (i.e. SNR) vs. capacity (bit/sup-sym) curves offers

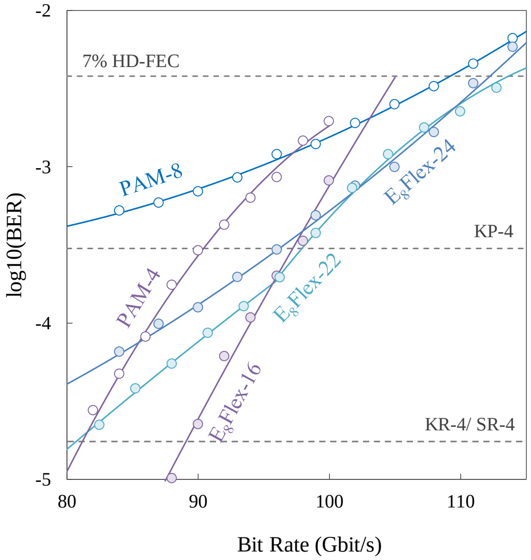

Figure 6.12: BER vs. pre-FEC bit-rate in OBTB mode for conventional PAM and E$_8$Flex-m.

convenience in designing the capacity aware transceivers.

6.3 Twenty four-dimensional rate flexible PAM: Jupiter

In the previous section, we discuss a multi-rate PAM family based on a hierarchy of set-partitioning on the E_8 lattice. In this section, we construct a 24-D format hierarchy with flexible bit-rate based on the Λ_{24} lattice as discussed in Chapter 5, named as Jupiter. The design philosophy is different with E$_8$Flex-m. It adopts the direct extension/partition of constellation set in each dimension, following the principle discussed in Sect. 6.1.3 and leading to a natural compatibility to a hypercuboid signal space, i.e. inconsistent length for different dimensions or equivalently unequal SNR.

6.3.1 Nomination

The name of Jupiter stems from the symbol of Jupiter as Fig. 6.15. We reserve two different nomination rules of Jupiter for differentiating various

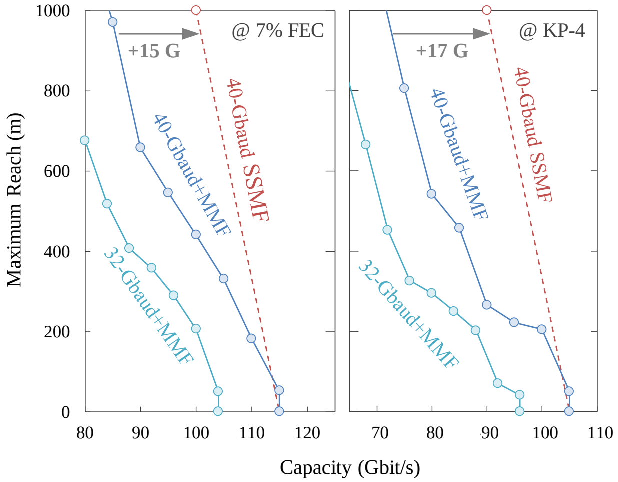

Figure 6.13: Maximum reach vs. channel capacity for 7% overhead hard-decision FEC BER threshold (left), and KP4 FEC BER threshold (right).

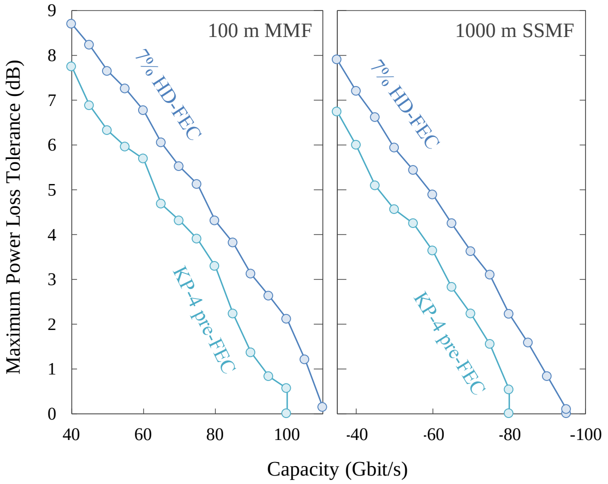

Figure 6.14: Maximum power loss tolerance vs. channel capacity for 100 m OM4 MMF link (left) and 1 km SSMF link (right).

Figure 6.15: Symbol of Jupiter, known as the symbol of 24.

cases. The lowercase name Jupiter-m indicates a 24-D format based on the Λ_{24}, with 12 2-D projections, loaded with the same constellation as Jupiter$_p$-m_p on each projection. Jupiter-m carries m bits for each super-symbol, with average m_p bits per projection, and obviously $m = 12m_p$. Meanwhile, the uppercase JUPITER-$\mathbf{M}$ represents the 24-D super-symbol, in which $\mathbf{M} = [\ m^0\ m^1\ \cdots\ m^{23}\ ]^{\mathrm{T}}$ denoted as the average bits carried by each regular symbol. Sometimes we also denote JUPITER$_{\mathrm{p}}$-$\mathbf{M}_p$, where $\mathbf{M}_p = [\ m_p^0\ m_p^1\ \cdots\ m_p^{11}\ ]^{\mathrm{T}}$, denoted as the average bits for per 2-D projection. It is then obvious that for Jupiter-48 is equivalent to the Leech24D-2 as discussed in Chapter5, which equals to JUPITER-$2\mathbf{I}^{24\times1}$ or JUPITER$_{\mathrm{p}}$-$4\mathbf{I}^{12\times1}$, where $\mathbf{I}$ is the identity matrix, and all of them have the same projection Jupiter$_p$-2.

6.3.2 Formalization

We assume for all Jupiter-m discussed here with $m > 24$. For a certain Jupiter-m, we can first extract an indicative parameter $\Delta m = m - 24$, which indicates the number of bits which are not modulated for constructing the Λ_{24} primitive cell.

As discussed as Eq. 5.3, Leech24D-m is constructed by the nesting of the primitive cell $\mathbf{L}_{24}^0$ on the lattice grids of Z^{24}. Referring to Eq. 6.5, we can formalize the format hierarchy as in:

$$\mathbf{C}_{Jupiter}^{m} = \mathbf{C}_{\Lambda 24}^{0} + \sum_{i=0}^{23} \mathbf{V}_i \mathbf{D}_i \mathbf{e}_i \tag{6.30}$$

in which $\mathbf{D}_i = [\ D_i^1\ D_i^2\ \cdots\ D_i^{\gamma_i}\ ]^{\mathrm{T}}$; D_i is the lattice constant in i-th dimension, and usually $\forall i \in \{0, 1, \cdots, 23\}$, $D_i \equiv D_0$; γ_i indicates the depth of the tessellation in i-th dimension. $\mathbf{V}_i = [\ v_{i,1}\ v_{i,2}\ \cdots\ v_{i,\gamma_i}\ ]$, $\mathbf{V}_i$ is the bits section used for the tessellation. $\mathbf{e}_i$ is a 12-element vector, with 11 zero elements except the i-th element equal to 1. Thus, is it obvious that Jupiter-m is actually the tessellation of the primitive cell of Leech24D, with different depth of nesting on the Z^{24} lattice.

Concretely, the input bit steam $\mathbf{B}$ is separated into m-bit sections $\mathbf{B}_k$, as $\mathbf{B} = [\ \mathbf{B}_0\ \mathbf{B}_1\ \cdots\ \mathbf{B}_k\ \cdots\ ]^{\mathrm{T}}$, with $\mathbf{B}_k = [\ b_k^0\ b_k^1\ \cdots b_k^e\ \cdots\ b_k^m\ ]^{\mathrm{T}}$

of each m-bit section, mapped into the regular symbol sequence $\mathbf{S}_k = [S_k^0\ S_k^1\ \cdots\ S_k^i\ \cdots\ S_k^{23}]^{\mathrm{T}}$. For each Jupiter-$m$ super-symbol[5], $\mathbf{S}_k \in \mathbf{C}^m$, in which $\mathbf{C}^m$ is the corresponding constellation set. m-bit section $\mathbf{B}_k$ is further divided into sections, reading as:

$$\mathbf{B}_k = [\ \mathbf{B}_{\Lambda_{24}}^0\ \mid \mathbf{V}_0 \mid \cdots \mid \mathbf{V}_i \mid \cdots \mid \mathbf{V}_7\ ]^{\mathrm{T}} \tag{6.31}$$

where the first 24 bits in $\mathbf{B}_{\Lambda_{24}}^0$ is used to construct the primitive cell and the rest sections $\mathbf{V}_i$ used for the constellation extensions in each dimension. From Eq. 6.30, it is obvious that:

$$\Delta m = \sum_{i=0}^{23} \lambda_i \tag{6.32}$$

By using such direct constellation extension, extra bit can be fed in the modulation framework. Such technique is straightforward. It increases the number of bits carried by each super-symbol and enables a rate-flexible transmission. However, it has two major drawbacks which can hardly solve by simple constellation extensions. The first one lays in the principle of tessellations. It uses the primitive cells as the building blocks. This implies a fact that the minimum bit/sym is limited by the 'brick's, equal to 1 bit/sym. According to the 2-D projections of $\mathbf{C}_{\Lambda 24}^0$, it is apparent that an arbitrary and direct chopping of the $\mathbf{C}_{\Lambda 24}^0$ breaks the dependences of the lattice. It means that the lattice structure Λ_{24} of is no more preserved. More rigorously, the structure of Λ_{24} is based on the extended Golay code as expressed in Eq. 5.1. After simple chopping, the subscripts of the remained constellations points is no more a codeword of the Golay codes, i.e. $\mathbf{P} \notin \mathbf{V}_{\mathcal{G}}$.

The second difficulties for the direct constellation extension is that after the extension, the size of the constellation set is not uniformed for different dimensions. More concretely as in Fig 6.16, we use the constellation in a certain projection as an illustrative example.

Even though we have mentioned previously that the constellation shaping based rate-flexible is naturally compatible for the SNR varying channels, for example the colorful channel with various SNRs for each subcarrier, the above-mentioned direct extension technique is not sufficient. For a concrete example, both in-phase (I) and quadrature (Q) components in one subcarrier share the same SNR, as they are subject to the same channel conditions.

---

[5] Note that we omit the subscript of $\mathbf{C}_{Jupiter}^m$ for concision.

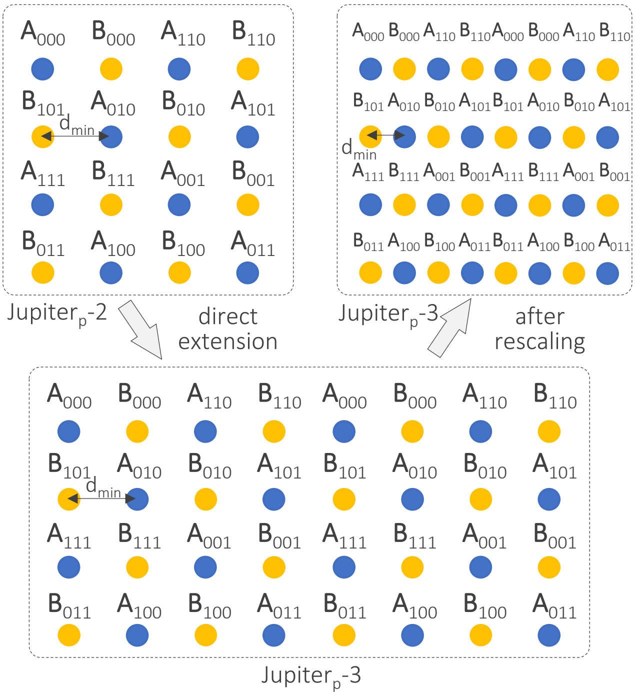

Figure 6.16: The illustrative example for the drawbacks of the direct constellation extension.

Therefore, the constellations in one projection should be symmetric enough and have equal scales in both dimensions.

One solution is to apply a set partitioning on the primitive cell, similarly like what is applied to E$_8$Flex-m. However, one major constraint is that there are too many constellation points and the geometrical dependence for Λ_{24} is not clear. Neither greedy search algorithm nor careful selection from the individual projection intuitively is realistic for construction the format hierarchy.

Therefore, a set of new constellation re-mapping techniques is proposed in this chapter.

6.3.3 Constellation re-mapping techniques

Similarly, the basic idea of the constellation re-mapping for achieving similar occupancies in each dimension of one projection plane is also based on the extension, i.e. translating the constellation points by certain times of lattice constant. However, differing from the direction constellation extension, in which the same operation applied on the whole constellation, the constellation re-mapping techniques apply an anisotropic operation on the different part of the parent constellation. More concretely, the parent constellation is divided into different groups. For constellation points in each group, they have the same constellation extension rules, but towards different directions.

Jupiter$_p - m_p$, when $m = 2, 4, 6$ are equivalent to projections belonging to Leech24D-1, Leech24D-2 and Leech24D-3 respectively. We shall not repeat these again. In the following, we emphasize the modulation of Jupiter$_p$-3, Jupiter$_p$-5 and Jupiter$_p$-1 successively, which correspond to 1.5 bit/sym, 2.5 bit/sym and 0.5 bit/sym respectively.

Re-mapping for Jupiter$_p$-3

Jupiter$_p$-3 adds one extra bit to one 2-D projection without destruct the primitive cell of Λ_{24}, leading to 3 bit per projection, i.e. an average 1.5 bit/sym for the symbols within the corresponding projection.

We assume that one JUPITER symbol $\mathbf{S}_k$ consists of 12 2-D projections, with a specific project as $\mathbf{P}_j = [\ S_k^{2j}\ S_k^{2j+1}\ ]^{\mathrm{T}}, \forall j \in 0,\ 1,\ \cdots,\ 11$. Without loss generality, we only consider the principle of adding extra bit into the projection $\mathbf{P}_j$. It implies that the bit sections $[\mathbf{V}_{2j}\mathbf{V}_{2j+1}]^{\mathrm{T}}$ contains one bit as $[\mathbf{V}_{2j}\mathbf{V}_{2j+1}]^{\mathrm{T}} = [v_j^0]^{\mathrm{T}}, \forall j \in \{0,\ 1,\ \cdots,\ 11\}$.

Conserving the intrinsic lattice structure, the bits is first modulated into pre-processed symbol t^i. according to Eq. 6.33-Eq. 6.34 (i.e. Eq. 5.16-Eq. 5.17) using the first 24 bits in $\mathbf{B}_{\Lambda_{24}}^0$.

$$t^{2j} = \mathrm{mod}(\ 2 \cdot ((x^j \wedge y^j) \oplus z^j) + w^j + x^j \oplus y^j,\ 4\ ) \tag{6.33}$$

$$t^{2j+1} = 2 \cdot ((x^j \wedge \overline{y^j}) \oplus z^j) + x^j \oplus y^j \tag{6.34}$$

for modulating the extra bit V_j for the j-th projection, we use a constellation re-mapping techniques. First we calculate the pre-mapping parameter ς^{2j}, ϱ^{2j}, ς^{2j+1}, and ϱ^{2j+1}, which follows Eq. 6.35-Eq. 6.38.

$$\varsigma^{2j} = (w^j \wedge \overline{x^j} \wedge \overline{y^j} \wedge z^j) \vee (w^j \wedge \overline{x^j} \wedge \overline{y^j} \wedge z^j) \vee (\overline{w^j} \wedge \overline{y^j} \wedge z^j) \tag{6.35}$$

$$\varrho^{2j} = (\overline{w^j} \wedge \overline{x^j}) \vee (\overline{w^j} \wedge z^j) \vee (\overline{y^j} \wedge z^j \wedge w^j) \tag{6.36}$$

$$\varsigma^{2j+1} = (w^j \wedge y^j \wedge z^j) \vee (w^j \wedge x^j \wedge \overline{y^j} \wedge \overline{z^j}) \vee (\overline{w^j} \wedge x^j \wedge \overline{y^j} \wedge \overline{z^j}) \tag{6.37}$$

$$\varrho^{2j+1} = \overline{\varrho^{2j}} \tag{6.38}$$

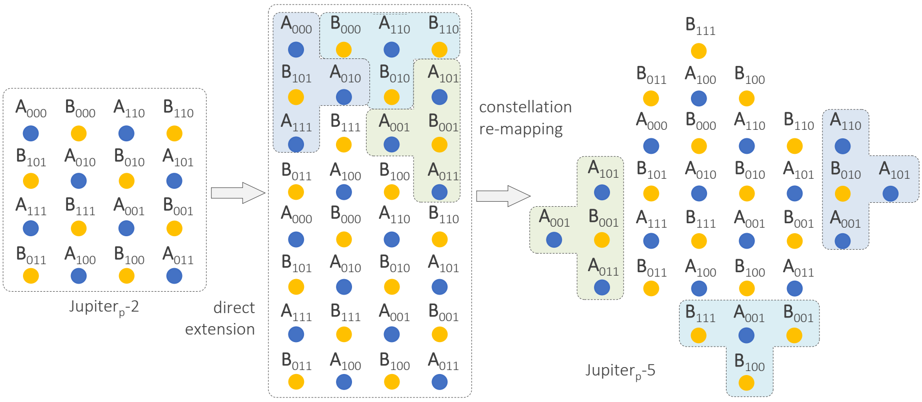

Figure 6.17: The illustration of the constellation re-mapping for Jupiter$_p$-3, with 1.5 bit/sym.

the output symbols are then modulated according to Eq. 6.39-Eq. 6.40.

$$S^{2j} = t^{2j} + 4 \cdot v_j(1 - 2\varsigma^{2j})\varrho^{2j} \tag{6.39}$$

$$S^{2j+1} = t^{2j+1} + 4 \cdot v_j(1 - 2\varsigma^{2j+1})\varrho^{2j+1} \tag{6.40}$$

The intuitive illustration of the constellation re-mapping of Jupiter$_p$-3 is shown in Fig. 6.17. The output constellation is very close to a square, which fits the hypercubic signal space. The constellation differs from a square with an extra 45° rotation. For the single carrier PAM, a simple inverse 45° rotation operation is necessary, which reduces the number of level on the projection in each dimension, i.e. each regular symbol. For multi-subcarrier systems, such operation is not inevitable, as the channel condition depends on the SNR, which is not orientation sensitive.

Re-mapping for Jupiter$_p$-5

For a Jupiter$_p$-5, three extra bits are added to one 2-D projection for maintaining the lattice structure of Λ_{24}, leading to 5 bit per projection, i.e. an average 2.5-bit/sym spectral efficiency (SE) for the symbols within the corresponding projection.

The bit sections for extra bits in j-th projection contains three bits as $[\mathbf{V}_{2j}\mathbf{V}_{2j+1}]^{\mathrm{T}} = [\ v_j^0\ v_j^1\ v_j^2\ ]^{\mathrm{T}}, \forall j \in \{0, 1, \cdots, 11\}$. The constellation re-mapping starts from the construction of the primitive cell by calculating the pre-processing symbols t^{2j} and t^{2j+1} as previously mentioned in Eq. 6.33-Eq. 6.34. For modulating the extra three bits, the pre-mapping symbols τ^{2j}

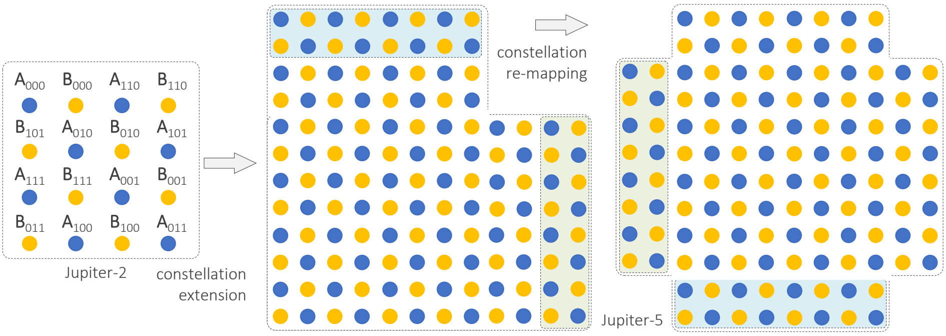

Figure 6.18: The illustration of the constellation re-mapping for Jupiter-5, with 2.5 bit/sym.

and τ^{2j+1} are first calculated as Eq. 6.41-Eq. 6.42 following the direction constellation extension mentioned previously.

$$\tau^{2j} = t^{2j} + 4 \cdot v_j^0 + 4 \cdot (v_j^0 \oplus v_j^1)(2 - v_j^0) \tag{6.41}$$

$$\tau^{2j+1} = t^{2j+1} + 4 \cdot v_j^1 + 4 \cdot (\overline{v_j^0 \oplus v_j^1})(2 - v_j^1) \tag{6.42}$$

And the output symbols reuse the pre-mapping symbols by applying the re-mapping rules as Eq. 6.43-Eq. 6.44

$$S^{2j} = \tau^{2j} - 12 \cdot \vartheta^{2j} \tag{6.43}$$

$$S^{2j+1} = \tau^{2j+1} - 12 \cdot \vartheta^{2j+1} \tag{6.44}$$

in which, ϑ^{2j} and ϑ^{2j+1} give the re-mapping condition, which follow the threshold behavior as Eq. 6.45.

$$\vartheta^{2j}/\vartheta^{2j+1} = \begin{cases} 1 & \tau^{2j}/\tau^{2j+1} > 9 \\ 0 & \tau^{2j}/\tau^{2j+1} \leq 9 \end{cases} \tag{6.45}$$

An intuitive illustration of the constellation re-mapping is shown in Fig. 6.18. The output constellation is the same with 128-QAM. However, applying the above-mentioned re-mapping rules, the intrinsic geometry of the lattice is conserved.

Re-mapping for Jupiter$_p$-1

To implement Jupiter$_p$-1, one needs to take away one bit from a certain projection. This means the primitive cells have to be broken and separated into subsets. It means that an arbitrary division o of the constellation destruct the lattice. We have known from Sect. 5.2 that a constellation point on one j-th projection is uniquely determined by a set of indices, as (w^j, x^j, y^j, z^j). w^j is shared by all projections. It implies that the subset selection based on w^j involves symbols in all projections. However, the direct selection based on the x^j, y^j, and z^j returns asymmetric constellations. It, therefore, underuses the signal spaces and adds difficulties to the realizations.

The principle of the bit reduction on a certain projection is based on the bit-level redundancy on the index z^j, namely $z^j \equiv 0$. The bit operation of the rest indices w^j, x^j, and y^j follows Eq. 6.46-Eq. 6.47 to generate the pre-processing symbols t^{2j} and t^{2j+1}.

$$t^{2j} = \mathrm{mod}(\ 2\cdot(x^j \wedge y^j) + w^j + (x^j \oplus y^j),\ 4\ ) \tag{6.46}$$

$$t^{2j+1} = 2 \cdot (x^j \wedge \overline{y^j}) + x^j \oplus y^j \tag{6.47}$$

The output symbols reuse the pre-mapping symbols by applying the re-mapping rules as Eq. 6.48-Eq. 6.49

$$S^{2j} = t^{2j} \tag{6.48}$$

$$S^{2j+1} = t^{2j+1} - 4 \cdot \vartheta^{2j+1} \tag{6.49}$$

in which, ϑ^{2j+1} give the re-mapping condition, which follow the threshold behavior as Eq. 6.50.

$$\vartheta^{2j+1} = \begin{cases} 1 & t^{2j+1} > 2 \\ 0 & t^{2j+1} \leq 2 \end{cases} \tag{6.50}$$

An intuitive illustration of the constellation re-mapping is shown in Fig. 6.19. The output constellation has 8 points. Rigorously, the constellation is not totally symmetric for both dimensions in the projection. Yet, as discussed before, for the multi-carrier transmission system, the symmetry of such constellation is sufficient considering the benefits from concision.

It is noteworthy that, z^j is not totally independent through whole 12 projections. It implies that maximumly only 11 projections can be loaded with Jupiter$_p$-1 simultaneously. This seems not perfect, but for the applications of multi-subcarrier systems, this is reasonable, for that multi-subcarrier modulations are usually used to enhance the spectral efficiency.

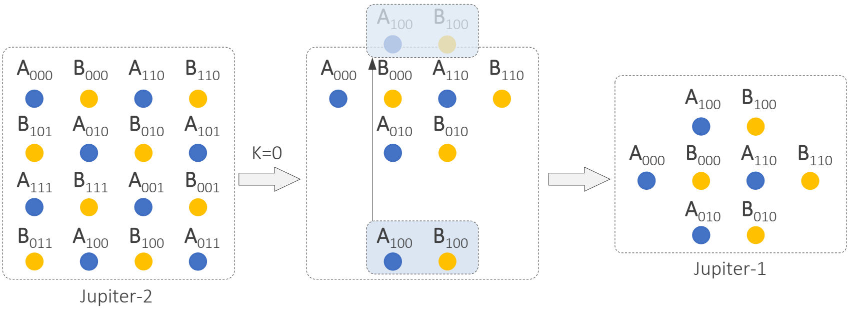

Figure 6.19: The illustration of the constellation re-mapping for Jupiter$_p$-1, with 0.5 bit/sym.

Therefore, at least one projection has a format large than Jupiter$_p$-1, i.e. 0.5 bit/sym, is necessary and reasonable. Otherwise, we can utilize a much easier way of implementation, e.g. PAM with lower baud-rate, instead of the complicated multi-subcarrier modulation schemes. Searching a more symmetric set of rate-flexible constellations based on Λ_{24} can rely on more rigorous group theory, which is far beyond the scope of this thesis, and will be considered in the future works.

Demodulation

The demodulation of Jupiter-m is similar to its Leech24D-m counterparts. The only difference where we should pay attention is that the hard decisions used for selecting the candidate point set are based on different thresholds, for that the subsets for Jupiter$_p$-m, when $m \neq 2, 4, 6$, are not similar. They have different structures according to the corresponding direction in 2-D projections, which shifts the threshold from the A_2 lattice.

6.4 Discussion

In this chapter, we discussed two rate-flexible MD PAM with different design rules. We propose a new flexible and fast 8-D format family and experimentally verify it within an 850 nm VCSEL based optical transceiver scheme, using a hierarchy of the set bipartition on the E_8 lattice. The proven merits of E$_8$Flex-m include: (1) a smooth and swift software defined transition between bit-rates without altering the hardware configuration or executing the resampling; (2) higher sensitivity in the low noise regime; (3) optimized usage of the hardware resources; (4) easy (de)mapping and (de)modulation procedures, as it utilizes the PAM-m signal basis; (5) it is intrinsically compatible with the future industry standard of multi-lane optical interconnects, e.g. octal small form-factor pluggable (OSFP) or quad small form-factor pluggable double density (QSFP-DD). A single format in the E_8Flex-m family can serve as a format for a specific fixed bit-rate system, offering more flexibility on the trade-off between the bandwidth utilization and performance in the system design. Apart from the 8-D rate-flexible format, we extend the 24-D PAM equipped with the granularity of one bit per regular symbol to 0.5-bit steps, and further extend it to a rate-flexible version, named as Jupiter, utilizing the lattice structure of Λ_{24}. Compared with the E_8Flex-m family, Jupiter is naturally compatible with SNR varying system, meaning the required SNR in each dimension is unequal. We will show the benefits of such feature when applying it into a 12-subcarrier carrier-less amplitude phase modulation (CAP) transmission system. In the next two chapters, we will discuss the performance of the multi-subcarrier transmissions loaded with the rate-flexible MD formats. Besides the IM-DD scenario, the rate-flexible PAM can also be considered as a candidate of the format for the bit-rate flexible transmission in the coherent systems.

The work summarized here is presented in **PAPER 3**.

Chapter 7

Multi-Subcarrier: Eight-Dimensional DMT

The bandwidth limitation of the optical components is a major constraint for the vertical-cavity surface-emitting laser (VCSEL) based intensity-modulated direct-detection (IM-DD) systems. It reins the further development of the pulse amplitude modulation (PAM) signal, especially non-return-to-zero (NRZ), which imposes even higher requirements on the integrated circuit (IC) designing. However, on the other hand, the multi-subcarrier modulation (MSM) systems divide the channel into multiple orthogonal branches and transport signal through each of them independently, so that the demanding requirements on the high-speed components are relieved. In addition, the finer spectral granularity provided by a MSM system fully utilizes the bandwidth resource and, therefore, maximizes the effective data rate. Further, for the time-varying channel, e.g. multi-mode fiber (MMF), the MSM system equipped with adaptive and flexible channel management on the resource allocation, e.g. bandwidth and power, via bit-loading and power-loading are naturally tolerant for the channel variations.

In the previous chapters, we discussed the multi-dimensional (MD) PAM over single carrier channels. From this chapter, we investigate into the applications of MD modulation format in the MSM systems, among which two typical schemes specifically used for the IM-DD cases are discussed, i.e. discrete multi-tone modulation (DMT) and carrier-less amplitude phase modulation (CAP), and reveal the benefits the MD formats bring for the performance of a MSM system in various aspects.

As real-valued version of orthogonal frequency division multiplexing

(OFDM), DMT has been treated as one of the promising formats for further boosting the data rate in an IM-DD system [45, 46, 198]. DMT utilizes the Hermitian symmetry to generate a real-valued output signal after fast Fourier transform (FFT) computation. It is straightforward in an IM-DD system. Compared with other technique schemes of modified OFDM adapted for IM-DD systems, where the up- and down-conversion are required, such signal conversion can be efficiently realized in the digital signal processing (DSP).

In the conventional DMT, two-dimensional m-ary quadrature amplitude modulation (QAM) formats, i.e. m-QAMs, are loaded on each subcarrier. Similar to cases of different multi-dimensional PAM (MD-PAM) [64, 199], a better bit error rate (BER) sensitivity is expected in DMT transmission by loading MD formats, i.e. MD coded modulations, on the subcarriers. The MD DMT benefit from the intrinsic MD geometric features of the densest lattice in the corresponding MD signal space. Such improvement can be further converted into the merits, e.g. the enhanced data rate, the extension of reach, and the tolerance for the insertion loss and thermal effects with respect to a given BER level. In addition, MD bit-loading has a finer spectral efficiency (SE) granularity, e.g. 0.25 bit instead of 1 bit per subcarrier[1] for E_8Flex-m. By doing so, we can adopt a direct bit-loading scheme without the complicated optimal power-loading algorithm. This enables a fast response to the channel variation, which is important for the low-latency, low-complexity optical interconnects.

In this chapter, we demonstrate novel DMT schemes with four-dimensional (4-D) and eight-dimensional (8-D) bit-loading, using an 850 nm 18 GHz multi-mode vertical-cavity surface-emitting laser (MM-VCSEL) and achieving a net bit-rate over 100 Gbit/s in terms of 7% forward error correction (FEC), and investigate its benefits from different aspects, e.g. the reach, the tolerance of insertion loss and thermal effects.

7.1 DMT in general

From this chapter, we start with formalizing the principle of the DMT transmission and formulating the so-called MD formats loaded DMT.

---

[1] Normally we denoted bit per subcarrier as bit/sc. In the following text, we reserve such notation.

7.1.1 Multi-subcarrier transmission

The MSM transmissions use multiple subcarriers to transmit signal. We denote the sequence of the MSM symbols with a matrix $\widetilde{\mathbf{D}} = [\ \mathbf{d}_0\ \mathbf{d}_1\ \cdots\ \mathbf{d}_m\ \cdots\ ]$, in which, $\mathbf{d}_m = [\ d_m^0\ d_m^1\ \cdots\ d_m^\nu\ \cdots\ d_m^{N_{sc}-1}\ ]^{\mathrm{T}}$ is a MSM super-symbol containing N_{sc} symbols corresponding to N_{sc} subcarriers. d_m^ν is the m-th symbol on the ν-th subcarrier. The MSM signal in the continuous time domain can be expressed in Eq. 7.1 [200].

$$d(t) = \sum_{m=-\infty}^{+\infty} \sum_{\nu=0}^{N_{sc}-1} d_m^\nu g_\nu(t - mT_s) \tag{7.1}$$

Obviously $m, \nu \in \mathbb{Z}$, $\nu \in [\ 0,\ N_{sc}\ ]$; T_s is the time duration of each symbol; $g_\nu(t)$ denotes the pulse shape on the ν-th carrier, which follows:

$$g_\nu(t) = \mathcal{G}(t) e^{j2\pi f_\nu t} \tag{7.2}$$

in which $\mathcal{G}(t)$ is the pulse shaping function; f_ν is the frequency of the ν-th subcarrier.

For demodulating the signal, we can use the corresponding matched filter, or use the correlator expressed in Eq. 7.3 [200].

$$\widehat{s}_{m\nu} = \frac{1}{T_s} \int_0^{T_s} r(t - mT_s) e^{-j2\pi f_\nu t} \tag{7.3}$$

where $r(t)$ is the received signal; $\widehat{s}_{m\nu}$ is the estimated symbol.

7.1.2 OFDM

For OFDM, the subcarriers are orthogonal, even though the sub-bands overlap. Thus, ideally no further inter-carrier interference (ICI) is introduced. The orthogonality is expressed in Eq. 7.4.

$$f_\nu - f_{\nu'} = \zeta \frac{1}{T_s} \tag{7.4}$$

in which, indices ν and ν' denote two arbitrary carriers; and $\zeta \in \mathbb{Z}$. As long as the subcarrier frequency is selected from the set of orthogonal frequency, the corresponding bands are independent and no ICI is introduced.

Considering a train of signal samplings, $\mathbf{q} = \left[\ \mathbf{q}_0^{\mathrm{T}}\ \mathbf{q}_1^{\mathrm{T}}\ \cdots\ \mathbf{q}_m^{\mathrm{T}}\ \cdots\ \right]^{\mathrm{T}}$, with a time interval of T_s/N, it samples the m-th slot, $\mathbf{q}_m$, into N points, as $\mathbf{q}_m = [\ q_{m\cdot N}\ q_{m\cdot N+1}\ \cdots\ q_{m\cdot N+\mu}\ \cdots\ q_{m\cdot N+m-1}\ ]^{\mathrm{T}}$, and the μ-th sample is denoted as $q_{m\cdot N+\mu}$; Obviously $\mu \in [0,\, N-1]$. For OFDM, we use the pulse shaping function, $\mathcal{G}(t)$, follows:

$$\mathcal{G}(t) = \begin{cases} 1 & \text{for } 0 \ < \ t \le T_s \\ 0 & \text{for } t \le 0 \ \text{ or } \ t > T_s \end{cases} \tag{7.5}$$

Then, we can separate a single OFDM symbol (or m-th time slot) and focus on it, i.e. omitting the subscript m. The μ-th sampling point in the N-element vector $\mathbf{q}$, i.e. $d[\mu]$, is expressed in Eq. 7.6[2].

$$d[\mu] = q_\mu = \sum_{\nu=0}^{N_{sc}-1} d^\nu \cdot e^{j2\pi\frac{\nu\mu}{N}} \tag{7.6}$$

If $N_{sc} = N$, for a more concise and compact form, we rewrite the above relation into Eq. 7.7.

$$\mathbf{q} = \widetilde{\mathbf{F}} \cdot \mathbf{d} \tag{7.7}$$

in which, $\widetilde{\mathbf{F}} = [F_{\nu\mu}] \in \mathbb{C}^{N\times N}$, for each $F_{\nu\mu} = e^{j2\pi\frac{\nu\mu}{N}}$, $\nu,\ \mu \in [\ 0,\ N-1\ ]$. The matrix conducts a inverse discrete Fourier transform (IDFT), formally, as:

$$\mathbf{q} = \mathcal{DFT}^{-1}\left\{\mathbf{d}\right\} \tag{7.8}$$

in which $\mathcal{DFT}^{-1}\{\cdot\}$ is a N-point IDFT. Correspondingly, the estimated symbol $\widehat{\mathbf{d}}$ can be simply achieved from the received samples $\mathbf{q}'$ by applying a N-point discrete Fourier transform (DFT) as:

$$\widehat{\mathbf{d}} = \mathcal{DFT}\left\{\mathbf{q}'\right\} \tag{7.9}$$

where $\mathbf{q}'$ is the sampling points received[3], from the m-th time slot of the received signal $r(t)$ with time intervals of T_s/N. Eq. 7.8 and Eq. 7.9 imply that we can utilize DFT and IDFT to realize the OFDM (de)modulation [201]. Further, by using the FFT/inverse fast Fourier transform (IFFT) algorithm, we can reduce the complexity of DFT/IDFT from $O(N)$ to $O(\frac{N}{2}log_2(N))$.

---

[2] Note that we use notation $[\cdot]$ only for the sampling point, which has physical meaning, like the uploading sequence to AWG.

[3] Note that here we implicitly assume that $\mathbf{q}, \mathbf{q}', \mathbf{d}, \widehat{\mathbf{d}} \in \mathbb{C}^{N\times 1}$.

7.1.3 DMT

While the conventional OFDM uses complex signal for the modulation, namely in Eq. 7.1, $d_m^\nu \in \mathbb{C}$, DMT is a real-valued version of OFDM, which generates real signal output. Compared with the complex valued OFDM, DMT is more compatible for the modulation of IM-DD systems. Yet, for DMT we use $2N$-point IFFT to generate the N-point real output sequence. Considering a $\mathbf{d} \in \mathbb{C}^{2N\times 1}$, the outputs sequence $\mathbf{q} \in \mathbb{R}^{2N\times 1}$ is generated after IFFT/FFT when $\mathbf{d}$ posses the Hermitian symmetry, which can be realized by using the condition as:

$$d_{2N-\nu} = d_\nu^\dagger \tag{7.10}$$

in which $\nu \in [\ 1,\ N-1\ ]$, and uniquely $d_0, d_N \in \mathbb{R}$. Due to the redundancy, only N points is used for modulation, instead of $2N$. It is actually understandable, as normally the intensity modulated signal uses only the amplitude modulation but not phase component, which loses half of the degree of freedom.

At the receiver side, the estimated symbol can be retrieved by applying FFT as Eq. 7.9.

7.1.4 Cyclic prefix

MMF channels surfer from the inter-modal dispersion, which imposes different group velocities for signal in different mode groups, which leads to the inter-symbol interference (ISI) between DMT symbols, spoils the orthogonality between subcarriers, and further results in ICI. To solve this problem, we add the cyclic prefix (CP) [202].

Assume we transmit signal over MMF with length L_{MMF}, and v_{gmin} is the minimum group velocity and v_{gmax} is the maximum group velocity among all the mode groups. The maximum signal delay caused from the inter-modal dispersion is estimated as:

$$t_d = \frac{L_{MMF}}{\|v_{gmax} - v_{gmin}\|} \tag{7.11}$$

Considering a N_g-point CP, the ICI free condition is expressed as:

$$t_d \ < \ N_g \cdot \frac{T_s}{N} \tag{7.12}$$

For adding the CP, we need simply extend the N-point transmitting sequence $\mathbf{q}$ to a $(N+N_g)$-point transmitting sequence $\mathbf{q}'$ as:

$$\mathbf{q}' = [\ \mathbf{q}_{-c}^{\mathrm{T}}\ \mathbf{q}^{\mathrm{T}}\ \mathbf{q}_{+c}^{\mathrm{T}}\ ]^{\mathrm{T}} \tag{7.13}$$

in which $\mathbf{q}_{-c} = [\, q_{N-N_g/2} \ \cdots \ q_{N-1} \,]^{\mathrm{T}}$ and $\mathbf{q}_{+c} = [\, q_0 \ \cdots \ q_{N_g/2-1} \,]^{\mathrm{T}}$.

7.1.5 Clipping ratio

Since each subcarrier of DMT is modulated independently, occasionally the high amplitude appears in the same time slot, leading to the high peak-to-average power ratio (PAPR). The PAPR can be formally defined as Eq. 7.14 [200].

$$\mathrm{PAPR} = 10\, lg \left(\frac{\max\limits_{0 \leqslant t < T_{DMT}} \|q(t)\|^2}{\mathbb{E}\left[\|q(t)\|^2\right]} \right) \ [\mathrm{dB}] \tag{7.14}$$

The modulation range for VCSEL is positive determined and limited. Especially, for avoiding the negative signal going below the threshold, we need to bias the laser and limit the modulation amplitude. On the other hand, we use the arbitrary waveform generator (AWG), which has the fixed output amplitude. However, the adaption of the uploading signal to the maximum range of AWG output leads to a reduced effective signal power for each subcarrier. Therefore an amplitude clipping is used to limit the PAPR straightforwardly. The amplitude limited signal $\overline{q}(t)$ can be formally expressed as:

$$\overline{q}(t) = \begin{cases} q(t) & \text{for } \|q(t)\| \leqslant Q \\ 0 & \text{otherwise} \end{cases} \tag{7.15}$$

in which Q is the amplitude limits. We can also define the relative clipping ratio as [200]:

$$C_L = 10\, lg \left(\frac{Q^2}{\mathbb{E}\left[\|q(t)\|^2\right]} \right) \ [\mathrm{dB}] \tag{7.16}$$

7.1.6 Power-loading and bit-loading

Normally the channel for a VCSEL data link is colorful, i.e. the frequency response of not flat. One major reason is that the phase relation of high-frequency components is not stable because of the differential mode delay (DMD), leading to the amplitude cancellation. Additionally, such channel is also time-varying, for that the modes excitation and coupling is very sensitive to the fiber bending and fluctuations. Therefore, for taking the full advantages of the channel resource, e.g. bandwidth and signal-to-noise ratio (SNR), a bit-loading strategy should be adopted. It means that we need

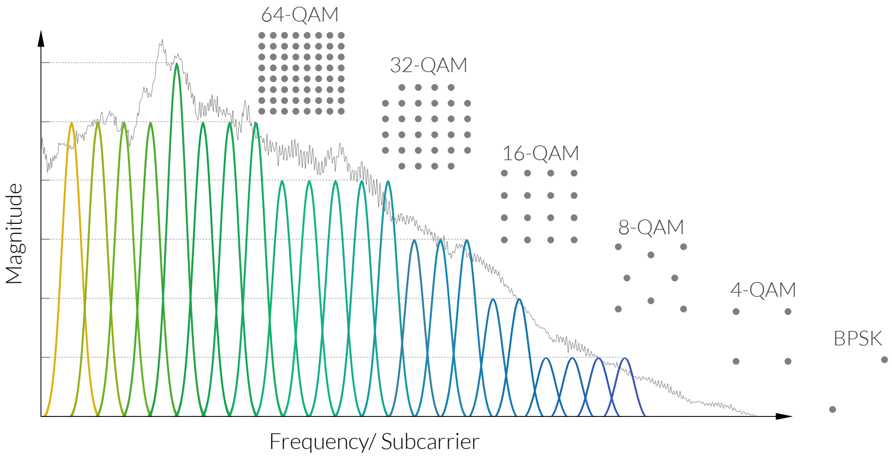

Figure 7.1: A schematic illustration for DMT bit-loading scheme with QAMs of granularity of 1 bit per subcarrier.

to load the subcarriers of different SNRs with formats of different spectral efficiency, namely constellations of different scale. When the SNR is high, we load large constellations, which carry more bits; When the SNR is low, we shrink the constellation size and ensure the successful transmission with a lower data rate. For conventional cases, we can simply realize such bit-loading scheme by using a serial of m-QAMs, scaling from 2-QAM (i.e. BPSK) carrying 1 bit/sc to 128-QAM carrying 7 bit/sc[4]. Such m-QAM family offers a constellation gearing with the granularity of 1 bit/sc. The schematic illustration is shown in Fig. 7.1.

Meanwhile, such coarse bit-loading scheme leaves non-optimal utilization of the channel resources, e.g. SNR and power. Thus, we adopt an additional power-loading algorithm to cooperate with the bit-loading, which multiplies an amplitude gain coefficient to each subcarrier according to the SNR condition and constellation scale, and remains the total power of the signal the same. During the process, we reduce the gain coefficient for the channel with surplus power and transfer the budget to the channel with insufficient power. With the debit and credit of power, we expect a better and balanced utilization of the channel resource. The optimal bit-loading and power-loading can be achieved by applying the water-filling algorithm [203]. Limited by the space, we do not explain here the details.

---

[4] Usually m-QAMs with $m > 128$ are not realistic due to the limitation of ENOB of the electrical parts.

It is noteworthy that, for time-varying channels, the channel condition for the subcarriers changes continuously. It implies that for keeping the optimal transmission, the optimal bit- and power-loading algorithm need to be conducted repetitively based on the channel monitoring.

7.2 DMT with finer granularity

As mentioned above, the bit-loading algorithm with the granularity of 1 bit/sc requires repetitive re-adjustment of the constellation scales and gain coefficients of the subcarriers. It imposes high computational consumptions and increases the complexity of the actual implementation. In this section, we focus on the DMT with a finer granularity, i.e. <1 bit/sc. We will elaborate the benefits of such bit-loading scheme and discuss the possible realizations.

7.2.1 DMT with bit-loading of finer granularity

For achieving the bit-loading with finer granularity, we can assume a serial of constellations, which have steps of bit adjustment smaller than 1 bit/sc, i.e. a certain fractional number. Fig 7.2 shows the possible modulations of the DMT with a finer granularity. We use 0.25 bit/sc, if without loss of generality, as an example to show the features of the possible formats with finer granularity. It is clear that subcarriers adapt better the channel responses with the decrease of the bit-steps. Especially for the high-frequency subcarriers, which cannot be loaded by any signal in the conventional DMT with 1 bit/sc, are now carrying information with fractional bits, like the subcarrier illustratively indicated in purple at the tails of the frequency response, as shown in Fig 7.2. Such finer adaption to the channel response brings a more thorough utilization of the bandwidth resources. No major waste of SNR is left between the spectral efficiency steps, even when the power-loading algorithm is non-optimal.

It can be mathematically proven that a direct bit-loading scheme with finer SE steps for the constellation loaded without extra power-loading brings additional SNR benefits compared with the coarse bit-loading scheme with the optimal power-loading. Limited by the space, it is not elaborated here and left as 'homework' for readers. The benefits of such so-called direct bit-loading algorithm are more than the simple benefits for the SNR benefits, but is also found in the flexibility of the system. With the direct bit-loading, no repetitive readjustment of the power gain efficient is not

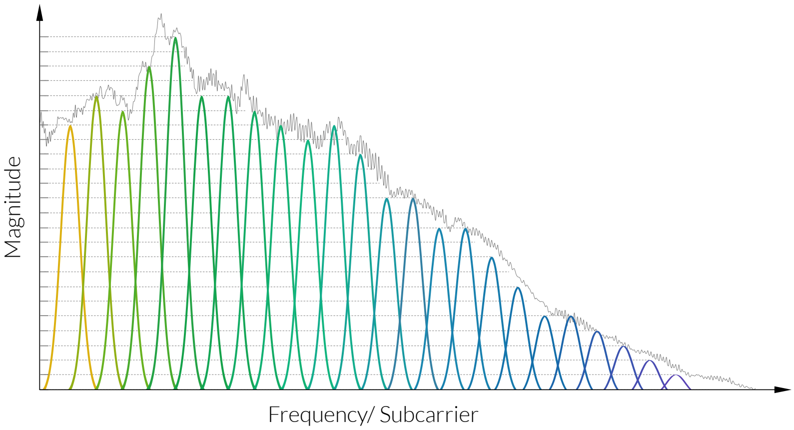

Figure 7.2: A schematic illustration for DMT bit-loading scheme with finer granularity: 0.25 bit/sc as an example.

necessary to repeat after a certain period of transmission and synchronize signal on the subcarriers, which impose a heavy burden on latencies. With direct bit-loading, the system only needs to monitor the channel condition, e.g. SNR, and re-adjust the constellation scale on the subcarrier individually, without the necessity of channel information of other subcarriers. By doing so, the subcarriers become truly independent and a flexible and agile transmission system becomes possible.

7.2.2 Realization of finer granularity

For the realization of the finer granularity, or equivalently the fractional bit/sc, there are different solutions. One straightforward solution is using the hybrid formats. For a concrete instance, for achieving 1.5 bit/sc, we can transmit 2-QAM and 4-QAM alternatively. However, such a scheme is not ideal, as the SNR on each channel is roughly the same. The BER performance depends on the symbols requiring higher SNR.

Alternatively, similarly as discussed in Chapter 4, we can consider using the MD formats, which imposes similar requirements on SNR for each subcarrier. From the previous mentioned rate-flexible MD formats, candidate formats include the 4-D set-partitioning (SP) QAMs, 8-D E_8Flex-m, and twenty-four-dimensional (24-D) JUPITER-$\mathbf{M}$. In this chapter for DMT modulations, we will focus on the former two and leave JUPITER-$\mathbf{M}$ for the next chapter in CAP transmission. Following, we shall elaborate the way of construction the MD signal space for a DMT transmission system.

7.2.3 Multi-dimensional signal space in DMT

As mentioned in Sect. 7.1, the symbols for a MSM system can arranged in a matrix $\widetilde{\mathbf{D}}^{N_{sc}\times\infty}$, which naturally offers two degrees of freedom, namely carrier frequency f_ν, or simply represented by ν, and time slot represented by subscript m. It implies that to construct a n-dimensional virtual signal space, one can choose any n symbol slots in $\widetilde{\mathbf{D}}$. The orthogonal basis set is represented by $\mathbf{\Pi} = \{\,(m_0,\nu_0),\,(m_1,\nu_1),\,\cdots,\,(m_i,\nu_i),\cdots,\,(m_{n-1},\nu_{n-1})\,\}$. Two typical construction of MD signal space include the intra-symbol modulation and inter-symbol modulation.

Intra-symbol modulation

Intra-symbol modulation is the case when the n-dimensional signal space spanned by the orthogonal basis represented by the set $\mathbf{\Pi}$ when $m_0{=}m_1{=}\cdots{=}m_{n-1}$. It means that the orthogonal basis is found within one symbol. Such construction is natural, but not suitable for the case of DMT for three reasons: (1) the number of subcarriers, i.e. N_{sc}, for a DMT symbol is large (>100). Therefore, either formats with very high dimensionality (i.e. $n = N_{sc}$) are required, or an n-element subset need to be chosen from these N_{sc} symbols. However, the difficulty is that unless N_{sc} is integer times of n, implying that the subcarriers are grouped into N_{sc}/n groups, no full utilization of the subcarrier can be guaranteed. (2) since the channel is assumed to be colorful, conditions of grouping the subcarriers with the same SNR without power-loading are not always ensured. It means that either the signal space is constructed by dimensions with unequal SNR, or extra power-loading is required, which takes away the desired benefits as discussed before. (3) the channel is time-varying, which implies that the optimal grouping of orthogonal basis changes from time to time.

The intra-symbol modulation is, however, natural for the 24-D CAP loaded with JUPTIER-**M** as discussed in Chapter 8. We will elaborate the details later. In this chapter for DMT we adopt an alternative scheme, known as inter-symbol modulation.

Inter-symbol modulation

The inter-symbol modulation requires the orthogonal basis $\mathbf{\Pi}$ when $m_0 \neq m_1 \neq \cdots \neq m_{n-1}$, meaning that the basis is found in n different sym-

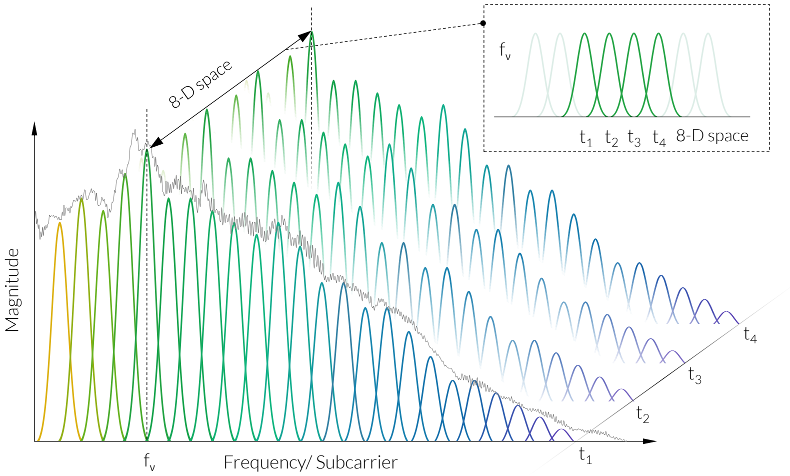

Figure 7.3: A schematic illustration of the construction of 8-D signal space for DMT with the four consecutive time slots on the same subcarrier.

bols. For a more specific case, $\nu_0{=}\nu_1{=}\cdots{=}\nu_{n-1}$, which implies that the n-dimensional signal space is found within the same subcarrier. In the DMT for this chapter, we impose a more strict condition, i.e. $m_i = m_0 + i$, $\forall i \in \mathbb{Z} \cup [\,0,\ n-1]$, and $i \in$. It means that the orthogonal for spanning the n-dimensional signal space is found in the subcarrier with the same carrier frequency f_ν of n consecutive MSM symbols. The reason for using such constructions is mainly based on the fact that the channel condition, i.e. SNR, is adiabatic, meaning that the change of condition is gradual during the transmission and much more slowly than the symbol rate. Therefore, a stable MD signal space is more easily found within the same subcarrier than the same symbol. However, the drawback seems also obvious that due to the presence of the nonlinearity of VCSELs and the time-dependent behavior, the subcarriers surfer from ICI, which spoils the benefits of MD modulations. In Fig. 7.3, the construction of the 8-D signal space is illustratively explained.

7.2.4 DMT loading four-dimensional formats

We use 4-D formats to achieve the 0.5-bit/sc granularity. To apply such formats in the IM-DD system, we combine two consecutive DMT symbols in one super-symbol to create the 4-D signal space on each subcarrier. Symbols on each subcarrier are complex, i.e. two-dimensional (2-D) real

Table 7.1: Modulation formats of 4-D bit-loading.

Bits/sc	0.5	1	1.5	2
Formats	BPSK	BPSK	PS-QPSK	PDM-QPSK
Bits/sc	2.5	3	3.5	4
Formats	32-SP-QAM	PDM-Star-8QAM	128-SP-16QAMM	PDM-16QAM
Bits/sc	4.5	5	5.5	6
Formats	512-SP-32QAM	PDM-32QAM	2048-SP-64QAM	PDM-64QAM
Bits/sc	6.5	7		
Formats	8192-SP-128QAM	PDM-128QAM		

space. We assume that after using the CP, the ISI is small enough to guarantee the orthogonality of the desired 4-D super-symbols. Tab. 7.1 shows the modulation formats used corresponding to different numbers of bit/sc per DMT symbol[5]. For the subcarriers loaded with integer bits per symbol, i.e. even bit numbers every two symbols, we choose regular polarization division multiplexing (PDM)-mQAM. For achieving the finer granularity, we load 4-D formats to the subcarriers having a half-integer number of bit/sc, i.e. odd number of bits per super-symbols, meaning 0.5-bit/sc scale of each symbol. For bit/sc >2, we use modified m-SP-QAM, which can be derived from PDM-mQAM by applying Ungerböck's set partitioning scheme [172]. For constellations with 1.5 bits/sc, we use polarization switching quadrature phase shift keying (PS-QPSK), which has been proven most power efficient [56]. For 0.5-bit level, we simply duplicate the BPSK signal in two consecutive symbols. Gray mapping is used in bit-to-symbol mapping for the regular PDM-mQAMs, whereas it is not applied to 4-D SP formats, where it is no more optimal.

7.2.5 DMT loading eight-dimensional formats

For 8-D case, we load 8-D formats to achieve the 0.25-bit granularity. We combine four consecutive DMT symbols on one subcarrier into a single super-symbol, to create the 8-D signal space. Each super-symbol is then

---

[5] For concision, we do not specifically mention that bit/sc is the value for per DMT symbol.

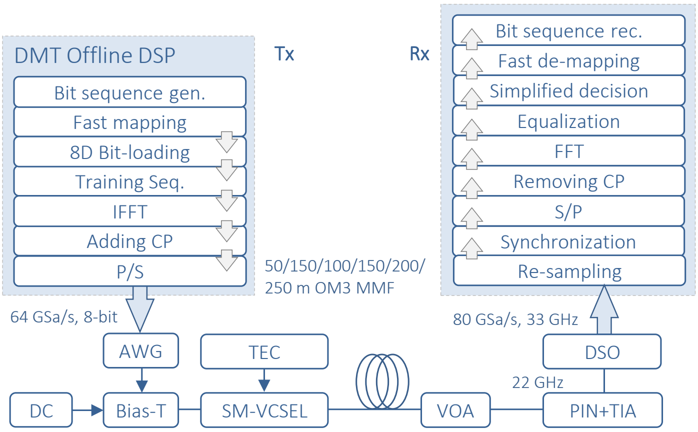

Figure 7.4: Schematics of the experimental setup for MD DMT.

loaded by an 8-D E_8Flex-m. The (de)modulation of E_8Flex-m has been explained in detail in Chapter 6.

7.3 Testbed

Fig. 7.4 depicts the schematics of the experimental setup. We used an 850 nm MM-VCSEL as the light source. It has an optical power output of 6.5 dBm and 3 dB bandwidth at 18 GHz when biased at 18.2 mA. It was modulated by the electrical signal of $1V_{pp}$. The VCSEL was mounted on an evaluation board (EVB) with the wire bonding. We adopted a pair of aspherical lenses to collect the light emitting from the laser. The lenses were mounted on the motorized stage with a mechanical resolution < 2 nm. The stage was then connected and controlled by a centralized computer. We used an adaptive algorithm to recouple the laser automatically. The VCSEL was placed on a heat sink, which was controlled by a thermoelectric cooler (TEC) controller, with adjustment resolution around 0.2 °C.

At the transmitter, the input bit streams were mapped into 4-D (or 8-D) super-symbols, and each super-symbol symbol was further divided into two (four) regular complex symbols. We added training symbols occupying the 1% of the total sequence. The sequence was then converted to the time domain with the IFFT. An 8-point CP was attached to each symbol. The signal is further serialized by a parallel-to-serial converter. The pre-processed sequence was then uploaded to a 64 GSa/s 8-bit AWG of 22 GHz analog bandwidth. The sequences were generated randomly every time before uploading, avoiding the impact from the patten dependent effects.

After transmission through spools of OM3 MMF, the optical signal was received by a calibrated 22 GHz 850 nm photoreceiver. Data traces were captured by an 80 GSa/s digital storage oscilloscope (DSO), with 5.2×10^7 samples for each. At the receiver side, the time window was synchronized before parallelizing the sequence and removing the CP. A fast Fourier transform (FFT) was used to convert the signal to the frequency domain. The signal was processed by 1-tap equalization, whose tap coefficients were obtained from the training sequence. The output bit sequence was then obtained after a bit-to-symbol de-mapping.

For each DMT, we allocated 256 subcarriers equal to 512 sampling points in each DMT symbol but filled 191 subcarriers, equal to 24 GHz. The modulation amplitude was limited by an optimal amplitude clipping ratio of 8.5 dB. For more detailed information on the parameters for an 8D-DMT transmission system, please see Tab. 7.2. The parameters for a 4D-DMT system are similar to Tab. 7.2.

7.4 Experimental results

7.4.1 DMT loaded with four-dimensional PAMs

We verified the performances of DMT with 4-D bit-loading and conventional QAMs in an optical back-to-back (OBTB) transmission and over 100 m and 200 m OM3 MMF. Fig. 7.5 shows an example of the bit-loadings with and without half-bit 4-D formats loaded in an OBTB transmission. As expected, the 4-D bit-loading adapts better the channel frequency response. The insets show the constellations of some typical modulation formats for both bit-loading solutions.

In Fig. 7.6, the experimental BER results are illustrated. The purple curves present the 4-D bit-loading, whereas the green ones give the results of the conventional scheme. For OBTB transmission, both modulations have a gross data rate of 126 Gbit/s at 7% FEC threshold, whereas the new modulation format outperforms with a rate increase of 7.1 Gbit/s at the 2.7% FEC threshold of 100BASE-SR4 and a rate increase of 4.2 Gbit/s at the 5.8% FEC threshold of 100BASE-KP4. For transmission over 100 m OM3 MMF, a gross line rate of 118 Gbit/s, equal to net 103.9 Gbit/s, is obtained at 7% FEC threshold and a 12.8% rate increase for the 4-D bit-loading at the 2.7% FEC threshold and a 6.2% increase for 5.8% KP-4 FEC. A gross line rate of 93 Gbit/s is archived over 200 m OM3 MMF above 7%

Table 7.2: The parameters of the experiment setup for verifying the 8D-DMT in a 100 G IM-DD system.

Parameter	Symbol	Value	Unit
Sequence length	-	2^{15}	-
Symbol rate	-	0.15	GBaud
Bit rate	-	60-130	Gbit/s
Formats	-	8D-DMT/DMT	-
Bias current	I_{bias}	18.5	mA
Output power	-	6.5	dBm
wavelength	λ	850	nm
Modulation amplitude	V_{pp}	1	V
AWG analogy frequency	$f^{AWG}_{-3\ dB}$	~ 20	GHz
AWG sampling rate	-	64	GSa/s
AWG vertical resolution	-	8	bit
DSO analogy frequency	$f^{DSO}_{-3\ dB}$	~ 33	GHz
DSO sampling rate	-	80	GSa/s
DSO vertical resolution	-	8	bit
VCSEL type	-	Multi-mode	-
VCSEL pigtail	-	MMF	-
MMF length	L_{MMF}	0-250	m
PR bandwidth	$f^{PR}_{-3\ dB}$	22	GHz
PR Gain	G	-80/-70	V/W
PR Output noise	N_{PR}	590	μVrms
PR Impedance	Z_{PR}	50	Ω
Ambient temperature	T	20-80	°C

FEC threshold. The 4-D bit-loading enables a >70 Gbit/s transmission over KP-4 threshold where the conventional one fails. The tendency of capacity increase also remains for the regimes of lower required BER. The net rate is with respect to 7% FEC threshold. The detailed values are listed in Tab. 7.3

7.4.2 DMT loaded with eight-dimensional PAMs

The concrete instances of the power loading (PL) coefficients in Fig. 7.7(a), (b), BER in Fig. 7.7.(c), (d) and SNR in Fig. 7.7(e), (f) of different subcarriers in a transmission of 110 Gbit/s (pre-FEC) over 100 m MMF are illus-

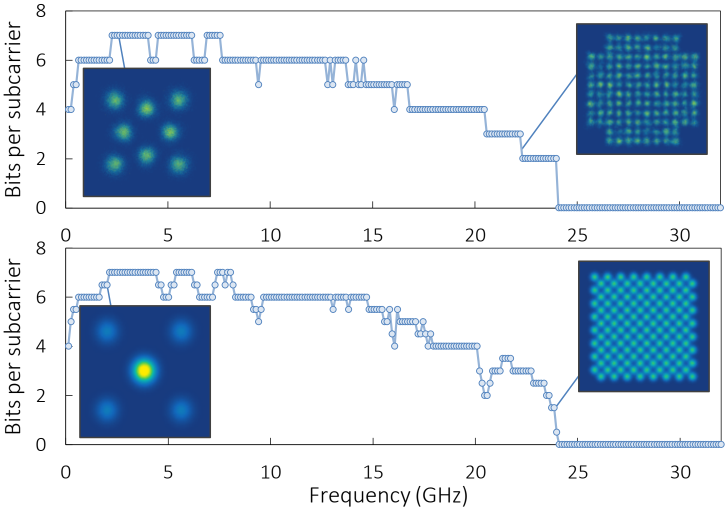

Figure 7.5: An example of the DMT transmission using bit-loading with QAM (upper) and 4-D formats (lower).

Table 7.3: BER vs. pre-FEC rate using DMT loading QAM and 4-D formats (unit Gbit/s).

FEC threshold	QAM (net)	4-D DMT (net)	Δ	Δ %
7 % HD-FEC OBTB	125.6(110.6)	126.1(111.1)	0.5(0.4)	0.4
KP-4 OBTB	99.5(87.7)	103.7(91.4)	4.2(3.7)	4.2
KR-4/SR-4 OBTB	81.6(71.9)	88.7(78.1)	7.1(6.3)	8.7
7 % HD-FEC 100 m OM3	116.7(102.8)	**118.0**(**103.9**)	1.3(1.1)	1.1
KP-4 100 m OM3	89.1(78.5)	94.6(83.3)	5.5(4.8)	6.2
KR-4/SR-4 100 m OM3	69.3(61.0)	78.2(69.3)	8.9(7.8)	12.8
7 % HD-FEC 200 m OM3	92.6(81.6)	93.7(82.5)	1.1(1.0)	1.2
KP-4 200 m OM3	69.2(61.0)	74.5(65.6)	5.3(4.7)	7.7
KR-4/SR-4 200 m OM3	-	-	-	-

trated with two loading schemes, i.e. the conventional QAMs and E_8Flex-m without the power-loading. The optimal power-loading algorithm adapted is similar to [203]. From the comparison of the power gain coefficient of both bit-loading schemes as shown in Fig. 7.7(a) and (b), we observe a serial of power coefficients with much smaller fluctuations. From Fig. 7.7(e) and

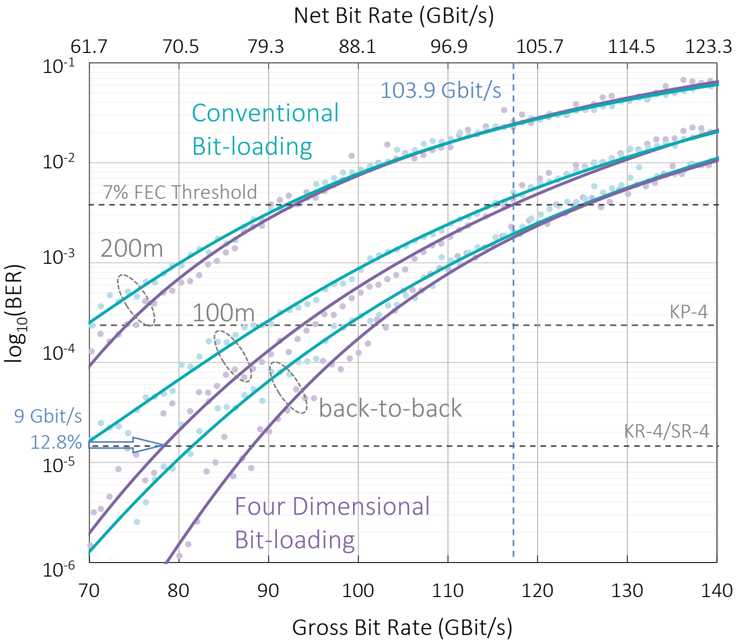

Figure 7.6: Gross and net data rates of BTB, 100 m and 200 m MMF transmission with (purple) and without (green) 4D bit-loading. Note that the net data rates indicated refer to 7% FEC.

(f), a better adoption to the channel response can be observed for the 8-D DMT, different from large bit steps of the conventional DMT. The insets in both Fig. 7.7(e) and (f) shows some typical constellations of format used for both cases.

Pre-FEC bit-rate

The BER changing with the increasing pre-FEC rate in the OBTB transmission as Fig. 7.8.(g) and over 100 m OM3 MMF as Fig. 7.8.(h) are initially investigated with three different loading schemes, i.e. the conventional QAMs (azure triangle), E_8Flex-m with power-loading (lemon grass circle) and without power-loading (tiffany blue diamond). On the 7% hard-decision (HD) FEC (3.8×10^{-3}) limits, the performances keep similar, i.e. $\sim$116 Gbit/s for OBTB and $\sim$110 Gbit/s for the fiber link. On the limit of KP-4 (2.2×10^{-4}), E_8Flex-m with and without power-loading earn the benefits of 9.2 Gbit/s and 6.3 Gbit/s over the conventional QAM loading scheme, reaching 94.0 Gbit/s and 91.1 Gbit/s respectively when transmit-

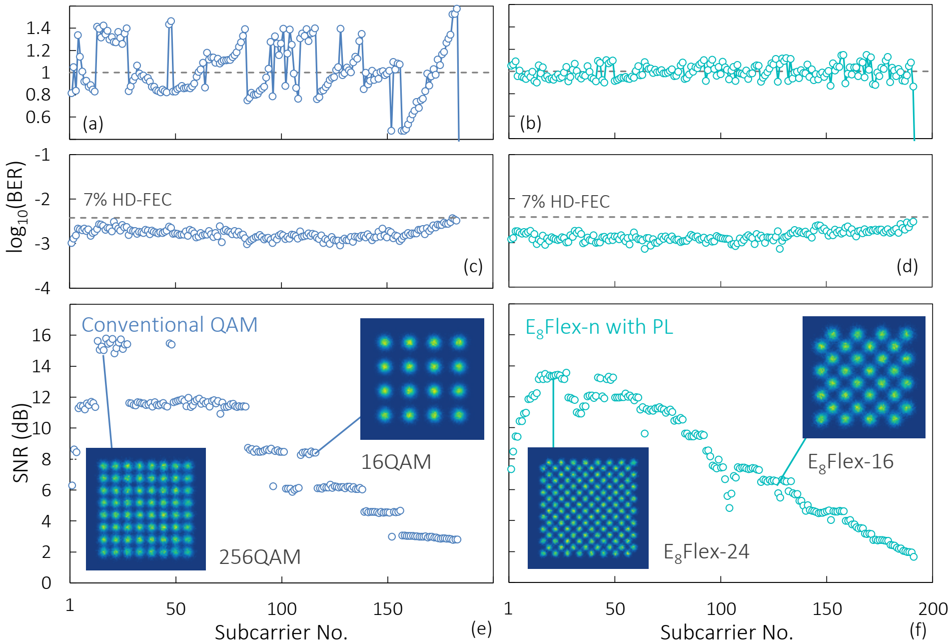

Figure 7.7: The performance comparison between the 8-D DMT compared and the conventional DMT: Coefficients of power-loading with QAM bit-loading (a) and 8D bit-loading (b); BER of different subcarriers with QAM bit-loading (c) and 8-D bit-loading (d); SNR of different subcarriers with QAM bit-loading (e) and 8-D bit-loading(f).

ted over 100 m MMF. Such gaps extend to 12.7 Gbit/s and 7.8 Gbit/s, giving the pre-FEC rate of 84.6 Gbit/s and 79.7 Gbit/s on the limit of the 100GBASE SR-4/KR-4 (1.46×10^{-5}). The benefits in the high SNR regime come from the enlarged minimum mutual Euclidean distance (MMED) and vanish in the low SNR regime due to the denser format configuration in MD space. In addition, it can be mathematically proven that the total energy is smaller by matching the channel response using bit-loading with finer granularity than adjusting the amplitude using optimal power-loading algorithm, leading the extra BER sensitivity. See more details in Tab. 7.4.

Reach extension

As in Fig. 7.9, the three loading schemes have similar reach in terms of 7% FEC. Meanwhile, the differences on the low overhead FEC limit are ineligible. An average 10 Gbit/s benefit is archived by E$_8$Felx-m power-

Table 7.4: BER vs. pre-FEC rate using the schemes of 8-D bit-loading with and without power-loading as well as the bit-loading with conventional QAMs with power-loading (unit Gbit/s).

FEC threshold	**QAM**	**E$_8$Flex w./o. PL**	Δ	**E$_8$Flex w. PL**	Δ
7 % HD-FEC OBTB	115.0	115.2	0.2	116.4	1.4
KP-4 OBTB	95.3	100.7	5.4	102.7	7.4
KR-4/SR-4 OBTB	84.2	92.1	7.9	94.6	10.4
7 % HD-FEC 100 m OM3	108.6	109.8	1.2	109.6	1.0
KP-4 100 m OM3	84.8	91.1	6.3	94.0	9.2
KR-4/SR-4 100 m OM3	71.9	79.7	7.8	84.6	12.7

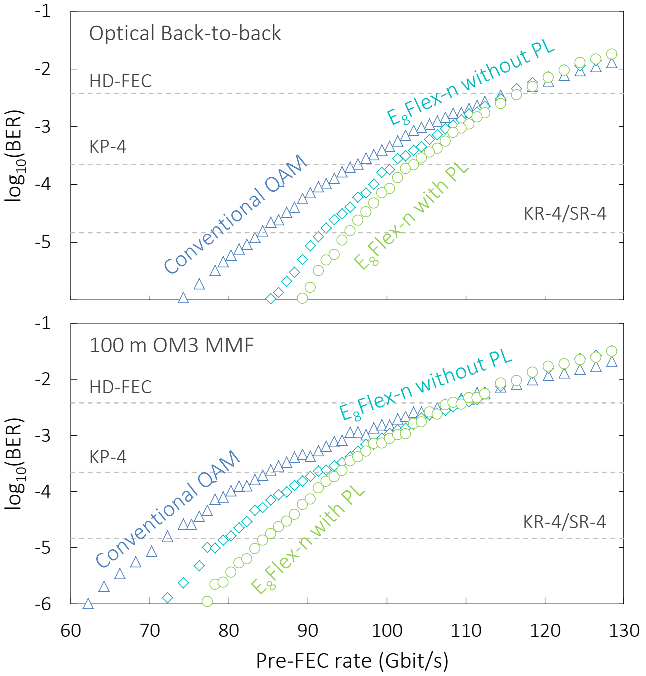

Figure 7.8: BER vs. pre-FEC rate using the DMT schemes of 8D bit-loading with (lemon grass circle) and without (tiffany blue diamond) power-loading as well as the bit-loading with conventional QAMs with power-loading (azure triangle) in optical back-to-back (g) and 100 OM3 MMF (h).

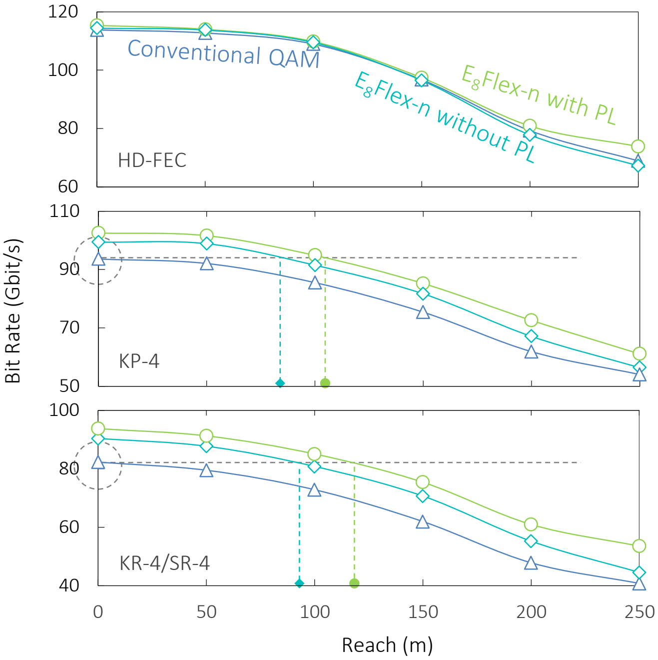

Figure 7.9: Bit-rate vs. transmission reach using the DMT schemes of 8-D bit-loading with (lemon grass circle) and without (tiffany blue diamond) power-loading as well as the bit-loading with conventional QAMs with power-loading (azure triangle) at different FEC threshold.

loading over QAM on KP-4, which increases to 12 Gbit/s on KR-4/KR-4. Similar features occur when switching off the power-loading, with the gaps of 6 Gbit/s and 8 Gbit/s respectively. Such benefits can be converted to the extension of reach. On KP-4, E_8Felx-m power-loading can convey 40 m longer with the same rate (85.5 Gbit/s) achieved by QAM through 100 m. Such merits can be also obtained on KR-4 with the extension of 50 m. In addition, turning off the power loading does not impede such reach extension significantly.

Table 7.5: Bit-rate vs. transmission reach using the schemes of 8-D bit-loading with and without power-loading as well as the bit-loading with conventional QAMs with power-loading at different FEC threshold (unit m).

FEC	**QAM**	**E_8Flex w./o. PL**	**Δ**	**E_8Flex w. PL**	**Δ**
7 % FEC	0/100	0/100	$\sim 0/\sim 0$	0/100	$\sim 0/\sim 0$
KP-4	0/100	88.2/139.9	88.2/39.9	104.5/161.2	104.5/61.2
KR-4/SR-4	0/100	92.1/149.6	92.1/49.6	122.4/167.8	122.4/67.8

Tolerance for the insertion loss

As illustrated in Fig. 3(b), there is no obvious difference of among bit-loading schemes on the tolerance, i.e. the reduction of rate per dB loss, on 7% FEC. The general tendency remains linear with 4 Gbit/s reduced in 1 dB power loss. For lower FEC limits, E_8Felx-m are more tolerant to the attenuation with respect to the same data rate. Initially, E_8Felx-m power-loading can accept a 4.4 dB power loss when it conveys bit at the same rate with the highest rate (87 Gbit/s) of QAM on KP-4. On KR-4, with 5.5 dB less power, E_8Felx-m can transmit as fast as QAM.

Table 7.6: Bit-rate vs. power loss using the schemes of 8D bit-loading with and without power-loading as well as the bit-loading with conventional QAMs with power-loading at different FEC threshold (unit dB).

FEC threshold	**QAM**	**E_8Flex w./o. PL**	**Δ**	**E_8Flex w. PL**	**Δ**
7 % HD-FEC	0	0	-	0	-
KP-4	0	3.6	3.55	0	4.5
KR-4/SR-4	0	4.4	4.4	0	5.1

Tolerance for the thermal degradations

Generally, the rates decrease linearly with the increase of laser temperature. However, the BER gaps between different modulation schemes offer the benefits of the thermal tolerance. For the KP-4 limit, E_8Felx-m power-loading has a 22 °C margin for transmitting faster than the conventional QAM with the achievable rate (90 Gbit/s) at 20 °C. Such thermal tolerance

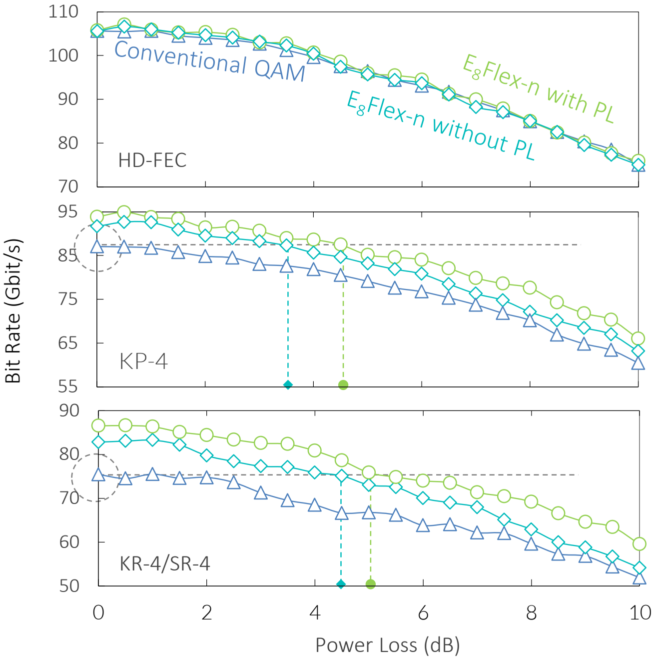

Figure 7.10: Bit-rate vs. power loss using the DMT schemes of 8-D bit-loading with (lemon grass circle) and without (tiffany blue diamond) power-loading as well as the bit-loading with conventional QAMs with power-loading (azure triangle) at different FEC threshold.

extends to 34 °C on the KR-4/SR-4 limit, meaning that the E_8Felx-m power-loading has the same bit-rate (75 Gbit/s) at 54 °C as the one for the conventional QAM at 20 °C.

Table 7.7: Bit-rate vs. operational temperature using the schemes of 8D bit-loading with and without power-loading as well as the bit-loading with conventional QAMs with power-loading at different FEC threshold (unit °C).

FEC threshold	**QAM**	**E_8Flex w./o. PL**	**Δ**	**E_8Flex w. PL**	**Δ**
7 % HD-FEC	20	29.8	9.8	29.6	9.6
KP-4	20	33.6	13.6	13.6	22.1
KR-4/SR-4	20	37.1	17.1	17.1	31.9

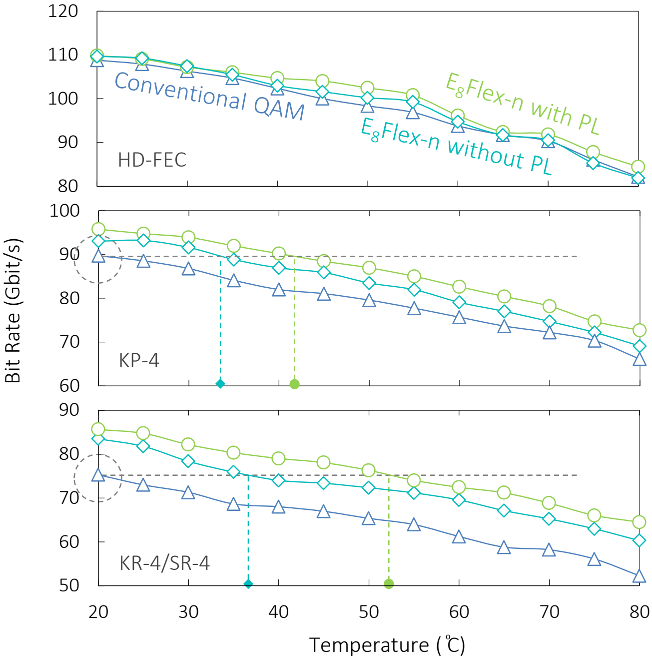

Figure 7.11: Bit-rate vs. operational temperature using the DMT schemes of 8D bit-loading with (lemon grass circle) and without (tiffany blue diamond) power-loading as well as the bit-loading with conventional QAMs with power-loading (azure triangle) at different FEC threshold.

7.5 Summary

In this chapter, we proposed two inter-symbol MD DMT modulations loaded with 4-D formats and 8-D formats respectively. We experimentally verify the performance enhancement of the 4-D DMT transmissions compared with its conventional counterparts in an OBTB and over 100/200 m MMF. The MD shows an apparent gain of sensitivity in the low noise regime. We also expend the idea to the 8-D scenario and demonstrate a 110-Gbit/s pre-FEC DMT transmission with the 8-D bit-loading schemes with and without the optimal power-loading and present the enhancement of the information rate (up to 20%), the extension of the reach (up to 50%) and the increased tolerance of power loss (up to 5.5 dB) and thermal effects (up to 34 °C) with respect to the 2.7% 100GBASE-SR4/KR-4 FEC, compared with the QAMs bit-loading. Such scheme relieves the requirement on the hardware system as well as the transmission conditions, which is critical for the cost-sensitive intra-datacenter interconnects. Moreover, it is intrinsically compatible with the future industrial standard of multi-lane optical interconnects, e.g. octal small form-factor pluggable (OSFP). Considering the requirements on data rate, latency, reliability and flexibility, DMT with 8-D bit-loading is a possible candidate for the future 100-G intra-data center optical interconnects.

The impact of the quantization noise from the limited number vertical resolution of the digital-to-analog converter (DAC) and analog-to-digital converter (ADC) of DMT [204] is one of the major consideration during the design of a DMT transmission system and has been treated as one challenging factor which steals the potential benefits and hinders its further application. Such effects may even further impact the performance of a MD DMT, since they normally offer benefits in a low noise regime. The detailed discussion on the potential impact of quantization noise is beyond the scope of this paper and will be elaborated in specific work in the future.

The work summarized here is presented in **PAPER 1** and **PAPER 5**.

Chapter 8

Multi-Subcarrier: Twenty Four-Dimensional CAP

In the last chapter, we introduce the application of the eight-dimensional (8-D) formats in a discrete multi-tone modulation (DMT) transmission system. Every four complex channels are combined into one super-channel. Thus, it is more natural to use the inter-symbol coded modulation, instead of the inter-subcarrier ones, meaning that it combines the symbols in different DMT symbols on the same subcarrier rather than ones on different subcarriers within a single DMT symbol. It is implicitly required due to the sub-band structure of DMT, since a normal DMT system tends to have finer bandwidth granularities and more than one hundred sub-carriers. It is essential to keep the orthogonality of each band for maintaining the consistency and effectiveness of the optimal bit-loading and power loading algorithm. Besides, the 8-D formats are designed base on the assumption that the signal-to-noise ratio (SNR) for each channel is similar. For the inter-subcarrier modulation, it is difficult to find four fixed sub-bands in the DMT channels which have the same SNR at any time instant. It implies that the power-loading algorithm has to be applied, which spoils the benefit of the so-called directly bit-loading as discussed in the last chapter.

Alternatively, the carrier-less amplitude phase modulation (CAP) has been reported as a promising 100 G solution [205] and have the potential of 100 G intra-datacenter transmission, i.e. 100 m multi-mode fiber (MMF) with 850 nm multi-mode (MM) vertical-cavity surface-emitting lasers (VCSELs) [54]. However, the nonlinearities of VCSELs in time domain generate the inter-carrier interference (ICI), which limits the achievable bit-rate. Like the 8-D format loaded DMT, we can expect an multi-dimensional (MD) format loaded CAP to enhance the tolerant for the interference by utilizing the increased minimum mutual Euclidean distance (MMED) resulting from the intrinsic MD geometries.

In this chapter, we investigate the performance of a twenty-four-dimensional (24-D) rate-flexible format, i.e. JUPITER-**M**, in a CAP system with 12 sub-bands, named as Leech-CAP. The format is designed based on a 24-D densest lattice structure, i.e. Λ_{24}, and loaded in an inter-subcarrier modulation. The compatibility between the format and the modulation schemes are implicitly ensured due to two facts: (1) for the usual practice, CAP has much fewer subcarriers than DMT. A uniform inter-subcarrier MD formats are then more probably to be designed in the corresponding dimensionality; (2) the new rate-flexible format, JUPITER-**M**, can adapt to the channels (or dimensions) with different SNR, meaning that the designing philosophy behind it differs from the previous E_8Flex-m. It intrinsically fits the coarsely divided CAP sub-bands, where the SNR of each are quite diverse.

We briefly introduce the CAP modulation in Section 8.1 and elaborate the principle of Leech-CAP in Section 8.2. The performance in different aspects are verified in an 850 nm vertical-cavity surface-emitting laser (VCSEL) based intensity-modulated direct-detection (IM-DD) data links. With the proposed scheme, a net 100 G transmission over 100 m MMF is achieved with the bit error rate (BER) requirement of 7% forward error correction (FEC). Moreover, various benefits are also observed, e.g. the reach extension and tolerance enhancement to different sort of system degradations.

8.1 CAP in general

We adopt in this chapter a multi-subcarrier transmission system named multi-band CAP. It stems from the classical work of the CAP in 1975 [206], which transmitted data through independent parallel streams via filtering with an orthogonal waveform set. It offers comparable spectral efficiency with the passband quadrature amplitude modulation (QAM), but with more realistic and cheaper digital implementations. It was popular in the applications of digital subscriber line (DSL) [207, 208]. It was proven that the conventional CAP is sensitive to non-flat frequency response [209], and requires complicated equalization. Applications of CAP in the short-reach optical data links were continuously reported during past years. A 3-D/4-D CAP using directly modulated VCSEL was reported in [210] and the applications for the datacenter interconnects in [211, 212]. M. I. Olmedo and et al. first realized the CAP to a multi-band version in a digital system [213, 214], to enhance the robustness and relieve the stress on the hardware system. It is also reported to be implemented in a coherent system, for extending the reach and increase the data rate [215].

8.1.1 CAP

CAP is one implementation of multi-subcarrier modulation (MSM) transmission, which we have formalized in Sect. 7.1.1. We briefly review the concept here and continue to formalize the CAP modulations. For the MSM symbols represented by a matrix $\widetilde{\mathbf{D}}^{N_{sc}\times\infty} = [\ \mathbf{d}_0\ \mathbf{d}_1\ \cdots\ \mathbf{d}_m\ \cdots\ ]$, in which, $\mathbf{d}_m = [\ d_m^0\ d_m^1\ \cdots\ d_m^\nu\ \cdots\ d_m^{N_{sc}-1}\ ]^{\mathrm{T}}$ is an super-symbol containing N_{sc} symbols. d_m^ν is the m-th symbol on the ν-th subcarrier. The MSM signal in the continuous domain can be expressed as:

$$d(t) = \sum_{m=-\infty}^{+\infty} \sum_{\nu=0}^{N_{sc}-1} d_m^\nu g_\nu(t - mT_s) \tag{8.1}$$

where $m, \nu \in \mathbb{Z}$, and $\nu \leq N_{sc}$; T_s is the time duration of each symbol; $g_\nu(\cdot)$ denotes the pulse function the ν-th carrier. And apparently, $g_\nu(t - mT_s)$ is time invariant, i.e. $g_\nu(t - mT_s) = g_\nu(t - (m - m_d)T_s)$, $\forall m_d \in \mathbb{Z}$; Beside, $g_\nu(t - mT_s)$ is orthonormal, namely following:

$$\int_{-\infty}^{+\infty} g_\nu(t - mT_s) g_{\nu'}(t - mT_s) dt = \begin{cases} 1 & \nu = \nu' \\ 0 & \nu \neq \nu' \end{cases} \tag{8.2}$$

And note that $\mathbf{d}_m \in \mathbb{R}_{sc}^N$ when $g_\nu(\cdot)$ is defined as real function. Otherwise $\mathbf{d}_m \in \mathbb{C}_{sc}^N$ when $g_\nu(\cdot)$ is complex. In the context of CAP, we usual adopt the former definition. Thus, the passband channel carrying complex symbols are normally seen as two-dimensional (2-D) CAP.

Normally in the description, we use the discretized form to express the digitalized CAP modulations. For consistency with the last chapter, We use $g_\nu[\mu_s]$ to express the $g_\nu(t)$ when $t = \mu_s T_0$, where $\mu_s \in \mathbb{Z}$, and T_0 is the time interval between sampling points. For concision, we omit the subscript for μ_s. The Eq. 8.1 is now rewrite as:

$$t[\mu] = \sum_{\nu=0}^{N_{sc}-1} d^\nu[\mu] * g_\nu[\mu] \tag{8.3}$$

in which $*$ denoted as the convolution operation. And more detailed, $d^{\nu}[\mu]$ following the condition in Eq. 8.4.

$$d^{\nu}[\mu] = \begin{cases} d^{\nu}_{m} & \text{for } \mu = mT_s \text{ with } m \in \mathbb{Z} \\ 0 & \text{otherwise} \end{cases} \tag{8.4}$$

At the receiver side, we sample the received signal $r(t)$ into $r[\mu]$[1]. So that we have similar relation like Eq. 8.3, but as in:

$$d^{\nu'} = f_{\nu'}[\mu] * r[\mu] \tag{8.5}$$

Assuming that we have the same sampling rate at the receiver side and the channel is ideal, we obtain the relation that transmit sequence $t[\mu]$ is the same with the received one $r[\mu]$, leading to relation:

$$d^{\nu'} = f_{\nu'}[\mu] * r[\mu] = f_{\nu'}[\mu] * t[\mu] = f_{\nu'}[\mu] * \left(\sum_{\nu=0}^{N_{sc}-1} d^{\nu} \right) [\mu] * g_{\nu}[\mu] \tag{8.6}$$

After expending Eq. 8.6, we can obtain the following Eq. 8.7, which full describes the principle of the (de)modulation process of a digital CAP.

$$d^{\nu'} = \sum_{\nu=0}^{N_{sc}-1} d^{\nu}_{m} \left(f_{\nu'} * g_{\nu} \right) [\mu - mT_s] \tag{8.7}$$

Based in this, we can extract the impulse responses function $h_{\nu\nu'}$, which follows the Eq. 8.8.

$$h_{\nu\nu'} = f_{\nu'} * g_{\nu}[\mu] \tag{8.8}$$

From Eq. 8.8, we can define an impulse response matrix $\mathbf{H}^{N_{sc} \times N_{sc}}[\mu]$, with $h_{\nu\nu'}$ as matrix elements. A good set of function g_{ν} need to be found to avoid the inter-symbol interference (ISI) and ICI. Therefore, the $\mathbf{H}[\mu]$ needs to fulfill the following conditions as:

$$\mathbf{H}[\mu] = \begin{cases} \mathbf{I} & \text{for } \mu = 0 \\ \mathbf{0} & \text{for } \mu = mT_s \end{cases} \tag{8.9}$$

in which $\mathbf{I}$ denoted as a $N_{sc} \times N_{sc}$ that for n of any other value, $\mathbf{H}$ is not defined.

---

[1] Note that here μ should be also μ_s for concision

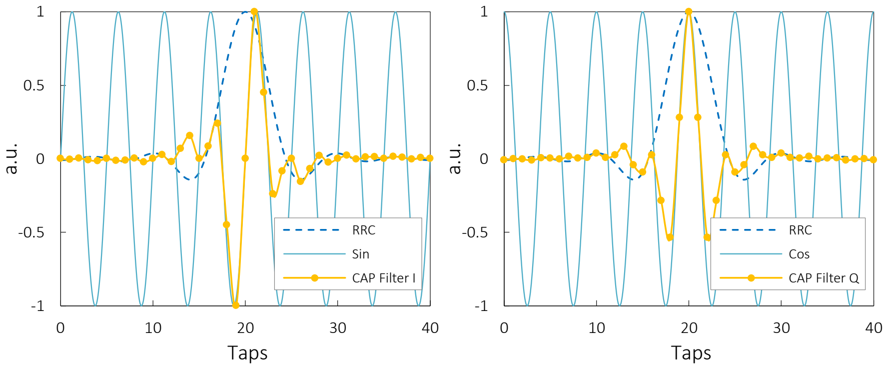

Figure 8.1: The taps of the FIR filter for generating a 2-D CAP using an orthogonal function pair: (left) the taps for the filter using sin function; (right) the taps for the filter using cos function. Both filter combines with a root-raised-cosine function with α=0.5.

Besides, for maximizing the SNR of the system, or the transmitter and receiver pair, we need to regulate that:

$$f_{\nu'}[\mu] = g_{\nu}[-n],\ \ or\ \ f_{\nu'}[-n] = g_{\nu}[\mu] \text{ when}\nu' = \nu \tag{8.10}$$

We then can rewrite Eq. 8.8 as following:

$$h_{\nu\nu'} = g_{\nu'}[-n] * g_{\nu}[\mu] \tag{8.11}$$

For the origin of CAP [206], the orthogonal function basis $g_{\nu}(\cdot)$ is found in Eq. 8.12 to construct the 2-D CAP with the flexible bandwidth occupancy, which is a combination of root-raised-cosine filter $R[\mu]$ and a the sinusoidal Hilbert-pair basis ({cos, sin}).

$$g_{\nu}[\mu] = f_{\nu'}[-n] = \begin{cases} R_{rrc}[\mu]\cos(2\pi f_c n) & \text{when } \nu = \nu'(\text{mod}2) \equiv 1 \\ R_{rrc}[\mu]\sin(2\pi f_c n) & \text{when } \nu = \nu'(\text{mod}2) \equiv 0 \end{cases} \tag{8.12}$$

in which $\nu \in \{0, 1\}$, meaning only two channels are considered with a single carrier with frequency of f_c.

The taps of the FIR filter are schematically shown in Fig. 8.1. The root-raised-cosine filter is expressed below [216]:

$$R_{rrc}[\mu] = \begin{cases} \dfrac{1}{T_s}\left[1+\alpha\left(\dfrac{4}{\pi}-1\right)\right] & \mu = 0 \\[2ex] \dfrac{\alpha}{T_s\sqrt{2}}\left[\left(1+\dfrac{2}{\pi}\right)\sin\left(\dfrac{\pi}{4\alpha}\right)+\left(1-\dfrac{2}{\pi}\right)\cos\left(\dfrac{\pi}{4\alpha}\right)\right] & \mu = \pm\dfrac{T_s}{4\alpha} \\[2ex] \dfrac{1}{T_s}\dfrac{\sin\left[\pi\dfrac{\mu}{T_s}(1-\alpha)\right]+4\alpha\dfrac{\mu}{T_s}\cos\left[\pi\dfrac{\mu}{T_s}(1+\alpha)\right]}{\pi\dfrac{\mu}{T_s}\left[1-\left(4\alpha\dfrac{\mu}{T_s}\right)^2\right]} & \text{otherwise} \end{cases} \tag{8.13}$$

where $\alpha \in [0, 1]$ is the roll-off factor. It is clear that the output sampled sequence $t[\mu]$ for a single sub-carrier 2-D CAP is express as:

$$\begin{aligned} t[\mu] = & \sum_{m=-\infty}^{+\infty} d_m^0 R_{rrc}[\mu - mT_s]\cos[2\pi f_c(\mu - mT_s)] \\ & + \sum_{m=-\infty}^{+\infty} d_m^1 R_{rrc}[\mu - mT_s]\sin[2\pi f_c(\mu - mT_s)] \end{aligned} \tag{8.14}$$

From the CAP filter expressed in Eq. 8.12, there are three important parameters to adjust the modulation, namely the carrier frequency f_c, the length of filter L_{rrc}, and the roll-off factor of the root-raised-cosine function α. They determine the spectral of the signal. f_c can be chosen arbitrarily as long as it is smaller than the highest frequency that the CAP filter can represent. The roll-off factor α is parameter of the root-raised-cosine function, which determines the reduction of spectral occupancies of the pulse shaping effects. The frequency occupancies of a passband signal is shaped into the following form:

$$B_s = R_s\,(1+\alpha) \tag{8.15}$$

in which, R_s is the symbol rate; B_s is the frequency occupancy of the signal band. It is clear that when α=0, the signal is actually shaped by a sinc function, whose frequency is rectangular with sharp edges, which occupies narrowest bandwidth equal to R_s. When α=1, it degenerates to the case with the same bandwidth consumption as the unshaped signal. The length of filter L_{rrc} is an essential parameter related to the system performance and complexity. With the reduction of the bandwidth occupancies by shaping

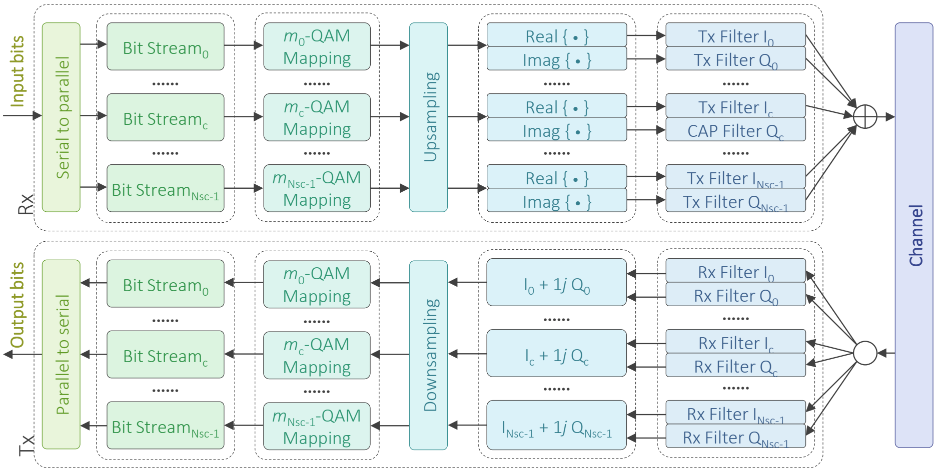

Figure 8.2: The principle of a multi-CAP transmission system.

the pulses with lower α values, it requires a longer filter, i.e. more filter taps.

8.1.2 Multi-CAP

Starting from Eq. 8.14, we can extend the single sub-carrier CAP to a multi-band CAP version. It can be express as following:

$$\begin{aligned} t[\mu] = & \sum_{m=-\infty}^{+\infty} \sum_{c=0}^{N_{sc}-1} d_m^{2c} R_{rrc}[\mu - mT_s] \cos[2\pi f_c(\mu - mT_s)] \\ & + \sum_{m=-\infty}^{+\infty} \sum_{c=0}^{N_{sc}-1} d_m^{2c+1} R_{rrc}[\mu - mT_s] \sin[2\pi f_c(\mu - mT_s)] \end{aligned} \tag{8.16}$$

The schematic illustration of the principle of a multi-CAP is shown in Fig 8.2.

The signal is first separated into multiple (denoted as N_{sc}) parallel streams, mapped into desired formats, e.g. m-QAMs and loaded onto sub-bands with different frequency f_ν, $\nu \in \{0, 1, \cdots, N_{sc} - 1\}$. For avoiding the ICI, frequency spacing ΔF is required to be larger than $R_s\,(1 + \alpha)$. For understanding the required sampling frequency, we refer to the similar discussion in [214]. We denote the sampling rate of the signal generation as F_{AWG}, which follows:

$$F_{AWG} = \frac{1}{N_{sc}} R_s N_{ss} \tag{8.17}$$

where N_{ss} indicates the number of samples per symbol. F_{AWG} should follow the Nyquist rules, which imposes the condition as:

$$F_{AWG} > F_{Nyquist} = 2R_s\left(1+\alpha\right) \tag{8.18}$$

which is converted to the condition for the sampling rate as

$$N_{ss} > 2N\left(1+\alpha\right) \tag{8.19}$$

Since the channel response is usually time-varying and non-flat, an adaptive optimal bit-loading and power-loading algorithm is necessary to achieve the optimal performance. The algorithm is similar to the bit- and power-loading algorithm used for the DMT transmission in Chapter 7.

8.2 24-D CAP: Leech-CAP

As other MSM transmissions, e.g. DMT, CAP is naturally MD. Therefore we can use MD coded modulation to enhance the performance. One possible solution is the so-called inter-symbol MD coded modulation. Such method has been applied to the 8D-DMT as discussed in the last chapter. It constructs the virtual MD signal space by combining the subcarriers with the same frequency through multiple MSM channels. As discussed, it is implicitly required by DMT, as the channel conditions are more stable for the inter-symbol combination than the intra-symbol super-channels. Without doubting, similar modulation schemes can be also applied to the multi-CAP transmission.

Meanwhile, compared with DMT, multi-CAP is also suitable for the intra-symbol MD coded modulations. The major reason is that a multi-CAP transmission has much fewer subcarrier than DMT does. For realizing the intra-symbol MD coded modulation, DMT subcarriers with similar SNR have to be grouped into different sets. However, the channel based on VCSEL is time-varying, meaning that the concrete condition on the specific subcarrier changes continuously. It implies that the similarity of the channel condition, which is the requirement for the subcarriers grouped together, is not always guaranteed. The continuous re-grouping, therefore, consumes extra computational resources and adds additional latencies. While MSM transmission can offer a MD signal space through the subcarriers in the entire symbol. Therefore, the adaptive adjustment will not be more complicated than the conventional QAM schemes.

More concretely, we can extend the multi-CAP to a 24-D by using 12 subcarriers, i.e. N_{sc}=12, with two real channels for each subcarrier. It

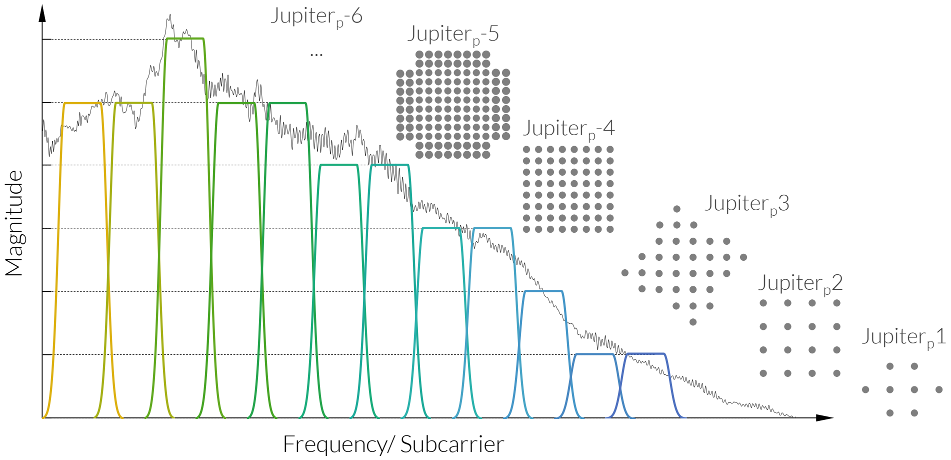

Figure 8.3: A schematic illustration of the construction of Leech-CAP.

implies that each 12-subcarrier CAP is inherently 24-D. For each subcarrier, two real channels are constructed by applying two orthogonal CAP filters. Conventionally, these 2-D channels can be loaded with the conventional QAMs. Besides, since the 12-subcarrier CAP symbols are intrinsically 24-D, it is also natural to consider loading with an entire CAP symbol with 24-D format, such as Leech24D-m. However, due to the non-flat responses of channels based on VCSEL, the SNR values for each subcarrier differ. Therefore, the rate-flexible SNR-adaptive 24-D format, JUPITER-**M** as discussed in Sect. 6.3, is a better candidate. A schematic illustration of the concept is shown in Fig. 8.3.

As the JUPITER-**M** offers $\text{Jupiter}_\text{p}\text{-}m_p$ on each subcarrier, having steps of spectral efficiency with one bit per projection. It is the same with the conventional QAM. Therefore, the typical bit- and power-loading algorithm is naturally applicable for $\text{Jupiter}_\text{p}\text{-}m_p$. It is also noteworthy that the estimation of the required SNR in term of a specific FEC threshold is no more exactly independent for each projection, but have to be calculated together with the constellation in other projections.

8.3 Experimental setups and methods

The schematic of the experiment setup is shown in Fig 8.4. At the transmitter, the input bits were mapped into 24-D super-symbols, and each

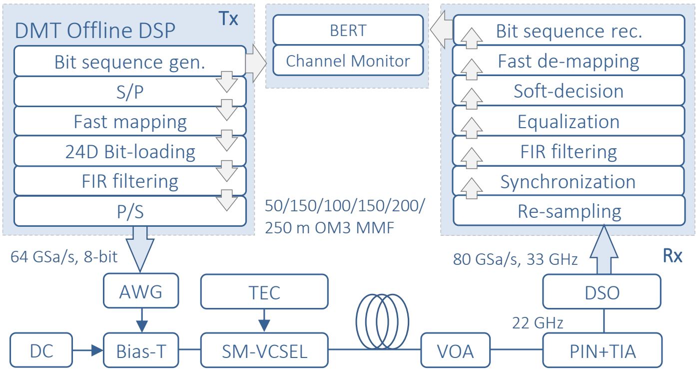

Figure 8.4: The schematic of the experimental setup for Leech-CAP.

super-symbol was further combined into 12 complex symbols, each for one subcarrier. Symbols for each subcarrier were processed by CAP filters, which is as to Eq. 8.16. The filters adopted the roll-off coefficient, α=0.02 and had a length of 30 symbols. The processed signal was uploaded to a 64 GSa/s 8-bit arbitrary waveform generator (AWG). It has a 33-GHz analog bandwidth. We used an 850 nm MM VCSEL as the light source. It has the optical power output of 6.5 dBm and 3 dB bandwidth at 19 GHz when biased at 18.5 mA. It was modulated by the electrical signal of 1 $\mathrm{V_{pp}}$. The VCSEL was mounted on an evaluation board (EVB) with wire bonding. We coupled the light from the laser to the MMF by an aspherical lenses pair. The lenses were mounted on the motorized stage with the mechanical resolution < 2 nm. The stage was then connected and controlled by a centralized computer. The VCSEL was placed on a heat sink, which was controlled by a thermoelectric cooler (TEC) controller, with adjustment resolution around 0.2 °C.

After transmission through a spool of OM3 MMF, the optical signal was received by a calibrated 22 GHz 850 nm photoreceiver.

Data traces were captured by an 80 GSa/s digital storage oscilloscope (DSO) of > 30 GHz analog bandwidth, with 5.2×10^7 samples for each. At the receiver side, the time window was resampled and synchronized before demodulated by the matched CAP filters. The two orthogonal inverted matched CAP filters of a specific subcarrier frequency demodulated the traces into two of the N_{sc} parallel steams of symbol on the corresponding subcarrier. A decision feedback equalizer of 20 T/2 forward taps and 4 feedback taps was applied to mitigate the linear interference. The output bit sequence was then obtained after a 24-D soft-decision and bit-to-symbol

Table 8.1: The parameters of the experiment setup for a Leech-CAP supported 100 G IM-DD transceiver.

Parameter	Symbol	Value	Unit
Sequence length	-	2^{15}	-
Symbol rate	R_s	1.88	GBaud
Bit rate	-	60-130	Gbit/s
Formats	-	Leech-CAP/Multi-CAP	-
Bands number	N_{sc}	12	12
Roll-off factor	α	0.02	-
Length of CAP filter	L_{rrc}	30	symbols
Bias current	I_{bias}	18.5	mA
Output power	-	6.5	dBm
wavelength	λ	850	nm
Modulation amplitude	V_{pp}	1	V
AWG analogy frequency	$f_{-3\ dB}^{AWG}$	$\sim$ 20	GHz
AWG sampling rate	F_{AWG}	64	GSa/s
AWG vertical resolution	-	8	bit
DSO analogy frequency	$f_{-3\ dB}^{DSO}$	$\sim$ 33	GHz
DSO sampling rate	-	80	GSa/s
DSO vertical resolution	-	8	bit
VCSEL type	-	Multi-mode	-
VCSEL pigtail	-	MMF	-
MMF length	L_{MMF}	0-200	m
PR bandwidth	$f_{-3\ dB}^{PR}$	22	GHz
PR Gain	G	-80/-70	V/W
PR Output noise	N_{PR}	590	μVrms
PR Impedance	Z_{PR}	50	Ω
Ambient temperature	T	20-80	°C

de-mapping. The decoded bit sequence was fed into the bit error rate tester (BERT), as well as the channel monitoring.

In the experiment, we first conducted an estimation on the channel condition by transmitting the signal with a rough estimation on the bit- and power-loading parameters. After the channel monitoring, i.e. the SNR calculation.

We allocated the bandwidth into 12 subcarriers, with each band of 1.88 GHz, i.e. 1.88 GBaud/s, and the band spacing at 1.02 of the baud

Table 8.2: BER vs. pre-FEC rate using the schemes of conventional CAP and Leech-CAP (unit Gbit/s) in OBTB and over 100 OM3 MMF.

Format	**QAM-CAP**	**Leech-CAP**	Δ	Δ (%)
7% FEC OBTB	113.2	116.5	3.1	2.7
KP-4 OBTB	90.0	103.2	13.2	14.7
SR-4/KR-4 OBTB	71.9	95.3	22.4	31.2
7% FEC 100 m OM3	97.9	107.3	9.4	9.6
KP-4 100 m OM3	77.2	96.0	18.8	24.4
SR-4/KR-4 100 m OM3	65.9	88.5	22.6	34.3

rate. The modulation amplitude was limited by an optimal clipping ratio of 10.5 dB. The bit and power loading were optimized by the water-filling algorithm, similar to [203]. The details of the parameter adopted in this experiment are referred to Tab. 8.1.

8.4 Experimental results

8.4.1 Pre-FEC bit-rate

Pre-FEC rate vs. BER is shown in Fig. 8.5 in an optical back-to-back (OBTB) transmission (upper) and over 100 m OM3 MMF (lower), with Leech-CAP and conventional CAP loaded with m-QAMs. On the 7% hard decision FEC (3.8×10^{-3}) limits, the Leech-CAP reaches 116.5 Gbit/s for OBTB and 107.3 Gbit/s for the fiber link, while 113.2 and 97.9 Gbit/s for the conventional one. The Leech-CAP gains an increase of bit-rate of 9.6% and enables the effective net 100 G transmission over 100 m OM3 MMF. On the limit of KP-4 (2.2×10^{-4}), the Leech-CAP earns the bit rate increase of 24.4% over the conventional CAP scheme, reaching 96 Gbit/s. Such increase extends to 22.6 Gbit/s, i.e. 34.3%, giving the pre-FEC rate of 88.5 Gbit/s on the limit of the 100GBASE SR-4/KR-4 (1.46×10^{-5}). The benefits of the high SNR regime come from the enlarged MMED by constructing the format set through all subcarriers. As expected, such MD geometry shaping can effectively relieve the ICI. See more detail in Tab. 8.2.

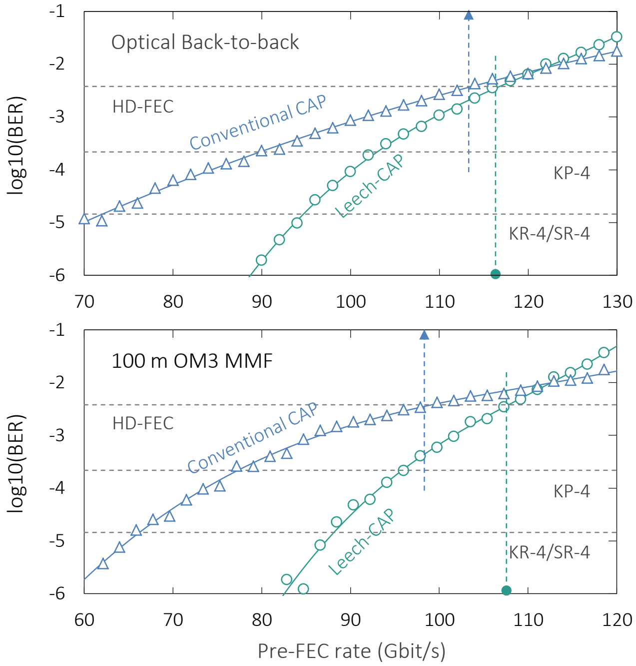

Figure 8.5: BER vs. pre-FEC rate using the CAP schemes of Leech-CAP with (green circle) and the conventional QAM loaded CAP (azure triangle) in optical back-to-back (upper) and 100 OM3 MMF(lower).

8.4.2 Reach extension

Leech-CAP provides effective reach extensions compared with its conventional counterpart. With the same achievable bit rate over 100 m MMF, the Leech-CAP extends the reach by 42%, 75% and 87% regarding the 7% FEC, KP-4 and KR-4/SR-4 respectively, reaching 142 m, 175 m and 187 m accordingly. See more detail in Tab. 8.3. It is clear that when entering the low noise regime, i.e. high SNR, the extension of the reach of Leech-CAP gets even higher.

8.4.3 Tolerance for the insertion loss

Tolerance of power loss is enhanced by using Leech-CAPs. They reduced the required optical power by 6.2 dB, 9.1 dB and 9.4 dB regarding the 7% FEC, KP-4 and KR-4/SR-4 respectively, reaching 12%, 32% and 400% accordingly. See more detail in Tab. 8.4.

Table 8.3: Bit-rate vs. reach using the schemes of conventional CAP and Leech-CAP (unit m).

Format	QAM-CAP	Leech-CAP	Δ	Δ (%)
7% FEC	0/100/178	68/142/200	68/42/22	-/42/12.4
KP-4	0/100/126	128/175/200	128/75/74	-/75/58.7
SR-4/KR-4	0/100/116	172/187/200	172/87/84	-/87/72.4

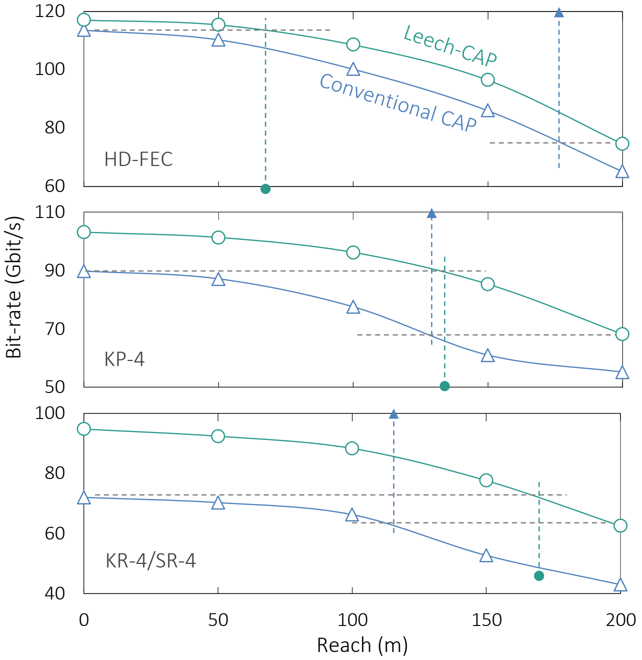

Figure 8.6: Bit-rate vs. reach using the CAP schemes of Leech-CAP with (green circle) and the conventional QAM loaded CAP (azure triangle) at different FEC threshold.

8.4.4 Tolerance for the thermal degradations

Thermal tolerance, the Leech-CAP is shown to have a higher thermal tolerance. It provides the same data rate as the conventional CAP does at 20 °C under higher operational temperatures, i.e. 40.3 °C, 51.2 °C, and 55.2 °C, with the corresponding FEC requirements. See more detail in Tab. 8.5.

Table 8.4: Bit-rate vs. power loss using the schemes of conventional CAP and Leech-CAP (unit dB).

Format	**QAM-CAP**	**Leech-CAP**	Δ	Δ (%)
7% FEC	0/8.9	6.2/10	1.1	-/12.4
KP-4	0/7.6	9.1/10	2.4	-/31.6
SR-4/KR-4	0/2	9.4/10	8	-/400.0

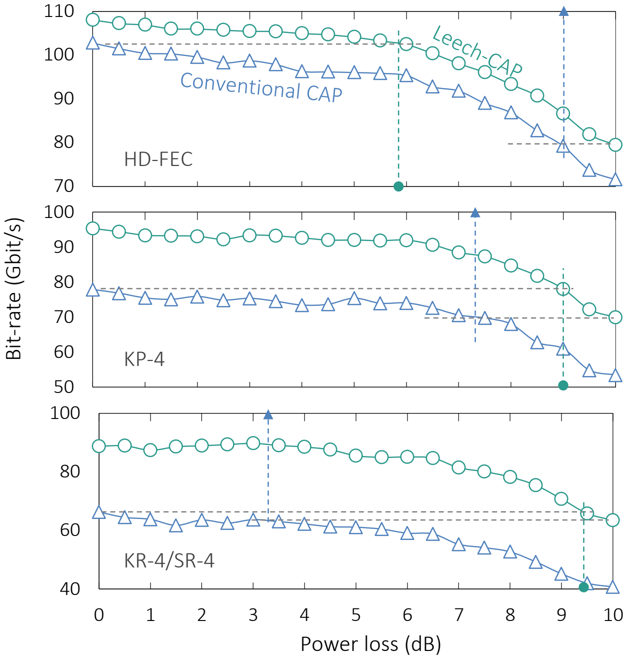

Figure 8.7: Bit-rate vs. power loss using the CAP schemes of Leech-CAP with (green circle) and the conventional QAM loaded CAP (azure triangle) at different FEC threshold.

8.4.5 Performance comparison with DMT

Net 100 Gbit/s transmission have been archived with DMT and multi-CAP MSM schemes based on the 850 nm VCSELs.

Compared with the DMT modulation schemes in Chapter 7, where the experimental setup is close, the performance of Leech-CAP with short transmitting distances lags slightly behind its DMT counterpart, when the

Table 8.5: Bit-rate vs. operational temperature using the schemes of conventional CAP and Leech-CAP (unit °C).

Format	QAM-CAP	Leech-CAP	Δ	Δ (%)
7% FEC	20/69	40.3/80	20.3/11	101.5/15.9
KP-4	20/48	51.2/80	31.2/32	156/66.7
SR-4/KR-4	20/36.7	55.2/80	35.2/43.3	176/118.0

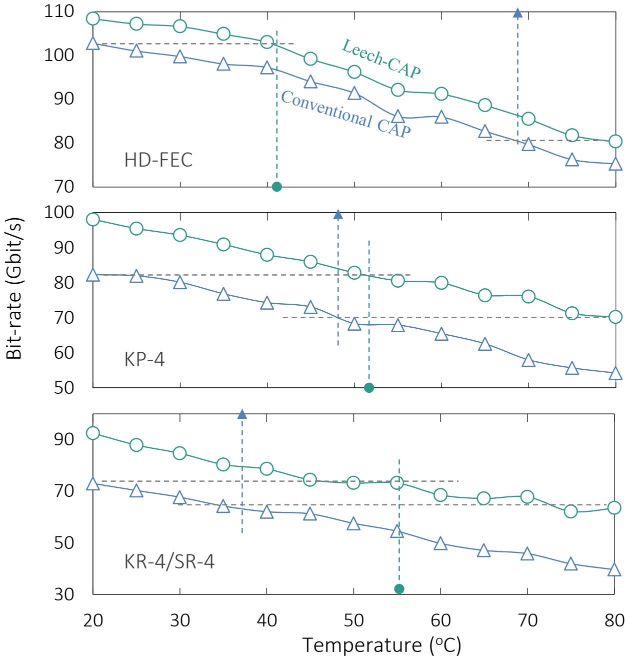

Figure 8.8: Bit-rate vs. operational temperature using the CAP schemes of Leech-CAP with (green circle) and the conventional QAM loaded CAP (azure triangle) at different FEC threshold.

conventional QAMs are loaded. However, the improvements of 24-D intra-symbol coded modulation is apparently larger than what brings from the 8-D version of DMT.

Compared with DMT, CAP or multi-CAP is more sensitive to the non-flat spectra and imposes higher requirements on SNR. While, on the other hand, CAP is expected to be realized with an analog framework, which

Table 8.6: Comprehensive comparison between QAM-DMT, QAM-CAP, 8D-DMT and Leech-CAP in OBTB and over 100 m MMF.

OBTB (Gbit/s)	7% HD-FEC	KP-4	KR-4/SR-4
QAM-CAP	113.2	90	71.9
QAM-DMT	115	95.3	84.2
Δ_c[2]	-1.8	-5.3	-13.3
Leech-CAP	116.5	103.2	95.3
8D-DMT	116.4	102.7	94.6
Δ_m	0.1	0.5	0.7
$\delta=\Delta_m-\Delta_c$	1.9	5.8	14

100 m MMF (Gbit/s)	7% HD-FEC	KP-4	KR-4/SR-4
QAM-CAP	97.9	77.2	65.9
QAM-DMT	108.6	84.8	71.9
Δ_c	-10.7	-7.6	-6.0
Leech-CAP	107.3	96	88.5
8D-DMT	109.6	94.0	84.6
Δ_m	-2.3	2.0	3.9
$\delta=\Delta_m-\Delta_c$	8.4	9.6	9.9

is critical for the future applications in the datacenter interconnects, as it avoids using expensive analog-to-digital converter (ADC), which offers a more affordable realization [209].

8.5 Summary

We design and demonstrate a 24-dimensional modulation, i.e. Leech-CAP, based on the framework of a CAP modulation with 12 subcarriers, namely JUPTIER-M. It enables the 100 Gbit/s transmissions over 100 m MMF with 850 nm multi-mode vertical-cavity surface-emitting laser (MM-VCSEL). It proves that applying an inter-subcarrier coded modulation based on the high-dimensional geometry can effectively improve the performance of a multi-subcarrier transmission. Such scheme can be considered as an alternative solution for the datacenter interconnection, where the design of physical layer is severer than the digital signal processing (DSP).

The work summarized here is presented in **PAPER 2**.

Chapter 9

Other Modulation Techniques

For enhancing the performance of the optical data links used inside mega-datacenters on the physical layer, various configurations and techniques have been proposed and investigated in recent years, including diverse multiplexing schemes, e.g. shortwave division multiplexing (SWDM) and mode division multiplexing (MDM), coherent and partial coherent frameworks, e.g. the direct detection for complex signals, sensitivity enhancing technology and mode-selective launching techniques. Among all, two alternative related link enhancing techniques are introduced in this chapter, including the mode-selective launching and the optical compensation for the MDM for orbital angular momentum (OAM) modes, i.e. optical vortex modes or simply optical vortices. A further discussion on their chances and challenges will be given later.

9.1 Mode-selective launching

The effective bandwidth of a multi-mode fiber (MMF) channel is limited mainly by differential mode delay (DMD). The group velocities for modes within different mode groups are diverse. If modes in more than one mode group are excited, the DMD generates the relative time delay between modes, i.e. intermodal interference (IMI). Such dispersive effect is the major limiting factor for the bandwidth degradation. By applying the mode controlling techniques, these deleterious effects can be suppressed. The idea in general leads to a class of mode excitation techniques, or launching techniques, known as the mode-selective launching. Among them, the most straightforward realization is on the laser-fiber interface [217]. Some other newly developed techniques, such as the mode selective laser [218], are beyond the scope of this paper.

It is known from previous research that the group velocity difference, or known as DMD, between mode groups of higher order is smaller than ones of a lower order, especially in the case where the fundamental mode is involved. Using precise central launch techniques, people can excite the fundamental mode only in the MMF. It can be realized by using the single-mode fiber (SMF)-MMF couple at the transmitter side by precisely controlling the relative position and tiling angle [219]. However, due to the imperfection of fiber dimensions, twisting and bending during the propagation, modes coupling is inevitable, which excites additional higher order modes, limits the purity of the fundamental mode, and degrades the performance consequently. Moreover, the precise mode launching needs high-quality fiber coupling, which adds the expenses accordingly. Alternatively, it is possible to use the single-mode (SM) light source. The recent works include a 54 Gibt/s transmission over 1 km OM4 and 20 Gibt/s over 2 km OM4 respectively [220, 221].

The third mode selective launching is so-called modes shaping techniques, or sometimes known as mode conversion. It is realized by shaping the modes output from the light source and shaping the mode order by using free-space technologies, such as wavefront engineering via diffractive optical elements [222] and spatial light modulator (SLM). Mode-selective launching investigations have been reported with different operational wavelength, including 1550 nm [223], 1300 nm [222], 850 nm [224], and 640 nm [225].

Apart from the fixed the phase pattern, by using the computer-generated holography (CGH), the adaptivity can be introduced in optimizing the phase pattern for achieving the optimal excited modes. It can be based on a different cost function, including the difference between the modulated field and the desired pattern [223], the eye open for the modulated signal [224], and signal to interference ratio [226].

In 2015, we demonstrated a mode-selective launching with a vortex mode shaping via using SLM. The vortices pattern is generated on SLM with a flexible change of the topological charge. The donut-like intensity profile can be observed in the far field, which is used to excite modes of higher order in MMF. An illustration of the phase pattern and simulated intensity profile, together with the observed pattern with an 850 nm camera are shown respectively in Fig. 9.1.(a), (b) and (c).

The experiment setup is shown in Fig. 9.2. It adopted a regular signal

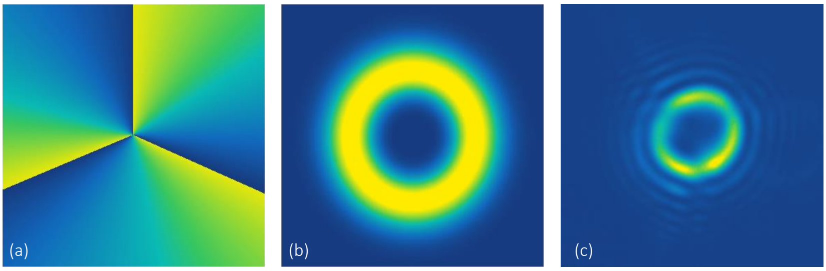

Figure 9.1: Generations of OAM modes. (a) the phase pattern to generate the OAM mode;(b) the simulated OAM mode;(c) the observed OAM mode, when topological charge l=3.

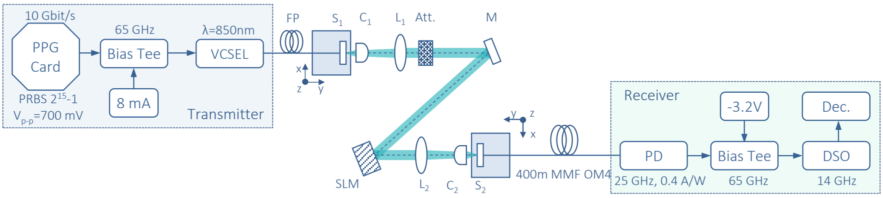

Figure 9.2: Schematics of the experimental setups for the MMF launching with mode shaping. Att.-Attenuator; C_1, C_2-Collimators; FP-Fiber Patchcord; M-Mirror; L_1, L_2-Lenses; S_1, S_2-xyz Stages; SLM-Spatial Light Modulator.

transmitter using an 850 nm vertical-cavity surface-emitting laser (VCSEL) as a light source. The output light beam was processed and modulated with a free-space setup. After the collimation, the light beam was modulated by a SLM, whose operational wavelength was centered at 850 nm. A donut-liked light profile was generated with a dark spot at the middle of the beam. The light beam was then focused on the fiber end of a piece of MMF. We demonstrated and verified the benefits of the mode-selective launching techniques with vortex modes in aspects of the enhanced sensitivity.

From Fig. 9.3, the improvement of the bit error rate (BER) sensitivity can be easily observed. We place the analysis in a long term evolution (LTE) radio-over-fiber (RoF) application scenario via 400 m OM4 MMF. In general, along with the increase of the topological charge of the vortex modes, i.e. the order of the modes, an increasingly improved transmission quality is observed. Specifically, at the standard 7% forward error correction (FEC) limit, the vortex mode launching with M_3 can offer an averagely 1.5 dB power benefit, compared with M_0, namely the fundamental mode, in both

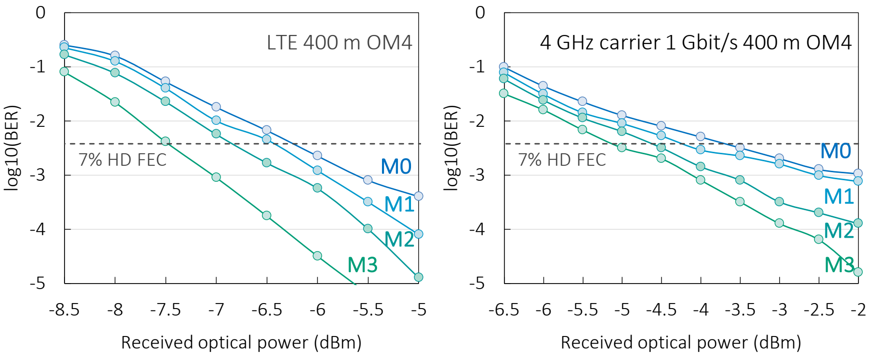

Figure 9.3: The BER performance of optical signal modulated with OAM modes of different topological charge over 400 m OM4 MMF, m=0,1,2,3.

cases following the LTE standards or 4 GHz carrier.

The mode-selective launching offers a low-cost solution of the link enhancement, as it can be easily realized by using the diffractive optical element (DOE), e.g. vortex lens or phase plates. While the drawbacks of such modulation are also apparent, laying the facts that: (1) the stability of coupling becomes a risky factor. Especially the collaborative effects between the mode shaping and imprecise coupling so-far remain insufficiently investigated. (2) the shaping of the phase front requires free-space propagations, implying an increased footprint of the optical module. (3) the modes propagation behavior inside the MMF remains unclear. Therefore, so-far it can only offer a qualitative analysis on such link enhancement, but makes it difficult to give a rigorous quantitative analysis.

9.2 Optical compensation for vortex modes

In **PAPER 12**, we demonstrated another link enhancement techniques. The study focuses on an all-optical mode compensation of the MDM system using optical vortex modes. Such technique is expected to enhance the channel capacity for a short-reach inter-datacenter transport. We used an 850 nm distributed feedback laser (DFB) laser as the light source while using standard single-mode-fiber (SSMF) as the channel. Thus, more than one mode can be accommodated in the SSMF, making it possible to be utilized as the few mode fiber (FMF) by reusing the deployed fiber resource, and expect to enhance the channel capacity. Besides, we used OAM modes with different topological charge as independent channels. However, optical vortices transported in the conventional SMF suffer from stochastic mode coupling due to fiber twisting, bending and imperfection. Thus, a multi-input multi-output (MIMO) based digital mode compensation is normally necessary [227,228]. However, for the application scenarios of the datacenter interconnects, such MDM is not favorable due to the facts including (1) an analog-to-digital converter (ADC) based quantization is inevitable, which adds the cost; (2) the digital signal processing increases the latencies, which is not preferred in a latency-sensitive application. Therefore, an all-optical based mitigation of the inter-modal crosstalk is an effective solution considering the power consumption and cost. We experimentally demonstrated an OAM mode compensation on the mode coupling effects over SSMF in a complete optical domain.

The experimental setup is shown in Fig. 9.4, where the key building blocks are two SLMs. The first one excited the optical vortices, and the second one was used for estimating the propagation matrix and conducting the mode compensation. We reconstruct the fiber complex propagation matrix by utilizing the azimuthal decomposition of the output field [229], which enables the determination of the matrix elements from the direct calculation of the field intensity in the corresponding diffraction orders. A patch cord (L = 4 m) made of SSMF was used. It behaves as a 3-mode fiber at the wavelength 848 nm. The reconstruction of the propagation matrix consisted of two steps. First, individual modes were transmitted. By doing so, the amplitudes of all elements and the phase differences within each column relative to the element on the main diagonal could be determined. Then the phase differences between columns were determined by using twin-mode superposition through adjacent modal channels, for details in [230].

We used a CGH to realize the inverse matrix for the fiber propagation. The CGH was defined as in Eq. 9.1.

$$\Psi_{\mathrm{SLM2}}(\mathbf{x}) = \sum_{\nu=1}^{N} \left(\sum_{\mu=1}^{N} u_{\nu\mu}^{-1} e^{-il_{\mu}\phi} \right) e^{i\mathbf{w}_{\nu}\mathbf{x}} \tag{9.1}$$

in which, $u_{\nu\mu}^{-1}$ is the element of the inverse of normalized propagation matrix; N is the number of modes considered; l_{μ} is the topological charge of the μ-th transmitted mode; $\mathbf{w}_{\nu}$ is the spatial carrier corresponding to the ν-th received mode; $\mathbf{x} = (x, y)$ is the coordinators of the screen. An illustration of the CGH is shown in Fig. 9.4.(b) and (c).

The brief illustration of the results is shown in Fig. 9.5. which shows

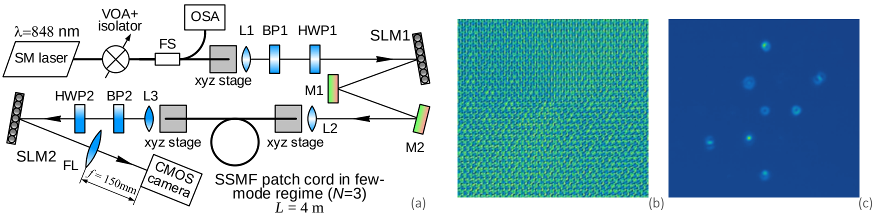

Figure 9.4: Schematics of the experimental setup.(a) Experimental setup for the fiber analysis and mode coupling compensation: SLM1, SLM2-spatial light modulators Hamamatsu X10468-02 (792×600 pixels); OSA-optical spectrum analyzer; FS-fiber splitter; L1-L3-lenses; FL-Fourier lens; HWP1, HWP2-halfwave plates; BP1, BP2-beam polarizers; M1, M2-mirrors; (b) Example of CGH pattern. (c) Example of the analysis pattern.

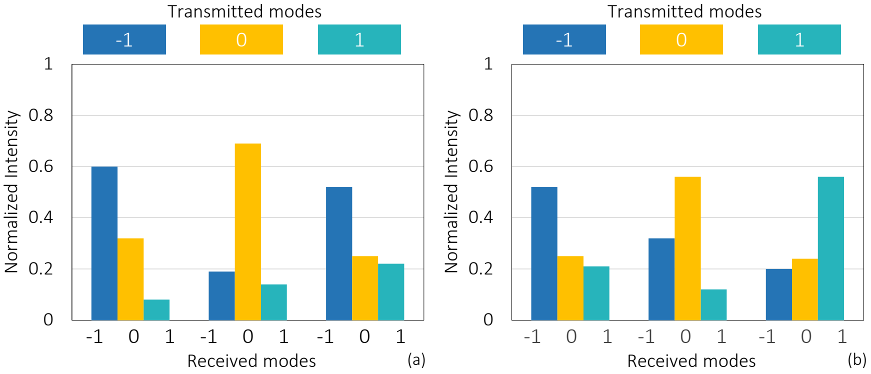

Figure 9.5: Experimental results of the CGH based all-optical modes compensation. (a) and (b) normalized intensity distribution between modes during fiber analysis and after optical compensation respectively.

the effectiveness of the CGH based all-optical compensation for OAM mode coupling in fiber channels. The experiment demonstrated an approach which allows a potential utilization of the vortex modes in an MDM communication system which has the potential to reuse the 850 nm optics and SSMF resources for the future datacenter interconnects.

9.3 Discussion

The above discussed two different schemes aiming to enhance the performance of the current generation of link configuration inside the mega-datacenters. Here, we discuss the technical features of these schemes and a vista of the future.

The mode-selective launching techniques have the technical and commercial potential in the current, and future generations of short-reach optical interconnects if the links of MM-VCSELs over MMFs are still the mainstream technologies. In fact, companies like, Finisar and IBM are actively investigating this specific direction. The possible difficulties are similar to the SM-VCSELs over MMF when the low-cost coupling become more expensive for the mode-selections. For instance, the off-set launching is the easiest way of generating the higher order excited modes. However, it implies, meanwhile, a high coupling precision. Various environment effects may deteriorate the advantages, such as thermal expansion. Moreover, the behavior of modes inside the MMF is stochastic. The performance benefits are not theoretically guaranteed. Besides, finding the realistic physical implementation is also challenging. Therefore, so for the mode-selective launching techniques are treated as engineering practice for the complementary of the current generation technologies, but perhaps not for a long term.

The optical compensation techniques for the MDM with optical vortex modes is initiated to the possible transmission schemes, i.e. using SSMF as FMF with a light source of short-waves, e.g. 850 nm. The current SSMF installation can support the few mode division multiplexing (FMDM) transmission. Such scheme may catch the chance of market when the current mega-datacenters evolve to ones with even larger scale. As well known that the MDM has encountered strong competitors of other spatial division multiplexing (SDM) schemes, e.g. multi-core fiber (MCF) [231], for that in the standard telecommunication scenarios, the SDM upgrade poses the question on the choice of the inevitable new fiber installation between FMF/MMF or MCF, instead of using shortwave carrier techniques over the current SSMF installation, due to the facts like the high attenuation and chromatic dispersion. Yet, since the market window is transient, it remains uncertain whether the actual product will appear before the window is closed when the MCF might become the dominating technology inside the mega-datacenters.

The work summarized here is presented in **PAPER 9** and **PAPER 10**.

Chapter 10

Conclusion

Through the whole thesis, several multi-dimensional (MD) formats for intensity-modulated direct-detection (IM-DD) applications have been proposed and investigated. We start from the fixed rate four-dimensional (4-D) and eight-dimensional (8-D) pulse amplitude modulation (PAM) with simplified modulations, followed by a twenty-four-dimensional (24-D) extension. These formats are then developed to the rate-flexible format family E_8Flex-m and JUPITER-$\mathbf{M}$ in 8-D and 24-D respectively. The potential of these two formats are then verified in a discrete multi-tone modulation (DMT) and a carrier-less amplitude phase modulation (CAP) system respectively.

10.1 MD coded modulation for IM-DD

How MD can help

From the previous chapters, we can conclude that the MD formats, i.e. MD coded modulations, can help to enhance the bit error rate (BER) performance if the other transmission conditions are the same compared with the uncoded formats, i.e. conventional PAMs, DMT or CAP in the low overhead (OH) forward error correction (FEC) threshold or asymptotically. The gaps generated on the BER values can be converted into the benefits in various aspects. For instance, for the same performance, the MD formats are proven more tolerant for the insertion loss and thermal degradations. Among the benefits, two are essential. One is the reach extension. The vertical-cavity surface-emitting laser (VCSEL)+multi-mode fiber (MMF) transceivers are limited by the inter-modal dispersion. Thus, for the same optical output power, the gap on BER offers a larger margin for tolerant for the degradation from the dispersion and, therefore, converted into the extended reach. The other benefits for the practical products lay in the potential reduction of cost. As discussed before, by using the format with finer granularities, the bandwidth resources can be fully utilized. It implies the possibility to use optical components in a lower class of specifications, e.g. narrower bandwidth and lower maximum output power.

Where comes from the benefits

From insights into the lattice structure and a deeper understanding of the (de)modulation of the MD lattice-based coded modulation with a more abstract perspective, we can find the source of the benefits for BER sensitivity from the utilization of the soft-information. The encoder, i.e. modulator, has essentially a higher resolution, or equivalently more digital-to-analog converter (DAC) bits. On the other hand, the soft-decision or the hyperspace hard-decision (HD) used for the MD format decision reserves the soft-information in each regular symbol. It implies that when applying the analog-to-digital converter (ADC) with lower resolution, it may degrade the performance of a certain MD modulation scheme. In this thesis, we also discuss a soft-decision scheme which directly uses the analog signal without quantization, where the soft information is naturally contained in the sampled sequence and not destructed by the ADC. By using a mixed integrated circuit (IC) design, we can abstractly propose an analog soft-decoding scheme. Such technique may benefit the all potential transmission systems which are supposed to avoid digital signal processing (DSP), such as IM-DD PAM transceivers using analogy equalization, e.g. continuous time linear equalization (CTLE). The other potential applications lay in the analog coherent transceiver for the future datacenter interconnects.

Collaborative effects with FECs

Collaborative effects between the coded modulation and FEC remains unknown. In all the works mentioned in the previous chapter, we adopt the standard FEC threshold, i.e. the required BER values, as the criteria of a successful transmission, for that the post-FEC BER is expected below 10^{-12} which is seen as error free. However, the fixed requirement on BER may not reasonable when other coded modulation schemes or FEC strategy are applied. In [232], Tobias and et al. suggest of using the generalized mutual information (GMI) to estimate the potential benefits when the hybrid channel coding-coded modulation schemes are adopted, which can be a strong tool to analyze this issue.

Will PCS help on VCSEL based IM-DD system

Probabilistic constellation shaping (PCS) is proposed for coded modulations in the coherent systems [233]. Higher dimensional probabilistic constellation shaping (PCS) is also processed include the 4-D PCS [234]. The applications of the PCS's in the IM-DD systems are also reported recently []. Whether the PCS also benefits the transmission for a VCSEL based IM-DD system is however controversial. In a talk in 2017 [235], X. Zhou and et al. pointed out that the PCS is based on the additive white Gaussian noise (AWGN) assumptions. While the noise distribution of a VCSEL based IM-DD system is no more rigorous Gaussian. Due to the nonlinear physical process and RIN-dispersion collaborative effects, the noise of the VCSEL output follows a mixed Gaussian, instead of pure Gaussian noise. Therefore, a careful design of the distribution matcher should be investigated. However, the benefits of the sensitivity come from similar sources, namely the utilization of the soft-information by adopting ADC or decode with finer granularity. The deeper investigation of the PCS in for a VCSEL based system is beyond the scope of this work.

10.2 A brief history of tomorrow

Deep learning based fast decoding for MD formats

The deep learning framework, or known as artificial neural networks with multiple hidden layers, is reported to be applicable in the channel decoding [236]. The similar techniques are expected in the decoding for a MD format. The potential benefit lays the consideration of the latencies and power consumption. The mixed IC design requires explicit digital components, e.g. cache and register, the latencies are mainly dependent on the speed of caching the temporary bit sections. Yet, if the neural nets inspired decode structure is feasible to provide comparable performance compared with the conventional optimal soft-decisions, the latencies resulting from the signal processing can be greatly reduced. Moreover, the stream based neural nets are generally power efficient, for that no extra bit cache is required during the process. And the spike neural networks are expected to provide even lower power consumption. Even though, the current generation of the neuromorphic chip is still digital, the pure analog neuromorphic chip is promising for the future channel decoding.

Trans-platform applications

The applications of MD formats investigated in this thesis also have the potential in other transmission systems, such as single-carrier and wavelength division multiplexing (WDM) coherent systems and mode division multiplexing (MDM) systems. The potential of the MD formats mentioned above lay in the bit-rate flexibility. The benefits of the BER sensitivity may not be the key for the coherent systems, as the on the standard 7% HD FEC, the performance difference between the MD formats and the regular quadrature amplitude modulation (QAM) is trivial. Besides, the noise of a coherent system with erbium doped fiber amplifier (EDFA) is modeled as AWGN. Therefore, even the asymptotic gain of the lattice-based constellations may be not better than the constellation shaping scheme, which follows the Gaussian probabilistic distributions. Yet, the benefits they provide hide behind the rate flexibility and smooth transitions at 7% FEC threshold. Today, the 4-D modulation formats for the coherent system have been adopted due to the 4-D nature of the electromagnetic field. The 4-D rate-flexible formats and the corresponding modulation schemes have been reported in [60, 63]. Thus, the E_8Flex-m is expected to be applied in the coherent system, as an 8-D version of the formats mentioned above.

We hope our works summarized in this thesis can open the new possibilities of the MD formats in more in-depth and broader applications.

Bibliography

[1] Facebook, “Introducing data center fabric, the next-generation Facebook data center network,” April 2018, [Online]. Available: https://code.facebook.com/posts/360346274145943/.

[2] D. Knowledge, “How is a mega data center different from a massive one?” October 2014, [Online]. Available: http://www.datacenterknowledge.com/archives/2014/10/15/how-is-a-mega-data-center-different-from-a-massive-one.

[3] X. Zhou, H. Liu, and R. Urata, “Datacenter optics: requirements, technologies, and trends,” *Chinese Optics Letter*, vol. 15, no. 5, May 2017.

[4] J. Chen, “Polymer waveguide based optical interconnects for high-speed on-board communications,” Ph.D. dissertation, University of Cambridge, Cambridge, UK, November 2016.

[5] I. Mackenzie and C. DeCusatis, “Sustaining innovation when outsourcing components in multi-technology, multi-component systems,” *Innovation Organization and Management*, vol. 15, no. 1, pp. 2–16, March 2013.

[6] Wikipedia, “100 Gigabit Ethernet, year=2018, month=April, note=[Online]. Available: https://en.wikipedia.org/wiki/100_Gigabit_Ethernet,,.”

[7] ——, “Terabit Ethernet,” April 2018, [Online]. Available: https://en.wikipedia.org/wiki/Terabit_Ethernet.

[8] D. Lewis and C. Cole, “100G CWDM4 MSA technical specifications,” November 2015, [Online]. Available: http://www.cwdm4-msa.org/wp-content/uploads/2015/12/CWDM4-MSA-Technical-Spec-1p1-1.pdf.

[9] G. P. MSA, “100G PSM4 specification,” September 2014, [Online]. Available: http://psm4.org/100G-PSM4-Specification-2.0.pdf.

[10] K. Schmidtke, “Designing 100G optical connections,” March 2017, [Online]. Available: https://code.facebook.com/posts/1633153936991442/designing-100g-optical-connections/,.

[11] I. T. Association, “InfiniBand roadmap,” February 2018, [Online]. Available: http://www.infinibandta.org/content/pages.php?pg=technology_overview.

[12] Wikipedia, “64b/66b encoding,” February 2018, [Online]. Available: https://en.wikipedia.org/wiki/64b/66b_encoding.

[13] ——, “InfiniBand,” February 2018, [Online]. Available: https://en.wikipedia.org/wiki/InfiniBandw.

[14] ——, “Multi-source agreement,” February 2017, [Online]. Available: https://en.wikipedia.org/wiki/Multi-source_agreement.

[15] D. M. Kuchta, “High capacity VCSEL-based links,” in *Proc. Optical Fiber Communication Conference (OFC)*, March 2017, paper Tu3C.4.

[16] Corning, “Corning® SMF-28e+® optical fiber,” July 2014, [Online]. Available: https://www.corning.com/media/worldwide/coc/documents/PI1463_07-14_English.pdf.

[17] Draka, “Single-mode optical fiber (SMF),” July 2014, [Online]. Available: https://www.prysmiangroup.com/sites/default/files/business_markets/markets/downloads/datasheets/SMF---Single-Mode-Optical-Fiber-SSMF.pdf.

[18] Z. Wang and A. Ghiasi, “400GE lane configurations v.s. FEC options,” July 2013, [Online]. Available: http://www.ieee802.org/3/400GSG/public/13_07/wang_400_01_0713.pdf.

[19] “IEEE standard for Ethernet - amendment 3: physical layer specifications and management parameters for 40 Gb/s and 100 Gb/s operation over fiber optic cables,” *IEEE Std 802.3bm-2015 (Amendment to IEEE Std 802.3-2012 as amended by IEEE Std 802.3bk-2013 and IEEE Std 802.3bj-2014)*, pp. 1–172, March 2015.

[20] J. Petrilla, “100G SR4 & RS (528, 514, 7, 10) FEC,” Avago Technologies, Tech. Rep., September 2012.

[21] P. Anslow, "RS(544,514) FEC performance including precoding," July 2016, [Online]. Available: http://www.ieee802.org/3/cd/public/July16/anslow_3cd_01_0716.pdf.

[22] D. M. Kuchta, A. V. Rylyakov, F. E. Doany, C. L. Schow, J. E. Proesel, C. W. Baks, P. Westbergh, J. S. Gustavsson, and A. Larsson, "A 71-Gb/s NRZ modulated 850-nm VCSEL-based optical link," *IEEE Photonics Technology Letters*, vol. 27, no. 6, pp. 577–580, March 2015.

[23] J. Lavrencik, S. Varughese, J. Gustavsson, E. Haglund, A. Larsson, and S. E. Ralph, "Error-free 100 Gbps PAM-4 transmission over 100 m wideband fiber using 850 nm VCSELs," in *Proc. European Conference on Optical Communication (ECOC)*, September 2017, paper W.1.A.3.

[24] D. M. Kuchta, A. V. Rylyakov, C. L. Schow, J. E. Proesel, C. Baks, P. Westbergh, J. S. Gustavsson, and A. Larsson, "64Gb/s transmission over 57m MMF using an NRZ modulated 850nm VCSEL," in *Proc. Optical Fiber Communication Conference (OFC)*, March 2014, paper Th3C.2.

[25] P. Westbergh, E. P. Haglund, E. Haglund, R. Safaisini, J. S. Gustavsso, and A. Larsson, "High-speed 850 nm VCSELs operating error free up to 57 Gbit/s," *Electronics Letters*, vol. 49, no. 16, pp. 1021–1023, August 2013.

[26] K. L. Chi, Y. X. Shi, X. N. Chen, J. J. Chen, Y. J. Yang, J. R. Kropp, N. Ledentsov, M. Agustin, N. N. Ledentsov, G. Stepniak, J. P. Turkiewicz, and J. W. Shi, "Single-mode 850-nm VCSELs for 54-Gb/s on-fff keying transmission over 1-km multi-mode fiber," *IEEE Photonics Technology Letters*, vol. 28, no. 12, pp. 1367–1370, June 2016.

[27] D. M. Kuchta, A. V. Rylyakov, C. L. Schow, J. E. Proesel, C. W. Baks, P. Westbergh, J. S. Gustavsson, and A. Larsson, "A 50 Gb/s NRZ modulated 850 nm VCSEL transmitter operating error free to 90 °C," *Journal of Lightwave Technology*, vol. 33, no. 4, pp. 802–810, February 2015.

[28] G. Stepniak, A. Lewandowski, J. R. Kropp, N. N. Ledentsov, V. A. Shchukin, N. Ledentsov, G. Schaefer, M. Agustin, and J. P. Turkiewicz, "54 Gbit/s OOK transmission using single-mode VCSEL

up to 2.2 km MMF," *Electronics Letters*, vol. 52, no. 8, pp. 633–635, April 2016.

[29] G. Stepniak, J. R. Kropp, N. N. Ledentsov, V. A. Shchukin, N. Ledentsov, G. Schaefer, and J. P. Turkiewicz, "54 Gbps OOK transmission using single mode VCSEL up to 1 km OM4 MMF," in *Proc. Optical Fiber Communication Conference (OFC)*, March 2016, paper Th4D.5.

[30] F. Karinou, N. Stojanovic, C. Prodaniuc, Z. Qiang, and T. Dippon, "112 Gb/s PAM-4 optical signal transmission over 100-m OM4 multimode fiber for high-capacity data-center interconnects," in *Proc. European Conference on Optical Communication (ECOC)*, September 2016, paper M.2.C.3.

[31] T. Zuo, L. Zhang, J. Zhou, Q. Zhang, E. Zhou, and G. N. Liu, "Single lane 150-Gb/s, 100-Gb/s and 70-Gb/s 4-PAM transmission over 100-m, 300-m and 500-m MMF using 25-G class 850nm VCSEL," in *Proc. European Conference on Optical Communication (ECOC)*, September 2016, paper Th.1.C.2.

[32] G. Stepniak, L. Chorchos, M. Agustin, J. R. Kropp, N. N. Ledentsov, V. A. Shchukin, N. Ledentsov, and J. P. Turkiewicz, "Up to 108 Gb/s PAM 850 nm multi and single mode VCSEL transmission over 100 m of multi mode fiber," in *42nd European Conference on Optical Communication (ECOC 2016)*, September 2016, paper W.4.P1.SC4.43.

[33] J. Lavrencik, S. Varughese, V. A. Thomas, G. Landry, Y. Sun, R. Shubochkin, K. Balemarthy, J. Tatum, and S. E. Ralph, "100Gbps PAM-4 transmission over 100m OM4 and wideband fiber using 850nm VCSELs," in *Proc. European Conference on Optical Communication (ECOC)*, September 2016, paper Th.1.C.5.

[34] S. M. R. Motaghiannezam, I. Lyubomirsky, H. Daghighian, C. Kocot, T. Gray, J. Tatum, A. Amezcua-Correa, M. Bigot-Astruc, D. Molin, F. Achten, and P. Sillard, "180 Gbps PAM4 VCSEL transmission over 300m wideband OM4 fibre," in *Proc. Optical Fiber Communication Conference (OFC)*, March 2016, paper Th3G.2.

[35] R. Motaghiannezam, I. Lyubomirsky, H. Daghighian, C. Kocot, T. Gray, J. Tatum, A. Amezcua-Correa, M. Bigot-Astruc, D. Molin,

F. Achten, and P. Sillard, “Four 45 Gbps PAM4 VCSEL based transmission through 300 m wideband OM4 fiber over SWDM4 wavelength grid,” *Optics Express*, vol. 24, no. 15, pp. 17 193–17 199, July 2016.

[36] S. M. R. Motaghiannezam and C. Kocot, “104 Gbps PAM4 transmission over OM3 and OM4 fibers using 850 and 880 nm VCSELs,” in *Proc. Conference on Lasers and Electro-Optics (CLEO)*, paper SW4F.8.

[37] Y. Sun, R. Lingle, R. Shubochkin, K. Balemarthy, D. Braganza, T. Gray, W. J. Fan, K. Wade, D. Gazula, and J. Tatum, “51.56 Gb/s SWDM PAM4 transmission over next generation wide band multimode optical fiber,” in *Proc. Optical Fiber Communication Conference (OFC)*, March 2016, paper Tu2G.3.

[38] J. M. Castro, R. Pimpinella, B. Kose, Y. Huang, B. Lane, K. Szczerba, P. Westbergh, T. Lengyel, J. S. Gustavsson, A. Larsson, and P. A. Andrekson, “48.7-Gb/s 4-PAM transmission over 200 m of high bandwidth MMF using an 850-nm VCSEL,” *IEEE Photonics Technology Letters*, vol. 27, no. 17, pp. 1799–1801, September 2015.

[39] J. Castro, R. Pimpinella, B. Kose, Y. Huang, B. Lane, K. Szczerba, P. Westbergh, T. Lengyel, J. Gustavsson, A. Larsson, and P. Andrekson, “Investigation of 60 Gb/s 4-PAM using an 850 nm VCSEL and multimode fiber,” *Journal of Lightwave Technology*, vol. 34, no. 16, pp. 3825–3836, August 2016.

[40] J. M. Castro, R. Pimpinella, B. Kose, Y. Huang, B. Lane, K. Szczerba, P. Westbergh, T. Lengyel, J. S. Gustavsson, A. Larsson, and P. A. Andrekson, “50 Gb/s 4-PAM over 200 m of high bandwidth MMF using a 850 nm VCSEL,” in *Proc. Optical Fiber Communication Conference (OFC)*, paper W1D.1.

[41] K. Szczerba, T. Lengyel, M. Karlsson, P. A. Andrekson, and A. Larsson, “94-Gb/s 4-PAM using an 850-nm VCSEL, pre-emphasis, and receiver equalization,” *IEEE Photonics Technology Letters*, vol. 28, no. 22, pp. 2519–2521, November 2016.

[42] K. Szczerba, P. Westbergh, M. Karlsson, P. A. Andrekson, and A. Larsson, “70 Gbps 4-PAM and 56 Gbps 8-PAM using an 850 nm VCSEL,” *Journal of Lightwave Technology*, vol. 33, no. 7, pp. 1395–1401, April 2015.

[43] ——, “60 Gbits error-free 4-PAM operation with 850 nm VCSEL,” *Electronics Letters*, vol. 49, no. 15, pp. 953–955, July 2013.

[44] K. Szczerba, P. Westbergh, J. Gustavsson, Å. Haglund, J. Karout, M. Karlsson, P. Andrekson, E. Agrell, and A. Larsson, “30 Gbps 4-PAM transmission over 200m of MMF using an 850 nm VCSEL,” in *Proc. European Conference on Optical Communication (ECOC)*, paper Tu.3.C.4.

[45] S. C. J. Lee, F. Breyer, S. Randel, D. Cardenas, H. P. A. van den Boom, and A. M. J. Koonen, “Discrete multitone modulation for high-speed data transmission over multimode fibers using 850-nm VCSEL,” in *Proc. Optical Fiber Communication Conference (OFC)*, March 2009, paper OWM2.

[46] C. Xie, P. Dong, S. Randel, D. Pilori, P. Winzer, S. Spiga, B. Kögel, C. Neumeyr, and M. C. Amann, “Single-VCSEL 100-Gb/s short-reach system using discrete multi-tone modulation and direct detection,” in *Proc. Optical Fiber Communication Conference (OFC)*, March 2015, paper Tu2H.2.

[47] W. A. Ling, I. Lyubomirsky, R. Rodes, H. M. Daghighian, and C. Kocot, “Single-channel 50G and 100G discrete multitone transmission with 25G VCSEL technology,” *Journal of Lightwave Technology*, vol. 33, no. 4, pp. 761–767, Februray 2015.

[48] C. Kottke, C. Caspar, V. Jungnickel, R. Freund, M. Agustin, and N. N. Ledentsov, “High speed 160 Gb/s DMT VCSEL transmission using pre-equalization,” in *Proc. Optical Fiber Communication Conference (OFC)*, March 2017, paper W4I.7.

[49] C. Kottke, C. Caspar, V. Jungnickel, R. Freund, M. Agustin, J. R. Kropp, and N. N. Ledentsov, “High-speed DMT and VCSEL-based MMF transmission using pre-distortion,” *Journal of Lightwave Technology*, vol. 36, no. 2, pp. 168–174, January 2018.

[50] I. C. Lu, C. C. Wei, H. Y. Chen, K. Z. Chen, C. H. Huang, K. L. Chi, J. W. Shi, F. I. Lai, D. H. Hsieh, H. C. Kuo, W. Lin, S. W. Chiu, and J. Chen, “Very high bit-rate distance product using high-power single-mode 850-nm VCSEL with discrete multitone modulation formats through OM4 multimode fiber,” *IEEE Journal of Selected Topics in Quantum Electronics*, vol. 21, no. 6, pp. 444–452, November 2015.

[51] B. Wu, X. Zhou, Y. Ma, J. Luo, K. Zhong, S. Qiu, Zhiyong, Feng, Y. Luo, M. Agustin, N. Ledentsov, J. Kropp, V. Shchukin, N. N. Ledentsov, I. Eddie, and L. Chao, "Close to 100 Gbps discrete multi-tone transmission over 100 m of multimode fiber using a single transverse mode 850 nm VCSEL," in *Proc. SPIE*, vol. 9766, march 2016.

[52] W. Bo, Z. Xian, M. Yanan, J. Luo, Q. Shaofeng, Z. Kangping, F. Zhiyong, L. Chao, V. Shchukin, J. Kropp, and N. Lendentsov, "Single-lane 112Gbps transmission over 300m OM4 multimode fiber based on a single-transverse-mode 850nm VCSEL," in *Proc. European Conference on Optical Communication (ECOC)*, September 2016, paper Th.2.P2.SC4.44.

[53] I. Lyubomirsky, W. A. Ling, R. Rodes, H. M. Daghighian, and C. Kocot, "56 Gb/s transmission over 100m OM3 using 25G-class VCSEL and discrete multi-tone modulation," in *Optical Interconnects Conference (OI)*, May 2014, paper TuC2.

[54] M. I. Olmedo, A. Tatarczak, T. Zuo, J. Estaran, X. Xu, and I. T. Monroy, "Towards 100 Gbps over 100m MMF using a 850nm VCSEL," in *Proc. Optical Fiber Communication Conference (OFC)*, March 2014, paper M2E.5.

[55] E. Agrell and M. Karlsson, "Power-efficient modulation formats in coherent transmission systems," *Journal of Lightwave Technology*, vol. 27, no. 22, pp. 5115–5126, November 2009.

[56] M. Karlsson and E. Agrell, "Which is the most power-efficient modulation format in optical links?" *Optics Express*, vol. 17, no. 13, pp. 10 814–10 819, June 2009.

[57] J. Karout, X. Liu, C. Sethumadhavan, E. Agrell, M. Karlsson, and R. Essiambre, "Experimental demonstration of an optimized 16-ary four-dimensional modulation format using optical OFDM," in *Proc. Optical Fiber Communication Conference (OFC)*, March 2013, paper OW3B.4.

[58] H. Bülow, "Polarization QAM modulation (POL-QAM) for coherent detection schemes," in *Proc. Optical Fiber Communication Conference (OFC)*, March 2009, paper OWG2.

[59] H. Bülow, X. Lu, L. Schmalen, A. Klekamp, and F. Buchali, "Experimental performance of 4D optimized constellation alternatives for

PM-8QAM and PM-16QAM," in *Proc. Optical Fiber Communication Conference (OFC)*, March 2014, paper M2A.6.

[60] J. K. Fischer, S. Alreesh, R. Elschner, F. Frey, M. Nölle, C. Schmidt-Langhorst, and C. Schubert, "Bandwidth-variable transceivers based on four-dimensional modulation formats," *Journal of Lightwave Technology*, vol. 32, no. 16, pp. 2886–2895, August 2014.

[61] A. Alvarado and E. Agrell, "Achievable rates for four-dimensional coded modulation with a bit-wise receiver," in *Proc. Optical Fiber Communication Conference (OFC)*, March 2014.

[62] T. A. Eriksson, T. Fehenberger, P. A. Andrekson, M. Karlsson, N. Hanik, and E. Agrell, "Impact of 4D channel distribution on the achievable rates in coherent optical communication Experiments," *Journal of Lightwave Technology*, vol. 34, no. 9, pp. 2256–2266, May 2016.

[63] J. K. Fischer, C. Schmidt-Langhorst, S. Alreesh, R. Elschner, F. Frey, P. Wilke-Berenguer, L. Molle, M. Nölle, and C. Schubert, "Generation, transmission, and detection of 4-D set-partitioning QAM signals," *Journal of Lightwave Technology*, vol. 33, no. 7, pp. 1445–1451, April 2015.

[64] T. Koike-Akino, D. S. Millar, K. Kojima, and K. Parsons, "Eight-dimensional modulation for coherent optical communications," in *Proc. European Conference on Optical Communication (ECOC)*, September 2013, paper Tu.3.C.3.

[65] M. Nakamura, M. Yoshida, F. Hamaoka, and K. Yonenaga, "Optical 8-dimensional time-polarization modulation using square- QAM-constellation and a simple decoding algorithm," in *Proc. Opto-Electronics and Communications Conference (OECC)*, June 2015.

[66] S. Ishimura and K. Kikuchi, "Multi-dimensional permutation-modulation format for coherent optical communications," *Optics Express*, vol. 23, no. 12, pp. 15 587–15 597, June 2015.

[67] D. S. Millar, T. Koike-Akino, S. O. Arik, K. Kojima, K. Parsons, T. Yoshida, and T. Sugihara, "High-dimensional modulation for coherent optical communications systems," *Optics Express*, vol. 22, no. 7, pp. 8798–8812, April 2014.

[68] J. Karout, E. Agrell, K. Szczerba, and M. Karlsson, “Optimizing constellations for single-subcarrier intensity-modulated optical systems,” *IEEE Transactions on Information Theory*, vol. 58, no. 7, pp. 4645–4659, July 2012.

[69] W. Mao and J. M. Kahn, “Lattice codes for amplified direct-detection optical systems,” *IEEE Transactions on Communications*, vol. 56, no. 7, pp. 1137–1145, July 2008.

[70] J. Renaudier, R. Rios-Müller, M. A. Mestre, H. Mardoyan, A. Konczykowska, F. Jorge, B. Duval, and J. Dupuy, in *Proc. Optical Fiber Communication Conference (OFC)*.

[71] R. Rios-Müller, J. Renaudier, M. A. Mestre, H. Mardoyan, A. Konczykowska, F. Jorge, B. Duval, and J. Dupuy, “Multi-dimension coded PAM4 signaling for 100Gb/s short-reach transceivers,” in *Proc. Optical Fiber Communication Conference (OFC)*, March 2016, paper Th1G.4.

[72] N. Stojanovic, C. Prodaniuc, F. Karinou, and Z. Qiang, “56-Gbit/s 4-D PAM-4 TCM transmission evaluation for 400-G data center applications,” in *Proc. Optical Fiber Communication Conference (OFC)*, March 2016, paper Th1G.6.

[73] C. Prodaniuc, N. Stojanovic, Z. Qiang, F. Karinou, T. Lee, K. Engenhardt, and R. Llorente, “Experimental demonstration of 56 Gb/s 4D-PAM-5 Trellis coded modulation for 400G WDM metro-access networks,” in *Proc. Optical Fiber Communication Conference (OFC)*, March 2016, paper Tu2A.6.

[74] A. Mutig, *High Speed VCSELs for Optical Interconnects.* Springer-Verlag Berlin Heidelberg, 2011.

[75] J. L. Jewell, A. Scherer, S. L. McCall, Y. H. Lee, S. Walker, J. P. Harbison, and L. T. Florez, “Low-threshold electrically pumped vertical-cavity surface-emitting microlasers,” *Electronics Letters*, vol. 25, no. 17, pp. 1123–1124, August 1989.

[76] L. A. Coldren and S. W. Corzine, *Diode Lasers and Photonic Integrated Circuits.* John Wiley & Sons, Inc., 1995.

[77] P. Moser, *Energy-Efficient VCSELs for Optical Interconnects.* Springer International Publishing, 2016.

[78] A. Ibaraki, K. Kawashima, K. Furusawa, T. Ishikawa, T. Yamaguchi, and T. Niina, "Buried Heterostructure GaAs/GaAlAs distributed Bragg reflector surface emitting laser with very low threshold (5.2 mA) under room-temperature CW conditions," *Japanese Journal of Applied Physics Part 2-letters*, vol. 28, no. 4, pp. L667–L668, 1989.

[79] I. A. Ukaegbu, D.-W. Kim, M. S. M. Shirazy, T.-W. Lee, M. H. Cho, and H.-H. Park, "Performance analysis of vertical and horizontal transmitter array modules using short- and long-wavelength VCSELS for optical interconnects," *IEEE Transactions on Components Packaging and Manufacturing Technology*, vol. 3, no. 5, pp. 740–748, 2013.

[80] K. Iga, F. Koyama, and S. Kinoshita, "Surface emitting semiconductor lasers," *IEEE Journal of Quantum Electronics*, vol. 24, no. 9, pp. 1845–1855, September 1988.

[81] A. Rissons and J.-C. Mollier, "The vertical-cavity surface emitting laser (VCSEL) and electrical access contribution," in *Optoelectronics*. Rijeka: InTech, 2011, ch. 12.

[82] M. R. T. Tan, "Commercial applications of vertical cavity surface emitting lasers," 2000, p. 201.

[83] K. L. Lear, V. M. Hietala, H. Q. Hou, J. Banas, B. E. Mammons, J. Zolper, and S. P. Kilcoyne, "Small and large signal modulation of 850 nm oxide-confined vertical-cavity surface-emitting lasers," in *Proc. Conference on Lasers and Electro-Optics (CLEO)*, May 1997, paper CWA2.

[84] M. Freebody, "Lasers evolve to meet the demands of optical communications," April 2018, [Online]. Available: https://www.photonics.com/a49950/Lasers_Evolve_to_Meet_the_Demands_of_Optical.

[85] G. Sialm, *VCSEL Modeling and CMOS Transmitters up to 40 Gb/s for High-Density Optical Links*. Konstanz, Germany: Hartung-Gorre, 2007.

[86] P. L. Division, *OptSim Models Reference: Volume II Block Mode*, RSoft Design Group, Inc., 400 Executive Boulevard, NY 10562, 2010.

[87] P. V. Mena, J. J. Morikuni, S. M. Kang, A. V. Harton, and K. W. Wyatt, “A comprehensive circuit-level model of vertical-cavity surface-emitting lasers,” *Journal of Lightwave Technology*, vol. 17, no. 12, pp. 2612–2632, December 1999.

[88] M. X. Jungo, D. Erni, and W. Bachtold, “VISTAS: a comprehensive system-oriented spatiotemporal VCSEL model,” *IEEE Journal of Selected Topics in Quantum Electronics*, vol. 9, no. 3, pp. 939–948, May 2003.

[89] J. W. Scott, R. S. Geels, S. W. Corzine, and L. A. Coldren, “Modeling temperature effects and spatial hole burning to optimize vertical-cavity surface-emitting laser performance,” *IEEE Journal of Quantum Electronics*, vol. 29, no. 5, pp. 1295–1308, May 1993.

[90] N. Bewtra, D. A. Suda, G. L. Tan, F. Chatenoud, and J. M. Xu, “Modeling of quantum-well lasers with electro-opto-thermal interaction,” *IEEE Journal of Selected Topics in Quantum Electronics*, vol. 1, no. 2, pp. 331–340, June 1995.

[91] M. Ariga, M. Arai, T. Kageyama, C. Setiagung, Y. Ikenaga, N. Iwai, H. Shimizu, K. Nishikata, A. Kasukawa, and F. Koyama, “Noise characteristics of GaInNAsSb 1300-nm-range VCSEL with optical feedback for isolator-free module,” *IEEE Journal of Selected Topics in Quantum Electronics*, vol. 11, no. 5, pp. 1074–1078, September 2005.

[92] N. Ledentsov, V. A. Shchukin, N. N. Ledentsov, J. R. Kropp, S. Burger, and F. Schmidt, “Direct evidence of the leaky emission in oxide-confined vertical cavity lasers,” *IEEE Journal of Quantum Electronics*, vol. 52, no. 3, pp. 1–7, March 2016.

[93] V. Shchukin, N. N. Ledentsov, J. Kropp, G. Steinle, N. Ledentsov, S. Burger, and F. Schmidt, “Single-mode vertical cavity surface emitting laser via oxide-aperture-engineering of leakage of high-order transverse modes,” *IEEE Journal of Quantum Electronics*, vol. 50, no. 12, pp. 990–995, December 2014.

[94] *Nonlinear Fiber Optics.* Singapore: Elsevier Inc.

[95] A. Gholami, D. Molin, and P. Sillard, “Physical modeling of 10 GbE optical communication systems,” *Journal of Lightwave Technology*, vol. 29, no. 1, pp. 115–123, January 2011.

[96] M. J. Adams, *Introduction to Optical Waveguides.* New York, NY: John Wiley & Sons, Inc., 1981.

[97] D. Gloge and E. A. J. Marcatili, "Multimode theory of graded-core fibers," *The Bell System Technical Journal*, vol. 52, no. 9, pp. 1563–1578, November 1973.

[98] B. E. A. Saleh and M. C. Teich, *Fundamentals of Photonics.* New York, NY: John Wiley & Sons, Inc., 1991.

[99] J. Gowar, *Optical Communication Systems.* New York, NY: Prentice Hall, 1984.

[100] D. G. Cunningham and W. G. Lane, *Gigabit Ethernet Networking.* Indianapolis, IN: Macmillan Technical Publishing, 1999.

[101] M. S. Sodha and A. K. Ghatak, *Inhomogeneous Optical Waveguides.* New York, NY: Plenum Press, 1977.

[102] A. R. Michelsone, *Guided Wave Optics.* New York, NY: Van Nostrand Reinhold, 1993.

[103] N. Guan, K. Takenaga, S. Matsuo, and K. Himeno, "Multimode fibers for compensating intermodal dispersion of graded-index multimode fibers," *Journal of Lightwave Technology*, vol. 22, no. 7, pp. 1714–1719, July 2004.

[104] T. I. Association, "TIA/EIA Standard: ANSI/TIA/EIA-568-B.3," April 2018, [Online]. Available: http://www.csd.uoc.gr/~hy435/material/TIA-EIA-568-B.3.pdf.

[105] P. Pepeljugoski, M. J. Hackert, J. S. Abbott, S. E. Swanson, S. E. Golowich, A. J. Ritger, P. Kolesar, Y. C. Chen, and P. Pleunis, "Development of system specification for laser-optimized 50- mu;m multimode fiber for multigigabit short-wavelength LANs," *Journal of Lightwave Technology*, vol. 21, no. 5, pp. 1256–1275, May 2003.

[106] P. Pleunis, "FO-4.2.1 Support for Dispersion Compensation," April 2018, [Online]. Available: http://www.ieee802.org/3/10GMMFSG/public/jan04/pleunis_1_0104.pdf.

[107] D. Molin, M. Bigot, F. Achten, A. Amezcua, and P. Sillard, "850-950nm wideBand OM4 multimode fiber for next-generation WDM

systems," in *Proc. Optical Fiber Communication Conference (OFC)*, March 2015, paper M3B.1.

[108] D. Molin, M. Bigot-Astruc, and P. Sillard, "New MMF and VCSEL metrics for system reach predictions," in *Proc. Optical Fiber Communication Conference (OFC)*, March 2014, paper Th3C.7.

[109] G. Kuyt and D. Comteq, "OM4 multimode fiber standardization," April 2018, [Online]. Available: http://www.ieee802.org/3/ba/public/jan08/kuyt_01_0108.pdf.

[110] "TIA standard for wideband multimode fiber, WBMMF, approved," [Online]. Available: http://www.cablinginstall.com/articles/2016/07/tia-standard-wbmmf-wideband-multimode-fiber.html.

[111] D. Kuchta, T. Huynh, F. Doany, A. Rylyakov, C. Schow, P. Pepeljugoski, D. Gazula, E. Shaw, and J. Tatum, "A 4-λ, 40Gb/s/λ Bandwidth Extension of Multimode Fiber in the 850nm range," in *Proc. Optical Fiber Communication Conference (OFC)*, March 2015, paper W1D.4.

[112] Y. Sun, R. Lingle, R. Shubochkin, A. H. McCurdy, K. Balemarthy, D. Braganza, J. Kamino, T. Gray, W. Fan, K. Wade, F. Chang, D. Gazula, G. Landry, J. Tatum, and S. Bhoja, "SWDM PAM4 Transmission Over Next Generation Wide-Band Multimode Optical Fiber," *Journal of Lightwave Technology*, vol. 35, no. 4, pp. 690–697, February 2017.

[113] M. Bigot, D. Molin, F. Achten, A. Amezcua-Correa, and P. Sillard, "Extra-Wide-Band OM4 MMF for Future 1.6Tbps Data Communications," in *Proc. Optical Fiber Communication Conference (OFC)*, March 2015, paper M2C.4.

[114] D. Molin, F. Achten, M. Bigot, A. Amezcua-Correa, and P. Sillard, "WideBand OM4 multi-mode fiber for next-generation 400Gbps data communications," in *2014 The European Conference on Optical Communication (ECOC)*, September 2014, paper P.1.6.

[115] S. E. Golowich, W. A. Reed, and A. J. Ritger, "A new modal power distribution measurement for high-speed short-reach optical systems," *Journal of Lightwave Technology*, vol. 22, no. 2, pp. 457–468, February 2004.

[116] G. Keiser, *Optical Fiber Communications*, 2011.

[117] H. Bülow, H. Al-Hashimi, and B. Schmauss, "Coherent multimode-fiber MIMO transmission with spatial constellation modulation," in *Proc. European Conference on Optical Communication (ECOC)*, September 2011, pp. 1–3, paper Tu.5.B.3.

[118] X. Liu, T. H. Wood, R. W. Tkach, and S. Chandrasekhar, "Demonstration of record sensitivity in an optically pre-amplified receiver by combining PDM-QPSK and 16-PPM with pilot-assisted digital coherent detection," in *Proc. Optical Fiber Communication Conference (OFC)*, March 2011, paper PDPB1.

[119] X. Liu, S. Chandrasekhar, T. H. Wood, R. W. Tkach, P. J. Winzer, E. C. Burrows, and A. R. Chraplyvy, "M-ary pulse-position modulation and frequency-shift keying with additional polarization/phase modulation for high-sensitivity optical transmission," *Optics Express*, vol. 19, no. 26, pp. B868–B881, December 2011.

[120] H. Bülow, U. Abay, A. Schenk, and J. B. Huber, "Coded modulation of polarization- and space-multiplexed signals," in *Proc. Asia Communications and Photonics Conference and Exhibition (ACP)*, November 2011, paper 3090W.

[121] J. A. Anguita, J. Herreros, and I. B. Djordjevic, "Coherent Multimode OAM Superpositions for Multidimensional Modulation," *IEEE Photonics Journal*, vol. 6, no. 2, pp. 1–11, April 2014.

[122] B. J. Puttnam, J. M. D. Mendinueta, R. S. Luś, T. A. Eriksson, Y. Awaji, N. Wada, and E. Agrell, "Single parity check multi-core modulation for power efficient spatial super-channels," in *Proc. European Conference on Optical Communication (ECOC)*, September 2014, paper Mo.3.3.5.

[123] G. Rademacher, B. J. Puttnam, R. S. Luś, Y. Awaji, N. Wada, E. Agrell, and K. Petermann, "Experimental investigation of a 16-dimensional modulation format for long-haul multi-core fiber transmission," in *Proc. European Conference on Optical Communication (ECOC)*, September 2015, paper P.5.10.

[124] B. J. Puttnam, J. M. D. Mendinueta, R. S. Luís, W. Klaus, J. Sakaguchi, Y. Awaji, N. Wada, T. A. Eriksson, E. Agrell, P. A. Andrek-

son, and M. Karlsson, “Energy efficient modulation formats for multicore fibers,” in *Proc. Opto-Electronics and Communications Conference (OECC)*, July 2014, pp. 694–696.

[125] H. Zhang, A. Turukhin, O. V. Sinkin, W. Patterson, H. G. Batshon, Y. Sun, C. R. Davidson, M. Mazurczyk, G. Mohs, D. G. Foursa, and A. Pilipetskii, “Power-efficient 100 Gb/s transmission over transoceanic distance using 8-dimensional coded modulation,” in *Proc. European Conference on Optical Communication (ECOC)*, September 2015, paper Th.2.2.1.

[126] A. D. Shiner, M. Reimer, A. Borowiec, S. O. Gharan, J. Gaudette, P. Mehta, D. Charlton, K. Roberts, and M. O’Sullivan, “Demonstration of an 8-dimensional modulation format with reduced interchannel nonlinearities in a polarization multiplexed coherent system,” *Optics Express*, vol. 22, no. 17, pp. 20 366–20 374, August 2014.

[127] S. Ishimura and K. Kikuchi, “Multi-dimensional permutation modulation aiming at both high spectral efficiency and high power efficiency,” in *Proc. Optical Fiber Communication Conference (OFC)*, March 2014, paper M3A.2.

[128] A. Ludwig, M.-L. Schulz, P. Schindler, S. Wolf, C. Koos, W. Freude, and J. Leuthold, “Stacked modulation formats enabling highest-sensitivity optical free-space links,” *Optics Express*, vol. 23, no. 17, pp. 21 942–21 957, August 2015.

[129] T. C. Hales, M. Adams, G. Bauer, D. T. Dang, J. Harrison, T. L. Hoang, C. Kaliszyk, V. Magron, S. McLaughlin, T. T. Nguyen, T. Q. Nguyen, T. Nipkow, S. Obua, J. Pleso, J. Rute, A. Solovyev, A. H. T. Ta, T. N. Tran, D. T. Trieu, J. Urban, K. K. Vu, and R. Zumkeller, “A formal proof of the Kepler conjecture,” in *eprint arXiv:1501.02155*, January 2015. [Online]. Available: https://arxiv.org/abs/1501.02155

[130] M. Viazovska, “The sphere packing problem in dimension 8,” in *eprint arXiv:1603.04246*, May 2016. [Online]. Available: https://arxiv.org/abs/1603.04246

[131] H. Cohn, A. Kumar, S. Miller, D. Radchenko, and M. Viazovska, “The sphere packing problem in dimension 24,” *Annals of Mathematics*, vol. 85, no. 3, pp. 1017–1033, August 2017.

[132] M. B. Othman, X. Zhang, L. Deng, M. Wieckowski, J. B. Jensen, and I. T. Monroy, "Experimental Investigations of 3-D-/4-D-CAP Modulation With Directly Modulated VCSELs," *IEEE Photonics Technology Letters*, vol. 24, no. 22, pp. 2009–2012, November 2012.

[133] G. Nebe and N. Sloane, "A catalogue of lattices," RWTH-Aachen University, April 2018, [Online]. Available: http://www.math.rwth-aachen.de/~Gabriele.Nebe/LATTICES/.

[134] J. H. Conway, N. J. A. Sloane, and E. Bannai, *Sphere-packings, Lattices, and Groups.* New York, NY: Springer-Verlag New York, Inc., 1987.

[135] Wikipedia, "16-cell honeycomb," April 2018, [Online]. Available: https://en.wikipedia.org/wiki/16-cell_honeycomb.

[136] ——, "E8 lattice," April 2018, [Online]. Available: https://en.wikipedia.org/wiki/E8_lattice.

[137] ——, "Leech lattice," April 2018, [Online]. Available: https://en.wikipedia.org/wiki/Leech_lattice.

[138] M. Karlsson and E. Agrell, "Multidimensional optimized optical modulation formats," pp. 13–64, 2016.

[139] N. J. A. Sloane, R. H. Hardin, T. D. S. Duff, and J. H. Conway, "Minimal-energy clusters of hard-spheres," *Discrete and Computational Geometry*, vol. 14, no. 3, pp. 237–259, 1995.

[140] ——, "Minimal energy clusters," April 2018, [Online]. Available: http://neilsloane.com/cluster/.

[141] G. F. Tóth, P. Gritzmann, and J. M. Wills, "finite sphere packing and sphere covering," *Discrete and Computational Geometry*, vol. 4, no. 1, pp. 19–40, 1989.

[142] J. E. Porath and T. Aulin, "Design of multidimensional signal constellations," *IEEE Proceedings-Communications*, vol. 150, no. 5, pp. 317–23–, October 2003.

[143] T. A. Eriksson, S. Alreesh, C. Schmidt-Langhorst, F. Frey, P. W. Berenguer, C. Schubert, J. K. Fischer, P. A. Andrekson, M. Karlsson,

and E. Agrell, “Experimental investigation of a four-dimensional 256-ary lattice-based modulation format,” in *Proc. Optical Fiber Communication Conference (OFC)*, March 2015, paper W4K.3.

[144] G. D. Forney and L. F. Wei, “Multidimensional constellations. I. Introduction, figures of merit, and generalized cross constellations,” *IEEE Journal on Selected Areas in Communications*, vol. 7, no. 6, pp. 877–892, August 1989.

[145] F. R. Kschischang and S. Pasupathy, “Optimal nonuniform signaling for Gaussian channels,” *IEEE Transactions on Information Theory*, vol. 39, no. 3, pp. 913–929, May 1993.

[146] D. S. Millar, T. Koike-Akino, K. Kojima, and K. Parsons, “A 24-dimensional modulation format achieving 6 dB asymptotic power efficiency,” in *Proc. Advanced Photonics*, July 2013, paper SPM3D.6.

[147] G. Welti and J. Lee, “Digital transmission with coherent four-dimensional modulation,” *IEEE Transactions on Information Theory*, vol. 20, no. 4, pp. 497–502, July 1974.

[148] L. Zetterberg and H. Brändström, “Codes for combined phase and amplitude modulated signals in a four-dimensional space,” *IEEE Transactions on Communications*, vol. 25, no. 9, pp. 943–950, September 1977.

[149] S. Betti, F. Curti, G. D. Marchis, and E. Iannone, “A novel multilevel coherent optical system: 4-quadrature signaling,” *Journal of Lightwave Technology*, vol. 9, no. 4, pp. 514–523, April 1991.

[150] S. Betti, F. Curti, G. de Marchis, and E. Iannone, “Exploiting fibre optics transmission capacity: 4-quadrature multilevel signalling,” *Electronics Letters*, vol. 26, no. 14, pp. 992–993, July 1990.

[151] R. Cusani, E. Iannone, A. M. Salonico, and M. Todaro, “An efficient multilevel coherent optical system: M-4Q-QAM,” *Journal of Lightwave Technology*, vol. 10, no. 6, pp. 777–786, June 1992.

[152] S. Benedetto and P. Poggiolini, “Theory of polarization shift keying modulation,” *IEEE Transactions on Communications*, vol. 40, no. 4, pp. 708–721, April 1992.

[153] S. G. Wilson, H. A. Sleeper, and N. K. Srinath, "Four dimensional modulation and coding: An alternate to frequency-reuse," vol. 2, 1984, pp. 919–923.

[154] E. Agrell and M. Karlsson, "Power-efficient modulation formats in coherent transmission systems," *Journal of Lightwave Technology*, vol. 27, no. 22, pp. 5115–5126, November 2009.

[155] F. Buchali and H. Bülow, "Experimental transmission with POLQAM and PS-QPSK modulation format using a 28-Gbaud 4-D transmitter," in *Proc. European Conference on Optical Communication (ECOC)*, September 2012, paper We.3.A.1.

[156] J. K. Fischer, S. Alreesh, R. Elschner, F. Frey, C. Meuer, L. Molle, C. Schmidt-Langhorst, T. Tanimura, and C. Schubert, "Experimental investigation of 126-Gb/s 6PolSK-QPSK signals," in *Proc. European Conference on Optical Communication (ECOC)*, September 2012.

[157] H. Bülow, T. Rahman, F. Buchali, W. Idler, and W. Kuebart, "Transmission of 4-D modulation formats at 28-Gbaud," in *Proc. Optical Fiber Communication Conference (OFC)*, March 2013, paper JW2A.39.

[158] D. Lavery, C. Behrens, S. Makovejs, D. S. Millar, R. I. Killey, S. J. Savory, and P. Bayvel, "Long-haul transmission of PS-QPSK at 100 Gb/s using digital backpropagation," *IEEE Photonics Technology Letters*, vol. 24, no. 3, pp. 176–178, February 2012.

[159] D. S. Millar, D. Lavery, S. Makovejs, C. Behrens, B. C. Thomsen, P. Bayvel, and S. J. Savory, "Generation and long-haul transmission of polarization-switched QPSK at 42.9 Gb/s," *Optics Express*, vol. 19, no. 10, pp. 9296–9302, May 2011.

[160] M. Nölle, J. K. Fischer, L. Molle, C. Schmidt-Langhorst, D. Peckham, and C. Schubert, "Comparison of 8 × 112 Gb/s PS-QPSK and PDM-QPSK signals over transoceanic distances," *Optics Express*, vol. 19, no. 24, pp. 24 370–24 375, November 2011.

[161] M. Sjödin, P. Johannisson, H. Wymeersch, P. A. Andrekson, and M. Karlsson, "Comparison of polarization-switched QPSK and polarization-multiplexed QPSK at 30 Gbit/s," *Optics Express*, vol. 19, no. 8, pp. 7839–7846, April 2011.

[162] L. E. Nelson, X. Zhou, N. M. Suibhne, A. D. Ellis, and P. Magill, "Experimental comparison of coherent polarization-switched QPSK to polarization-multiplexed QPSK for 10 × 100 km WDM transmission," *Optics Express*, vol. 19, no. 11, pp. 10 849–10 856, May 2011.

[163] T. A. Eriksson, P. Johannisson, M. Sjödin, E. Agrell, P. A. Andrekson, and M. Karlsson, "Frequency and polarization switched QPSK," in *Proc. European Conference on Optical Communication (ECOC)*, September 2013, paper Th.2.D.4.

[164] J. K. Fischer, L. Molle, M. Nölle, D. D. Groß, and C. Schubert, "Experimental investigation of 28-GBd polarization-switched quadrature phase-shift keying signals," in *Proc. European Conference on Optical Communication (ECOC)*, September 2011, paper Mo.2.B.1.

[165] J. Renaudier, O. Bertran-Pardo, H. Mardoyan, M. Salsi, P. Tran, E. Dutisseuil, G. Charlet, and S. Bigo, "Experimental comparison of 28Gbaud polarization switched-and polarization division multiplexed-QPSK in WDM long-haul transmission system," in *Proc. European Conference on Optical Communication (ECOC)*, September 2011, paper Mo.2.B.3.

[166] P. Poggiolini, G. Bosco, A. Carena, V. Curri, and F. Forghieri, "Performance evaluation of coherent WDM PS-QPSK (HEXA) accounting for non-linear fiber propagation effects," *Optics Express*, vol. 18, no. 11, pp. 11 360–11 371, May 2010.

[167] R. Elschner, F. Frey, C. Meuer, J. K. Fischer, S. Alreesh, C. Schmidt-Langhorst, L. Molle, T. Tanimura, and C. Schubert, "Experimental demonstration of a format-flexible single carrier coherent receiver using data-aided digital signal processing," in *Proc. European Conference on Optical Communication (ECOC)*, September 2012, paper We.1.A.4.

[168] J. K. Fischer, S. Alreesh, R. Elschner, F. Frey, M. Nölle, and C. Schubert, "Bandwidth-variable transceivers based on 4D modulation formats for future flexible networks," in *Proc. European Conference on Optical Communication (ECOC)*, September 2013, paper Tu.3.C.1.

[169] M. Sjödin, T. A. Eriksson, P. A. Andrekson, and M. Karlsson, "Long-haul transmission of PM-2PPM-QPSK at 42.8 Gbit/s," in *Proc. Optical Fiber Communication Conference (OFC)*, March 2013, paper OTu2B.

[170] G. Ungerboeck, “Trellis-coded modulation with redundant signal sets Part I: Introduction,” *IEEE Communications Magazine*, vol. 25, no. 2, pp. 5–11, February 1987.

[171] ——, “Channel coding with multilevel/phase signals,” *IEEE Transactions on Information Theory*, vol. 28, no. 1, pp. 55–67, January 1982.

[172] L. D. Coelho and N. Hanik, “Global optimization of fiber-optic communication systems using four-dimensional modulation formats,” in *Proc. European Conference on Optical Communication (ECOC)*, September 2011, paper Mo.2.B.4.

[173] M. Karlsson and E. Agrell, “Spectrally efficient four-dimensional modulation,” in *Proc. Optical Fiber Communication Conference (OFC)*, March 2012, paper OTu2C.1.

[174] J. Renaudier, A. Voicila, O. Bertran-Pardo, O. Rival, M. Karlsson, G. Charlet, and S. Bigo, “Comparison of set-partitioned two-polarization 16QAM formats with PDM-QPSK and PDM-8QAM for optical transmission systems with error-correction coding,” in *Proc. Optical Fiber Communication Conference (OFC)*, September 2012, paper We.1.C.5.

[175] T. A. Eriksson, M. Sjödin, P. A. Andrekson, and M. Karlsson, “Experimental demonstration of 128-sp-qam in uncompensated long-haul transmission,” in *Proc. Optical Fiber Communication Conference (OFC)*, March 2013, paper OTu3B.2.

[176] B. Zhu, T. Taunay, M. Fishteyn, X. Liu, S. Chandrasekhar, M. F. Yan, J. M. Fini, E. M. Monberg, and F. V. Dimarcello, “112-Tb/s Space-division multiplexed DWDM transmission with 14-b/s/Hz aggregate spectral efficiency over a 76.8-km seven-core fiber,” *Optics Express*, vol. 19, no. 17, pp. 16 665–16 671, August 2011.

[177] C. Okonkwo, R. van Uden, H. Chen, H. de Waardt, and T. Koonen, “Advanced coding techniques for few mode transmission systems,” *Optics Express*, vol. 23, no. 2, pp. 1411–1420, January 2015.

[178] S. Alreesh, C. Schmidt-Langhorst, F. Frey, P. W. Berenguer, C. Schubert, and J. K. Fischer, “Transmission Performance of 4D 128SP-QAM With Forward Error Correction Coding,” *IEEE Photonics Technology Letters*, vol. 27, no. 7, pp. 744–747, April 2015.

[179] H. Sun, R. Egorov, B. E. Basch, J. McNicol, and K. T. Wu, "Comparison of two modulation formats at spectral efficiency of 5 bits/dual-pol symbol," in *Proc. European Conference on Optical Communication (ECOC)*, September 2013, paper Th.2.D.3.

[180] J. Renaudier, O. Bertran-Pardo, A. Ghazisaeidi, P. Tran, H. Mardoyan, P. Brindel, A. Voicila, G. Charlet, and S. Bigo, "Experimental Transmission of Nyquist Pulse Shaped 4-D Coded Modulation using Dual Polarization 16QAM Set-Partitioning Schemes at 28 Gbaud," in *Proc. Optical Fiber Communication Conference (OFC)*, March 2013, paper OTu3B.1.

[181] B. J. Puttnam, R. S. Luís, W. Klaus, J. Sakaguchi, J. M. D. Mendinueta, Y. Awaji, N. Wada, Y. Tamura, T. Hayashi, M. Hirano, and J. Marciante, "2.15 Pb/s transmission using a 22 core homogeneous single-mode multi-core fiber and wideband optical comb," in *Proc. European Conference on Optical Communication (ECOC)*, paper PDP.3.1.

[182] J. K. Fischer, C. Schmidt-Langhorst, S. Alreesh, R. Elschner, F. Frey, P. W. Berenguer, L. Molle, M. Nölle, and C. Schubert, "Transmission of 512SP-QAM Nyquist-WDM signals," in *Proc. European Conference on Optical Communication (ECOC)*, September 2014, paper Tu.3.3.2.

[183] M. Karlsson and E. Agrell, "Four-dimensional optimized constellations for coherent optical transmission systems," in *Proc. European Conference on Optical Communication (ECOC)*, September 2010, paper We.8.C.3.

[184] J. Karout, X. Liu, S. Chandrasekhar, E. Agrell, M. Karlsson, and R. J. Essiambre, "Experimental demonstration of an optimized 16-ary four-dimensional modulation format using optical OFDM," in *Proc. Optical Fiber Communication Conference (OFC)*, March, paper OW3B.4.

[185] M. Sjödin, E. Agrell, and M. Karlsson, "Subset-optimized polarization-multiplexed PSK for fiber-optic communications," *IEEE Communications Letters*, vol. 17, no. 5, pp. 838–840, May 2013.

[186] G. D. Forney, "Coset codes. I. Introduction and geometrical classification," *IEEE Transactions on Information Theory*, vol. 34, no. 5, pp. 1123–1151, September 1988.

[187] S. Hranilovic and F. R. Kschischang, “Optical intensity-modulated direct detection channels: signal space and lattice codes,” *IEEE Transactions on Information Theory*, vol. 49, no. 6, pp. 1385–1399, June 2003.

[188] J. Karout, G. Kramer, F. R. Kschischang, and E. Agrell, “A two-dimensional signal space for intensity-modulated channels,” *IEEE Communications Letters*, vol. 16, no. 9, pp. 1361–1364, September 2012.

[189] K. Szczerba, J. Karout, E. Agrell, P. Westbergh, M. Karlsson, P. Andrekson, and A. Larsson, “Demonstration of 8-level subcarrier modulation sensitivity improvement in an IM/DD system,” in *Proc. European Conference on Optical Communication (ECOC)*, September 2011, paper We.10.P1.117.

[190] K. Szczerba, J. Karout, M. Karlsson, P. A. Andrekson, and E. Agrell, “Optimized lattice-based 16-level subcarrier modulation for IM/DD systems,” in *Proc. European Conference on Optical Communication (ECOC)*, September, paper Mo.1.B.4.

[191] J. Karout, E. Agrell, K. Szczerba, and M. Karlsson, “Designing power-efficient modulation formats for noncoherent optical systems,” in *Proc. IEEE Global Telecommunications Conference (GLOBECOM)*, December 2011.

[192] C. Prodaniuc, N. Stojanovic, F. Karinou, Z. Qiang, and R. Llorente, “Performance comparison between 4D Trellis coded modulation and PAM-4 for low-cost 400 Gbps WDM optical networks,” *Journal of Lightwave Technology*, vol. 34, no. 22, pp. 5308–5316, November 2016.

[193] Y. Fu, M. Bi, D. Feng, X. Miao, H. He, and W. Hu, “Spectral efficiency improved 2D-PAM8 Trellis coded modulation for short reach optical system,” *IEEE Photonics Journal*, vol. 9, no. 4, pp. 1–8, August 2017.

[194] K. Szczerba, P. Westbergh, M. Karlsson, P. A. Andrekson, and A. Larsson, “70 Gbps 4-PAM and 56 Gbps 8-PAM using an 850 nm VCSEL,” *Journal of Lightwave Technology*, vol. 33, no. 7, pp. 1395–1401, April 2015.

[195] K. Szczerba, P. Westbergh, J. Karout, J. S. Gustavsson, Å. Haglund, M. Karlsson, P. A. Andrekson, E. Agrell, and A. Larsson, “4-PAM for

high-speed short-range optical communications," *IEEE/OSA Journal of Optical Communications and Networking*, vol. 4, no. 11, pp. 885–894, November 2012.

[196] G. Ungerboeck, "Trellis-coded modulation with redundant signal sets Part II: State of the art," *IEEE Communications Magazine*, vol. 25, no. 2, pp. 12–21, February 1987.

[197] Y. Be'ery, B. Shahar, and J. Snyders, "Fast decoding of the Leech lattice," *IEEE Journal on Selected Areas in Communications*, vol. 7, no. 6, pp. 959–967, August 1989.

[198] J. Lee, P. Dong, N. Kaneda, and Y. K. Chen, "Discrete multitone transmission for short-reach optical connections," in *Proc. Optical Fiber Communication Conference (OFC)*, March 2016, paper Th1G.1.

[199] A. Alvarado and E. Agrell, "Four-dimensional coded modulation with bit-wise decoders for future optical communications," *Journal of Lightwave Technology*, vol. 33, no. 10, pp. 1993–2003, May 2015.

[200] W. Shieh and I. Djordjevic, *OFDM for Optical Communications.* Singapore: Elsevier, 2011.

[201] S. Weinstein and P. Ebert, "Data transmission by frequency-division multiplexing using the discrete Fourier transform," *IEEE Transactions on Communication Technology*, vol. 19, no. 5, pp. 628–634, October 1971.

[202] R. P. Shinsuke Hara, *Multicarrier Techniques for 4G Mobile Communications.* Boston: Artech House, 2003.

[203] J. Campello, "Practical bit loading for DMT," in *Proc. IEEE International Conference on Communications*, vol. 2, Vancouver, BC, Canada, June 1999, pp. 801–805.

[204] S. C. J. Lee, F. Breyer, S. Randel, H. P. A. van den Boom, and A. M. J. Koonen, "High-speed transmission over multimode fiber using discrete multitone modulation," *Journal of Optical Communications and Networking*, vol. 7, no. 2, pp. 183–196, February 2008.

[205] J. L. Wei, L. Geng, R. V. Penty, I. H. White, and D. G. Cunningham, "100 Gigabit Ethernet transmission enabled by carrierless amplitude

and phase modulation using QAM receivers," in *Proc. Optical Fiber Communication Conference (OFC)*, 2013.

[206] D. D. Falconer, "Carrierless AM/PM," NJ, USA, July 1975.

[207] A. F. Shalash and K. K. Parhi, "Multidimensional carrierless AM/PM systems for digital subscriber loops," *IEEE Transactions on Communications*, vol. 47, no. 11, pp. 1655–1667, November 1999.

[208] G. H. Im, D. B. Harman, G. Huang, A. V. Mandzik, M. H. Nguyen, and J. J. Werner, "51.84 Mb/s 16-CAP ATM LAN standard," *IEEE Journal on Selected Areas in Communications*, vol. 13, no. 4, pp. 620–632, May 1995.

[209] J. Gao and Y. H. Leung, "A new adaptive equalizer for carrierless amplitude and phase (CAP) receivers," in *Proc. IEEE International Symposium on Circuits and Systems (ISCAS)*, vol. 3, July 1999, pp. 90–93.

[210] M. B. Othman, X. Zhang, L. Deng, M. Wieckowski, J. B. Jensen, and I. T. Monroy, "Experimental Investigations of 3-D-/4-D-CAP Modulation With Directly Modulated VCSELs," *IEEE Photonics Technology Letters*, vol. 24, no. 22, pp. 2009–2012, November 2012.

[211] J. D. Ingham, R. V. Penty, I. H. White, and D. G. Cunningham, "Carrierless amplitude and phase modulation for low-cost, high-spectral-efficiency optical datacommunication links," in *Proc. Conference on Lasers and Electro-Optics/ Quantum Electronics Laser Science Conference (CLEO/QELS)*, 2010, paper CThC5.

[212] ——, "40 Gb/s carrierless amplitude and phase modulation for low-cost optical datacommunication links," in *Proc. Optical Fiber Communication Conference (OFC)*, March 2011, paper OThZ3.

[213] M. I. Olmedo, Z. Tianjian, J. B. Jensen, Z. Qiwen, X. Xiaogeng, and I. T. Monroy, "Towards 400GBASE 4-lane solution using direct detection of MultiCAP signal in 14 GHz bandwidth per lane," in *Proc. Optical Fiber Communication Conference (OFC)*, March 2013, paper PDP5C.10.

[214] M. I. Olmedo, T. Zuo, J. B. Jensen, Q. Zhong, X. Xu, S. Popov, and I. T. Monroy, "Multiband carrierless amplitude phase modulation for

high capacity optical data links," *Journal of Lightwave Technology*, vol. 32, no. 4, pp. 798–804, February 2014.

[215] J. Estaran, M. I. Olmedo, D. Zibar, X. Xu, and I. T. Monroy, "First experimental demonstration of coherent CAP for 300-Gb/s metropolitan optical networks," in *Proc. Optical Fiber Communication Conference (OFC)*, March 2014, paper Th3K.3.

[216] J. Proakis, *Digital Communications.* New York, NY: McGraw-Hill, 2001.

[217] A. Tatarczak, M. A. Usuga Castaneda, and I. Tafur Monroy, "OAM-enhanced transmission for multimode short-range links," *Proc. SPIE*, vol. 9390, p. 93900E, 2015.

[218] S. Motaghiannezam, A. Tatarczak, H. Chen, J. Tatum, and C. Kocot, "51.56 Gbps PAM4 transmission over up to 2.3 km OM4 Fiber using mode selective VCSEL," in *Proc. Optical Fiber Communication Conference (OFC).* Optical Society of America, 2018, paper M1I.3.

[219] Z. Haas and M. A. Santoro, "A mode-filtering scheme for improvement of the bandwidth-distance product in multimode fiber systems," *Journal of Lightwave Technology*, vol. 11, no. 7, pp. 1125–1131, July 1993.

[220] G. Stepniak, J.-R. Kropp, N. N. Ledentsov, V. A. Shchukin, N. Ledentsov, G. Schaefer, and J. P. Turkiewicz, "54 Gbps OOK Transmission Using Single Mode VCSEL up to 1 km OM4 MMF," in *Proc. Optical Fiber Communication Conference (OFC)*, March 2016, paper Th4D.5.

[221] R. Safaisini, E. Haglund, P. Westbergh, J. S. Gustavsson, and A. Larsson, "20 Gbit/s data transmission over 2 km multimode fibre using 850 nm mode filter VCSEL," *Electronics Letters*, vol. 50, no. 1, pp. 40–42, January 2014.

[222] L. Geng, S. H. Lee, K. Williams, R. Penty, I. White, and D. Cunningham, "Symmetrical 2-D Hermite-Gaussian square launch for high bit rate transmission in multimode fiber links," in *Proc. Optical Fiber Communication Conference (OFC)*, 2011, paper OWJ5.

[223] J. Carpenter and T. D. Wilkinson, "Characterization of multimode fiber by selective mode excitation," *Journal of Lightwave Technology*, vol. 30, no. 10, pp. 1386–1392, May 2012.

[224] E. Alon, V. Stojanovic, J. M. Kahn, S. Boyd, and M. Horowitz, "Equalization of modal dispersion in multimode fiber using spatial light modulators," in *Proc. IEEE Global Telecommunications Conference (GLOBECOM)*, vol. 2, November 2004, pp. 1023–1029.

[225] G. Stepniak, L. Maksymiuk, and J. Siuzdak, "Binary-phase spatial light filters for mode-selective excitation of multimode fibers," *Journal of Lightwave Technology*, vol. 29, no. 13, pp. 1980–1987, July 2011.

[226] R. A. Panicker and J. M. Kahn, "Algorithms for compensation of multimode fiber dispersion using adaptive optics," *Journal of Lightwave Technology*, vol. 27, no. 24, pp. 5790–5799, December 2009.

[227] C. Koebele, M. Salsi, D. Sperti, P. Tran, P. Brindel, H. Mardoyan, S. Bigo, A. Boutin, F. Verluise, P. Sillard, M. Astruc, L. Provost, F. Cerou, and G. Charlet, "Two mode transmission at 2x100Gb/s, over 40km-long prototype few-mode fiber, using LCOS-based programmable mode multiplexer and demultiplexer," *Optics Express*, vol. 19, no. 17, pp. 16 593–16 600, August 2011.

[228] S. Randel, R. Ryf, A. Gnauck, M. A. Mestre, C. Schmidt, R. Essiambre, P. Winzer, R. Delbue, P. Pupalaikis, A. Sureka, Y. Sun, X. Jiang, and R. Lingle, "Mode-Multiplexed 6×20-GBd QPSK Transmission over 1200-km DGD-Compensated Few-Mode Fiber," in *Proc. Optical Fiber Communication Conference (OFC)*. Optical Society of America, March 2012, paper PDP5C.5.

[229] I. A. Litvin, A. Dudley, F. S. Roux, and A. Forbes, "Azimuthal decomposition with digital holograms," *Optics Express*, vol. 20, no. 10, pp. 10 996–11 004, May 2012.

[230] V. S. Lyubopytov, V. K. Bagmanov, and A. K. Sultanov, "Adaptive SLM-based compensation of intermodal interference in few-mode optical fibers," *Proc. SPIE*, vol. 9216, p. 92160I, 2014.

[231] X. Pang, J. V. Kerrebrouck, O. Ozolins, R. Lin, A. Udalcovs, L. Zhang, S. Spiga, M. C. Amann, G. V. Steenberge, L. Gan, M. Tang, S. Fu, R. Schatz, G. Jacobsen, S. Popov, D. Liu, W. Tong, G. Torfs, J. Bauwelinck, X. Yin, and J. Chen, "7×100 Gbps PAM-4 transmission over 1-km and 10-km single mode 7-core fiber using 1.5-μm SM-VCSEL," in *Proc. Optical Fiber Communication Conference (OFC)*, 2018, paper M1I.4.

[232] T. Fehenberger and N. Hanik, “Multi-dimensional demappers for optical fiber systems with soft-decision forward error correction,” in *Proc. International Conference on Transparent Optical Networks (ICTON)*, July 2016, pp. 1–4.

[233] F. Buchali, G. Böcherer, W. Idler, L. Schmalen, P. Schulte, and F. Steiner, “Experimental demonstration of capacity increase and rate-adaptation by probabilistically shaped 64-QAM,” in *Proc. European Conference on Optical Communication (ECOC)*, September 2015, pp. 1–3, paper Mo.3.3.5.

[234] P. Schulte, F. Steiner, and G. Bocherer, “Four dimensional probabilistic shaping for fiber-optic communication,” in *Advanced Photonics 2017 (IPR, NOMA, Sensors, Networks, SPPCom, PS)*, July 2017, paper SpM2F.5.

[235] X. Zhou and H. Liu, “Constellation Shaping: Can It be Useful for Datacenter Reach Communication?” April 2017, [Online]. Available: https://static.googleusercontent.com/media/research.google.com/zh-CN//pubs/archive/46401.pdf.

[236] T. Gruber, S. Cammerer, J. Hoydis, and S. ten Brink, “On deep learning-based channel decoding,” in *eprint arXiv:1701.07738*, January 2015. [Online]. Available: https://arxiv.org/abs/1701.07738

List of Acronyms

2-D	two-dimensional
3-D	three-dimensional
24-D	twenty-four-dimensional
4-D	four-dimensional
5G	fifth generation
8-D	eight-dimensional
ADC	analog-to-digital converter
APE	asymptotic power efficiency
DSL	digital subscriber line
AOC	active optical cable
ASE	amplified spontaneous emission
AWG	arbitrary waveform generator
AWGN	additive white Gaussian noise
BER	bit error rate
BERT	bit error rate tester
BTB	back-to-back
CAP	carrier-less amplitude phase modulation
CDR	clock and data recovery
CFM	constellation figure of merit
CGH	computer-generated holography
CP	cyclic prefix
CTLE	continuous time linear equalization
CWDM	coarse wavelength division multiplexing
DAC	digital-to-analog converter
DBR	distributed Bragg reflector
DC	direct current
DCI	datacenter interconnection
DFB	distributed feedback laser

DFE	decision feedback equalizer
DFT	discrete Fourier transform
DMD	differential mode delay
DMT	discrete multi-tone modulation
DOE	diffractive optical element
DSO	digital storage oscilloscope
DSP	digital signal processing
EAM	electro-absorption modulator
EB	effective bandwidth
ED	Euclidean distance
EDFA	erbium doped fiber amplifier
EF	encircled flux
EM	electromagnetic
EMB	effective modal bandwidth
EVB	evaluation board
FEC	forward error correction
FFE	feed-forward equalizer
FFT	fast Fourier transform
FMF	few mode fiber
FMDM	few mode division multiplexing
GMI	generalized mutual information
HD	hard-decision
HD-FEC	hard-decision feed-forward error correction
HPC	high performance computing
I	in-phase
IC	integrated circuit
ICI	inter-carrier interference
IDFT	inverse discrete Fourier transform
IFFT	inverse fast Fourier transform
IIR	infinite impulse response
IM-DD	intensity-modulated direct-detection
IM	intensity-modulated
IMI	intermodal interference
ISI	inter-symbol interference
L-I	light-current
L-I-V	light-current-voltage
LED	light-emitting diode
LG	Laguerre-Gaussian
LMS	least-mean-square

LNA	low-noise amplifier
LP	linearly polarized
LPF	low-pass filter
LTE	long term evolution
LUT	look-up table
MCF	multi-core fiber
MD	multi-dimensional
MD-PAM	multi-dimensional PAM
MDM	mode division multiplexing
MicroQSFP	micro quad small form-factor pluggable
MIMO	multi-input multi-output
ML	maximum likelihood
MLSE	maximum likelihood sequence estimation
MM-VCSEL	multi-mode vertical-cavity surface-emitting laser
MMED	minimum mutual Euclidean distance
MMSE	minimum mean square error
MM	multi-mode
MMF	multi-mode fiber
MPN	mode partition noise
MSA	multi-source agreement
MSM	multi-subcarrier modulation
MTF	modulation transfer function
MZM	Mach-Zehnder modulator
NRZ	non-return-to-zero
OAM	orbital angular momentum
OBTB	optical back-to-back
OFDM	orthogonal frequency division multiplexing
OFL	over-filled launching
OH	overhead
OOK	on-off keying
OSFP	octal small form-factor pluggable
OTN	optical transmission network
PAM	pulse amplitude modulation
PAM-2	pulse amplitude modulation with 2 levels
PAM-4	pulse amplitude modulation with 4 levels
PAM-8	pulse amplitude modulation with 8 levels

PAPR	peak-to-average power ratio
PCB	printed circuit board
PCS	probabilistic constellation shaping
PD	photodiode
PDM	polarization division multiplexing
PDM-QAM	polarization division multiplexing quadrature amplitude modulation
PDM-QPSK	polarization division multiplexing quadrature phase shift keying
PL	power loading
PPM	pulse position modulation
PRBS	pseudo random bit sequence
PS-QPSK	polarization switching quadrature phase shift keying
Q	quadrature
QAM	quadrature amplitude modulation
QPSK	quadrature phase shift keying
QSFP	quad small form-factor pluggable
QSFP28	quad small form-factor pluggable with 4×28 Gb/s interface
QSFP-DD	quad small form-factor pluggable double density
RF	radio frequency
RIN	relative intensity noise
RoF	radio-over-fiber
ROSA	receiver optical subassembly
RS	Reed-Solomon
SD	soft-decision
SDM	spatial division multiplexing
SE	spectral efficiency
SER	symbol-to-noise ratio
SFP	small form-factor pluggable
SG	sub-group
SLM	spatial light modulator
SM	single-mode
SMF	single-mode fiber
SSMF	standard single-mode-fiber
SNR	signal-to-noise ratio
SP	set-partitioning

SPC	single parity check
SWDM	shortwave division multiplexing
TCM	trellis coded modulation
TEC	thermoelectric cooler
TIA	trans-impedance amplifier
TOR	top-of-rack
TOSA	transmitter optical sub-assembly
VCSEL	vertical-cavity surface-emitting laser
VCSELs	vertical-cavity surface-emitting lasers
VNA	vector network analyzer
VOA	variable optical attenuator
WDM	wavelength division multiplexing